



Durham E-Theses

X-ray luminous clusters of galaxies at $z = 0.3$

Courtney, Nathan James Daniel

How to cite:

Courtney, Nathan James Daniel (2003) *X-ray luminous clusters of galaxies at $z = 0.3$* , Durham theses, Durham University. Available at Durham E-Theses Online: <http://etheses.dur.ac.uk/4001/>

Use policy

The full-text may be used and/or reproduced, and given to third parties in any format or medium, without prior permission or charge, for personal research or study, educational, or not-for-profit purposes provided that:

- a full bibliographic reference is made to the original source
- a [link](#) is made to the metadata record in Durham E-Theses
- the full-text is not changed in any way

The full-text must not be sold in any format or medium without the formal permission of the copyright holders.

Please consult the [full Durham E-Theses policy](#) for further details.

X-Ray Luminous Clusters of Galaxies at $z > 0.3$

Nathan James Daniel Courtney

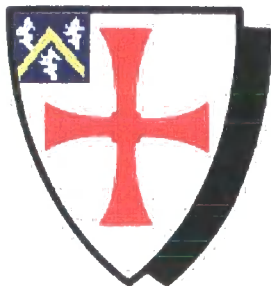
A dissertation submitted to the University of Durham
in accordance with the regulations for
admission to the degree of Doctor of Philosophy.

The copyright of this work rests with the author at all times.
No quotation from it should be published without his prior written
consent and information derived from it shall be acknowledged.

Department of Physics, University of Durham.

October 2003.

**A copyright of this thesis rests
with the author. No quotation
from it should be published
without his prior written consent
and information derived from it
should be acknowledged.**



- 2 JUN 2004

Ph.D. THESIS ABSTRACT

X-RAY LUMINOUS CLUSTERS OF GALAXIES AT $z > 0.3$

NATHAN JAMES DANIEL COURTNEY (2003)

This thesis presents optical CCD imaging taken as part of the follow-up programme to the Massive Cluster Survey, a ROSAT All-Sky Survey based cluster survey aiming to discover X-ray luminous galaxy clusters at redshifts above 0.3. A data-reduction pipeline is developed to process the V, R and I band imaging of 111 clusters observed with the University of Hawaii 2.2 metre telescope and 57 with the ESO NTT.

The galaxian population is examined and all clusters but one contain enough galaxies to account for the X-ray flux. The cluster red-sequence is used to constrain the star-formation epoch to high ($z > 1.7$) redshift and as a basis for photometric redshifts. The symmetry properties of the clusters are examined to probe merger activity, the cluster selection exhibiting no bias towards, or against, merging clusters.

The BCG population is examined. The degree to which the BCG dominates the cluster galaxy population displays no trend with either redshift or cluster X-ray luminosity, indicative of considerable previous as well as ongoing evolution. A quarter of the BCG population show bluer colours than would be expected for an elliptical galaxy at the appropriate redshift, some with known line emission, proving that BCGs are not purely passively evolving galaxies.

Multi-object spectroscopy of two clusters is used to confirm these as being massive. Colour-magnitude diagrams of spectroscopically selected galaxies are used to determine that the major source of error in the photometry is the flux limit of the imaging not the techniques applied.

The Veron-Cetty Veron AGN catalogue is cross-correlated with the Abell catalogue to reveal a sample of AGN in clusters which are found to be distributed within clusters as ordinary galaxies, making contamination to the observed X-ray flux a possibility.

A search for gravitationally lensed galaxies reveals such objects in 23% of the clusters imaged.

Contents

Abstract	ii
Preface and Declaration	xii
Acknowledgements	xiv
1 Introduction	1
1.1 The journey of discovery begins	1
1.2 Clusters of Galaxies	3
1.3 Finding Galaxy clusters	5
1.4 The Massive Cluster Survey	9
1.5 Scope and Outline of this Thesis	13
2 Data Reduction	17
2.1 Introduction	17
2.2 Observing strategy	18
2.3 Basic Image Processing	22
2.4 Photometric Calibration	23
2.5 Seeing measurement and matching	27
2.6 Magnitude Measurements	31
2.7 Object Extraction	35
2.8 Star-Galaxy Separation	36
2.9 Astrometry	46
2.10 Summary	47

3	Examining the cluster Colour-Magnitude sequence	48
3.1	Introduction	48
3.2	Optical Cluster Richness	60
3.3	Cluster Symmetry	68
3.4	Conclusions	82
4	Brightest Cluster Galaxies	84
4.1	Introduction	84
4.2	Brightest Cluster Galaxies	85
4.3	Selecting the Brightest Cluster Galaxy	88
4.4	Brightest Colour Galaxy Magnitude	92
4.5	Brightest Cluster Galaxy Colour	112
4.6	Brightest Colour Galaxy-Cluster Alignment	123
4.7	Future Aims	129
4.8	Conclusions	129
5	Finding Clusters - MACS in the South	132
5.1	Sunyaev-Zel'dovich effect observations at the South Pole	132
5.2	MACS in the South	133
5.3	Observing strategy	136
5.4	Data-reduction	137
5.5	Cluster Identification	147
5.6	Photometric Redshifts	150
5.7	Summary	158
5.8	Addendum	161
6	MACS Spectroscopy and Data Reduction	163
6.1	Introduction	163
6.2	The Gemini Multi-Object Spectrograph	164
6.3	MACS Spectroscopy	166
6.4	Data-reduction	174
6.5	Spectroscopically selected cluster members	184
6.6	Conclusions	187

7	Active Galactic Nuclei in Clusters of Galaxies	188
7.1	Introduction	188
7.2	The Nature of AGN	190
7.3	Establishing an Excess	193
7.4	Surface Density	195
7.5	Velocity Structure	197
7.6	Conclusions	199
8	Miscellaneous Objects	200
8.1	Introduction	200
8.2	Gravitational Arcs	200
8.3	A Ram pressure stripped galaxy?	217
8.4	Conclusions	217
9	Conclusions	219
A	MACS Colour-Magnitude diagrams	224
	Bibliography	241

List of Figures

1.1	Hubble ‘tuning fork’ diagram of Galaxy classification	2
1.2	Selection function of major X-ray cluster surveys of the past decade.	10
2.1	Quantum efficiency of the University of Hawaii 2.2m optical detectors.	19
2.2	Transmission curves of the University of Hawaii 2.2m optical filters	20
2.3	Magnitude difference against colour for stars in the field of Landolt 98	25
2.4	Magnitude difference against airmass for stars observed in the field of Landolt 98	26
2.5	Schematic of the effect of seeing on aperture magnitudes	28
2.6	Histogram of seeing during the MACS observation campaign.	30
2.7	The different SExtractor magnitude apertures	33
2.8	Histogram of magnitudes of 5σ I-band detections	37
2.9	$\Delta_{2''-4''}$ aperture magnitude against I-band total magnitude used for star-galaxy separation.	38
2.10	I-band CLASS_STAR against I-band total magnitude	39
2.11	Star-Galaxy separation in the R and V bands	40
2.12	Colour-magnitude diagrams of stars, galaxies and unclassified objects in the field of MACSJ0717.5+3745	42
2.13	Star-galaxy separation as a function of galactic latitude.	44
2.14	Star-galaxy separation as a function of the input seeing	45
3.1	Evolution of the slope of the colour-magnitude sequence with redshift.	52
3.2	Evolution of red-sequence slope for clusters at $z < 0.4$	54
3.3	Colour-magnitude sequence fit evaluated at 19th magnitude against redshift	58
3.4	Scatter in the evaluated colour of the fit to the cluster red-sequence.	59

3.5	Cluster membership selection in MACSJ1206.2-0847	61
3.6	Richness of MACS clusters based on number of galaxies	64
3.7	Aperture virial radius as a measure of cluster richness.	66
3.8	Histogram showing the scatter in Virial radius about the power-law fit	67
3.9	Schematic diagram of the symmetry of a relaxed cluster	70
3.10	Bright object masks used for calculating symmetry factor.	72
3.11	Distribution of symmetry factor for 87 MACS clusters	73
3.12	X-ray luminosity against symmetry factor for 87 MACS clusters . .	74
3.13	X-ray luminosity against symmetry factor	75
3.14	Symmetry factor with redshift	77
3.15	Finding the centres of clusters using symmetry	80
3.16	Relative positions of the symmetry, BCG and X-ray centres.	81
4.1	3×3 arcmin I-band image of MACSJ0913.7+4056	89
4.2	Colour-Magnitude diagram of MACSJ0913.7+4056	91
4.3	Variation of 5arc-second aperture magnitude of BCGs with redshift	93
4.4	Variation of total magnitude of BCGs with redshift	95
4.5	Variation in BCG 32Kpc aperture apparent magnitude with redshift	100
4.6	Variation in BCG absolute magnitude with redshift	101
4.7	Variation in BCG absolute magnitude with cluster X-ray luminosity	103
4.8	3×3 arcmin I-band image of MACSJ2243.3-0935	105
4.9	Degree of BCG dominance against redshift	107
4.10	Histograms showing degree of dominance of BCG galaxies	108
4.11	Degree of BCG dominance against its absolute magnitude	110
4.12	Degree of BCG dominance against cluster X-ray luminosity	111
4.13	Brightest Cluster Galaxy colour against redshift	113
4.14	Histogram showing scatter in BCG colour	114
4.15	Scatter in BCG colours against X-ray luminosity.	116
4.16	Cumulative distribution of scatter in BCG colour for high and low X-ray luminosity sub-samples.	118
4.17	Scatter in BCG colour against degree of dominance.	120
4.18	Cumulative distribution of scatter in BCG colour for high and low degree of dominance sub-samples.	121

4.19	Schematic of the rotation between base vectors	125
4.20	Histogram showing difference in angle between BCG and cluster . . .	126
4.21	Distribution of the angle between BCGs and their host cluster . . .	128
5.1	SUSI2 filter transmissions curves	135
5.2	Schematic of NTT data structure	139
5.3	SUSI2 bias structure	140
5.4	Bias structure in SUSI flatfields	141
5.5	Scattered light in SUSI2 frames	144
5.6	Variation in standards	146
5.7	Cluster identification	148
5.8	Cluster Identification by number of galaxies	149
5.9	Colour-Magnitude diagrams of clusters observed with SUSI2	152
5.10	Photometric redshifts from Colour-Magnitude sequence fit	153
5.11	Brightest Cluster Galaxy redshift against C-M redshift	155
5.12	5 arcsec aperture magnitude of the Brightest Cluster Galaxy redshift against C-M redshift	156
5.13	Redshift distribution of MACS and NTT clusters	157
5.14	Estimated against spectroscopic redshift for the NTT clusters . . .	162
6.1	Layout of the GMOS instrument	164
6.2	GMOS filter and grating transmission curves.	167
6.3	Spectroscopic target selection for MACSJ1731.6+2252	170
6.4	GMOS Pre-imaging of MACS1720.2+3536	171
6.5	Schematic diagram of the patrol area of the OIWFS relative to the GMOS CCD detectors	172
6.6	Readout directions of GMOS-North CCDs	175
6.7	GMOS-North bias frame.	177
6.8	Rectifying spectra using gstransform	179
6.9	Example spectra from MACSJ1731.6+2252	181
6.10	Velocity dispersions of MACSJ1720.2+3536 and MACSJ1731.6+2252	183
6.11	Colour-magnitude diagrams for spectroscopically selected cluster mem- bers.	185
7.1	The unified model of AGN emission.	191

7.2	Cumulative frequency AGN with separation from a cluster centre	194
7.3	Surface density profiles for AGN in Abell clusters	196
7.4	Velocity dispersions of AGN in Abell clusters	198
8.1	The production of multiple images by gravitational lensing	201
8.2	Gravitational arcs in MACSJ0014.3-3022, MACSJ0027.8+2616, MACSJ0110.1+3211 and MACSJ0110.1+3211	204
8.3	Gravitational arcs in MACSJ0152.5-2852, MACSJ0242.5-2132, MACSJ0257.6-2209 and MACSJ0326.8-0043	206
8.4	Gravitational arcs in: MACSJ0404.6+1109, MACSJ0416.1-2403, MACSJ0449.3-2848 and MACSJ0451.9+0006	208
8.5	Gravitational arcs in MACSJ0520.7-1328, MACSJ0947.2+7623, MACSJ0949.8+1708 and MACSJ1115.2+5320	210
8.6	Photometric classification of the giant arc in MACSJ1206.2-0847	213
8.7	Gravitational arcs in MACSJ1133.2+5008, MACSJ1142.4+5831, MACSJ1206.2-0847 & MACSJ1226.8+2153	214
8.8	Gravitational arcs in MACSJ1305.9+2630, MACSJ1319.9+7003, MACSJ1347.5-1144 & MACSJ1354.6+7715	216
8.9	Gravitational arc in MACSJ1526.7+1647 and MACSJ1738.1+6006	217
8.10	A possible ram-pressure stripped galaxy	218
A.1	Colour-magnitude diagrams of clusters in the MACS survey	225

List of Tables

2.1	Summary of the characteristics of the UH 2.2 metre optical camera used for the MACS multi-colour imaging campaign	18
2.2	Summary of the MACS imaging campaign	21
2.3	The star-galaxy separation of MACSJ0717.5+3745. Shown are the number of objects being classed as stars in each of the three bands. Galaxies are first selected in the I-band with unclassified objects being passed to the R and V bands.	41
3.1	Difference in the position of the centre of a cluster between X-ray, cD and Symmetry methods	82
4.1	Magnitude and colours of brightest cluster galaxies.	96
4.2	The number of BCGs significantly ($> 3\sigma$) brighter than the normal colour distribution for the I, R and V bands.	115
4.3	Statistics for the high ($\geq 10^{45}$ ergs/s) and low ($< 10^{45}$ ergs/s) cluster X-ray luminosity sub-samples. Shown are the sample mean and median, the probability (P) that the samples are drawn from the same parent population based upon the K-S statistic and the bootstrap fit slope of the linear trend fit to the data	117
4.4	Statistics for the high ($\Delta m > 0.67$) and low ($\Delta m \leq 0.67$) cluster X-ray luminosity sub-samples. Shown are the sample mean and median, the probability (P) that the samples are drawn from the same parent population based upon the K-S statistic and the bootstrap fit slope of the linear trend fit to the data	122
5.1	Summary of the characteristics of the SUSI2 detector array	134
5.2	Summary of observations taken with the New Technology Telescope	138

5.3	Summary of NTT observing run	159
6.1	Summary of the characteristics of the GMOS North detector array .	166
6.2	GMOS observation of MACS clusters taken in the 2002A semester .	173
6.3	The slope of the fit to the cluster red sequence for photometrically and spectroscopically selected cluster galaxies.	186

Preface and Declaration

The work presented in this thesis was carried out between 2000 and 2003 while the author was a research student under the supervision of Dr Alastair Edge and Dr Richard Bower, in the Department of Physics at the University of Durham.

This study is a small part of a wider, international collaboration between the author, Dr Harald Ebeling (Institute for Astronomy, University of Hawaii, USA), Dr Alastair Edge (University of Durham), Professor J. Patrick Henry (Institute for Astronomy, University of Hawaii, USA), Elizabeth Barrett (Institute for Astronomy, University of Hawaii, USA), David Donovan (Institute for Astronomy, University of Hawaii, USA), Professor Nick Kaiser (Institute for Astronomy, University of Hawaii, USA) and the late Leon VanSpeybroek (formally of the High Energy Astrophysics Division of the Harvard-Smithsonian Center for Astrophysics.)

The major part of the work presented in this thesis is the authors own work, except where explicitly stated in the text, summarised below:

- The University of Hawaii 2.2m observations at the heart of this thesis were taken by a combination of members of the MACS collaboration, in particular the author, Dr H. Ebeling, Professor J.P. Henry and D. Donovan.
- The basic reduction of this UH 2.2m data describing in section 2.3 was performed using a pipeline developed and run by Dr H. Ebeling
- The NTT observations described in chapter 5 were taken by the author and Dr Christopher Mullis (European Southern Observatory, Garching, Germany.)
- The cluster galaxy redshifts used in section 6.5 were taken by Dr H. Ebeling using the LRIS instrument on the Keck II telescope based upon object selection by the author. The redshift measurements were made by E. Barrett

Refereed Papers

Details of the MACS project are available in the following publications:

- “MACS: A quest for the most massive galaxy clusters in the universe.” H.Ebeling, A.C. Edge, J.P.Henry, 2001 ApJ, 553,668.
- “The discovery of two distant, massive clusters of galaxies in the ROSAT All-Sky Survey.” A.C. Edge, H. Ebeling, M. Bremer, H. Röttgering, M.P. van Haarlem, R. Rengelink and N.J.D. Courtney, 2003 MNRAS, 339, 913,
- “An X-ray / Optical study of the massive, lensing cluster MACSJ1206.2-0847” H. Ebeling, N.J.D. Courtney, E. Barrett, J.-F. Borgne, A.C. Edge, J.-P. Kneib, In preparation.

This research has made use of the NASA/IPAC Extra-galactic Database (NED) which is operated by the Jet Propulsion Laboratory, California Institute of Technology, under contract with the National Aeronautics and Space Administration.

Acknowledgements

Three years blood, sweat and tears later and finally I'm the proud owner of a thesis. Of course, no project of this size is ever undertaken in isolation and there are a few people that deserve thanks for helping me along the way.

Firstly, I must give a huge grateful thank you to my supervisors, Alastair Edge and Richard Bower, for keeping me on the straight and narrow and for tolerating my occasionally bitter sarcasm with good humour, I really couldn't have got this done without you. I should also acknowledge the financial support given to me by PPARC which made this work possible. I also owe a great deal to Harald Ebeling who has acted as an extra supervisor and who made me very welcome on my trips to Hawaii. Harald, if you're ever in the UK, I definitely owe you dinner.

There are several people from the Durham astronomy group (past and present) who have helped me massively on the way. In no particular order, I'd like to thank Ian Smail for answering technical telescope questions and Shaun Cole and Vince Eke for giving me the theorist point of view and for solving all those little mathematical bits and pieces that cropped up from time to time. I'm also indebted to Grahame Smith, Steve Quinney and Kevin Pimbblet for taking me under their respective wings and initiating me into the deeper mysteries of the dark art of photometry. I'd also like to thank Dorothy Jenkins for being a true superwoman and Alan Lotts, UNIX guru extraordinaire, for answering my endless tirade of questions and for indulging my many, many, obscure computing requests.

There are a few individuals who deserve a medal for being landed me as an office mate; Carlos Calcanéo-Roldan, Geoff Buswell, Stelios Kazantzidis, Richard McDermid, John Helly and Mark Swinbank, cheers guys!

Karen Bower (nee Brazier) gets a big thank-you for picking me up and restoring my self-confidence when all the world looked bleak and I thought that nobody was ever going to give me a job. I'd also like to thank Colin Wilson, Marek Gierlinski, Chris Done and Chris Simpson for ensuring that coffee times were never dull.

Away from the office, there are several people who have helped to keep me sane. Lynda Boothroyd and Helen 'Tigger' Vaughan get warmly thanked for all the supportive emails that they've sent me over the closing months of this project. I promise that I'll return the favour over the coming years! Despite buying him a new box, I still owe Andy Knighton about a hundred cups of tea, they were very much appreciated!

There are probably a hundred people that I could mention here who've helped me through my time in Durham; the drunken bums, the various members of Treasure-Trap through my seven year stay, Anne Greatrix, Sarah Archibald, Gemma Edwards, Al Macleod, Catheryn Bowen, Si Childs, Jules Fattorini, my sister Siân and countless, countless, others; thank you one and all. To anybody I've missed, I'm sorry, please forgive a poor exhausted Ph.D. student for his honest mistake.

There are three people to whom I owe more than I could possibly express here. My parents, Fay and Stan, who have stood by me and loved me down the years and supported me in everything that I have done. Even though we've not seen each other as much as any of us would've liked, I've always known that you've been there for me.

Finally, to Charlotte Lucy Bond who has most definitely gone above and beyond the call of duty over the last year keeping me sane, fed and loved. After tens of thousands of words that have gone into this thesis, I'm left with none to adequately express my gratitude, I simply could not have done this without you.

Nathan J.D. Courtney

October 2003

*You are a child of the universe,
no less than the trees and the stars:
you have a right to be here.
And whether or not it is clear to you,
no doubt the universe in unfolding as it should.*

'Desiderata' by Max Ehrmann

Chapter 1

Introduction

1.1 The journey of discovery begins

The history of the discipline of Astronomy is very long and it is often given the honour of being referred to as the oldest of the sciences, its roots running through the evolution of human civilisation. As the first humans sat and looked at the heavens above, they must have wondered at the significance of the thousands of pinpoints of light that pepper the night sky. Although our tools for examining the night sky have become ever more sophisticated, this wondering continues to the present day as modern astronomers struggle to comprehend the workings of our universe.

It was the Greeks who first attempted (in the Western world) to quantify and parameterise the heavens and many of their interpretations lasted right through the middle ages, particularly the geo-centric model of the solar system proposed by Ptolemy, until the renaissance of the 15th and 16th centuries brought in new theories. As is so common in the sciences, it was a technological development that brought about a change in thinking, in particular the development of the telescope. The Danish noble Tycho Brahe (1546-1601), who can be thought of as being the first professional astronomer, set up an observatory on the island of Hven. It was Brahe's observations of a supernova that changed the long held idea that the heavens were immutable, an idea that up until that point had not been challenged. Modern astronomers should remember this lesson from history; no matter how established a theory is and however well it appears to fit the observations, it is still not necessarily correct.

The father of modern observational extra-galactic astronomy is, without a doubt, Edwin Hubble. In a series of papers in the 1920s and 30s, Hubble showed that 'neb-

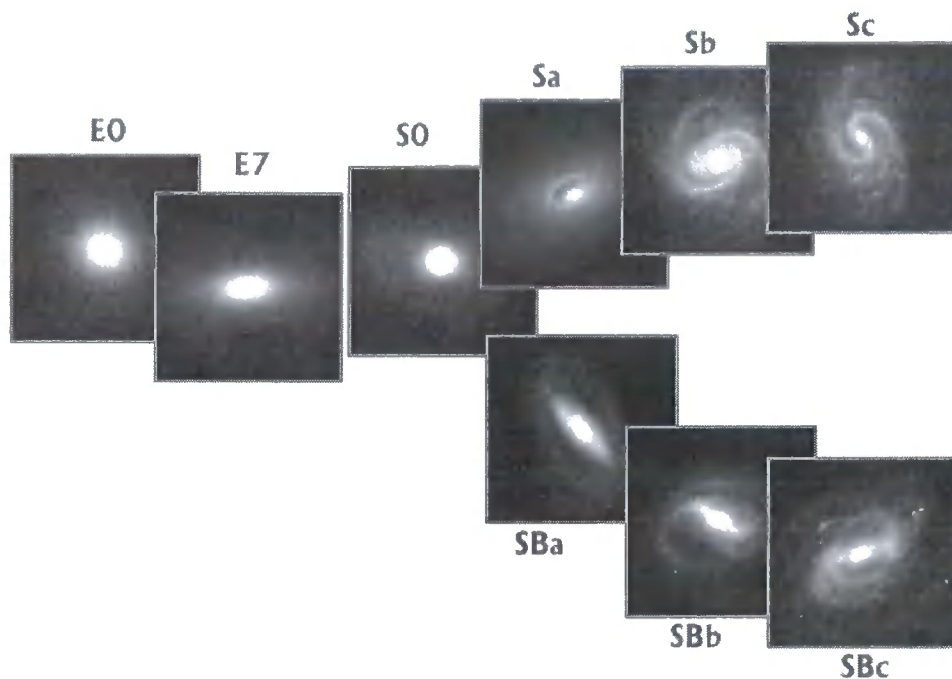


Figure 1.1: Hubble 'tuning fork' diagram of Galaxy classification (Image credit <http://www.astro.psu.edu/users/niel/astro1/slideshows/class21/slides-21.html>)

ula', such as the Andromeda galaxy, were actually external, self contained systems, galaxies similar to our own. He made this discovery through the observation of Cepheid variables, an extremely useful type of star that has a relationship between the period of its variations and its luminosity, making them an idea standard candle to use for measuring distance as they can be readily identified through their spectra. The distances that he measured to these variable stars in Andromeda were so much larger than anything else measured within the Milky Way that these systems could not be part of our galaxy and had to be independent systems in their own right.

Following on from this discovery, Hubble (1936) went on to classify the different type of galaxy, producing the classic 'tuning fork' diagram, an example of which is shown in figure 1.1. Hubble classified galaxies into 9 different types based on their appearance, going from apparently circular (E0) galaxies through to grand design spiral galaxies, separated into those that appear to have a central bar (SBa, SBb & SBc) and those that don't (Sa, Sb and Sc.) Hubble proposed that these classifications represented an evolutionary sequence, running from left to right (i.e. from E0 to either Sc or SBc.) Although this is now thought not to be the case (or

even that it is an evolutionary sequence but that it runs in the opposite direction) Hubble's conjecture remains in astronomical terminology as elliptical galaxies are often referred to as being 'early' type galaxies and spirals as being 'late' type. There is an extra class of galaxy missing from the classical Hubble tuning fork diagram, that of the irregular galaxies. These objects are occasionally included on the far right of the tuning fork diagram.

Hubble's other great discovery was that of the phenomenon of redshift. While looking at the spectra of galaxies, Hubble noticed that many of the spectral features were shifted in wavelength relative to what is observed at rest in a laboratory experiment. Hubble realized that these changes in wavelength were due to Doppler shifts, caused by the relative motion of the observed galaxy with respect to the Milky Way. He then noticed that there were more galaxies that appeared to be moving away from the Milky way (red-shifted) than towards it (blue-shifted.) He then made one of the most important observational discoveries of the twentieth century; by using directly determined distances to galaxies, he discovered that there was a direct relationship between the distance to an object and its recessional velocity, with more distant galaxies receding faster than nearby ones. In this series of observations, Hubble discovered both the phenomenon of redshift as an indirect way of measuring the distance to an object and the homogeneous expansion of the universe. Such was the importance of this discovery that the constant of proportionality between recessional velocity and distance (H_0) bears Hubble's name.

For the majority of applications in extra-galactic astronomy, i.e. for objects so distant that standard candle methods such as Cepheid variable stars cannot be isolated, the redshift of an object remains the only way of measuring the distance to it and so it is this measure that is quoted to indicate the distance to a galaxy.

1.2 Clusters of Galaxies

The nature of the 'nebulae' that Hubble investigated had been the subject to debate long before the revelations of the 1920s and 30s. In particular, Wolf (1865) observed that these nebulae were not randomly distributed, but showed a tendency to be clustered together. As we have probed deeper into space, galaxies can be seen in

a variety of environments from isolated, individual, galaxies to groups of galaxies containing a handful of members (the Milky Way and its nearest neighbour, the Andromeda galaxy, constitute such a group) up to massive clusters of galaxies containing many hundreds of galaxies. The clustering of galaxies doesn't end with massive clusters, the clusters themselves are not randomly distributed but they congregate together into super-clusters (see de Vaucouleurs 1961 for a review.)

Clusters of galaxies constitute the largest gravitationally relaxed bodies in the universe and are extremely useful probes of galaxy evolution as they are made up of (potentially) a large number of galaxies at the same distance within the same region of space allowing many galaxies to be observed at the same time. Clusters also provide excellent testing grounds for theories of galaxy evolution, in particular the interaction between a galaxy and its environment. It is clear that there is some sort of interaction of this type, as the cores of (particularly rich) clusters are dominated by apparently passively evolving early type galaxies (Hubble and Humason 1931) whereas those galaxies outside of clusters (referred to as being in the field) are predominantly late type galaxies, although the exact cause of this density-morphology relationship remains a subject of investigation and debate.

The evolution of clusters is driven by gravitational processes and are believed to be formed from small matter over-densities in the very early universe that have grown and accreted matter over time to form the vast objects that we observe at the present epoch. Clearly, the number and the size of clusters of galaxies is going to depend on the number, size and density of the initial fluctuations and also the rate at which the clusters can accrete material, all of which are controlled by the cosmology of the universe in which we live.

The dependence of the number and size of clusters on the universes initial conditions means that the current abundance of such objects can be used to constrain cosmological models. However, the rate of evolution of these objects is dependent upon their mass with more massive objects evolving more quickly. This means that, in principle, cosmological studies can be performed using clusters of any size although, due to their slower rate of evolution, very large, statistically well defined samples of poor clusters at high ($z > 1$) redshift would be needed to obtain significant constraints on the world models using poor groups. In contrast, the rapid

evolution of the most massive systems places constraints on cosmological models with fewer objects at much lower redshift, for large clusters with intra-cluster gas temperatures of $kT \sim 7$ KeV there is an order of magnitude difference in the predicted number of such clusters at $z=1$ between an open universe model with $\Omega_0 = 0.3$ and a closed one with $\Omega_0 = 1$ (Ebeling, Edge and Henry 2001.) For even more massive systems, the evolution of their number density is predicted to be more rapid still.

Clearly, if cosmology models are to be tested using clusters of galaxies, what is needed is a statistically well defined sample of the most massive clusters at high redshifts as these will provide the most sensitive test of the differing world models as well as being the clusters for which there is the greatest contrast in environment between the dense cluster core and the field for testing galaxy evolution.

1.3 Finding Galaxy clusters

So, having seen that clusters are important testing grounds for both cosmology and galaxy evolution, how are these objects to be found? Many thousands of galaxy clusters have so far been found in the universe, detected through either their optical or X-ray properties; the two main cluster finding techniques, with a third technique which is nearing maturity, are described here.

1.3.1 Optical selection

Clusters of galaxies are, primarily, defined as being over-densities in the spatial distribution of galaxies and so the simplest, in theory, method for searching for clusters is to make a survey of the sky and look for regions of high galaxy density.

This technique was used by Abell to produce his 1958 cluster catalogue which despite it being over 40 years since its publication, remains as the standard source of massive clusters in the local universe. Abell examined photographic plates from the Palomar Sky Survey, by eye, as part of his thesis work to look for areas of high galaxy density. It is a well known piece of Astronomy folklore that Abells eyesight suffered greatly as a direct result of the strain involved in doing this, thankfully

such sacrifices are not a compulsory part of doctoral research. Abell used a number of criteria to select his clusters of galaxies. Firstly, the candidate cluster must contain more than 50 galaxies within the magnitude range $m_3 \rightarrow m_3 + 2$ where m_3 is the magnitude of the third brightest galaxy. Secondly, these galaxies must be contained within a circular aperture of radius $R_A = \frac{1.7}{z}$ arcmin (R_A being denoted as the ‘Abell’ radius) and z being the (estimated) redshift to the cluster. This radius corresponds to a physical scale of approximately 3Mpc * at the redshift of the bulk of the Abell clusters. In total, 1682 clusters were selected by Abell that satisfy these criteria out of a total of 2712 candidates within the area studied, the Northern Sky at $\delta > -27$. Collaborating with Corwin and Olowin, Abell (1989) extended his original catalogue to include the Southern sky and probed poorer clusters, using a detection limit of 30 members within the $m_3 \rightarrow m_3 + 2$ magnitude range, increasing the catalogue size to 4073.

Abell, Corwin and Olowin are not the only people that have used optical imaging to find galaxy clusters. The Edinburgh-Durham cluster catalogue (Lumsden et al 1992) made the first machine-based sample of galaxy clusters, based upon scans of plates from the UK Schmit telescope made using the COSMOS scanning machine. This catalogue contains 737 clusters which they claim is complete to m_{10} (magnitude of the 10th brightest galaxy in the cluster) = 18.75 (in the B_j band.) More recently, the APM survey (Dalton et al. 1994) produced a catalogue of 228 clusters, of which 188 were new discoveries and in the near future, the Sloan survey (York et al 2000) will release its own catalogue of optically selected clusters.

These survey methods, based upon counting the number of galaxies are, as can be judged by the number of clusters selected in the example surveys described above, extremely effective at finding over-densities of galaxies, indicative of the presence of a cluster. However, this technique is only truly effective for wide, relatively shallow surveys selecting low redshift clusters i.e. where the depth of the imaging prevents detection of background galaxies and the limited volume ensures limited foreground contamination. Optical surveys of this kind also suffer from a major limitation due to projection effects. Imaging shows a two dimensional projection of the three dimensional distribution of galaxies and it is entirely possible for there to be two

*A discussion of the cosmology used to calculate this number is given in section 1.5

smaller groups of galaxies along the line of sight. When viewed in projection, these two groups will appear to be a single, rich cluster; it has long been suggested that there are significant projection effects in the Abell catalogue (Lucey 1983) though the exact degree of contamination is uncertain (Collins et al 1995.)

Despite this potentially major source of contamination, cluster surveys based upon optical imaging remain attractive as optical imaging is cheap to obtain, compared with the long integrations required at radio wavelengths and the expense of building and launching X-ray satellites.

Modern optical cluster surveys have attempted to both select high redshift clusters and virtually eliminate this projection effect by selecting galaxies by both apparent colour, which gives an estimation of the redshift of an object, as well as galaxy concentration. The Red Cluster Sequence survey of Gladders and Yee (2000) uses a sophisticated detection algorithm which searches for excesses of red galaxies, the elliptical galaxy population, which dominates the cores of clusters and which appears to be considerably redder than both field spiral and foreground galaxies. In essence, clusters are selected by having an over-density of galaxies in a series of slices of colour space, they claim that this method reliably generates a complete sample of galaxy clusters out to redshift $z \simeq 1$.

1.3.2 X-ray selection

Galaxies are not the sole constituent of clusters. The galaxies that we see sit in a gravitational potential well which also contains a large volume of gas. Rood (1965) first suggested that this gas may exist in the core of clusters when he found that in a dynamical study of the Coma cluster,[†] the galaxies alone did not constitute enough mass to form a gravitational potential sufficiently large to account for the motion of the galaxies, suggesting that a non-negligible portion lay between the galaxies forming an intra-cluster medium. Direct observational evidence for the presence of this gas came from X-ray observations of clusters where the central gas was found to be a source of diffuse X-ray emission. The emission mechanism for these X-rays

[†]The Coma Cluster, otherwise known as Abell 1656, is a massive cluster of galaxies at $z \sim 0.023$ (Colless & Dunn 1995) and is named for the constellation in which it appears to reside.

is believed to be thermal bremsstrahlung (Sarazin 1988) from the intra-cluster gas which has been heated to plasma temperatures by the energy injected into it by the gravitational collapse of the cluster.

This diffuse emission has been used successfully as a way of detecting rich clusters of galaxies and this method has the immediate advantage that the luminosity of the X-ray luminous gas is proportional to the square of the density of that gas. Consequently, the possibility of confusion due to chance alignments is much reduced. Secondly, only massive clusters contain enough hot gas to be detected and so X-ray selection inherently preferentially selects the most massive clusters.

Cluster catalogues have been collated from successive X-ray satellites but in particular much work has been done on the X-ray data collected from the all-sky survey conducted by the ROSAT mission (Trümper et al 1993). The X-ray surveys based upon ROSAT data can be divided into two broad categories, those based upon serendipitous detections (eg. RDCS, Rosati et al 1998 & WARPS, Jones et al. 1998) and those based upon contiguous areas from the all-sky survey (eg. BCS, Ebeling et al. 1998; REFLEX, Guzzo et al. 1999). The fundamental difference between these two types of surveys is in their depth and sky coverage, the contiguous area surveys covering a larger area but to a lower overall flux limit. This difference has major consequences in the number and type of clusters found. Due to their high X-ray luminosity, rich clusters of galaxies will be seen in both contiguous area and serendipitous surveys, however due to the rarity of these objects and the associated low projected density of these objects on the sky, it will be the large area surveys that recover large number of these most massive systems. Conversely, the smaller area, deep surveys will recover larger numbers of the slightly poorer systems and systems at higher redshifts.

There is a new generation of X-ray satellite currently in operation, the NASA Chandra and the ESA XMM-Newton missions. These missions constitute a major advance in both sensitivity and resolution over the previous generations of X-ray telescopes. However, although projects are underway to retrieve serendipitous detection of clusters from observations made with these instruments (eg. Romer et al 2001b), which will almost certainly reveal many currently unknown high redshift clusters, the limited area that these observatories will cover makes it unlikely that

a large number of the most massive objects will be found by these telescopes.

1.3.3 The Sunyaev-Zel'dovich effect

The Sunyaev-Zel'dovich (SZ) effect is not yet a mature technique for finding galaxy clusters but it may well play an important part in our understanding of clusters in the future and so it is mentioned here for completeness.

The SZ effect arises from photons from the cosmic microwave background being scattered to higher energies through Compton scattering as they pass through the hot intra-cluster medium. Consequently, clusters can be observed as being distortions in the spectrum of the microwave background. This method is appealing as, due to the effect being observed as a spectral change, the magnitude of the effect is independent of the redshift of the cluster. This potentially makes the SZ effect an extremely powerful tool for revealing clusters at the highest redshifts, although this redshift independence could also be a hindrance to the follow-up campaigns to pure SZ surveys. With no redshift information available, it will be difficult to plan more detailed observations of the candidate clusters with no guidance as to the likely magnitude of the constituent galaxies of the cluster.

The second possible drawback to SZ detections is that the SZ effect arises from the passage of the CMB photons through all gas along the line of sight, with the associated projection problems, similar to those suffered by optical surveys. Several SZ programmes are being planned and for more information, the reader is directed to the many reviews available on the subject, eg. those of Bartlett (2002) and Birkinshaw (2000)

1.4 The Massive Cluster Survey

The preceding section has shown how thousands of clusters have been detected using a variety of methods, so why do we need to go looking for any more? Figure 1.2 (reproduced from Ebeling, Edge and Henry 2001) shows the detection limits of the major X-ray based surveys of the past decade. As described earlier, the clusters that are of the most interest are the most massive ones that show the most

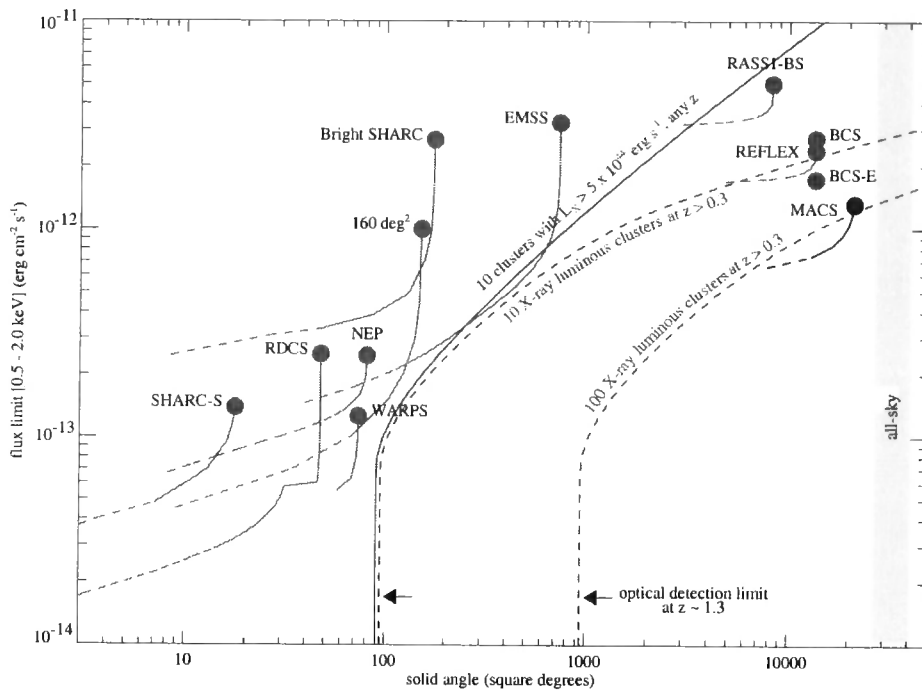


Figure 1.2: The selection function of all major X-ray cluster surveys of the past decade. Also shown is the solid angle required at a given flux limit to (statistically) detect 10 (or 100) X-ray luminous clusters at any redshift (or at $Z > 0.3$). Of the previous surveys, only the EMSS, BCS and REFLEX projects are sensitive enough to detect a modest number of such clusters (reproduced from Ebeling, Edge and Henry 2001.)

rapid evolution and by selecting clusters in the X-ray, any survey is assured to be detecting such objects. However, as with the majority of applications in astronomy, the best constraints can be applied to cosmological models by considering objects at high redshift. As can be seen from figure 1.2, the existing surveys will only recover a handful of clusters at redshift above 0.3.

The Massive Cluster Survey (MACS) was designed to bridge the gap between the large number of rich clusters found at low redshift by the previous wide and shallow surveys and the highest redshift objects found in serendipitous surveys. As figure 1.2 shows, MACS is the only survey that will recover a significant number of X-ray luminous (and hence massive) clusters above a redshift of 0.3.

1.4.1 X-ray selection criterion

MACS is based, as are several other surveys, on the ROSAT All-sky Survey bright source catalogue (RASS-BSC, Voges et al. 1999) and aims to achieve the goal of revealing the population of high redshift, massive clusters by combining the largest solid angle of any ROSAT All-sky Survey based cluster survey with the lowest possible X-ray flux limit. The survey is based upon the list of 18,811 sources listed in the RASS-BCS detected in the 0.1 - 2.4 keV band. The MACS survey applies the following X-ray selection criteria (reproduced from Ebeling, Edge and Henry 2001):

- $|b| \geq 20^\circ$, $-40^\circ \leq \delta(\text{J2000}) \leq 80^\circ$ to ensure observability from Mauna Kea; the resulting geometric solid angle is 22,735 deg²; 11,112 RASS-BSC sources fall within this region
- X-ray hardness ratio (the ratio of ‘hard’ to ‘soft’ X-rays) HR greater than $\text{HR}_{\min} = \max \left[-0.2, -0.55 + \log \left(\frac{n_H}{10^{20} \text{ cm}^{-2}} \right) \right]$ as derived from the ROSAT Brightest Cluster Sample (Ebeling et al. 1998) with the additional constraint that $\text{HR}_{\min} < 0.7$; HR is defined as $(h - s)/(h + s)$ where s and h are the PSPC count rates in the soft (PHA channels 11 to 41) and hard bands (PHA channels 52 to 201), respectively; 6,750 X-ray sources remain. This cut is made to exclude sources of soft X-rays (eg. stars).

- $f_X \geq 1 \times 10^{-12}$ erg cm⁻² s⁻¹ where f_X is the detect cell flux in the 0.1–2.4 keV band; 5,654 RASS-BSC sources remain
- detected net count limit of 17 photons; 5504 sources remain

1.4.2 Cluster identification

Having compiled the list of candidate X-ray detections, known counterparts to these X-ray detections were sought by cross-correlating the source list with all objects in the SIMBAD and NED databases. The APM catalogue (Maddox et al 1990) was also cross-correlated for extremely blue or red counterparts to tentatively identify stars and AGN.

CCD imaging was then taken using the University of Hawaii 2.2m telescope in the R band for X-ray bright ($f_x \geq 2 \times 10^{-12}$ erg cm⁻² s⁻¹), and I band for X-ray faint ($f_x < 2 \times 10^{-12}$ erg cm⁻² s⁻¹), sources lacking a firm identification of the X-ray source. At exposure times of 3×2 minutes in R and 3×3 minutes in I, these imaging exposures are sufficiently deep to unambiguously detect rich clusters through the apparent over-density of galaxies at the X-ray position. This technique was successfully used by the WARPS team to detect rich clusters out to $z \sim 0.8$ (Ebeling et al 2000.)

Follow-up spectroscopy was then obtained with the UH2.2m and Keck 10m telescopes of all clusters with estimated redshifts greater than 0.2 based upon the appearance of the cluster field in Digital Sky Survey images. Clusters are finally being accepted as MACS clusters if multiple, concordant redshifts greater than 0.3 were obtained. A full, detailed, description of the MACS survey characteristics, which have only been summarised here, is presented in Ebeling, Edge and Henry 2001. These objects accepted as being clusters are then imaged in the V, R and I bands, this imaging lying at the heart of the work presented here.

At the time of writing, the MACS survey contains 120 spectroscopically confirmed clusters at $z \geq 0.3$, of which only 29 were previously known, making it the largest survey of massive clusters at this redshift.

1.5 Scope and Outline of this Thesis

The MACS survey constitutes the largest, both in terms of number of objects and sky coverage, survey of highly luminous clusters of galaxies at this redshift range. This thesis aims to examine the multi-band imaging of the detected clusters with the following goals:

- Provide accurate photometry for galaxies in the field of the candidate clusters and establish accurate astrometry for these objects to allow spectroscopic follow-up to confirm their identification as massive clusters through their velocity dispersions.
- Develop reliable methods for selecting cluster member galaxies and use those selected galaxies to independently measure the richness of the MACS cluster candidates to confirm the presence of a cluster sufficiently massive to account for the X-ray emission
- Establish a method of measuring photometric redshifts appropriate to rich clusters at these redshifts to allow the identification and immediate follow-up of the most interesting, highest redshift clusters in future surveys.
- Assess the possibility of contamination of the observed X-ray flux from objects such as AGN, or processes such as mergers, that may act to boost the X-ray emission
- Identify individual objects of scientific interest that warrant more in-depth study.

To these ends, the outline of this thesis is as follows:

In Chapter 2, the data-reduction process used to handle the V, R and I band imaging of the MACS clusters that lies at the heart of this thesis, taken using the University of Hawaii 2.2 metre telescope, is described. The basic data processing and photometric calibration steps are outlined and then particular attention is paid to the method by which the object catalogues are obtained, especially the method by which the variable seeing conditions are accounted for by the production of

seeing matched frames for the accurate measurement of aperture colours. Finally, the technique for determining accurate star-galaxy separation is described.

In Chapter 3, the colour-magnitude sequence of the MACS clusters is examined through the production of colour-magnitude diagrams. The colour-magnitude sequence is then used, first as a method for constraining the star-formation epoch of the elliptical galaxies in the cores of the MACS clusters and then as a basis for a photometric redshift measurement technique. The richness of the clusters is then measured using first a simple galaxy counting technique and then the Virial radius. These measures are then used to identify clusters which are apparently too poor to account for their X-ray luminosity. Finally, the symmetry properties of the MACS clusters are investigated to assess the effect of mergers on their X-ray luminosity.

Chapter 4 contains a study of the population of Brightest Cluster Galaxies. The method of identifying these galaxies through a combination of colour and position is outlined and a comparison of the reliability of several magnitude measurement techniques is tested to establish these objects as potential standard candles. The colour of the brightest colour galaxy is examined as well as the degree to which this galaxy dominates the rest of the cluster elliptical population. Finally, the alignment of the brightest cluster galaxy with its host cluster is examined as a possible clue to its, and the host cluster's, evolution.

An extension to the cluster finding technique employed for the MACS survey is presented in chapter 5 for an independent sample of clusters South of the area covered by the main MACS survey. The data-reduction techniques specific to these data are discussed and then the photometric redshift techniques developed in the preceding chapters are applied to the clusters in this sample.

Multi-object spectroscopy is a major factor in the MACS follow-up programme and chapter 6 gives an example of the multi-object spectroscopy for two clusters observed with the 8 metre Gemini-North telescope. Redshifts taken as part of the MACS follow-up programme are used to produce colour-magnitude diagrams consisting of only spectroscopically selected galaxies and are used to constrain the sources of error in their purely photometric equivalents.

In order to attempt to better understand the possible effect of contamination due to unresolved AGN in clusters, a cross-correlation between the Veron-Cetty

Veron AGN catalogue with the Abell cluster catalogue is presented in chapter 7 with the aim of determining the spatial and velocity distributions of AGN within clusters.

Chapter 8 contains a miscellany of objects, primarily gravitationally lensed galaxies that are not studied in detail, but that are present as a reference for future work in this area. The findings of this thesis are then summarised in chapter 9.

Finally, the colour-magnitude diagrams for the MACS clusters, discussed in chapter 3, are presented in full as appendix A.

What's Missing?

As was mentioned in the preface to this volume, the work presented in this thesis represents only a small part of the total work on the Massive Cluster Survey being undertaken by an international collaboration. The fact that this survey is not yet public presents the author with the problem in that there is much data that this thesis relies on that is not yet in the public domain, nor is it the author's place to release that data in this thesis. Consequently this thesis is missing one of the usual features of such a work, namely a large data table presenting all the information used to generate the figures.

That said, it is the author's intention that this information be published to the astronomical community once the core of the MACS survey has been made public. When combined with the main MACS data release, this should include: Cluster identification and position, cluster redshift, X-ray luminosity, Virial radius (cf. section 3.2.3), position angle of the major axis and the symmetry factor (cf. section 3.3.1), the fits to the cluster red sequence (cf. 3.1.2 and the properties of the brightest cluster galaxy population.

A short note on cosmology.

During the lifetime of the work presented in this thesis, there have been major changes to the accepted values of the various cosmological parameters. For example,

during the author's undergraduate studies (1996 - 2000), Einstein's cosmological constant was presented as being his 'greatest mistake.' Then work was published by the supernovae cosmology project (see, for example, Perlmutter et al 1999) that claimed that the cosmological constant may well exist. More recently, the first results from the WMAP satellite (Spergel et al 2003) have constrained the suite of cosmological parameters (including the cosmological constant) with unprecedented accuracy.

As a consequence of this results, various combinations of cosmological parameters have passed in and out of fashion during the lifetime of this project, necessitating a choice of cosmology. Throughout this thesis, unless explicitly stated otherwise, a cosmology of $H_o = 65 \text{ Kms}^{-1}/\text{Mpc}$, $\Omega_m = 0.3$ and $\Omega_\lambda = 0.7$ has been used throughout.

2.1 Introduction

In this chapter the data-reduction strategy for processing the multi-colour (V, R and I band) imaging that is at the core of the Massive Cluster Survey follow-up imaging campaign is described. The details of the University of Hawaii 2.2 metre telescope and the optical camera used to take this data are presented and the data-reduction techniques used to process the raw telescope data are described. The method by which the seeing conditions are accounted for are demonstrated and in particular the dependence of the reliability of the star-galaxy separation on the accuracy of the determination of the seeing conditions is discussed along with the details of how the seeing conditions are measured automatically. The way in which the final object catalogue lists were generated is detailed with a description of how the frames are photometrically calibrated through the observation of Landolt standard star fields and astrometrically calibrated by comparison with the APM survey catalogue.

For almost every application in modern astronomy at optical wavelengths, CCDs are the detector of choice in the vast majority of instruments, completely replacing and superseding traditional photographic film in all but the most specialist wide-angle applications. This is not surprising as using CCDs circumvents many of the problems associated with photographic film, such as non-repeatability, modest quantum efficiency and non-linearity. Even with all the advantages of CCD cameras, care must still be taken with the manner in which the raw data is handled as any errors made in the basic raw data processing will propagate right through the analysis of the data and will effect the conclusions drawn.

Table 2.1: Summary of the characteristics of the UH 2.2 metre optical camera used for the MACS multi-colour imaging campaign

University of Hawaii 2.2m telescope optical camera	
Detector	Tektronic 2048x2048, 24 μ m pixels
Pixel Scale	0.22 arcsec per pixel
Read Noise	20 electrons
Gain	1.74
Field of View	7.5 x 7.5 arcmin
Quantum efficiency	(90%) (at 750nm)

2.2 Observing strategy

Following the identification of the MACS clusters outlined in section 1.4, an imaging campaign was undertaken to take multi-colour imaging for each of the clusters to allow further study of the entire MACS cluster catalogue. At the time of writing (October 2003), the MACS multi-colour imaging campaign is 92% complete with 111 clusters out of a total of 120 having been observed in this way.

The multi-colour imaging was taken using the University of Hawaii 2.2 metre telescope located near the summit of Mauna Kea on the island of Hawaii. The imaging campaign began in June 1999 and continues at the present time. The CCD detector used in the optical camera of the UH 2.2m is a Tektronic 2048 \times 2048 CCD. This detector is cosmetically very good with only a few small flaws visible in the raw frames. It is thinned and back-side illuminated, resulting in a high quantum efficiency from blue wavelengths through to 1 μ m. The quantum efficiency for a Tektronic 1024 \times 1024, the predecessor to the 2048 \times 2048, which has near identical quantum efficiency is shown in figure 2.1. The 2048 \times 2048 has 24 μ m pixels which results in a pixel scale of 0.22 arc-seconds per pixel and a field of view of 7.5 \times 7.5 arcmin.

The UH 2.2 metre telescope has available a set of U', B, V, R and I band filters (the transmission curves of which are shown in figure 2.2) which are based on the Mould BVRI system (similar to the Kron-Cousins system.) For the MACS survey,

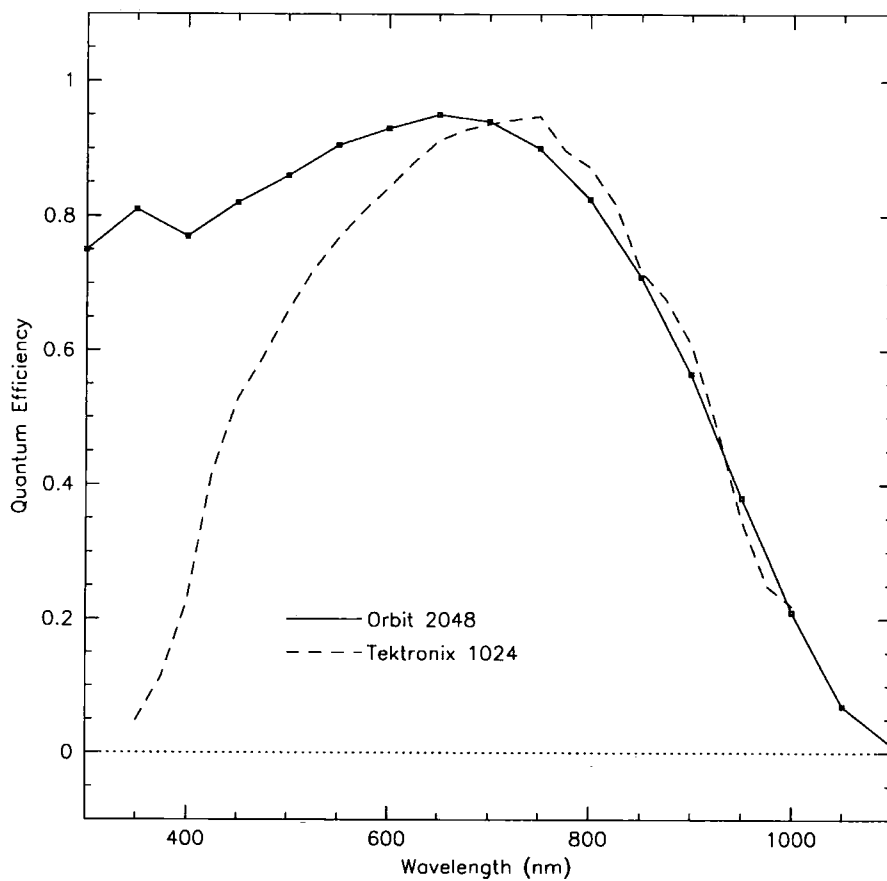


Figure 2.1: The quantum efficiency of the UH2.2m optical detectors. The Tektronic 2048 \times 2048 CCD is an updated version of the Tektronic 1024 \times 1024 chip shown here but the quantum efficiencies of the two chips are nearly identical. Figure taken from the UH2.2m user guide (<http://www.ifa.hawaii.edu/88inch/manuals/user.pdf>)

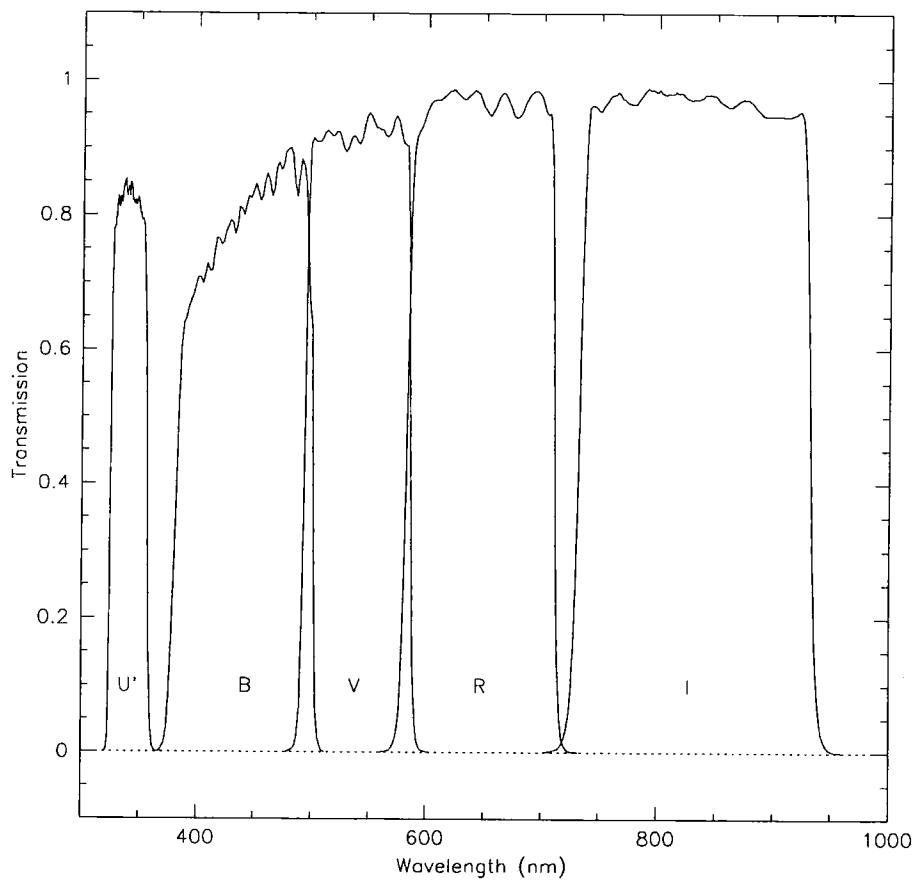


Figure 2.2: Transmission curves of the available filters on the UH2.2m optical camera, of which the V, R and I band filters were used. Figure taken from the UH2.2m user guide (<http://www.ifa.hawaii.edu/88inch/manuals/user.pdf>)

Table 2.2: Summary of the MACS imaging campaign

Date	Clusters observed [#]	Seeing(["]) ^{&}	Photometric
14th-16th June 1999	5	0.71-1.0	Yes
10th-12th July 1999	4	0.68-1.0	Yes
5th-8th August 1999	10	0.70-0.91	Yes
2nd-7th July 2000	12	0.77-1.3	Yes
22nd-25th September 2000	7	0.85-1.0	No
24th-25th October 2000	6	0.80-1.0	Yes
28th-31st January 2001	18	0.75-1.4	Yes
24th-28th May 2001	19	0.64-1.5	Partially
23rd-26th October 2001	11	0.82-1.3	Yes
9th-15th January 2002	3	0.90-1.1	Yes
13th-16th June 2002	5	0.86-1.2	Yes
27th-28th November 2002	8	0.80-1.1	Yes
28th-30th December 2002	11	1.0-1.4	partially
26th-27th March 2003	3	0.78-1.0	Yes

[#] This number includes re-observations and so the total number of observations (122) is greater than the number of MACS clusters observed(111)

[&] This is the I-band seeing. The seeing is typically 10% worse in the R-band and 20% worse in the V-band

high quality CCD imaging was taken in the V, R and I band in a standard dither pointing pattern of 3 separate exposures of 240 seconds (identical for each band) with an offset of 10 arc-seconds in both RA and Dec between the three separate pointings. Offsetting the sub-exposures allows the removal of cosmetic features in the images and allows for the removal of short-duration phenomenon such as cosmic ray hits. A summary of the MACS imaging campaign is given in table 2.2

In this table, an observing run is classified as being non-photometric if the Landolt standard stars (c.f. section 2.4) show large (> 0.05 magnitudes) scatters and partially photometric if the standards appear to be photometric but there are anomalous cluster observations. The number of clusters observed as listed in table 2.2 should not be used as an indication of the efficiency of the MACS observing

campaign as the reported number only counts the MACS multi-colour imaging taken whereas the telescope time was also taking either single band (cluster identification) imaging or data for other projects, most notably the WARPS (Scharf et al. 1997) and CIZA (Ebeling et al. 2002) cluster surveys during any given MACS observing run.

2.3 Basic Image Processing

The basic data-reduction of the raw data obtained from the UH 2.2 metre telescope was reduced at the University of Hawaii using a pipeline developed by Harald Ebeling. Although this primary data-reduction was not performed by the author, details of the process are presented here for the sake of completeness.

Twilight flat-field frames were taken at the beginning and end of each night in all three of the filters and are debiased using the IRAF command `CCDPROC`. These debiased flat-field exposures are then median combined using the IRAF command `IMCOMBINE` to make flat-field images for each imaging band for each night.

Having successfully produced a suitable flat-field, each of the individual science exposures is then individually de-biased and flat-fielded and the over and pre-scan regions trimmed off, also using the IRAF `CCDPROC` command. In order to flat-field a frame, the flat-field generated from the twilight observations must be normalised to unity as the flat-field is divided out of the science frames to remove variations in the CCD response, this normalisation process is handled internally by the `CCDPROC` command. In order to combine the individual pointings for each observed band, the three exposures were then aligned using the `IMALIGN` task.

`IMALIGN` registers images using a combination of the offsets between the images (which is known to a suitable degree of accuracy from the telescope offset between each pointing in the exposure pattern) and from a list of registration objects. The registration objects are the x and y coordinates of suitable objects (i.e. non-saturated bright stars) in the frame to which the others are to be aligned, usually the first image taken in the dither pattern. `IMALIGN` coarsely centres the images using first the offset provided between the frames and then computes the centroid of each of the reference objects on each of the three frames and then uses this to

accurately calculate the offsets between the images and register them accordingly. This process results in three individual exposures that have been aligned, de-biased and trimmed, they are then median combined using the IMCOMBINE task. Median combining images works to suppress the background noise the same way that simply co-adding the images does. However, median combining has the advantage that it virtually eliminates the effects of short time duration phenomena such as cosmic ray events and satellite trails (As these events only occur in one of the three dither pointings, the median process throws out these high pixel values) in contrast to co-adding the images where the final output image contains all of these events from each of the frames.

Now that each of the V, R and I bands have been de-biased, flat-fielded, aligned and median combined, IMALIGN was again used to align each of the three bands, to leave aligned frames suitable for science use. The aligning process involves trimming away the area of the chips that are not covered by all three of the separate exposures in the dither pattern and again trims off the areas not covered by all three of the bands (due to telescope pointing errors.) After this processing has been performed, the science images are typically 2000×1970 pixels in size, corresponding to a field of view of 7.3×7.2 arcmin.

Once the raw telescope data had been processed into its final form, a pipeline was developed to ensure that all of the imaging data from the separate UH 2.2 metre imaging runs was reduced in exactly the same manner.

2.4 Photometric Calibration

The initial stage in the processing was to calibrate the imaging data via the observations of standard star fields selected from the Landolt (1992) catalogue of equatorial standard stars. Standard star fields were observed at a range of airmasses across each night in each of the bands used for imaging. Aperture magnitudes using an arbitrary photometric zero-point were then measured for the standard stars using an identical aperture size to that used by Landolt (a circular aperture of 14 arc second diameter) and then compared to the values quoted by Landolt.

The final photometric zero-point for a given night is of the form:

$$\begin{aligned}
\text{I band: } M_{0i} &= M'_0 + \Delta M_{0i} + A_i \sec Z + B_i(B - I) - 2.5 \log \left(\frac{\text{exp}_{\text{science}}}{\text{exp}_{\text{standard}}} \right) \\
\text{R band: } M_{0r} &= M'_0 + \Delta M_{0r} + A_r \sec Z + B_r(B - R) - 2.5 \log \left(\frac{\text{exp}_{\text{science}}}{\text{exp}_{\text{standard}}} \right) \\
\text{V band: } M_{0v} &= M'_0 + \Delta M_{0v} + A_v \sec Z + B_v(B - V) - 2.5 \log \left(\frac{\text{exp}_{\text{science}}}{\text{exp}_{\text{standard}}} \right)
\end{aligned}$$

Where M_0 is the overall zero-point for a given science frame, M'_0 is the arbitrary zero-point with which the Landolt standard frames were reduced, ΔM_0 is the difference in zero-point between the arbitrary value and that of the Landolt standards. $A \sec Z$ is the airmass (atmospheric extinction) term, $B(B-I)$ is the colour term and $2.5 \log \left(\frac{\text{exp}_{\text{science}}}{\text{exp}_{\text{standard}}} \right)$ corrects the zero-point for the difference in exposure time between the science and standard frames. While the values of B and ΔM_0 remain constant (being due to the telescope filter set, detector and optics), obviously, the value of A (being due to the atmosphere) will be different for each of the different bands and will vary from night to night.

In order to calculate the colour term, B , which arises from the CCD response and the filter transmission not being perfect, the difference in magnitude between the Landolt standard stars and the MACS measured value is plotted against the colour of the Landolt stars. This is done for a single observation so that there are absolutely no airmass or other time-dependent factors affecting the measured magnitudes. Figure 2.3 shows the variation in the measured V-band magnitude against the standard star B-V colour for the stars observed in the field of Landolt SA98 observed on the night of the 31st December 2002. It can be clearly seen that there is a strong trend in the difference in observed magnitude with colour which allows the colour-term to be accurately determined. Obviously, this analysis needs to be repeated for each of the filters used for the MACS imaging. When a large number of these observations are considered, the colour-term for these filters and CCD combinations are found to be in very good agreement with the values of $-0.058(B-V)$ for the V band, $0.006(B-R)$ for the R band and $0.011(B-I)$ for the I band as quoted in the UH 2.2m users guide.

Atmospheric extinction is caused by the absorption of light by the Earth's atmosphere and is a function of how much of the atmosphere a light ray must pass through before it reaches the telescope detector. Clearly, this is defined by the angle of the telescope (Z , measured from zenith) at which the observations were

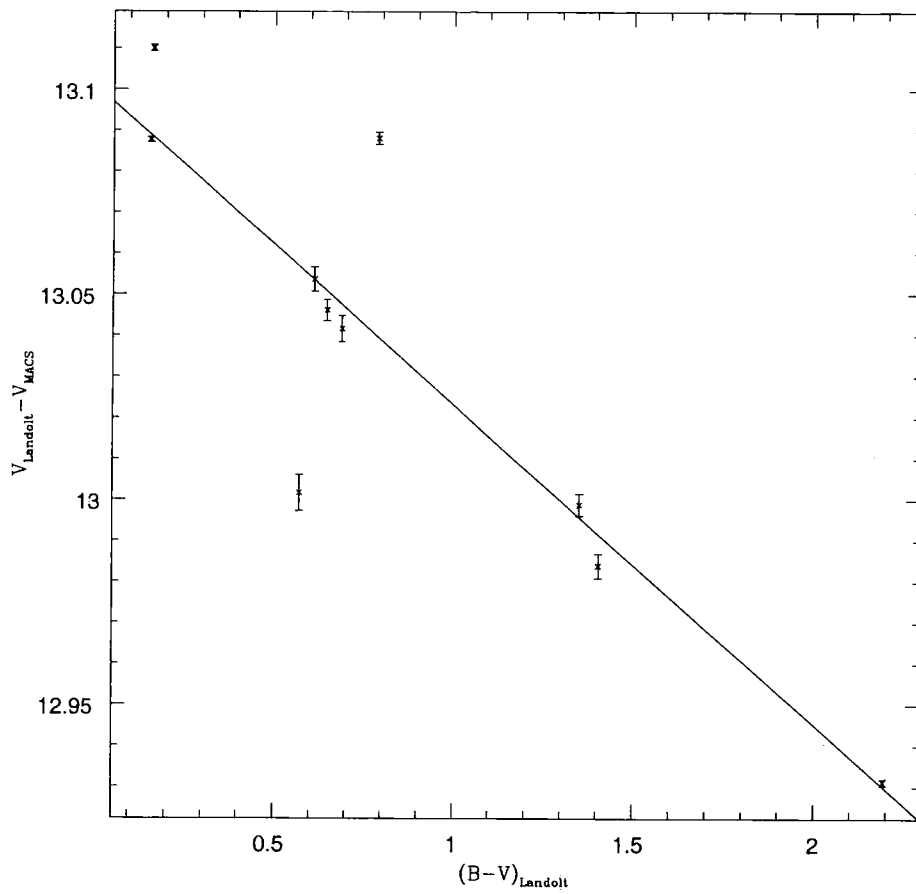


Figure 2.3: Variation in the measured V-band magnitude against the standard star B-V colour for the stars observed in the field of Landolt SA98 observed on the night of the 31st December 2002

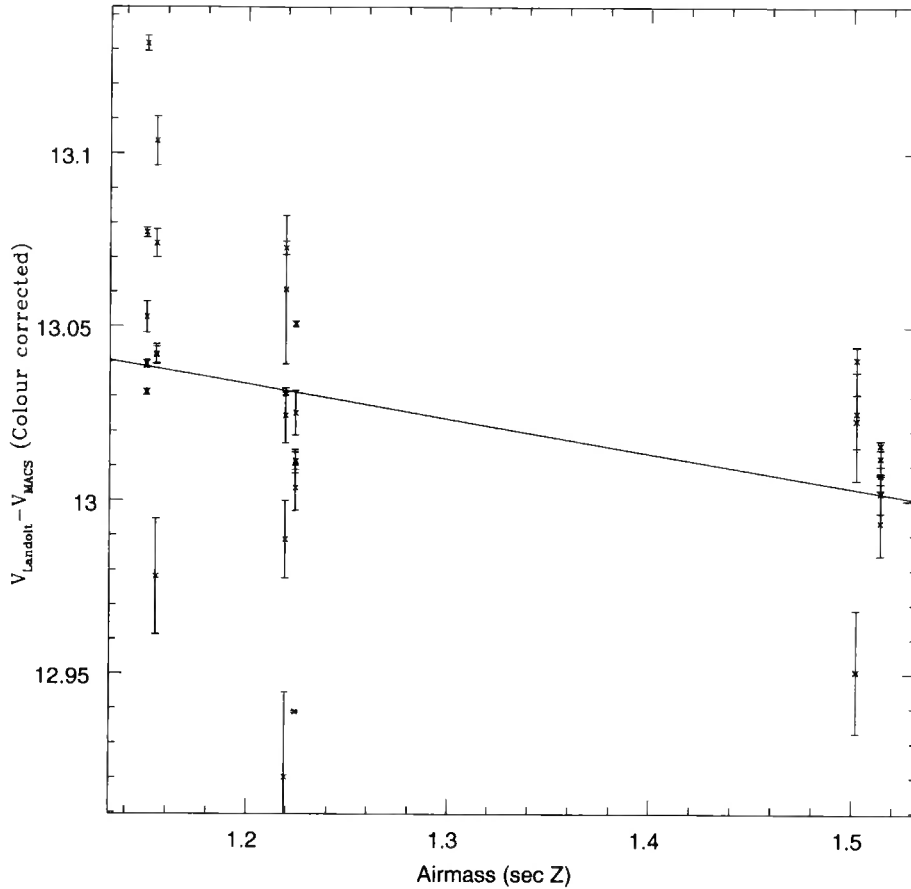


Figure 2.4: Variation in the measured V-band magnitude against the airmass for the standard stars observed on the night of the 31st December 2002

taken. Once the standard star observations have been corrected for their colour, the atmospheric extinction term, A , and the telescope zero-point can be solved for by plotting the difference between the colour-corrected measured magnitudes and the Landolt magnitudes against the airmass ($\sec Z$) at which the standard-star observations were taken. An example of this is shown in figure 2.4 The best fit linear relationship to this plot of the difference in magnitude yields both the coefficient, A , of the extinction term and the telescope zero-point. This analysis must be repeated for each observed band for each night of observations. As a check as to the photometric nature of a given night, the zero-point measure from the fit to the variation in magnitude with colour and the zero-point measured from the variation in magnitude with airmass is compared and a night is classified as being photometric if these zero-points agree to within 1σ .

Having measured all of the coefficients of the photometric solution equation, the zero-point for an individual science frame can be calculated using the airmass of the observation and the exposure time (240 seconds for the science observations and typically 20 seconds for the Landolt star observations), known from the observation log and the fits file header, and the expected colour of the cluster galaxies. These colours are calculated using the estimated colour for an elliptical galaxy from King and Ellis 1985 at the relevant redshift of the target cluster.

2.5 Seeing measurement and matching

Seeing, the effect caused by the transit of light through the Earth's atmosphere, acts to blur out the images of objects and the effect of the seeing effects both the resolution of an image and the photometric results. Without the effect of the Earth's atmosphere, the resolution of images would be determined by the diffraction limit of the telescope optics, this is approximately 0.1 arcsec for a 2.2 metre telescope in the I-band. The values of the seeing shown in table 2.2 are an order of magnitude greater than this which shows that quality of the images obtained is dominated by the effect of the atmosphere. Consequently, the seeing is a time-variable factor out of the control of the observer and so it must be corrected for in each observation individually.

More importantly, this blurring caused by the atmosphere has a considerable effect on the aperture magnitudes measured from the science frames. Figure 2.5 shows a 1-D schematic of a star of fixed flux (and therefore magnitude) under three different seeing conditions. It is clear that although the brightness of the star has not changed, it can be seen that a fixed aperture will report very different magnitudes for the same object. This variation is entirely an artifact of the seeing and must be accounted for. As has been mentioned, the atmosphere has a different effect on light at different wavelengths and so the seeing is different between the V, R and I band observations, even though these observations were taken consecutively to minimise the temporal variations. In order to accurately measure aperture colours for these objects it is imperative that the seeing is correctly accounted for.

Before the seeing can be accounted for, it must first be measured on each of

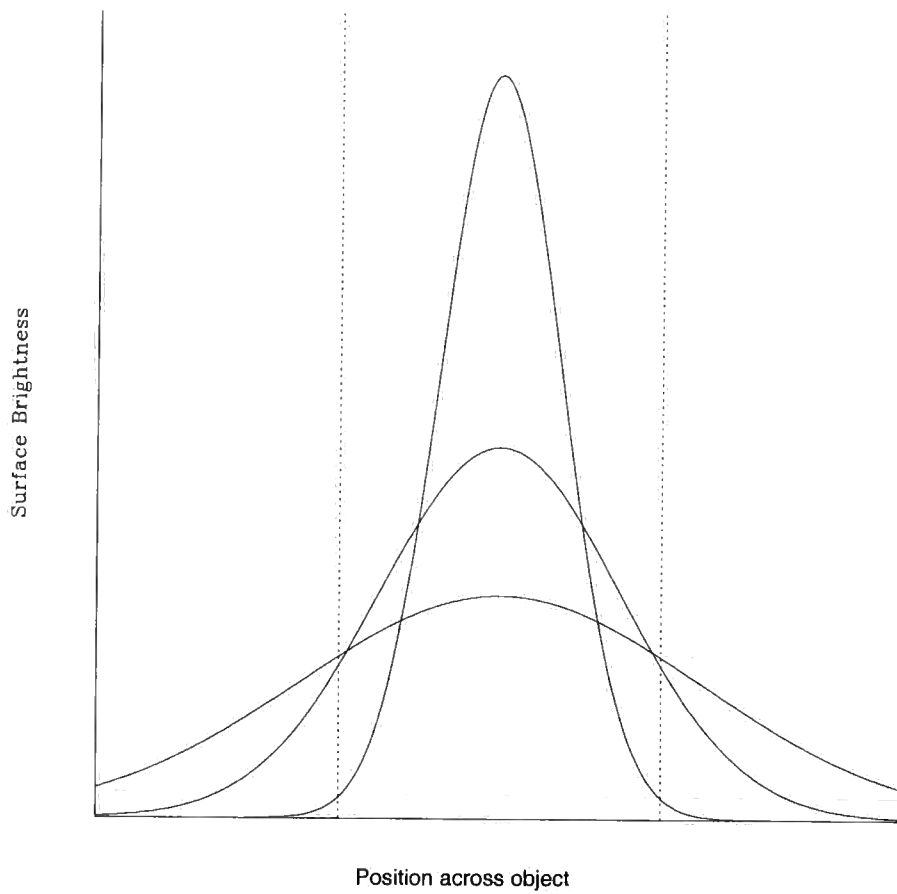


Figure 2.5: Schematic diagram of the 1-D surface brightness profile of a star under three different seeing conditions. The dashed lines represent a fixed aperture size. Clearly the amount of flux falling within the fixed aperture is affected by the seeing.

the three frames. Initially a method was used in which stars were identified by eye and then the seeing was estimated from the median value of the full-width half-maximum (FWHM) of the surface-brightness profile of these galaxies obtained using the IRAF IMEXAMINE task. However, this method was deemed to be unacceptable as firstly, it is extremely time-consuming and not practical in the light of the large amount of imaging data presented in this thesis, and secondly it was found to be systematically over-estimating the value of the seeing. This systematic error was traced to the selection of stars for the seeing measurement. With no seeing information available to enable stars to be separated from galaxies (star-galaxy separation is discussed in section 2.8 and will be shown to be highly dependent upon the seeing conditions), only those objects that can categorically identified as being stars (based predominantly upon their ellipticity) were chosen to be the basis of the seeing measurement. Obviously, this preferentially selects the brightest stars in the field. Although those stars that are clearly saturating the CCD detector are easily removed, a small fraction of stars remain which, although not bright enough to fully saturate the CCD detector, can be entering the region of non-linearity. This will reduce the measured maximum surface brightness of the star, artificially inflating the measured value of the seeing.

Instead, a fully automated method of measuring the seeing was developed. For a given frame, a first pass of SExtractor (Bertin & Arnouts 1996) was made and all the objects that are classified as being stars, i.e. all those that are classified by SExtractor as having `CLASS_STAR > 0.9` and that are acceptable detections (`FLAGS < 4`) were selected and then the median of the full-width half-maxima of these objects was then taken as a first measure of the seeing. As has been mentioned, the accuracy of the star-galaxy separation is highly dependent of the value of the seeing given to SExtractor as an input value. Consequently, it is highly likely that this first measure of the seeing is contaminated at some unknown level by the presence of galaxies. In order eliminate this contamination, a second pass of SExtractor was made using the measured value of the seeing as the input value. A much stricter star-galaxy separation criterion of `CLASS_STAR > 0.95` was then applied to ensure that only stars were selected. It is still possible that this method will incorrectly measure the seeing if the original input value was too far from the actual one. However, in these

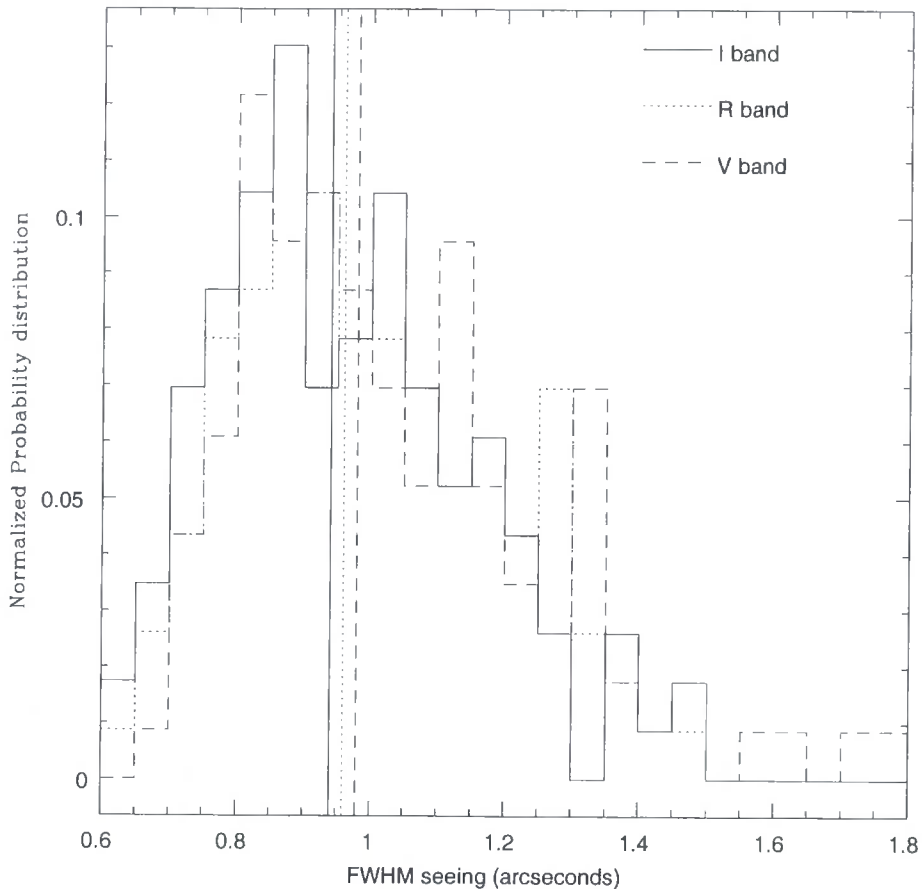


Figure 2.6: Histogram showing the measured seeing conditions in each of the MACS cluster observations. The vertical lines mark the position of the median seeing in each band.

cases the 1σ scatter about the median is high, greater than 0.1 arc-seconds. Where the method has correctly measured the seeing, the scatter is typically 0.07 arcsec.

In order to demonstrate the excellent seeing conditions in which the MACS imaging was taken, the distributions of the measured seeing of each of the V, R and I bands are shown in figure 2.6. Included in this figure are all of the observations taken, including those that were repeated due to being of insufficient quality. This figure shows that the majority of the imaging has been taken in sub-arcsecond seeing conditions; the median values of the seeing are 0.939, 0.959 and 0.979 arcsec in the I, R and V bands respectively.

Having measured the seeing on each of the V, R and I frames, the frames were then ‘seeing matched’, a process which involves degrading the seeing on the two

frames with the best seeing to match that of the worst. For each of the frames the GAUSS task was used to apply a Gaussian smoothing (with a FWHM σ) to the image, effectively increasing the seeing. After applying the Gaussian smoothing, the seeing of the degraded frame was measured using the automated method described above. This process was then iteratively repeated, altering the value of σ until the seeing matches that of the worst frame to better than 0.01 arc-seconds. This accuracy in the seeing matching process ensures that aperture effects due to variable seeing become negligible.

At this stage in the data-reduction process, the steps undertaken so far result in there being 5 separate images, the original V, R and I band images and the two frames where the seeing has been degraded to match the worst value. i.e. In the most frequent situation where the I band seeing is the best, followed by the R band and then the V band with the worst seeing, the five frames are the original V, R and I band frames, an I band frame degraded to the V band seeing and a R band image similarly degraded.

2.6 Magnitude Measurements

As the whole point of photometry is to derive accurate measures of the magnitudes of astronomical objects, some time is taken here to discuss the way in which SExtractor calculates the different measures of magnitude. Different groups of astronomers use different methods of determining magnitudes and so while the work in this thesis is based upon SExtractor's methods of magnitude measurement, future studies may use an alternative method. In order to allow a direct comparison of the different magnitudes, it is vital that the differences between the different detection methods are understood.

2.6.1 Aperture Magnitude

The simplest and also the most commonly used magnitude is the aperture magnitude. A diameter (in pixels) is given as an input value to SExtractor and this is used to define a circular aperture centred on the detected object. SExtractor loops

over the pixel values and sums up all pixels which lie within this defined circular aperture, the aperture magnitude is then given by the standard relationship:

$$m_{aper} = -2.5 \log F_{aper} + c$$

where m_{aper} is the aperture magnitude, F_{aper} is the sum of the flux of the pixels within the defined aperture and c is the zero-point of the CCD frame that was calculated from the standard star observations (c.f. section 2.4) and includes the correction for the exposure time. For the MACS survey, a 5 arc-second diameter aperture magnitude was used. This value was chosen as a compromise between being sufficiently larger than the seeing that a minimal amount of light was wasted and being small enough to avoid excessive aperture crowding in the densest parts of the cores of the highest redshift clusters.

2.6.2 Total Magnitude

Obviously, when measuring the magnitudes of objects that are inherently ellipsoidal and therefore elliptical in projection, using a circular aperture (and certainly using one of a fixed size) will be a poor measure of the magnitude, getting poorer with increasing ellipticity (for example an edge-on spiral.) In order to measure the total magnitude of an object, the SExtractor MAG_BEST is used as the total magnitude measure. MAG_BEST is actually, in the majority of cases, an adaptive aperture magnitude (MAG_AUTO) unless SExtractor determines that the contamination due to a nearby source exceeds 10% of the total measured flux for a object, in which case the corrected isophotal magnitude (MAG_ISOCORR) is used.

The adaptive aperture method is an extension of the method used by Kron (1980) and Infante (1987). These authors found that a circular aperture of radius kr_1 contains an almost constant fraction of the flux of an object, assuming standard star and galaxy profiles convolved with Gaussian seeing. r_1 is referred to as the “first moment” of the brightness distribution and is defined as:

$$r_1 = \frac{\Sigma r I(r)}{\Sigma I(r)}$$

. This method can be extended to elliptical apertures, where the major and minor axes of the ellipse are defined by ekr_1 and kr_1/e where e is the ellipticity determined

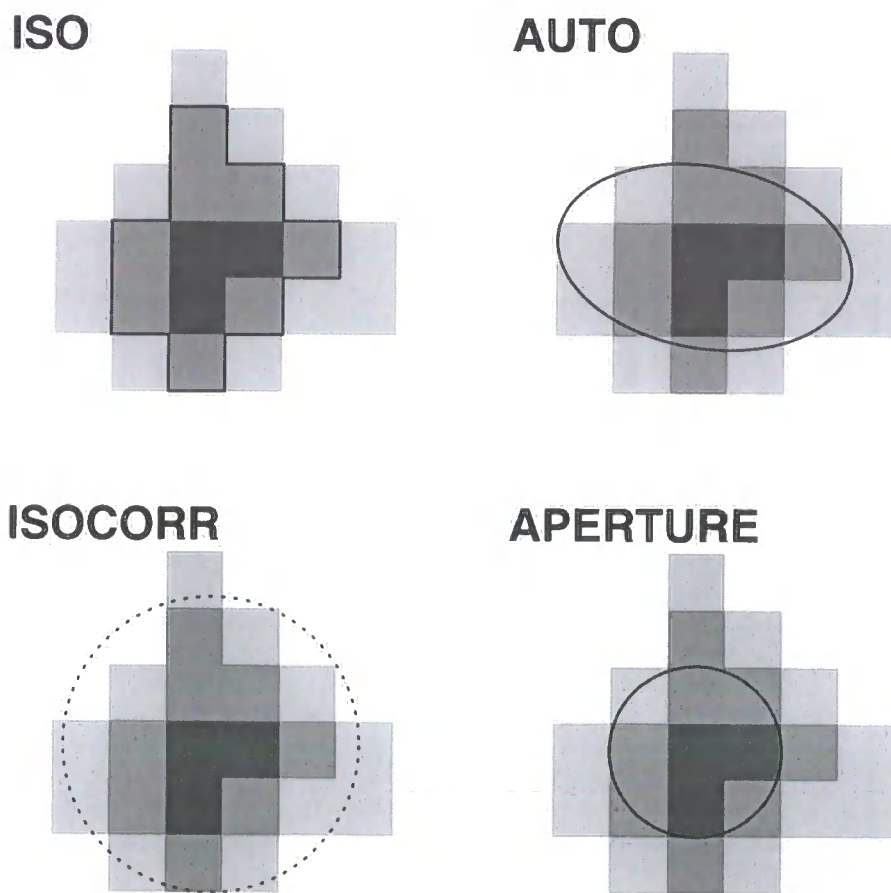


Figure 2.7: Illustration of the different apertures possible; ISO, ISOCOR, AUTO and APER. (Taken from "Source Extractor for dummies")

from the second order moments of the brightness distribution. By using $k=2.5$, a fixed fraction of 6% of the light is missed through this measurement, corresponding to the total magnitude of a galaxy being underestimated by 0.06 magnitudes. As this is a self-consistent offset within the MACS imaging, this correction factor has been neglected.

The isophotal magnitude is calculated by summing the flux from all pixels associated with the detection of an object that are brighter than a given surface brightness threshold. This effectively defines a surface density contour around the object which defines the area in which the flux is integrated. Obviously, this can lead to difficulties in measuring magnitudes for low surface brightness objects and excludes an uncertain proportion of the flux. To compensate for this, the corrected isophotal magnitude (`MAG_ISOCORR`) attempts to estimate the magnitude difference between the simple isophotal magnitude and the true total magnitude. If the source intensity profiles (I_{iso} and I_{tot}) can be assumed to be Gaussian because of the atmospheric seeing, the fraction of the total flux, η , measured within the isophotal aperture can be defined (Maddox et al. 1990) using the relation:

$$\left(1 - \frac{1}{\eta}\right) \ln(1 - \eta) = \frac{A.t}{I_{iso}}$$

where $\eta = \frac{I_{iso}}{I_{tot}}$, A is the area and t is the threshold that defines the isophotal area. η cannot be solved for directly, but can be approximated via:

$$\eta \approx 1 - 0.1961 \frac{A.t}{I_{iso}} - 0.7512 \left(\frac{A.t}{I_{iso}}\right)^2$$

The difference between the isophotal and total magnitudes is then given by $2.5 \log \eta$ and so the corrected isophotal magnitude is given by:

$$m_{isocorr} = -2.5 \log F_{iso} + 2.5 \log \eta + c$$

The main difference between `MAG_AUTO` and `MAG_ISOCORR` is that `MAG_ISOCORR` produces more reliable results in crowded fields but is inaccurate for extended sources. `SExtractor` automatically selects which of `MAG_AUTO` and `MAG_ISOCORR` is more appropriate for the object being detected and reports this magnitude as `MAG_BEST` and it is this which is used as the total magnitude measurement for this work.

2.6.3 Overlapping Detections

As has been mentioned, in the cores of the richest clusters, it is entirely possible for there to be aperture crowding i.e. overlap between the photometric apertures (however defined) of two independent objects. In this case, there are a variety of ways in which corrections can be applied. The SExtractor software supports three aperture corrections techniques, NONE, BLANK and CORRECT. The first of these NONE does exactly as it's name suggest, no correction is applied and the pixel values within each aperture, including the obvious contamination, are included in the flux calculation. The BLANK correction sets all overlapping pixels to zero, eliminating aperture cross-talk. Although at first glance this may not seem an intelligent thing to do, it can be useful when measuring aperture colours to ensure that it is only the target object that is being sampled. The CORRECT correction attempts to reconstruct the original object surface density profile by replacing pixels in the overlap region with their counterparts symmetric to them. Obviously, this correction is only viable when dealing with symmetrical objects with sufficient surface brightness that the centre is clearly defined. For this study, the CORRECT masking was used for both the total and aperture magnitude measurements.

2.7 Object Extraction

Now that the frames have been prepared, the final object detection and photometry was performed, again using SExtractor, this time using the two-frame mode. When operated in this mode, one frame is given to SExtractor to be used as a reference frame and it is from this frame that all of the object detections are made. Photometry is then performed on the second frame at the positions defined by the detected objects in the reference frame. As the V-I and R-I colours for elliptical galaxies are positive across the redshift range of the MACS survey, objects appear to be brighter in the I band than in the R and V bands and so the I band was chosen to provide the reference images. As such, the photometry presented in this thesis represents an I-band selected sample. SExtractor was run in two-frame mode (using the original I-band frame as the reference) for each of the three bands on

both of the original and seeing matched frames (obviously, for the band with the worst seeing, the original and seeing matched frames are one and the same.) All object parameters were measured in each band from the original frames as these are the ones that have the best seeing and have undergone the least processing with the exception of the aperture magnitude, which is measured from the seeing matched frames to allow accurate aperture colours to be calculated.

For the final object catalogues, objects were detected on the basis of having 3 contiguous pixels more than 2σ above the background level in the I-band. Although this may seem to be an extremely low threshold, spurious detections are easily rejected via their subsequent non-detection in the R and V bands. In order to better judge the depth of the imaging, all objects detected on the basis of having a single pixel more than 5σ above the background level in the field of the observation of the redshift 0.55 cluster MACSJ0717.5+3745 (Edge et al 2003) are shown in figure 2.8. From this figure, it can be seen that the absolute limit of detection for objects detected with 5σ confidence is $I \approx 22.3$ and (from the turnover in the number counts) the completeness limit is estimated to be $I \approx 20.1$. Obviously this completeness limit is only relevant to the 5σ detection criterion as it is highly likely that there will be low surface brightness objects that have total magnitudes lower than $I=20.1$ (i.e. below the completeness limit) that have been missed due to none of their individual pixel values being sufficiently great to satisfy the detection criterion.

2.8 Star-Galaxy Separation

Performing accurate star-galaxy separation is an essential part of any extra-galactic survey. In order to measure the properties of the galaxies in an image, a robust separation technique must be developed to completely remove the stellar contamination while retaining the maximum number of galaxies which will in turn effect the efficiency of follow-up projects.

Following the approach of Reid et al. (1996), the difference in magnitude between a 4.0" and 2.0" aperture on the I band frame was plotted against the total magnitude for each source and is shown in figure 2.9. As stars can be considered

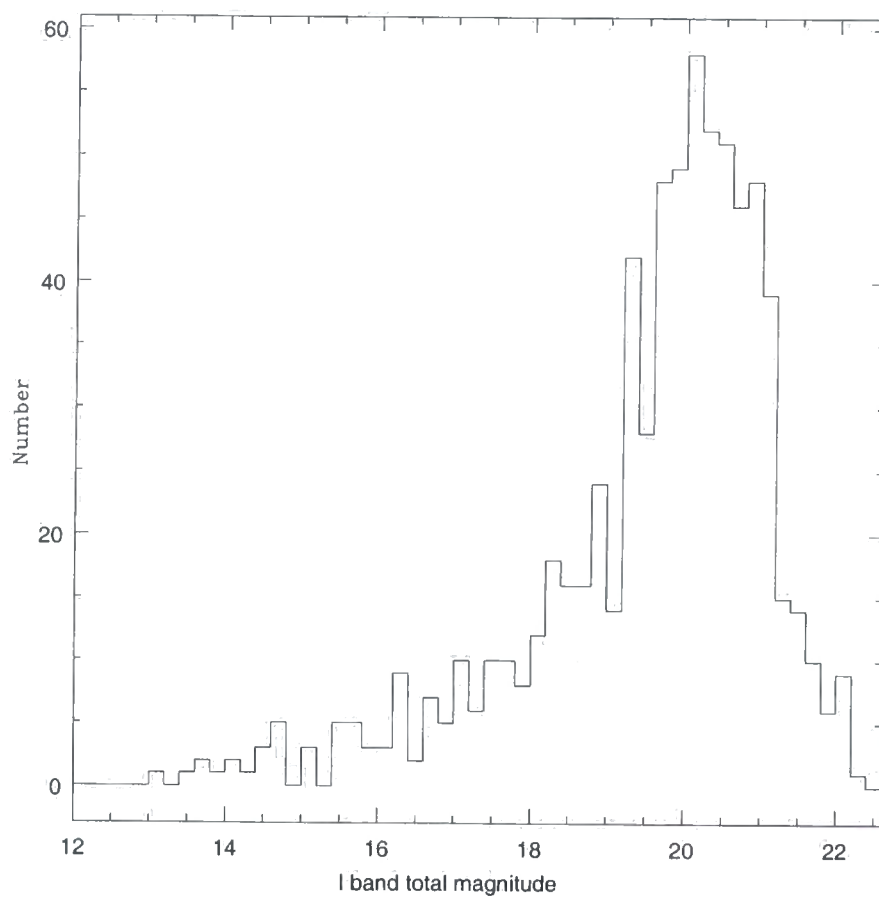


Figure 2.8: Histogram showing the magnitude of all objects that have a 5σ detection in the I-band image of MACSJ0717.5+3745

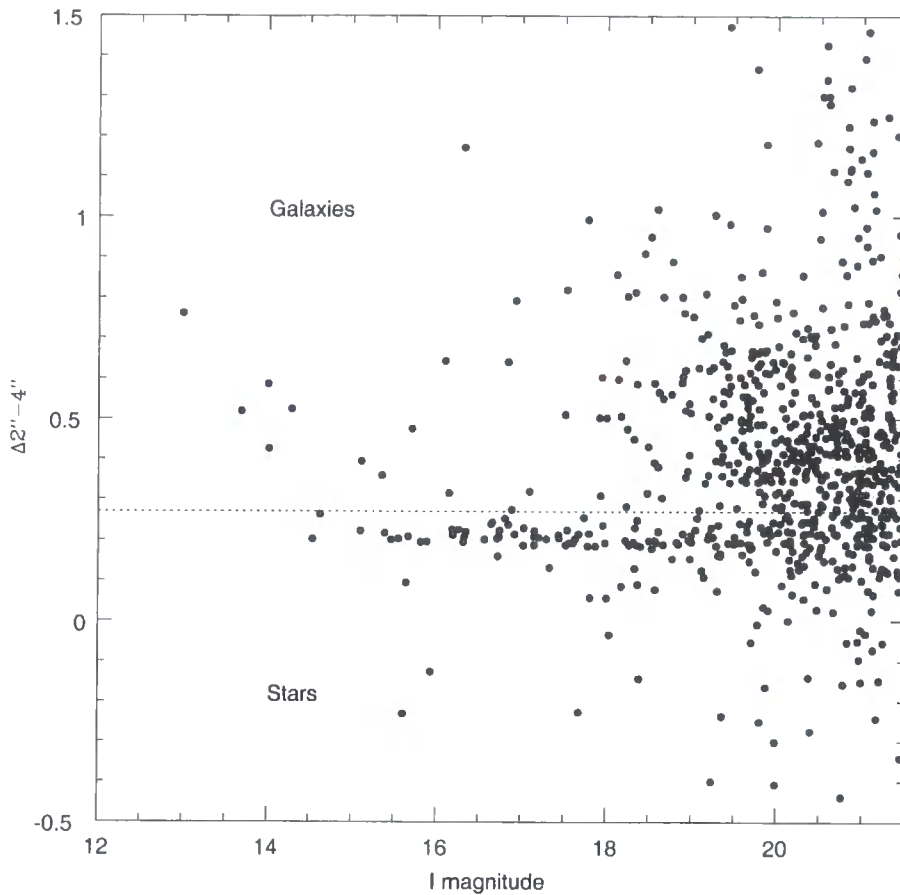


Figure 2.9: Difference between the I-band 2'' and 4'' aperture magnitude versus total I-band magnitude for all objects in the field of MACSJ0717.5+3745 to a limit of 21.5 magnitudes (chosen to exclude objects near the detection limit with noisy detections.)

to be point-sources convolved with the atmospheric seeing, the fraction of the total flux of a stellar source falling within a fixed aperture should be constant, and so the stars would be expected to trace out a horizontal locus in the $\Delta 2''-4''$ - total magnitude plane.

As can be seen from this figure, there is indeed a clear horizontal band of objects as predicted, confirming that this method can be used for adequate star-galaxy separation. However, the division between stars and galaxies depends on the seeing conditions. As the MACS observations have been taken over the course of several years, with the associated variation in conditions, this means that the star-galaxy separation would have to be continuously re-tuned. This is an extremely undesirable feature of any data-reduction process and certainly for the imaging campaign for a

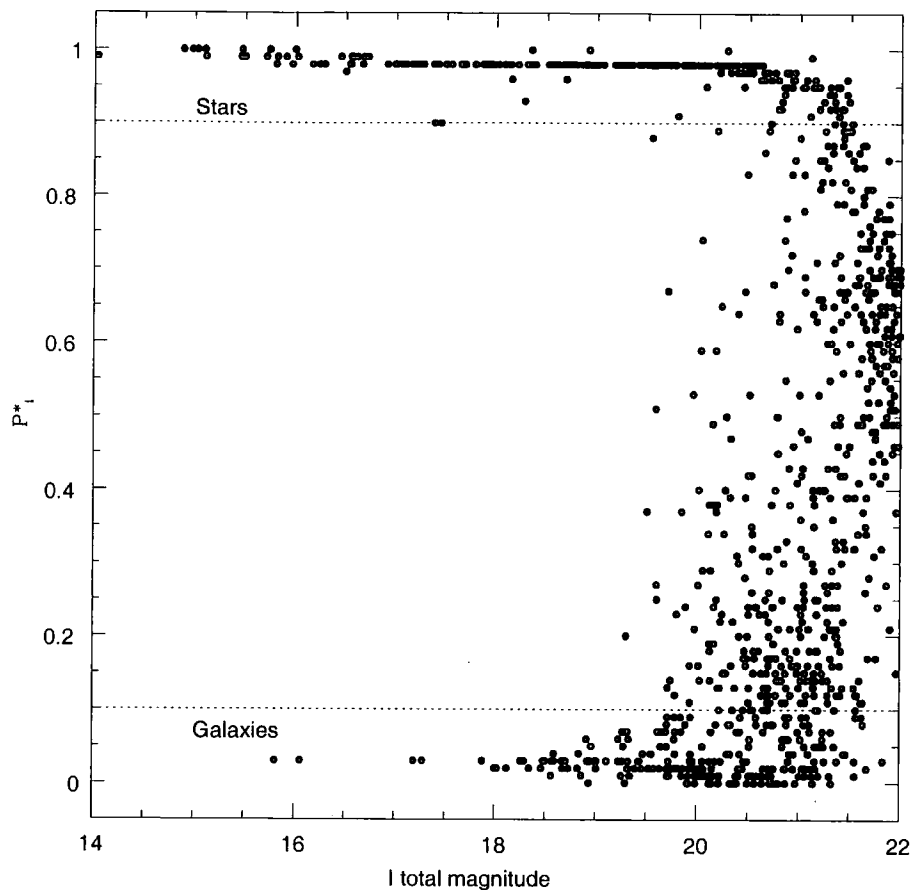


Figure 2.10: Star-galaxy separation using SExtractor's `CLASS_STAR` as measured in the I-band. The dashed lines show the boundaries between those objects being classified as being a star ($P^* > 0.9$) and those being a galaxy ($P^* < 0.1$)

survey.

Instead, star-galaxy separation was performed using SExtractor's own parameterisation, `CLASS_STAR`. `CLASS_STAR` is based upon several of the observable properties of an object, including an object's FWHM relative to the seeing, the ellipticity of the object and the concentration of the object (Abraham et al. 1994). From these observables, SExtractor uses a neural-network classifier that assigns each object a probability (P^*) of being a star. Figure 2.10 shows the distribution in values of P^* as measured in the I-band for a typical frame.

It can be seen that there is a clear bi-modality in the distribution of the values of P^* between those objects that are definitely a star ($P^* > 0.9$) and those that are definitely a galaxy ($P^* < 0.1$). Using these boundaries, out of a total of 1267

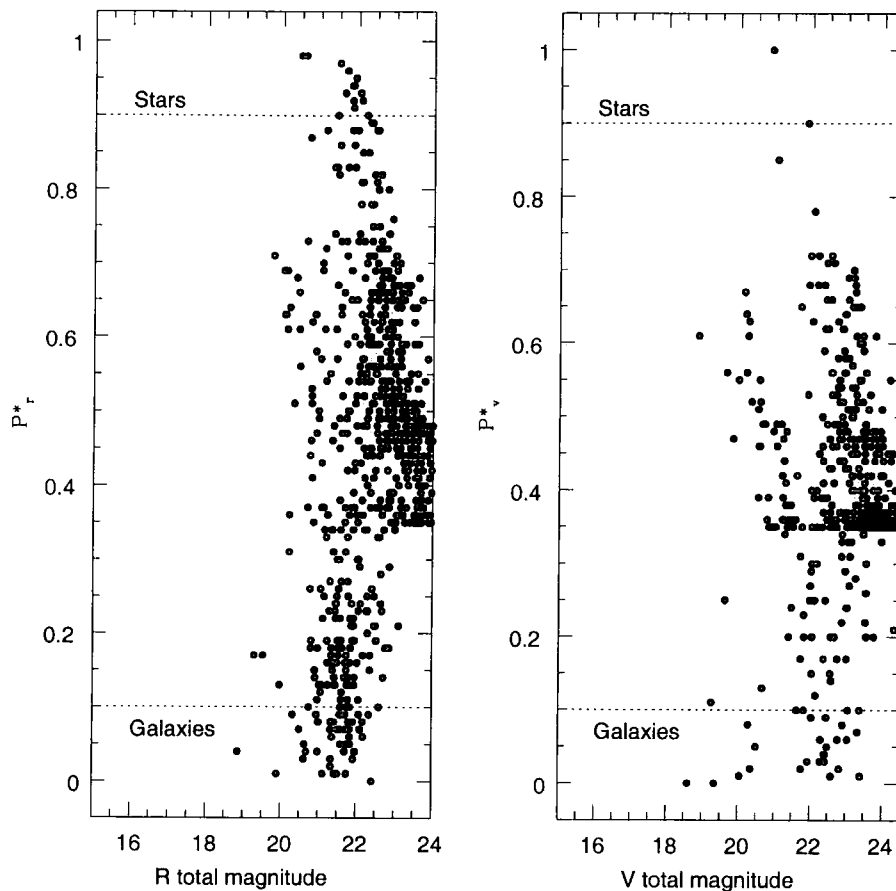


Figure 2.11: Star-galaxy separation for (left) objects in the R band that were unclassified in the I band and (right) objects in the V band that were unclassified in both the I and R bands. The horizontal 'shelf' seen in both plots represents the detection limit introduced by requiring 3 contiguous pixels for object detection.

objects detected in the observation of 0717, 242 (19%) are classified as being stars and 237 (18%) are galaxies. As figure 2.10 demonstrates, there are a large number of objects (788) that remain unclassified by this method. Of course, the MACS imaging contains more than just one band and the other two bands were utilised to aid in the star-galaxy process. For all the objects that have ambiguous values of P^* in the I band ($0.1 < P^*_I < 0.9$), the value of P^*_R was used to perform a secondary separation and is shown in the left hand panel of figure 2.11. It can clearly be seen that objects can be classified, based upon their R-band P^* characteristic, as being stars (14 objects, 1% of the total) and galaxies (53 objects, 4% of total). This process can be repeated, passing the remaining unclassified objects to the V-band

Table 2.3: The star-galaxy separation of MACSJ0717.5+3745. Shown are the number of objects being classed as stars in each of the three bands. Galaxies are first selected in the I-band with unclassified objects being passed to the R and V bands.

Stars	242 $P^*_I > 0.9$ 211 $P^*_R > 0.9$ 145 $P^*_V > 0.9$
I-band Galaxies	248
R-band Galaxies	53
V-band Galaxies	31
Total	257 Stars 332 Galaxies 678 Unclassified

(right panel in figure 2.11) where a further 2 objects are classified as being stars and a further 31 objects are classified as being galaxies. This process of identifying galaxies using P^* in the three bands was refined to provide the final method by which the star-galaxy separation was performed. Firstly, any object that is classified as being a star in any of the three bands ($P^*_I > 0.9$ or $P^*_R > 0.9$ or $P^*_V > 0.9$) is eliminated. Objects with $P^*_I < 0.1$ are then selected as being galaxies. The unidentified sources are then passed to the R-band for identification where those objects with $P^*_R < 0.1$ are accepted as being galaxies. Finally the remaining unidentified sources are examined in the V-band to recover the final objects that can be classified as being galaxies. This process is summarised in table 2.3.

As table 2.3 shows, a large proportion of the objects detected in the field of MACSJ0717.5+3745 remain unclassified. Figure 2.12 shows colour-magnitude diagrams (c.f. section 3.1) of the objects classified as being galaxies, those as stars and those without a firm classification to the 5σ completeness limit of 20.1 magnitudes in I to assess the impact of these unclassified objects. This diagram shows that there are no unclassified objects with I band total magnitudes brighter than 19.1 magnitudes in the I band, showing that this SExtractor CLASS_STAR based star-galaxy separation technique differentiates between objects to a similar magnitude

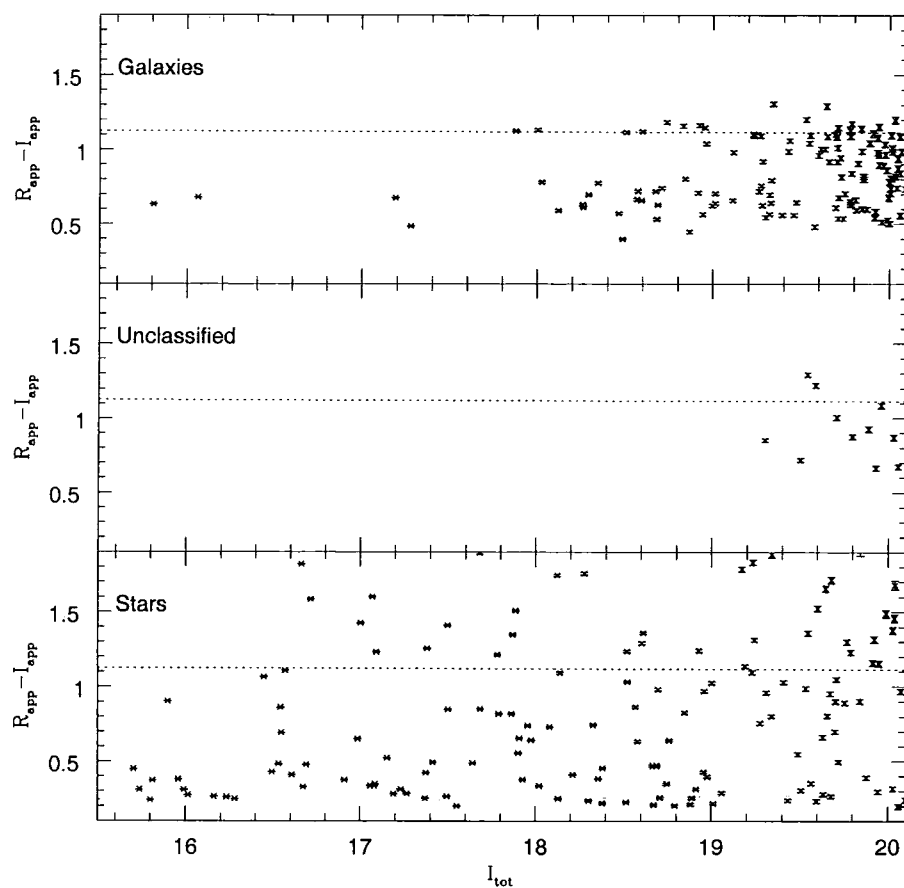


Figure 2.12: Colour-magnitude diagrams of stars, galaxies and unclassified objects in the field of MACSJ0717.5+3745 to the 5σ detection limit of 20.1 mag in the I band. The dotted line marks the fit to the cluster red sequence (c.f. section 3.1.2)

limit of the more traditional technique shown in figure 2.9. This value of $I=19.1$ represents the limit of completeness for star-galaxy separation and matches the empirical expectation that star-galaxy should be possible to within 1 magnitude of the completeness limit (in light of this being $I=20.1$ for the MACS observations.) The figures quoted in table 2.3 show the number of objects in each class of all objects detected in the frame whereas figure 2.12 shows that, to the imaging completeness limit, there are 126 objects classified as being a galaxy, 154 classified as being a star and only 11 (only 4% of the objects detected to this magnitude limit) with no clear determination. The dotted line on each panel in this figure shows the fit to the colour-magnitude sequence (c.f. section 3.1.2) and shows that there is no bias in the unclassified objects toward or against them being cluster galaxies. As the primary purpose of the UH2.2m imaging was to provide pre-imaging for the spectroscopic follow-up campaign, no further attempt was made to determine the identity of these objects. It should be stressed that this example has been for one of the highest redshift clusters in the survey, consequently one for which the star-galaxy separation will be most difficult.

As a final test of the star-galaxy separation technique, the number of objects in each cluster classified as being a star, a galaxy and the number that remain unclassified to the completeness limit of $I=20.1$ was plotted against the absolute galactic latitude of that cluster, the results of which are shown in figure 2.13. As might be expected, the number of objects classified as being a star rises with decreasing galactic latitude while the number classified as being a galaxy is approximately constant across the range of angles. The number of unclassified objects can be seen to be extremely low for all the MACS clusters and decreases with increasing galactic latitude. Consequently the bulk of these objects are believed to be stars and, combined with their small numbers, are not considered to be a major contaminating factor and can be ignored.

As has been stated, SExtractor used the FWHM as one of the parameters in its determination of the P^* parameter. Clearly, the measured value of the seeing will have an effect on the efficiency of the star-galaxy separation process. Figure 2.14 shows how the number of objects classified as being a galaxy ($P^* < 0.1$) or a star ($P^* > 0.9$) changes with the value of the seeing given to SExtractor. It can be seen

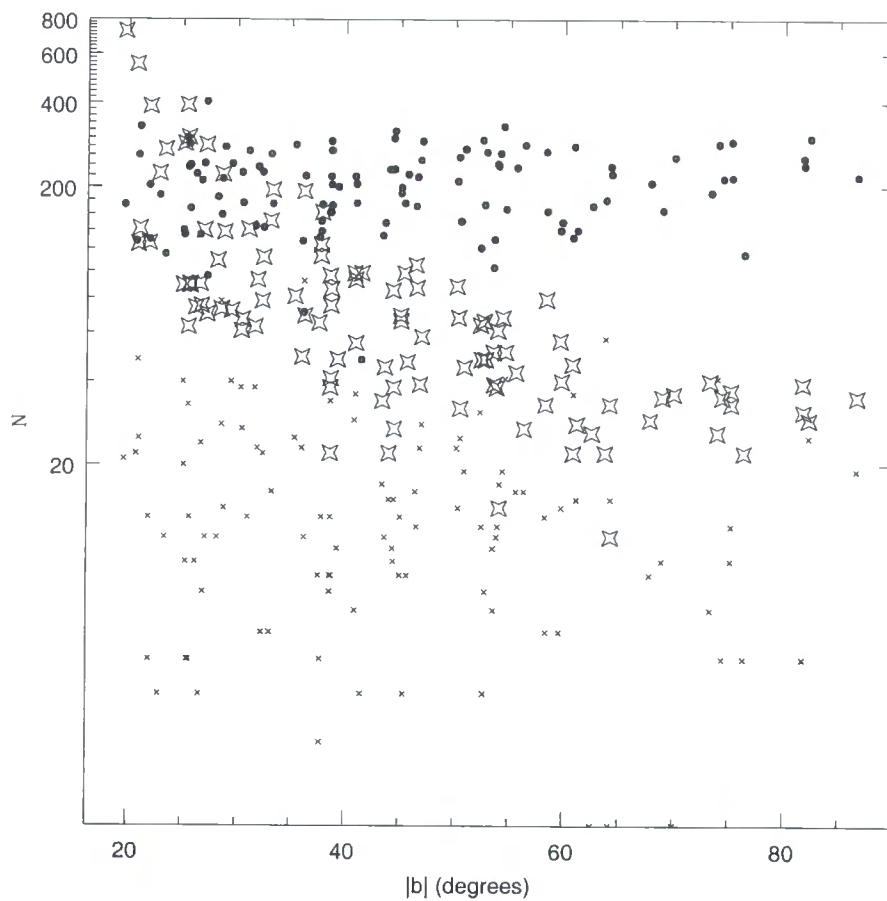


Figure 2.13: The number of objects classified as being a star (open stars), a galaxy (filled circles) or unclassified (small crosses) in each cluster against the absolute galactic latitude of that cluster.

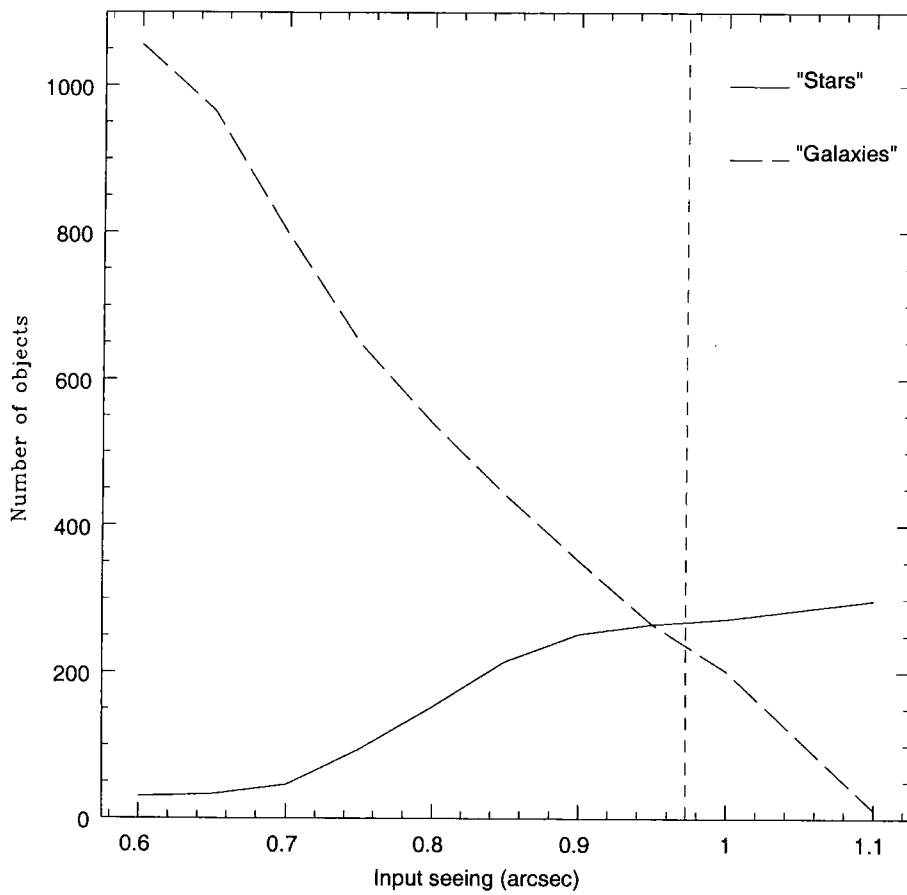


Figure 2.14: The number of objects classified as being a galaxy ($P^* < 0.1$) and the number being classified as being a star ($P^* > 0.9$) against the value of the seeing given as an input to SExtractor. The vertical line marks the actual measured value of the seeing

that the star-galaxy separation process requires an accurate determination of the seeing which is why the automatic process, described earlier, was developed.

2.9 Astrometry

One of the main driving forces behind the MACS three-band imaging campaign was to enable the images to be used for target selection for subsequent spectroscopic follow-up. Consequently, achieving an accurate astrometrical calibration for the UH2.2m imaging is essential.

Astrometry was performed by comparing the positions of stars (selected by the star-galaxy selection process described above) with the positions of these objects in the APM (Maddox et al. 1990; <http://www.ast.cam.ac.uk/apm/>) survey.

The process was undertaken using a shell-script that was initially co-written by Kevin Pimblett, Ian Smail and Alastair Edge which was subsequently modified for use with the MACS UH2.2m data. Stars from the MACS imaging are interactively matched to their APM counterparts and then the CCD position is then transformed to match the positions of these objects. This typically involves a small rotation ($< 5^\circ$), a translation and a magnification. Initially, the fit between the MACS and APM positions is confused by the presence of a small number of objects that have large differences in position between the two sets of imaging. These mismatching objects are either stars with high proper motions that have moved in the years between the APM and MACS imaging was taken, or bright stars that are nearing saturation and so do not have accurately determined centres. These objects with large residual differences in their positions are clipped out and the CCD transformation is recalculated.

This process is iteratively repeated until no object has a residual larger than $0.5''$ and the rms residual of the astrometry is better than $0.3''$, adequate for the needs of the follow-up spectroscopic campaign.

2.10 Summary

In this chapter, the details of the optical follow-up campaign to the MAssive Cluster Survey (MACS) have been given along with the details of the University of Hawaii 2.2 metre telescope which was used for these observations. The process why which the raw telescope was reduced was described along with the method by which SExtractor was used to detect objects. Particular attention was paid to the way in which the seeing conditions were measured and the importance of the value of the seeing on the accuracy of the star-galaxy separation.

Chapter 3

Examining the cluster Colour-Magnitude sequence

3.1 Introduction

The Colour-Magnitude relationship red-sequence is a well known feature of galaxy clusters. Visvanathan and Sandage (1977) noticed from their data on 9 nearby clusters that the brightest, early-type galaxies tended to have redder colours than then the rest of the cluster population. Bower, Lucey & Ellis (1992) later studied the colour-magnitude relation in detail using high-precision photometry of early-type galaxies in the Virgo and Coma clusters. They found that the elliptical galaxies in these clusters form a red sequence with a well defined slope with only small scatter about this relation, implying that there is a strong homogeneity in the present-day elliptical cluster galaxy population. More recent results from the Hubble Space telescope show that there is a red-sequence, comparable in scatter and slope to the colour-magnitude relationship of the Coma and Virgo cluster, in clusters at high redshifts. (Stanford et al. 1998, Ellis et al. 1997). Although the presence of a red-sequence at low-redshift can be explained by either an age or a metallicity effect, the existence of the red-sequence at high redshift makes the age explanation unlikely (Kodama et al. 1998) and implies that the observed red-sequence is a result of a mass-metallicity relationship rather than an age effect.

There are two differing theories as to how this mass-metallicity relationship could form. The first is that ellipticals form in a monolithic collapse at high redshifts and evolve passively after this initial burst of star-formation (Eggen et al. 1962).

In this monolithic collapse scenario, supernovae from massive stars (i.e. type II supernovae) formed in the initial star-burst heat the interstellar medium and can combine to form a galactic wind when the heat injected into the gas by the exploding stars exceeds the binding energy of the galaxy. In this model, because of their shallower potential wells, smaller galaxies are more susceptible to having their gas stripped by this process whereas high-mass galaxies tend to retain more of their gas, naturally leading to a correlation between galaxy mass and star-formation history and therefore colour, seen at the current epoch as a difference in colour with mass.

The alternative explanation is provided by Kauffmann and Charlot (1998) where by elliptical galaxies form through the merger of several smaller disk systems. In this model, there is the same mass-metallicity relationship as in the monolithic collapse scenario in the initial disk systems and then the modern-day massive ellipticals found in the cores of massive clusters are formed from the most massive of the progenitor disk systems, producing the mass-colour relationship.

In this chapter, the colour-magnitude relationship for the MACS clusters is examined and used to constrain the epoch of star-formation. The colour-magnitude relationship is then used as a basis for photometrically selecting cluster member galaxies and as for the basis of a photometric redshift measurement for clusters. The colour-selected galaxies are then used to measure the richness of the MACS clusters, primarily to look for apparently under-rich clusters, and also to look for signs of merger events that could be biasing the X-ray luminosity measurements toward merging systems.

3.1.1 Producing Colour - Magnitude diagrams

For each of the MACS clusters, colour-magnitude diagrams were produced for each of the R-I, V-I and V-R colours and are shown in full in Appendix A. Each colour-magnitude diagram shows the 5" aperture colour of each detected object classified as being a galaxy plotted against the I band total magnitude for that object. The galaxy colours and I-band magnitudes have been corrected for galactic extinction using the Schlegel (1998) maps via the NASA Extra-galactic database interface (<http://nedwww.ipac.caltech.edu/forms/calculator.html>). All observed clus-

ters (111 in total) are shown regardless of whether that cluster was taken in photometric conditions or not, it should be noted that the three band imaging of clusters MACSJ0011.7-1523, MACSJ0152.5-2852, MACSJ0159.8-0849, MACSJ0850.1+3604, MACSJ1246.1-2547, and MACSJ2046.0-3430 were taken in non-photometric conditions and so these colour-magnitude diagrams are for demonstration of the cluster red-sequence and to demonstrate that there is indeed a rich cluster at this position. Although, obviously, these clusters are excluded from any study requiring absolute photometry, they are included in those studies that only require photometry relative to the other cluster members.

It can be seen from the diagrams in Appendix A, that strong red sequences are visible for the vast majority of the MACS clusters in all three colours, confirming that there is a massive cluster at each of these positions. It can also be seen that, for the most distant clusters (eg. MACS0744.8+3927, the highest redshift cluster in the survey to date) that the red-sequence is not as pronounced as in other clusters. This is due entirely to the imaging of these clusters being too shallow for accurate star-galaxy separation and so these clusters appear to be poorer than they, in all likelihood, are. In the subsequent analysis, care has been taken to account for this selection effect caused by the fixed exposure time.

3.1.2 Fitting the red-sequence

For each of the clusters, the colour-magnitude sequences were fit in each of the R-I, V-I and V-R colours against the I-band total magnitude. The method of fitting the colour-magnitude sequence was based upon that used by Beers, Flynn and Gebhardt (1990), Terlevich (1998) and Pimblet et al (2002) in that a robust bi-weight method was used to fit the colour-sequence. In a departure from the technique used by Pimblet et al. a fixed apparent magnitude of $I_{tot} < 20.5$ was used, in contrast to their use of a fixed luminosity limit of $M_v = -21.8$. As has been stated, the depth of the imaging for the highest redshift clusters is insufficiently deep for the red-sequence to be sharply defined over a large range of magnitudes. Taking a similar luminosity cut to the one used results in a limiting apparent I-band magnitude of 21 for those clusters at redshift 0.5. From the colour-magnitude

diagrams shown in Appendix A, the red-sequence is not sharply defined for any of the clusters at this magnitude so, instead, a fixed apparent magnitude limit of $I_{tot} < 20.5$ mag was used. This limit ensures that the fit to the red-sequence is not dominated by the noisy, faint galaxies close to the detection limit in the highest redshift clusters and allows the extra depth in the sequence to be used to reduce the error in the fit for the lowest redshift clusters.

A study of six $0.2 < z < 0.75$ clusters by Gladders et al (1998) using the Hubble Space telescope showed that there is no variation in the slope of the colour-magnitude relationship over 5 orders of magnitude. Given this, the effect of fitting the colour-magnitude sequence with a fixed apparent magnitude rather than luminosity limit is expected to be negligible. In order to exclude the effect of environment on colour as shown for massive clusters of galaxies at $z \sim 0.1$ by Pimbblet et. al. (2002), partly an offshoot from the density-morphology relationship, the fit to the colour-magnitude relationship was made using only those galaxies within a circular aperture of 0.5 Mpc radius, centred on the apparent centre of the cluster, defined by the position of the brightest cluster galaxy. The fits to the colour-magnitude sequence are shown by the solid lines on the colour-magnitude diagrams presented in Appendix A.

The error on the fit was calculated by taking those galaxies within 0.2 magnitudes in R-I, 0.3 magnitudes in V-I and 0.25 magnitudes in V-R of the fit to the colour-magnitude sequence evaluated at $m_I = 19$. The fit to the colour-magnitude sequence was then bootstrapped against those galaxies within this slice of colour-magnitude space to calculate the error on the fit to the slope.

3.1.3 Trends in cluster red-sequence slope

Having fitted the cluster red-sequence, the slope of the colour-magnitude sequence was used to attempt to constrain the star-formation history of the cluster galaxies, the evolution of the slope of the fit to the red-sequence in the $R_{app}-I_{app}$ against I_{tot} colour-magnitude sequence with redshift is shown in figure 3.1. Included in the dataset for this figure are all the cluster red-sequences presented in Appendix A with the exception of the clusters MACSJ0011.7-1523, MACSJ0152.5-2852, MACSJ0159.8-

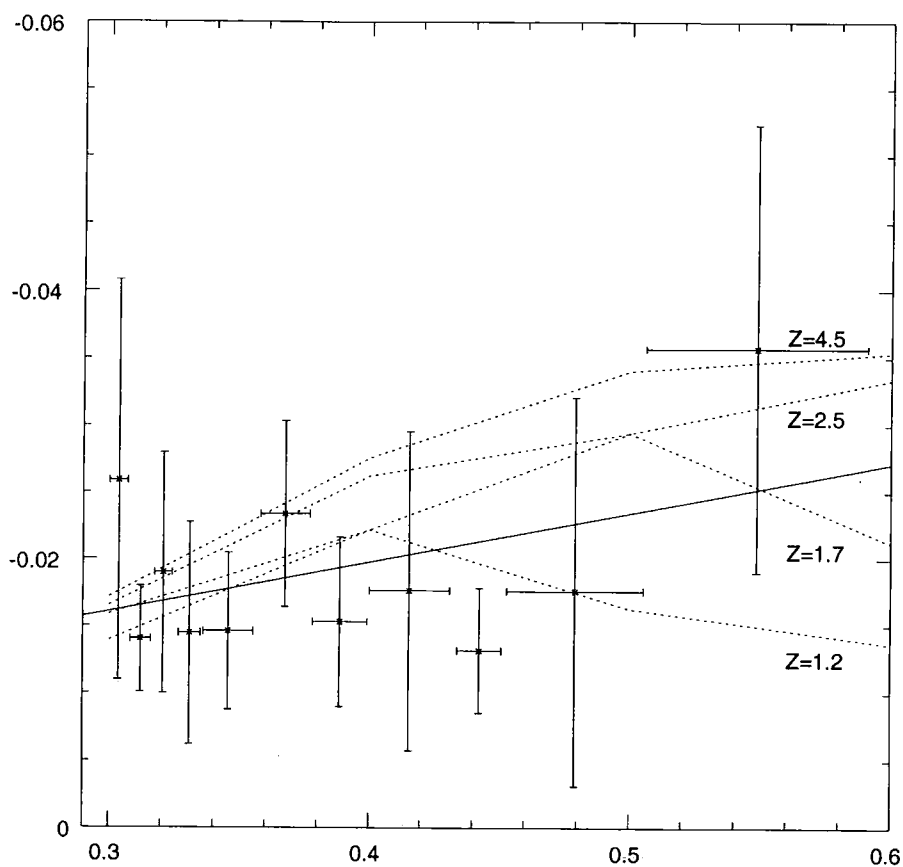


Figure 3.1: The evolution with redshift of the $R_{app}-I_{app}$ against I_{tot} colour-magnitude sequence, the solid line marks the best fit linear relationship to the data. The dotted lines trace the predicted evolution of the slope of the cluster red sequence (from the Kodama and Arimoto 1987 model) with redshift for clusters with four different epochs of formation (taken from Gladders et al. 1998).

0849, MACSJ0850.1+3604, MACSJ1246.1-2547 & MACSJ2046.0-3430 which were taken in non-photometric conditions. Although colour-magnitude sequences have been calculated for the V_{app} - I_{app} and V_{app} - R_{app} against I_{tot} sequences, the depth of the V band imaging is too shallow to allow the fits to these sequences to be determined sufficiently accurately and so the slopes obtained in these colours is dominated by the photometric errors and so are not shown.

It can be seen from figure 3.1 that within the MACS sample, the slope of the red-sequence is increasing weakly with redshift. i.e. clusters at higher redshift have steeper slopes than those at lower redshifts, the evolution of the slope of the red-sequence is measured to be -0.03689 ± 0.018 magnitudes per unit redshift. This is unlikely to be an artifact of the higher redshift clusters having insufficiently deep imaging as the noise introduced by the poorer photometry will act to wash-out the cluster red-sequence and bias the bi-weight fit toward finding a flatter slope, the opposite of what is observed.

There is a possible bias introduced from the fact that MACS is an X-ray flux limited sample, poorer clusters are only selected at the lowest redshifts, which leads to a direct correlation between redshift and cluster richness which could be the cause of the trend seen in figure 3.1. In order to test this, the slope of the R_{app} - I_{app} against I_{tot} colour-magnitude sequence was plotted against the cluster X-ray luminosity (used as a measure of the mass of the cluster), using only those clusters with redshifts less than 0.4, the result of this is shown in figure 3.2. It can be seen from this figure that there is no trend in the slope of the red-sequence with X-ray luminosity, the best fit to the data shows a trend of $-4.0 \times 10^{-5} \pm 2.7 \times 10^{-4}$ per 10^{44} erg/s, i.e. consistent with zero. From this result, it is concluded that the slope of the cluster red-sequence is independent of richness and that, for a given redshift, this slope is universal, confirming at the redshifts of the MACS clusters what was found at much lower redshifts (Bower et al. 1992.)

The presence of a strong red-sequence at the redshift of the MACS sample is further evidence that the apparent reddening of massive galaxies is the result of a mass-metallicity relationship rather than an age effect (Kodama & Arimoto 1997; Kauffmann & Charlot 1998; Kodama 1997.) If the red-sequence was due to an age effect then no such sequence would be expected to be seen at these

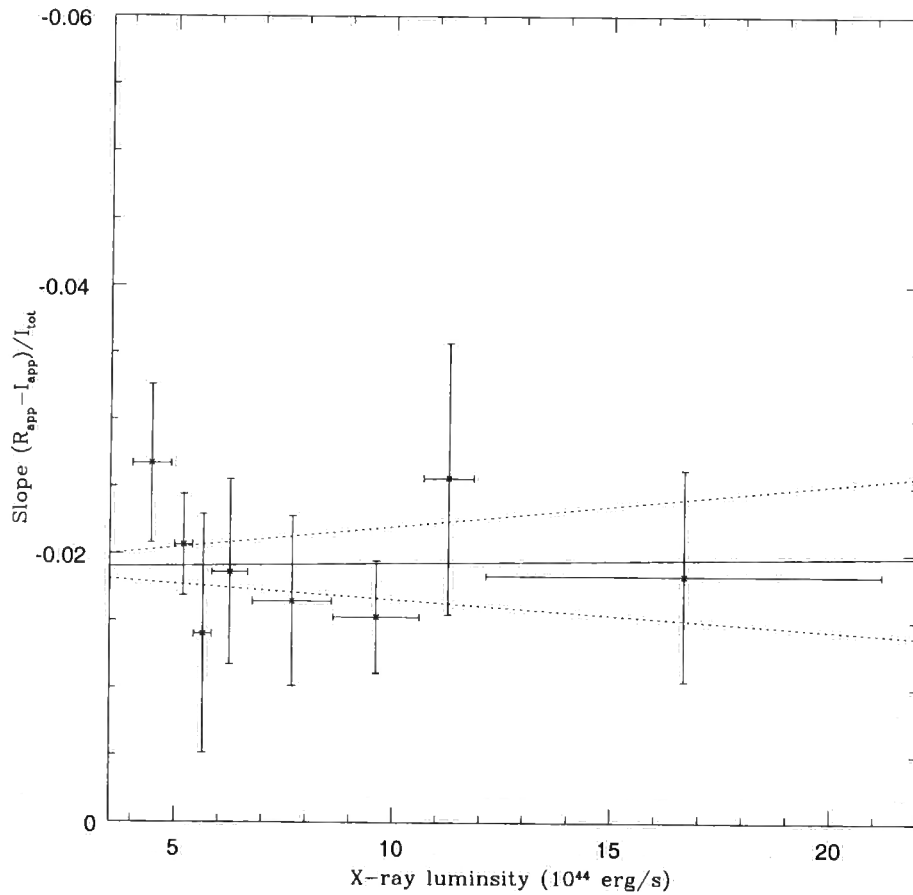


Figure 3.2: Evolution of the slope of the fit to the cluster $R_{app}-I_{app}$ against I_{tot} colour-magnitude sequence against X-ray luminosity for clusters with $z < 0.4$, used to test the effect of cluster mass on the observed slope of the red-sequence.

redshifts. This lack of trend would be expected to be especially noticeable in the clusters selected by the MACS survey as these are the most massive objects at these redshifts, representative of the population expected to be undergoing to most noticeable evolution. Hence, the clusters in the MACS survey would be expected to be the ones most sensitive to age related effects.

Having shown that slope of the colour-magnitude relationship is not dependent on the age of the cluster, the slope of the cluster-red sequence can be used to constrain the star-formation history of the cluster galaxies. Gladders et al (1998) showed that for 3 clusters at redshifts comparable to those of the MACS survey i.e. $z > 0.3$, the slope of the cluster red-sequence was consistent with the elliptical galaxies being formed of a passively evolving single age stellar population that formed at high, $z > 2$, redshift. The models that Gladders et al used are plotted with the MACS data in figure 3.1. Before any direct comparisons are drawn, it should be noted that these models were originally calculated for the Hubble Space Telescope F555 and F814 filters and Gladders et al calculate their slopes in the $(F555 - F814)/F814$ colour. Consequently, a large filter correction has had to be applied to these model data to convert it to the Kron-Cousins based $(R - I)/I$ colour calculated for the MACS clusters.

Figure 3.1 shows that there is variation in the slope of the cluster red sequence for all model clusters, regardless of the epoch of formation of that cluster. This may seem surprising as the clusters with the highest redshifts would maybe be expected to have completed the majority of their evolution and to be, at these redshifts, essentially passively evolving. However, the apparent evolution of the slope of these clusters can be attributed to the 4000 angstrom break moving through the apparent wavelength range at these redshifts.

Figure 3.1 also shows that the large errors on the MACS data points mean that they cannot be used to accurately constrain the epoch of formation. Having previously shown that the slope of the cluster red sequence appears to be a ubiquitous feature of galaxy clusters, clearly the best approach for constraining the epoch of galaxy formation is to take high quality, deep, imaging of a limited number of clusters (as done by Gladders et al.) rather than the wide and shallow approach taken by the MACS collaboration.

Given these large errors, a detailed, quantified analysis of the differences between the MACS data and the models shown in figure 3.1 would be futile. However, this does not mean that these data cannot be used to qualitatively constrain the epoch of formation. It can be seen from the models that these clusters with later (i.e. lower redshift) epochs of formation have turnovers in the evolution of their red sequence with redshift i.e. the slope gets shallower with redshift rather than steepening. The MACS data shows that to at least 1σ confidence, there is no such turnover visible in the MACS data. From this lack of turnover, it would appear that the MACS clusters favour models where the galaxies formed the bulk of their stars at $z > 1.7$, consistent with the previous work that used a much smaller sample at these redshifts.

3.1.4 Sequence Colours

If the red-sequence of a galaxy cluster is a universal feature, then can this be used as an effective standard colour to allow the measurement of photometric redshifts? Obtaining an estimated redshift in this way is desirable for several reasons. Firstly, imaging is much cheaper in terms of telescope time and so any method that can fully exploit such data will have obvious efficiency benefits. Secondly, many photometric redshift techniques rely on using a single object, for example in the case of clusters, the brightest cluster galaxy (BCG) has often been used as a standard candle. While having the advantage of being simple, any technique based upon the observation of a single object is inherently flawed as every galaxy in the universe is unique and under no obligation to follow any trends set by other galaxies. Using the cluster red-sequence avoids this problem as, by fitting the entire cluster population, individual anomalous galaxies (eg. star-bursts, AGN, serendipitous supernovae etc.) will not significantly effect the trend laid out by the rest of the cluster galaxy population.

Obviously, establishing photometric redshifts for the MACS survey is not inherently useful, as all of the MACS clusters already have spectroscopic confirmations, although it has provided a useful double check to the spectroscopic results. However, this does allow the MACS sample to be used as a basis for establishing the technique for upcoming clusters. To this end, the fit to the colour-magnitude se-

quence was evaluated at 19th (apparent) magnitude and this evaluated colour is shown for the R-I/I, V-I/I and V-R/I colours against redshift in figure 3.3. It can be seen that this evaluated colour traces out the expected colour for an elliptical galaxy at the relevant redshift (the solid line in figure 3.3) as predicted by King and Ellis (1985). It should be noted that the V filter used at the University of Hawaii 2.2m telescope is significantly bluer than a standard Kron-Cousins filter, this results in a correction of 0.4 magnitudes blue-wards needing to be applied to the V-I and V-R models. As this correction is consistent and in the same sense for these two colours, this is clearly due to the filter colour rather than any systematic error in the line-fitting.

Before being used for photometric redshifts, this colour-redshift relationship was used initially as a check to the quality of the fit to the red-sequence and finally to identify non-photometric clusters by their large scatter from this relationship, objects were rejected as being non-photometric if they showed anomalous colours in any two of the three used, indicative of there being a problem with at least one of the individual images. The non-photometric clusters are not shown in figure 3.3.

The scatter of the evaluated colours around the prediction is 0.04, 0.06 and 0.06 magnitudes for the R-I, V-I and V-R colours respectively, the scatter of the evaluated colour about the King and Ellis model being shown in figure 3.4. As is discussed in section 5.6.2, this corresponds to an error on the determination of photometric redshifts of ~ 0.03 . The distribution of the scatter is entirely consistent with these being random distributions and the magnitude is comparable to the scatter being dominated by systematic errors carried over from the photometric calibration of the imaging from the Landolt standards, borne out by the fact that these scatters are consistent with, and in some cases better than, the scatter observed in the aperture magnitudes of the BCG population (cf. table 4.2 in section 4.5). It should again be stressed that this is only modest depth imaging taken on a small telescope over the course of several years with the associated variable atmospheric conditions, demonstrating how well the seeing matching process, applied in order to counteract the effects of the seeing, compensates for these variable conditions. Fitting the red-sequence shows only the same degree of scatter as using a single object (eg. the BCG) but without the associated problem of individual

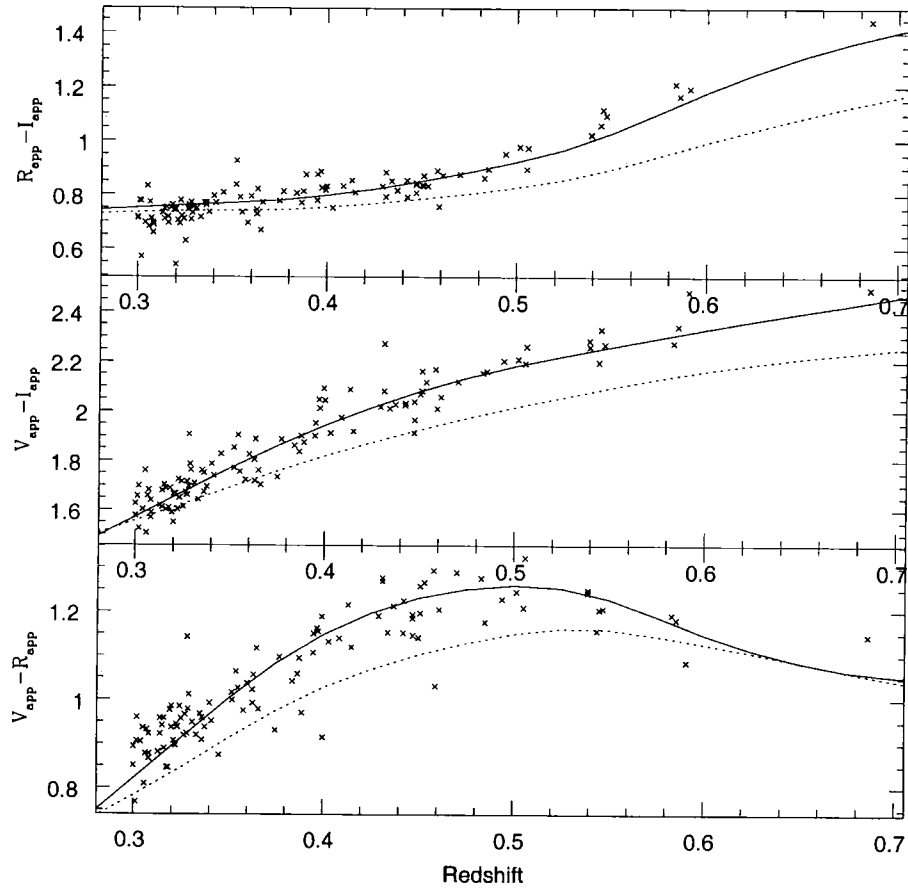


Figure 3.3: The colour obtained by evaluating the fit to the $R_{app}-I_{app}$ (Top), $V_{app}-I_{app}$ and $V_{app}-R_{app}$ red-sequences at 19th magnitude plotted against cluster redshift. The solid lines denote the predicted colour for an elliptical galaxy (with luminosity L^*) at these redshifts (King and Ellis 1985). For comparison, the dotted lines show the predicted colour for a similar luminosity S0 galaxy. The $V_{app}-I_{app}$ and $V_{app}-R_{app}$ models have been fitted to the data by applying a 0.4 magnitude filter correction.

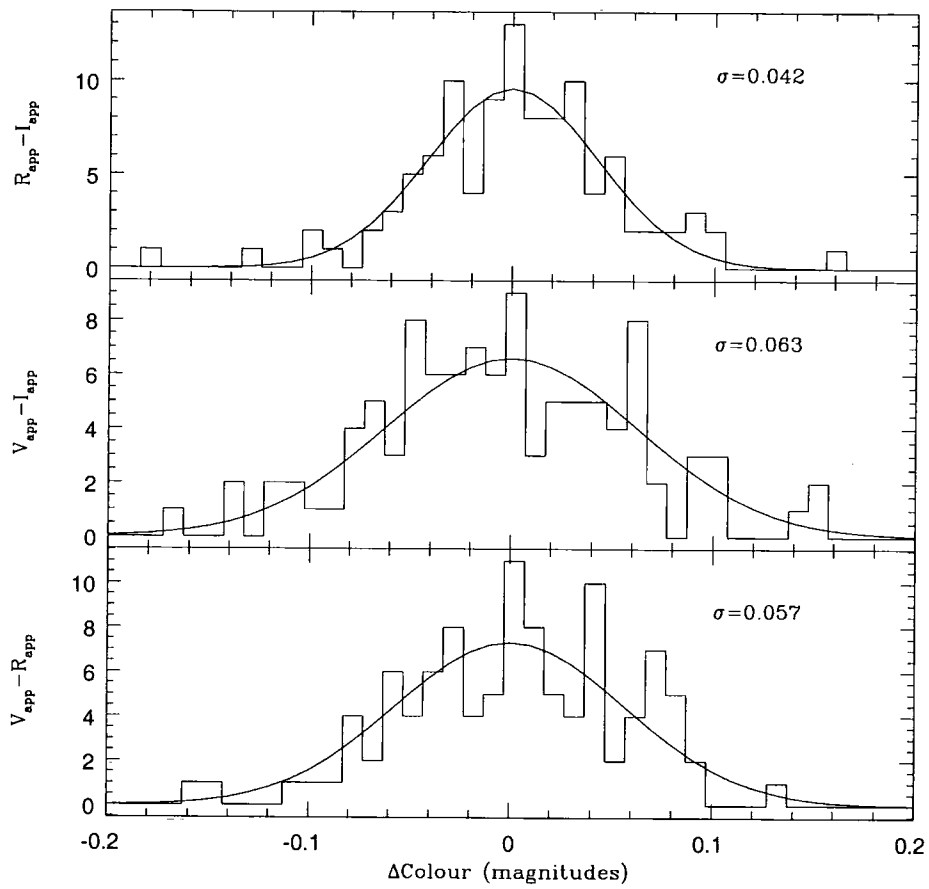


Figure 3.4: The scatter in the colour of evaluated fit to the cluster red-sequence about the predicted (King and Ellis 19985) colour for an elliptical galaxy at the relevant redshift.

objects with anomalous colours. This shows that even with shallow imaging, the cluster red-sequence can be used as a standard candle for estimating the distance to a cluster. This technique was used successfully for a sample of MACS-like clusters in the southern hemisphere, detailed in chapter 5.

3.2 Optical Cluster Richness

Finding clusters of galaxies at redshifts greater than 0.3 was only one part of the MACS survey goals, the aim was to find the most massive clusters of galaxies at these redshifts. As described in section 1.4, using the X-ray emission from clusters only selects massive clusters of galaxies, as it is only these clusters which contain a sufficient mass of hot gas to be X-ray luminous. The secondary selection of requiring over-densities of galaxies in the direction of the X-ray emission should eliminate isolated X-ray point sources, such as AGN, from the survey sample. There remains the possibility that the MACS survey could select an inherently poor cluster of galaxies where the X-ray emission has been boosted by the presence of an X-ray emitter additional to the inherent cluster X-ray luminosity (the possibility of AGN in clusters is described in depth in chapter 7.)

In order to ensure that the MACS sample is selecting only clusters of galaxies, optical richness measures were used to examine the MACS clusters to look for clusters that appear to be significantly poorer than the rest of the MACS sample, indicative of possible contamination.

3.2.1 Selecting cluster members

Before any richness measures can be made, it is necessary to develop a method to select potential cluster member galaxies. Obviously, the only truly reliable method for performing this selection would be to make a full spectroscopic survey of each cluster, but this is clearly impractical due to the enormous amount of telescope time that would be required. Instead the fit to the cluster red-sequence was used to define a region of the colour-magnitude diagram that contains cluster member galaxies.

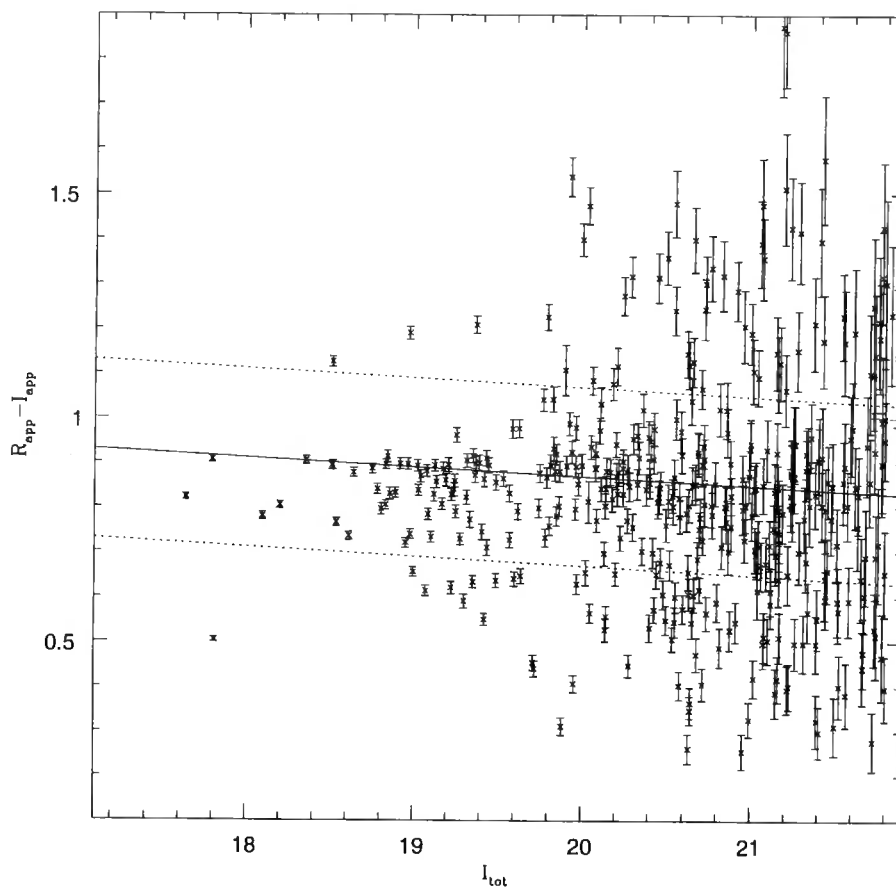


Figure 3.5: $R_{app}-I_{app}$ against I_{tot} colour-magnitude diagram for all galaxies in the field of MACSJ1206.2-0847 showing (solid line) the bi-weight fit to the cluster red-sequence and (dotted line) the bound of the area within which galaxies are classified as being within the cluster.

For each cluster, a galaxy was selected to be a cluster member if it has a colour that lies within 0.2, 0.25 and 0.3 magnitudes in each of the R-I, V-I and V-R colours i.e. a region is defined in the three available colour-magnitude diagrams using a constant offset from the fit to the cluster red-sequence and a galaxy must lie within all three regions to be selected.

Figure 3.5 shows this selection in the R-I/I colour-magnitude diagram for the redshift 0.44 cluster MACSJ1206.2-0847. Shown is the fit to the cluster red-sequence (solid line) and the bounds of the region 0.2 magnitudes from the fit. On first inspection, this appears to be an extremely poor constraint, and if only this one colour were used then a much stricter selection would be needed. However, by using three separate colours, non-cluster galaxies are excluded by their having sufficiently different colours in at least one of the colour-magnitude diagrams. Object selection using this method has been used as part of the MACS follow-up campaign (cf. chapter 6) and non-cluster galaxy contamination was found to be low, only 4-6% of the galaxies for which redshifts were obtained.

This method of selecting cluster member galaxies was used for the following section of this chapter and any other time when cluster membership is required, in particular the dominance of the brightest cluster galaxy (cf. section 4.4.3) and its alignment with its host cluster (cf. section 4.6.)

3.2.2 Number of Galaxies

The very simplest method of measuring the richness of a cluster of galaxies is to simply count the number of galaxies within the field of view of the cluster. In his original cluster catalogue, Abell imposed the criterion for selection that a cluster must contain more than 50 galaxies not more than 2 magnitudes fainter than the third brightest cluster galaxy. This measure of richness, counting the number of galaxies between N_3 and $N_3 + 2$ (also known as the Bahcall (1975) number), is a relatively standard measure of the richness of the cluster although it has several drawbacks.

Firstly, this number can be measured within a number of different apertures, which will effect the number of galaxies selected. In surveys based upon large

panoramic surveys, such as the Palomar Sky survey used by Abell, this is not a problem as the large sky coverage will fill even the largest aperture. This is not the case for pointed observations such as those used in this work. Care must be taken that the observed area completely contains the aperture within which galaxies are counted.

Secondly, there is the question of how cluster membership is assigned. As has been seen in the previous section, photometric cluster membership selection is not clear-cut and an optimised method must be used. Again, differing methods of galaxy selection will select differing numbers of objects, systematically altering the derived richness. However so long as sufficient care is taken to control these selection effects, this method is suitable for comparing the clusters within a particular survey.

Figure 3.6 shows the number of galaxies selected as being cluster members no more than 2 magnitudes fainter than the third brightest galaxy within a 1Mpc aperture centred on the brightest cluster galaxy for all clusters with redshifts less than 0.4, as measured in each of the I, R and V bands, plotted against the X-ray luminosity of the host cluster. Any clusters where, due primarily to the position of the BCG, the 1Mpc aperture is not completely covered by the imaging have been excluded from this study. The redshift limit was imposed on this test as the highest redshift objects do not have sufficiently deep imaging to allow this richness measure to be made. For the cluster MACSJ1206.2-0847 at redshift 0.44, the I-band magnitude of the third brightest galaxy is 18.46 mags, with the corresponding boundary of the richness test being 20.46 magnitudes. As seen in figure 2.10, this is at the limit of the reliable star-galaxy separation and so the richness measure will, at these redshifts, be dominated by the reliability of the star-galaxy separation process rather than the inherent richness of the cluster, hence the exclusion of clusters at $z > 0.4$

Figure 3.6 shows the limitation of this method as a way of establishing the richness of a cluster. Although, as expected, the apparent richness of a cluster rises with increasing X-ray luminosity, there is extremely large scatter about the trend and it is impossible, based upon this data, to make any quantifiable statement about which clusters are apparently underpopulated.

This figure also highlights a second limitation of this measure, the richness

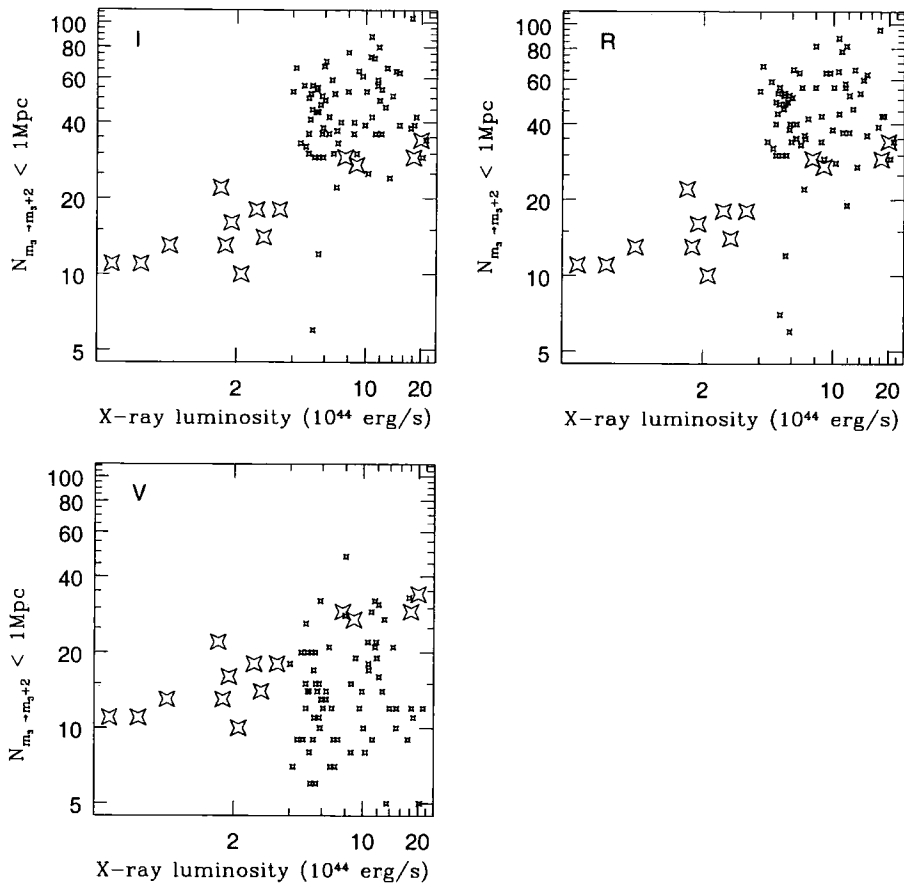


Figure 3.6: Number of galaxies with magnitudes between the third brightest cluster galaxies and a limit two magnitudes fainter than this for cluster galaxies within 1Mpc of the brightest cluster galaxy as measured in the I-band (top left), R-band (top right) and V-band (bottom.) Shown also, for comparison only (large stars), are the similar numbers for a sample of X-ray luminous galaxies taken from Edge and Stewart (1991). The MACS data points are in qualitative agreement with the trend set by the Edge and Stewart data.

determination has been plotted using the same scale for the three pass-bands to highlight that a different value of the richness of a cluster is obtained depending on what band the cluster is studied in, the bluer bands produce lower apparent richnesses. This effect is not due to selection, as each of the measures were made using the same list of colour-selected galaxies and so any incompleteness will be present in, and affecting, all three measures equally. Clearly such a dependence on the observed wavelength makes such a measure of richness extremely unreliable. There is another possible source of incompleteness arising from the fact that cluster member galaxies have been selected on the basis of having a observed colour close to the trend defined by the cluster elliptical population, which will exclude any inherently blue cluster galaxies. However, this effect is neglected as it is believed to be small as only a very limited number of blue galaxies are found in the core of massive clusters at these redshifts, Smail et al 1998 find that only 4% of galaxies in the cores of rich clusters are blue.

3.2.3 Virial Radius

Having shown that simple number counting does not return a reliable measure of the cluster richness, the Virial radius was used to evaluate the physical size of a cluster. Relaxation processes in clusters naturally lead to the formation of physical cores in clusters of galaxies (see, eg. King 1966, Lynden-Bell 1967, Peebles 1970; Sarazin 1980) and various methods have been used to characterise the size of this core of galaxies, including the commonly used King surface density profile (see, e.g., Bahcall 1977 and reference therein) However, for this work, due to the relatively modest number of galaxies in some of the more distant clusters, the Virial radius (see e.g. Limber and Matthews 1960, Girardi et al. 1994) was used as the preferred measure of richness. In this study, the two-dimensional virial radius is considered:

$$R_{vir} = \frac{N^2}{\sum_{1 \neq j}^N R_{ij}^{-1}}$$

where N is the number of cluster members and R_{ij} is the projected distance between the i and j th cluster member galaxies.

This quantity was calculated for the MACS clusters considering all galaxies within a projected 1Mpc aperture. Evidently, this imposed aperture, used for obvi-

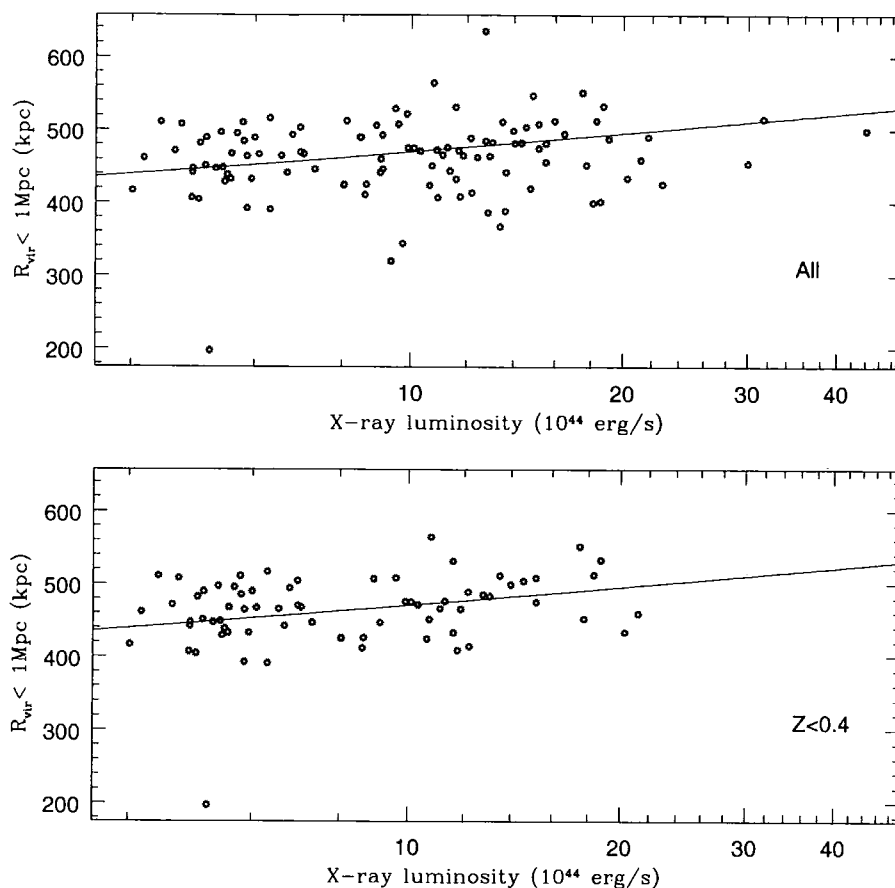


Figure 3.7: Virial radius of cluster galaxies with a 1Mpc aperture, used as a measure of cluster richness, for (top) all cluster and (lower) clusters at $z < 0.4$.

ous observational reasons, means that this is not a true virial radius (the calculation of which requires the positions of all of the galaxies in a cluster) as may be calculated in numerical simulations. As before, clusters for which there is not complete coverage of this aperture have been omitted. Figure 3.7 shows the distribution of virial radius with X-ray luminosity for both the full MACS sample and those at redshift less than 0.4, both fitted with a simple power-law. It can be seen that the distribution of Virial radii form a relatively tight trend around the power-law (the scatter about the power-law is shown in figure 3.8) which makes this test suitable for determining between contaminated and uncontaminated clusters, the 1σ dispersion in the Virial radii being only 40 Kpc. This result is in contrast to the one found by Donahue et al. (2001) who claim that there is a large scatter between the optical and X-ray properties of clusters. A quick inspection of figure 3.7 shows that there

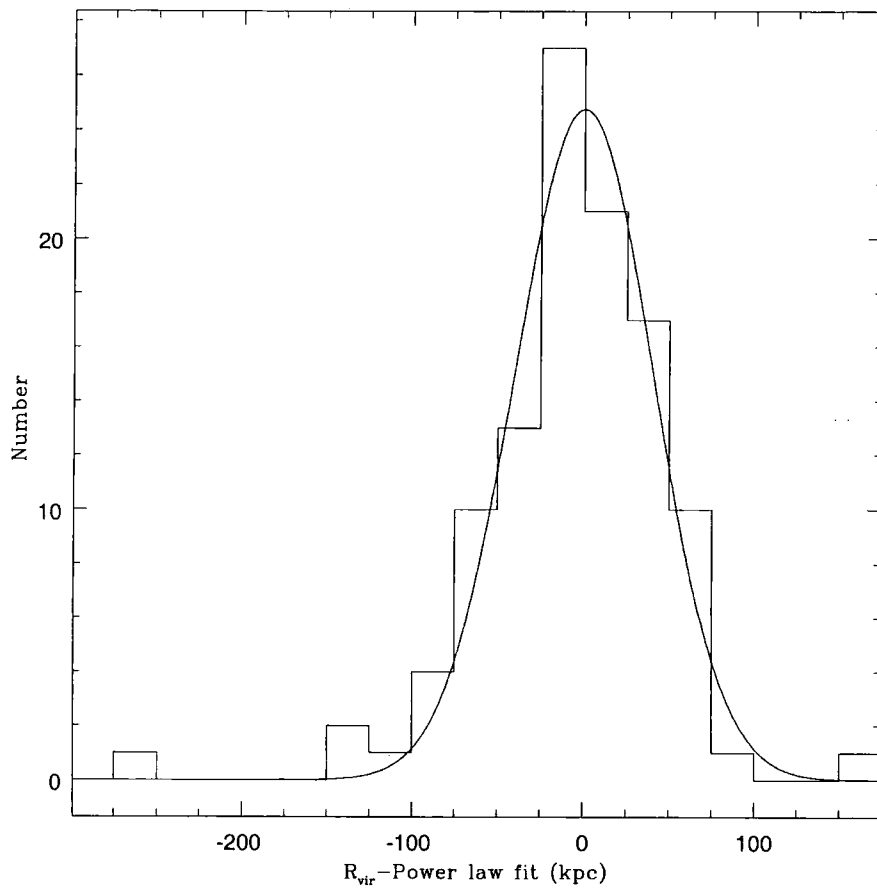


Figure 3.8: Scatter in virial radius about the power-law fit shown in the top panel of figure 3.7

is an object which appears to be much poorer than would be expected for a cluster if it's X-ray luminosity. This cluster is MACSJ2135.2-0102, potentially a redshift 0.325 cluster. While there is clearly an over-density of galaxies in the direction of this X-ray source (otherwise it would not have passed the pre-imaging stage of the MACS selection,) the colour-magnitude diagram presented in appendix A for this object shows that it does not have a particularly prominent red-sequence, again an indication that the observed concentration of galaxies may not be the source of all of the detected X-rays. This object will now be studied in more depth to look for any other potential sources of the X-ray emission to determine whether or not this object is a rich cluster or not.

There is a second cluster that is more than 3σ poorer in virial radius than would be expected and this is MACSJ1411.3+5212, otherwise known as the cluster surrounding the radio source 3C 295. This cluster is host to a well studied cooling-flow (Allen et al 2001), which will account for it being more compact than would be expected from its cooling-flow boosted X-ray emission.

It appears as though, as expected, simple counting of galaxies is not a suitable way of establishing a measure of richness for clusters. However, an aperture virial radius reveals a relationship between it and X-ray luminosity that is sufficiently well constrained as to allow it to be used to test for contamination in the MACS cluster sample, as shown by the case of MACSJ2135.2-0102. Other than this object, constituting less than 1% contamination, all of the objects selected by the MACS selection criteria do indeed appear to be massive, rich, clusters of galaxies.

3.3 Cluster Symmetry

One aspect of X-ray selected surveys that is often neglected is that of the effect of mergers on the X-ray luminosity. One of the first assumptions in the calculation of cluster properties is that the cluster is dynamically relaxed and that the cluster gas is in hydrostatic equilibrium. However, as the X-ray luminosity of a cluster is directly proportional to the square of the density of the X-ray luminous gas, any processes that disturb the equilibrium of the gas, eg. the in-fall of a galaxy group into a cluster, could have a large effect on the observed X-ray luminosity. Indeed,

theoretical simulations by Randall, Sarazin and Ricker (2002) show that the effect of the boost in the X-ray luminosity due to mergers could lead to the number of clusters with temperatures $T > 10keV$ at redshifts greater than 1 being boosted by a factor of 9.5. Evidently, the effect of mergers is non-trivial and any X-ray selected survey should attempt to constrain the contamination due to non-relaxed systems.

3.3.1 The symmetry factor

In an attempt to determine the effect on the X-ray luminosity due to mergers, the symmetry properties of the clusters are used as a test of merger activity. For a cluster, the symmetry factor is defined as:

$$\frac{1}{n} \sum_{i=1}^n \log_{10} \left(\frac{\overline{d}_5(i)}{d_5(i)} \right)$$

where n is the number of colour-selected galaxies, d_5 is the distance to a galaxy's 5th nearest neighbour and \overline{d}_5 is the distance to the 5th nearest neighbour of the symmetry point of the galaxy, making this a dimensionless measure. In order to demonstrate what is explored by this factor, a schematic layout of two idealised clusters is shown in figure 3.9

This figure shows two clusters, one is completely relaxed and so will appear to be circular in projection. The other is a similar cluster, but with an in-falling group. For the relaxed group, for any galaxy and its symmetry point (the small circles in the upper part of figure 3.9) the distance to the 5th nearest neighbour will be identical for the galaxy and its symmetry point and so the symmetry ratio for this galaxy will be zero. As this equivalence will be true for all of the galaxies in this cluster, the overall symmetry factor of a perfectly symmetrical cluster will be zero.

In the case of the merging system, it is clear that the symmetry factor for all of the galaxies in the main, relaxed part of the cluster will sum to zero, but for a galaxy in the in-falling group, the distance to the 5th nearest neighbour of the symmetry point will be considerably larger than that of the galaxy, leading to a non-zero symmetry factor. Consequently, it can be seen that the symmetry factor will ignore the majority of the relaxed galaxy cluster and can be used as an indicator of variations in the galaxy density which could be indicative of variations

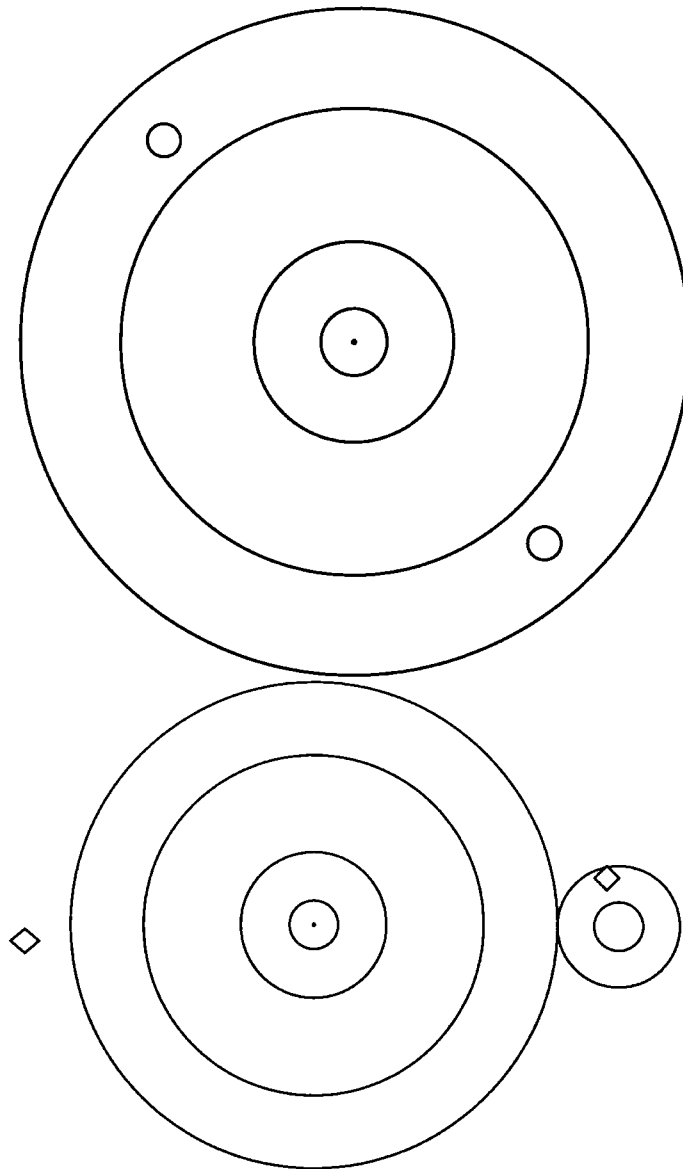


Figure 3.9: Schematic of a perfectly relaxed cluster (top) with a galaxy / symmetry point pair (small circle) and a relaxed cluster with a small, merging group (bottom) with a galaxy symmetry point pair (diamonds). In both cases, the centre of the cluster will be at the middle of the potential well of the large cluster (marked with the dot.)

in the density of the intra-cluster medium. The symmetry factor is normalised by the number of galaxies in the system as a whole to account for the impact of the in-falling group on the cluster, i.e. a group of 10 galaxies will have less of an effect on a cluster of 100 members than one of 50 members.

3.3.2 Symmetry of MACS clusters

For each MACS cluster the symmetry ratio was calculated from the colour-selected galaxies within 1Mpc of the location of the Brightest Cluster Galaxy. The location of the brightest cluster galaxy was chosen as, in simulation of clusters (see, eg. Benson et al. 2000) dynamical friction will cause the most massive, and hence brightest, galaxy to sink to the middle of the cluster potential. Perturbations to the position of the BCG will move it away from the point of maximum symmetry of the projected galaxy distribution, increasing the measured symmetry factor. However, perturbations to the cluster potential can only realistically be achieved by merger events, the very process that the symmetry ratio is attempting to detect.

A major possible source of contamination to the cluster symmetry signal is the presence of large foreground objects that obscure part of the cluster field, for example, the halo of bright stars or large foreground galaxies. To compensate for the galaxies that are ‘missing’ behind these objects, a mask was made to cover the obscured area, shown in figure 3.10.

The mask of each object was then translated to the opposite symmetry point and any cluster galaxies falling within this translated region were clipped out. This results in preserving the overall symmetry of the cluster system. For some of the cluster fields, the position of the BCG is sufficiently close to the edge of the image that there is not a complete circle of projected 1Mpc radius. These clusters are excluded from the symmetry analysis as there is no way of reconstructing the unseen galaxy distribution without making assumptions about the symmetry of the cluster, the very thing that is being tested.

Additionally, to ensure that the symmetry properties of sufficiently large number of galaxies were being tested, clusters that didn’t have sufficiently deep imaging to have a reliable $N_3 \rightarrow N_3 + 2$ richness measure were also excluded, a sample of 87

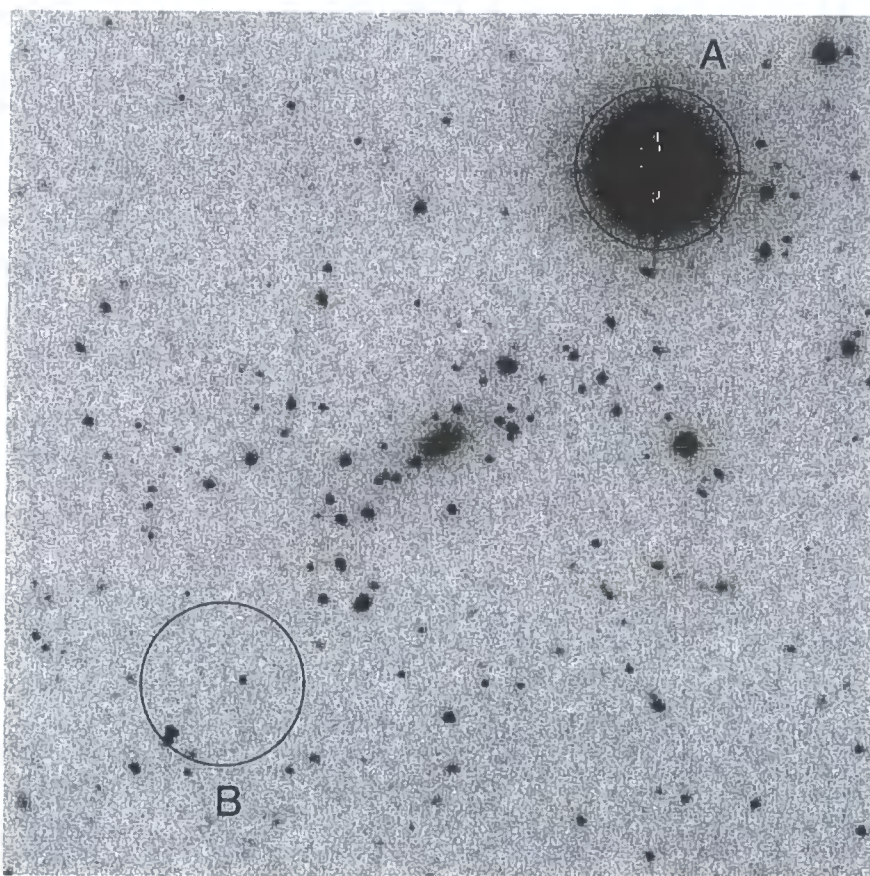


Figure 3.10: $3' \times 3'$ I-band image showing the centre of the redshift 0.354 cluster MACSJ0035.4-2015 and an example of the star masking process. For each bright star, a mask is created that covers the halo of the star (A). This halo is then transformed to the symmetry point of the cluster (B). Any colour selected galaxies that lie within the region of the transformed mask are excluded from the calculation of the symmetry factor.

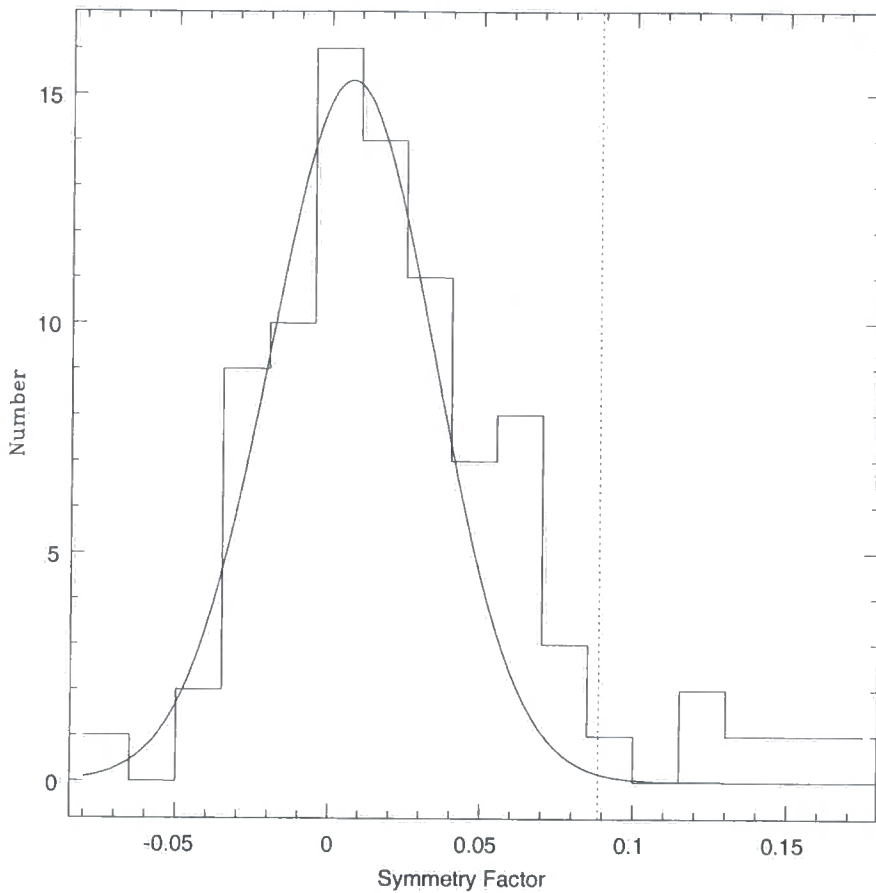


Figure 3.11: Histogram showing the distribution of the symmetry factor for the 87 cluster deemed to have sufficiently deep imaging. The solid line shows the best fit Gaussian curve and the dashed line marks the 3σ deviation.

clusters remained from the full MACS sample of 111 clusters.

A histogram of symmetry factor for these 87 clusters is shown in figure 3.12. As might be expected, distribution of symmetry appears to be Gaussian, but there is a tail of clusters with significantly higher symmetry factors than would be expected from the distribution of the rest of the sample. These 5 clusters are MACSJ0717.5+3745, MACSJ1131.8-1955, MACSJ1226.8+2153, MACSJ1236.9+6311 and MACSJ1354.6+7715, all of which appear to be highly disturbed when the images of these clusters are examined, confirming that the symmetry factor is finding clusters that appear to be in the process of merging.

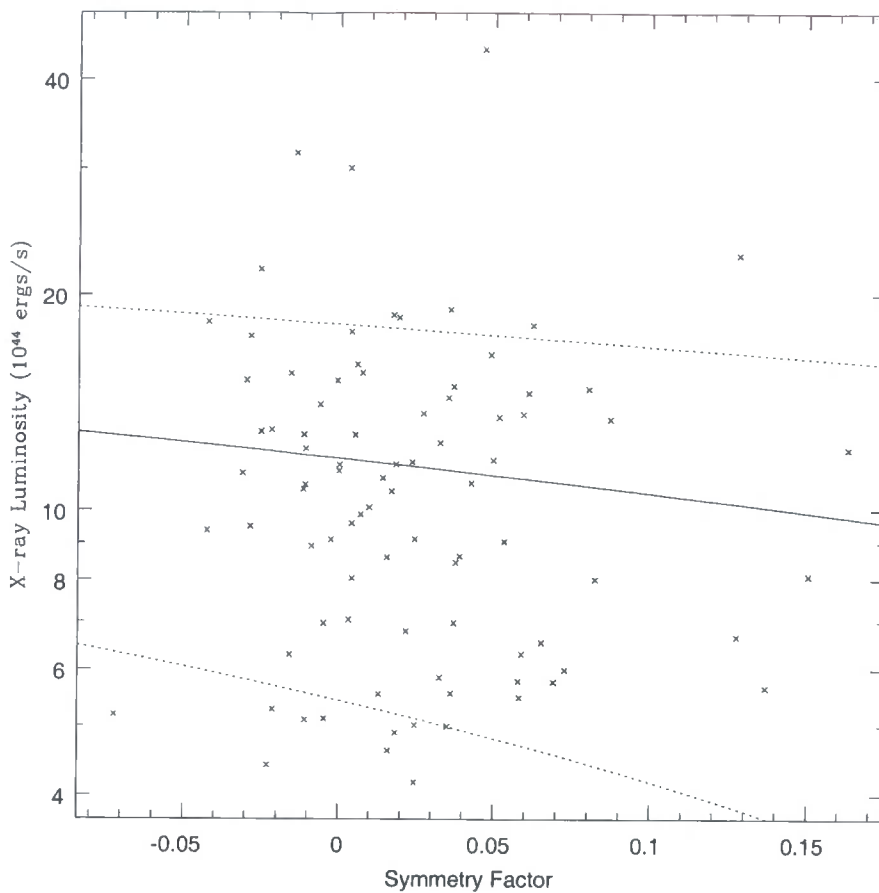


Figure 3.12: X-ray luminosity against symmetry factor for the 87 MACS clusters with sufficiently deep imaging. The solid line denotes the fit to the data and the dotted lines the 1σ confidence limit.

Symmetry properties with X-ray luminosity

In order to test the effect of mergers on the X-ray luminosity, the luminosity of the 87 clusters with sufficiently deep imaging was compared against the X-ray luminosity for that cluster, shown in figure 3.12. Firstly, it can be seen from Figure 3.12 that there is no strong trend between luminosity and symmetry. Indeed, bootstrap fitting a straight line to the X-ray / symmetry data gives a slope of $-12 \pm 9 \ 10^{44}$ erg/s per unit symmetry with a scatter of $6.4 \ 10^{44}$ erg/s per unit symmetry about this relationship. Although by using only those clusters with an acceptable measure of optical richness, it is still possible that the measured slope is due to evolution of the symmetry properties with redshift and the observational bias towards higher

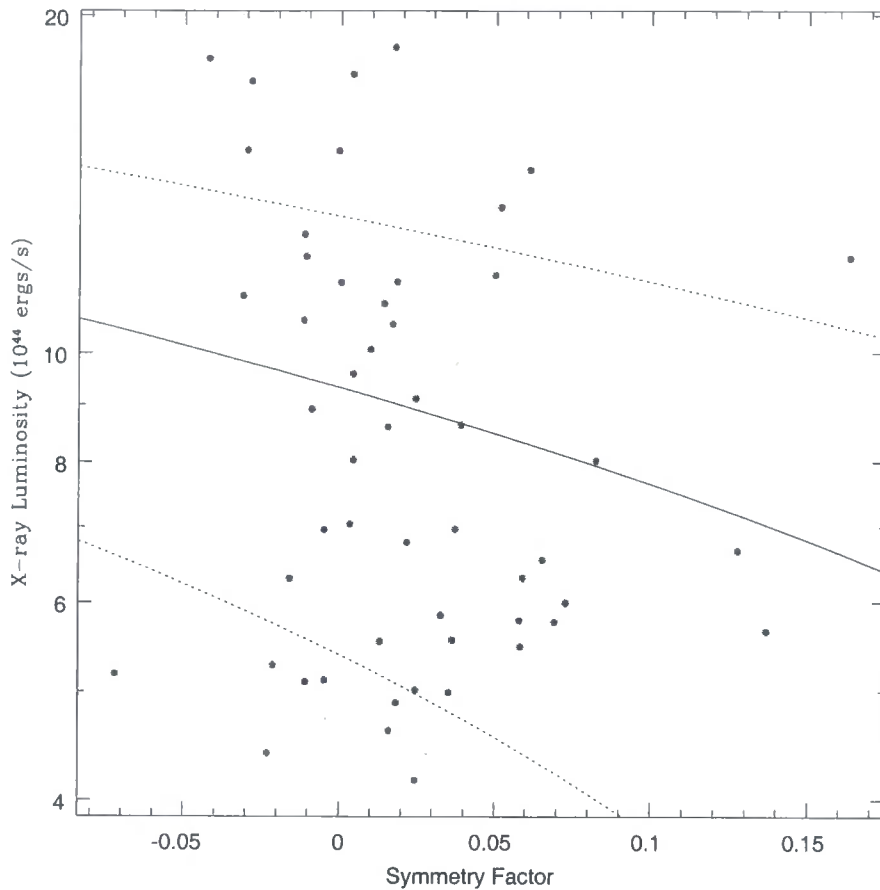


Figure 3.13: X-ray luminosity against symmetry factor for the 52 MACS clusters with sufficiently deep imaging at $z \leq 0.4$. The solid line denotes the fit to the data and the dotted lines the 1σ confidence limit.

luminosities at higher redshifts. In order to eliminate this possibility, the X-ray luminosity was plotted against the symmetry factor for only those cluster at $z < 0.4$ and are shown in Figure 3.13. The variation in the X-ray luminosity against symmetry for these lower redshift clusters can be seen to be extremely similar to that of the wider population. In this case the trend of luminosity against redshift is $-16 \pm 13 \text{ } 10^{44} \text{ erg/s}$ per unit symmetry with a scatter of $3.9 \text{ } 10^{44} \text{ erg/s}$ per unit symmetry, a stronger trend but still statistically insignificant.

From these fits, it is clear that disturbances in the distribution of galaxies have very little effect on the X-ray luminosity of a cluster. In fact, contrary to what might be expected, the negative slope of the trend suggests that those clusters that have disturbed morphologies may actually have lower X-ray luminosities. With such a

low statistical significance in the detected slope, meaningful statements as to the likely cause of this effect are impossible to make. However, the current generation of X-ray telescopes are allowing the X-ray emitting cores of massive clusters to be explored in much greater detail than has been possible before. In several clusters, so called 'cold fronts' have been reported (see, for example, Markevitch, Vikhlinin et al 2000). If these fronts are a universal property of galaxy cluster mergers, then it could be the case that rather than shock-heating the Intra-cluster medium, merging groups deposit cold gas into the core of the cluster, slightly reducing the X-ray luminosity. However, testing this hypotheses is beyond the scope of this imaging campaign, although it could be tested using an independent measure of cluster mass, such a weak lensing to study the relationship between X-ray temperature, luminosity and cluster mass for merging and non-merging systems. If the cold-gas hypothesis is correct, for similar cluster masses, merging systems would have systematically lower X-ray temperatures.

Regardless of the effect of mergers on the X-ray luminosity, figures 3.12 and 3.13 show that there is no significant trend in the X-ray luminosity with symmetry and thus the MACS survey cannot be said to be biased toward merging systems.

Variation in symmetry with Redshift

Hierarchical merging scenarios suggest that clusters, in a similar way to galaxies, build up through the accretion of smaller groups. If this is correct, then as we look back in time (i.e. to clusters at higher redshifts) this merger activity would be expected to be seen as clusters at higher redshifts having more disturbed morphologies than those at lower redshifts. Figure 3.14 shows the variation in the symmetry of the same 87 clusters with redshift.

Again, as with the X-ray properties, it can be seen that there is no strong trend in the symmetry properties with redshift. Bootstrapping a linear trend to this data gives a slope of 0.018 ± 0.06 , i.e. consistent with zero. As has been stated, an increase in the symmetry with redshift would be expected from hierarchical merging scenarios, but with the lack of significance within this data set it is impossible to disentangle the variation in symmetry with redshift from the X-ray luminosity / symmetry relationship as observational bias preferentially selects higher luminosity

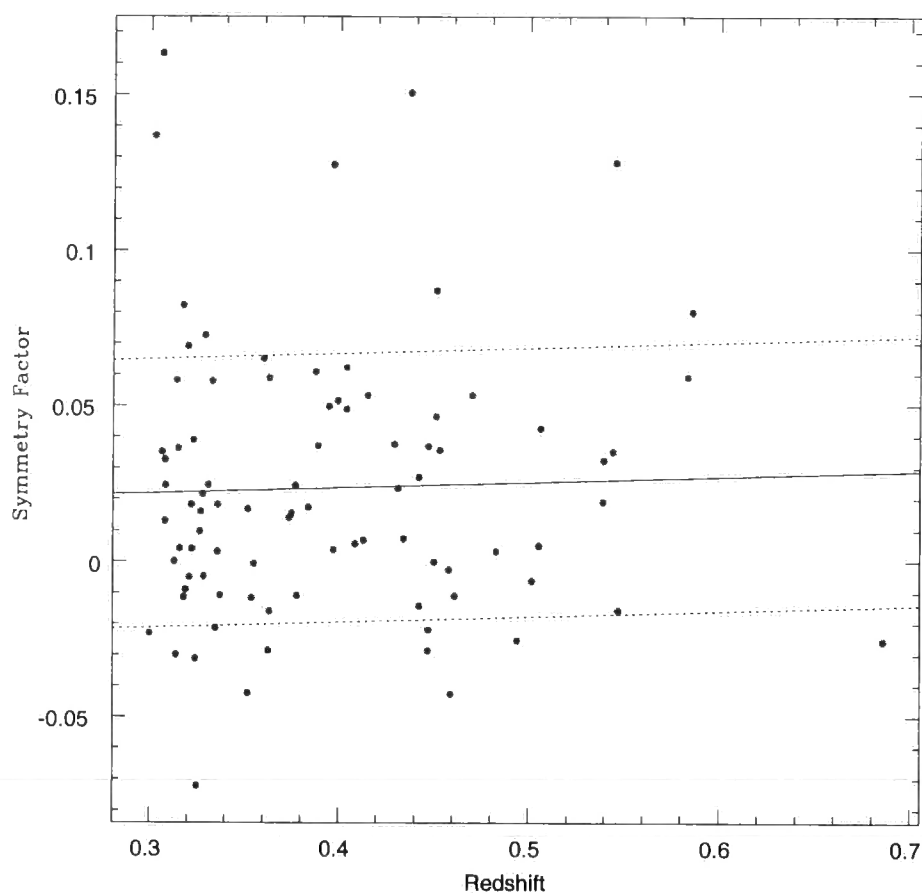


Figure 3.14: Symmetry factor of all 111 MACS clusters with redshift. The solid line denotes the fit to the data and the dotted lines the 1σ confidence limit.

clusters at higher redshifts.

This study has shown that there are no statistically significant trends in the symmetry of clusters with either X-ray luminosity or redshift and so it can safely be said that, within these large errors, there is no observed variation in the symmetry properties of the MACS clusters with redshift and that the survey is not biased towards or against merging systems in any interval of X-ray luminosity, redshift or cluster richness.

3.3.3 Finding the centre of clusters via symmetry

The problem of defining the centre of clusters is an old one. A cluster is made up of individual galaxies and as such there is no reliable marker of the centre of the gravitational potential. This problem of marking the centre has been around since the beginning of galaxy cluster surveys, in his original paper, Abell (1958) only quotes the position of his galaxy clusters to the nearest arcmin due to the uncertainty in positioning the true centre of a cluster. This problem is often avoided by choosing the position of the brightest cluster galaxy but, as has been discussed, the brightest cluster galaxy may not lie at the centre of the potential well, for example in the Coma cluster of galaxies, there are two bright galaxies at the centre, clearly they cannot both mark the centre. A way around this problem is to use the X-ray emission from the cluster as the hot gas in the centre of the cluster does trace the cluster gravitational potential. However, this is not an option for poor clusters or clusters without X-ray observations. Consequently, an attempt was made to develop a method to determine the centre of a galaxy cluster from the galaxy distribution alone.

Looking at the schematic drawings of an idealised cluster (figure 3.9) it is clear that evaluating the symmetry factor at the centre will give a smaller value than if it were evaluated at any other point. Consequently, the centre of any distribution of objects should coincide with the point of maximum symmetry. This is, of course, dependent on the assumption that the region in question contains only a single cluster within the limits of the colour-selection. Fortunately, the space density of MACS clusters is sufficiently low that even the clusters that are the closest in spatial

projection are still several degrees away from each other. There is, consequently, no chance of overlap in the 7×7 arcmin square VRI imaging. For each cluster the centre of the imaging was chosen as an arbitrary starting point. The symmetry factor, as described in section 3.3.1, is then calculated for this point with the slight modification that all colour selected galaxies within the largest circular aperture possible for this point is used i.e. a circle with radius equal to the distance to the nearest chip edge is used, shown schematically in figure 3.15

Clearly, if away from the point of maximum symmetry, the symmetry factor will be non-zero and the distance ratio $\frac{d_s}{d_b}$ will be greatest for the galaxy closest to the true centre as shown by the arrow in figure 3.15. The direction to this point is trivial to calculate from the centre-point used and the coordinates of this galaxy. The position of the assumed centre is then moved in this direction by an amount equal to the symmetry factor and the process is repeated, resizing the circular aperture as appropriate. As has been discussed, the symmetry factor has the property that it decreases as centres nearer to the point of maximum symmetry are considered and so this process has a natural reduction in the step size and so the iterations can continue until the point of maximum symmetry is reached. This process was carried out in pixel coordinate space which was then transferred to RA and Dec via the astrometric solution obtained in section 2.9

The effectiveness of this centre-finding algorithm is tested against other centre-finding markers in figure 3.16 which shows the difference in the centre between the position of the cD galaxy, the centred determined by the symmetry and apparent centre of the X-ray emission. The RMS differences between the centres given by these three methods are shown in table 3.1

As might be expected, the scatter in the positions obtained from the BCG and the X-ray emission shows the smallest scatter at $42''$, comparable to the point-spread function of the ROSAT All-sky Survey data. The difference between the symmetry position and that of the X-ray emission is only 14 percent poorer in predicting the centre of the cluster. This is a surprisingly good result considering that this method is attempting to fit the continuous gravitational potential using a relatively low number of discreet galaxies as the probe with the associated problems such as projection effects that plague such optical studies. It can also be seen from

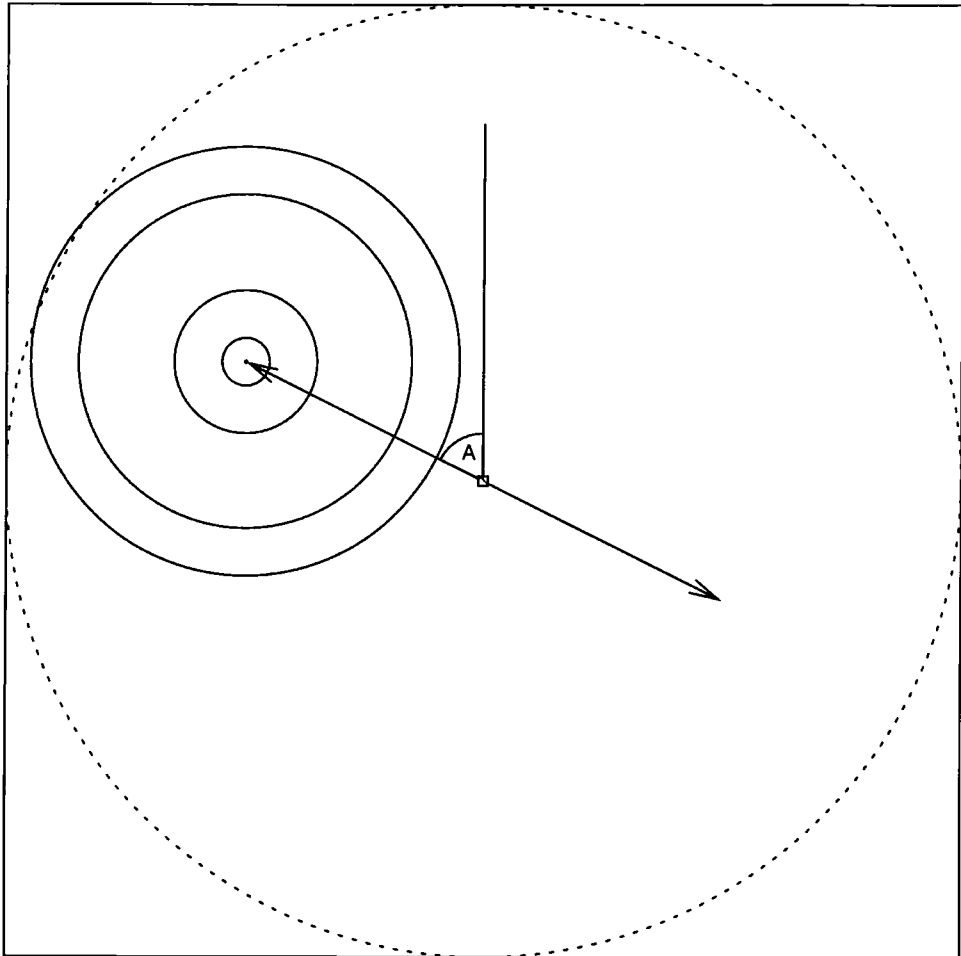


Figure 3.15: Schematic diagram showing cluster centre finding routine. The centre of the cluster is guessed to be at the centre of the chip (marked by the square.) All colour-selected cluster galaxies within the largest possible circular aperture (dotted line) are considered. The direction to the centre of the cluster is determined by the galaxy with the largest symmetry ratio (the centre and its symmetry point are shown by the double headed arrow.) The 'centre' position is then moved in this direction and the process iterated until the solution converges on the cluster centre.

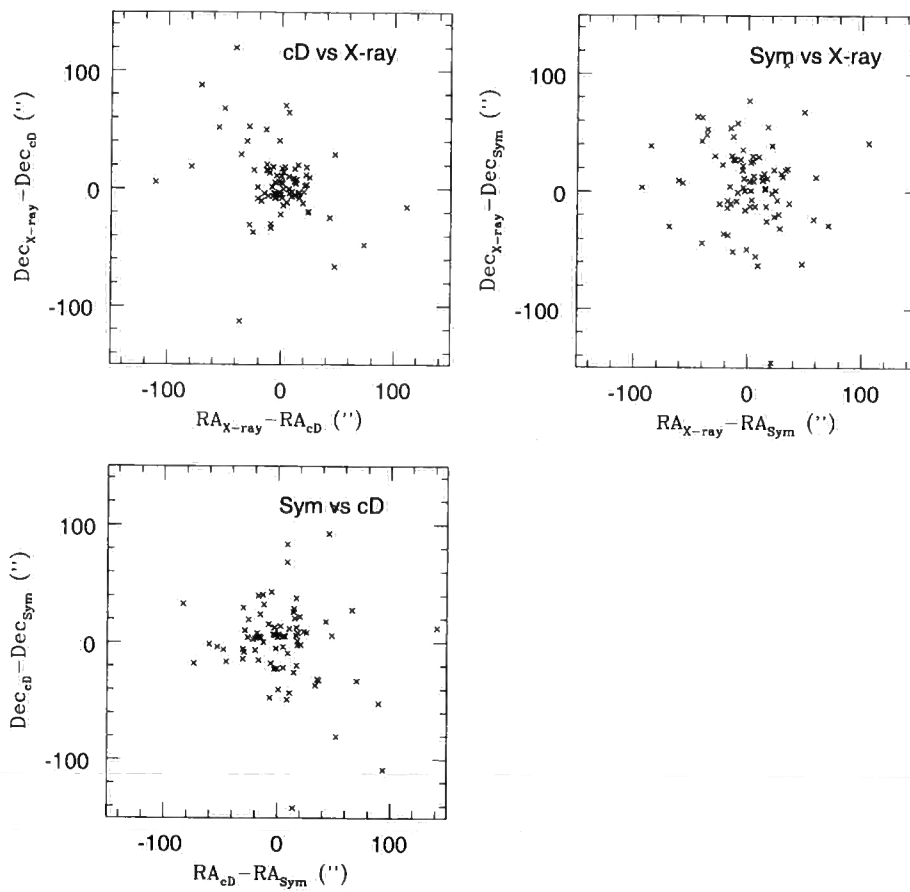


Figure 3.16: Relative positions of the centres of MACS clusters as determined by Symmetry, BCG position and X-ray emission.

Table 3.1: Difference in the position of the centre of a cluster between X-ray, cD and Symmetry methods

Comparison	Scatter (arcsec)
cD / X-ray	42
Symmetry / X-ray	48
Symmetry / cD	52

the plot of the difference in position between the symmetry position and cD position that the same clusters show large scatter between both X-ray and cD centre and symmetry and cD centre demonstrating that the symmetry position is not biased towards any individual galaxy and that it is tracing the underlying galaxy distribution.

From this study into the symmetry properties of clusters, it can be seen that, as has long been known, the X-ray emission from a cluster is the most secure way of tracing a clusters gravitational potential. However, in situations where X-ray data is unavailable, using the symmetry properties of a cluster can be used as a substitute way of tracing out the cluster centre.

3.4 Conclusions

This chapter aimed to study the properties of the galaxies in the MACS cluster. Initially, the method by which colour-magnitude diagrams were produced for each of the MACS cluster was detailed, the diagrams themselves being shown in Appendix A. The method by which the cluster red-sequence was fitted using a bi-weight routine was described. The slope of the resulting fits was then used to attempt to constrain the star-formation epoch of the elliptical galaxies in the cores of the MACS clusters and this was found to be in agreement with previous work, in that a star-formation epoch at redshift greater than 1.7 was required. The trend in slope of the red-sequence was tested against the X-ray luminosity of the clusters to ensure that the observed trend with redshift was not due to cluster richness. No trend with X-ray luminosity was found, confirming that the cluster red-sequence appears to be

a universal property of galaxy clusters.

The fit to the cluster sequence was then used as a basis for a photometric redshift technique. The scatter in this redshift indicator was found to be 0.042, 0.063 and 0.057 magnitudes in the R-I, V-I and V-R bands respectively, comparable to the error found in the aperture magnitudes of BCG galaxies, a commonly used standard candle.

Two measures of the cluster richness were made. The method involving counting the number of galaxies within a fixed magnitude and aperture was rejected as it does not discriminate between rich and poor cluster. An aperture Virial radius was calculated and found to be a suitable test of richness and consequently one cluster candidate was identified as possibly not being sufficiently rich to warrant inclusion in the final MACS catalogue.

An attempt was made to assess the effect of mergers on the observed X-ray luminosity of the MACS clusters, using the symmetry of the clusters as an indicator of possible mergers. No evidence was found for bias due to mergers with either X-ray luminosity or redshift.

Chapter 4

Brightest Cluster Galaxies

4.1 Introduction

Brightest Cluster Galaxies (BCGs) provide a unique sub-population of galaxies in that they are, in terms of starlight alone, the most luminous objects in the universe and occupy a position at (or very near to) the centre of a galaxy cluster's gravitational potential.

In this chapter, the V,R and I band properties of the MACS BCGs are studied, the method of selecting the Brightest Cluster Galaxy is described and shown that only a combination of magnitude, colour and position correctly identifies the BCG.

The 5 arcsec aperture magnitude is extracted and used to set-up a basis for future use as a standard candle for cluster photometric redshifts. The SExtractor MAG_AUTO is investigated as a measure of the total magnitude of a BCG but is found to incorrectly measure the magnitude due to the presence of an extended halo of starlight around a proportion of BCGs. The 32Kpc (projected) aperture magnitude is used and the absolute magnitudes of the BCGs are shown to be correlated with the X-ray luminosity of host clusters. The BCG degree of dominance (the amount by which the BCG is brighter than the second and third brightest cluster galaxies) is calculated and found not to vary with either redshift or X-ray luminosity.

The aperture colours of the BCGs are extracted and the BCG population is shown to have up to 26% of galaxies bluer than expected when compared against a no-evolution model. This scatter in the colour of the BCGs is found to be correlated with both the X-ray luminosity and (more weakly) the degree of dominance.

The alignment of the BCG with its host cluster is examined and it is found that a significant excess of galaxies show such an alignment. The alignment is found to be of equal strength in highly and weakly dominated clusters in contrast with similar studies of poorer clusters.

4.2 Brightest Cluster Galaxies

Recent studies of the brightest cluster galaxies have concentrated on the K-band properties of these objects (eg. Aragón-Salamanca 1998, Baugh & Kauffmann 1998; Collins & Mann 1998.) This is not without reason as the K-band luminosity suffers from less extinction than in other wavelengths and the K-band is relatively insensitive to the recent star-formation history of these galaxies, allowing the stellar mass of these galaxies to be studied (eg. Madau, Pozzetti & Dickinson 1998). But why bother to pay so much attention to these particular galaxies? Their position in the very centres of clusters means that these objects occupy a unique position in the centre of a large volume of X-ray emitting (and therefore cooling) gas, providing the central galaxy with a possibly large supply of material for star-formation. Brightest cluster galaxies are therefore used as a probe of what is happening in the very cores of clusters and the link between cooling gas and star-formation. There has been much debate over the last few years, in light of data from the current generation of X-ray satellites, over the fate of the gas in the centres of massive clusters, in particular the phenomenon of ‘cooling flows’.

In a very simplistic manner, the cooling flow paradigm is that the X-ray emission from the core of a cluster leads to cooling of the gas in that core. In order to maintain the hydrostatic equilibrium in the core, hot gas must move toward the centre of the cluster leading to the ‘flow’ of material into the centre of clusters. X-ray observations made before the launch of the Chandra and XMM-Newton satellites were broadly consistent with the cooling flow picture, although there was still uncertainty in the interpretation of this effect (see Fabian 1994 for a review and Makishima et al. 2001 for an opposing opinion)

One of the main sticking blocks in the acceptance of cooling flows has been the fate of the cooled gas. With the amount of gas that appears to be cooling from

the X-ray emission, large amounts of star-formation would be expected to be seen in cooling flow clusters and, given their position at the centres of the gravitational potential, this star-formation would be expected to be seen in the BCG galaxies. The rates of star formation predicted from the X-ray profiles of the clusters (based on pre-Chandra and XMM data) is in the range of 100s to more than $1000 M_{\odot}\text{yr}^{-1}$ for some clusters. At these rates of star formation, the BCG galaxies would be expected to be very bright and blue, indicative of a population of young stars. In several cases, (Johnstone, Fabian & Nulsen 1987; Allen 1995; Cardiel et al. 1998; Crawford et al. 1999) the BCG galaxies have been observed to have excess blue light, indicative of star formation, but at rates 10 to 100 times lower than the X-ray deduced cooling rates.

This is not to say that BCG galaxies can only grow through the accretion of cold gas. It is believed that large galaxies grow through the accretion of other, smaller galaxies. If a group of galaxies is left undisturbed for a sufficient length of time, it is possible that the centrally dominating galaxy will merge with all the other group member galaxies, leaving only the X-ray halo and a single, large elliptical galaxy, a so called 'fossil' group. (Jones et al 2003.)

The situation has become clearer with the launch of the XMM-Newton and Chandra satellites which have allowed high spatial resolution imaging and high spectral resolution spectroscopy respectively of the cores of many clusters. These observations have shown that the cores of clusters are complex systems with features such as bubbles from radio sources (eg. McNamara et al. 2000, Fabian et al. 2000) and cold fronts (Markevitch et al. 2000; Vikhlinin et al 2000) visible. These features have led to the explanation of the lower than expected observed star-formation rates being due to heating effect (feedback) from, in particular, central radio sources which are not considered in the simple cooling flow paradigm.

At around the same time that these X-ray observations were appearing, evidence for both warm (Jaffe & Bremer 1997; Donahue et al 2000; Edge et al 2000) and cold (Edge 2001) molecular gas at the centres of cooling flow clusters began to emerge. In some extreme cases, there may be as much as $10^{11}M_{\odot}$ of cold gas at the centres of clusters. The presence of dust in these regions has also been demonstrated from the visible dust lanes along with sub-mm and IR detections (Edge et al. 1999; Allen

et al. 2001; Irwin, Stil & Bridges 2001).

It is clear that, at some level, cooling flows must exist. X-ray emission is observed from clusters and so the intra-cluster gas must be losing thermal and kinetic energy to account for energy required to maintain this X-ray luminosity. The detection of gas and dust in the centres of such clusters, in addition to the blue colours of BCG galaxies, prove that gas must have cooled in these systems. Additionally, numerical simulations which include radiative cooling of the gas in clusters (eg Pearce et al. 2001) find cooling flows in their simulated clusters, although these simulations require tuning to produce this effect. The presence of the bubbles and cold fronts in the X-ray profiles show that heating from radio sources and in-falling groups is physically possible although whether this heating is sufficient to balance the radiative cooling over the large (\sim Mpc) scales required is not yet clear. It is clear that cooling does happen in the cores of clusters and that this effect is much smaller than was first thought, although the amount by which the cooling rates must be reduced, whether it is by a few, tens or factors of hundreds is not yet clear.

What is clear is that whatever happens to the gas in the clusters, gravity demands that it is, eventually, going to end up deposited near the centre of the gravitational potential of the cluster. As this position is, in the majority of clusters, occupied by the BCG, it would seem safe to assume that whatever is happening to the cluster at large will have an effect on the BCG and that these effects should be observable. Indeed, it has been shown that knowledge of the X-ray luminosity of a cluster is vitally important in the study of BCG evolution (Edge 1991)

Many of the studies of the BCG population (eg Brough et al. 2002; Aragón-Salamanca, Baugh & Kauffmann 1998; Collins & Mann 1998.) concentrate on the K-band properties of these galaxies. But, as has been shown, the interaction between the BCG and its host galaxy cluster will be through the accretion of cooling gas which could be seen in the form of ongoing star formation which will be seen preferentially in bluer filters. Concentrating solely on the K-band properties will not reveal this star formation (or the output from an AGN) and so much of the information relating the BCG - cluster relationship will be lost.

This chapter aims to investigate the properties of the brightest cluster galaxy using the V, R & I band imaging of the MACS survey to probe the relationship

between the BCG and its host cluster for this statistically well defined sample of extremely massive clusters at relatively high redshift. As cooling flows are an X-ray phenomenon, the MACS clusters are perfect for this study as it contains only X-ray luminous, extremely massive clusters in which radiative cooling and therefore any interaction between BCG and host cluster would be expected to be at its greatest. The use of V-band imaging for this work is particularly useful as, at the redshifts of the MACS survey, this bands begins to probe the rest-frame UV emission of the cluster galaxies which is extremely sensitive to any ongoing star-formation.

4.3 Selecting the Brightest Cluster Galaxy

In theory, selecting the brightest cluster galaxy is a simple matter, it will be the largest and most luminous galaxy, usually considerably brighter than the other galaxies. The X-ray position can also be used as an indicator as to the identification of the Brightest Cluster Galaxy as, as has already been discussed, the BCG is preferentially found at the centre of the cluster gravitational potential. However, in the case of the MACS survey, the clusters are detected from a modest number of photons and, as shown in figure 3.16, there can be a significant difference between the X-ray position of the cluster and the position of what is actually the brightest cluster galaxy.

Even with multi-colour imaging there is the problem that, as has been described, BCG galaxies might be expected to be undergoing star-formation or may contain an AGN and so could be considerably bluer than the rest of the cluster elliptical population. This causes the very real possibility of contamination due to foreground galaxies which will also be brighter than the rest of the cluster population as well as being bluer. Figure 4.1 shows the I-band image of an extreme example of this confusion, MACSJ0913.7+4056. In this figure, the galaxy identified as being the BCG is ringed and the X-ray position of the cluster marked by the cross.

This cluster has for its BCG the most luminous galaxy in the IRAS survey, IRAS 09104+4109* and the redshift of this object is known to be 0.442 (Hewitt

*Being the most luminous galaxy in the IRAS survey, there is a large amount of published information available on this object, a NED search reveals 58 references for this galaxy.

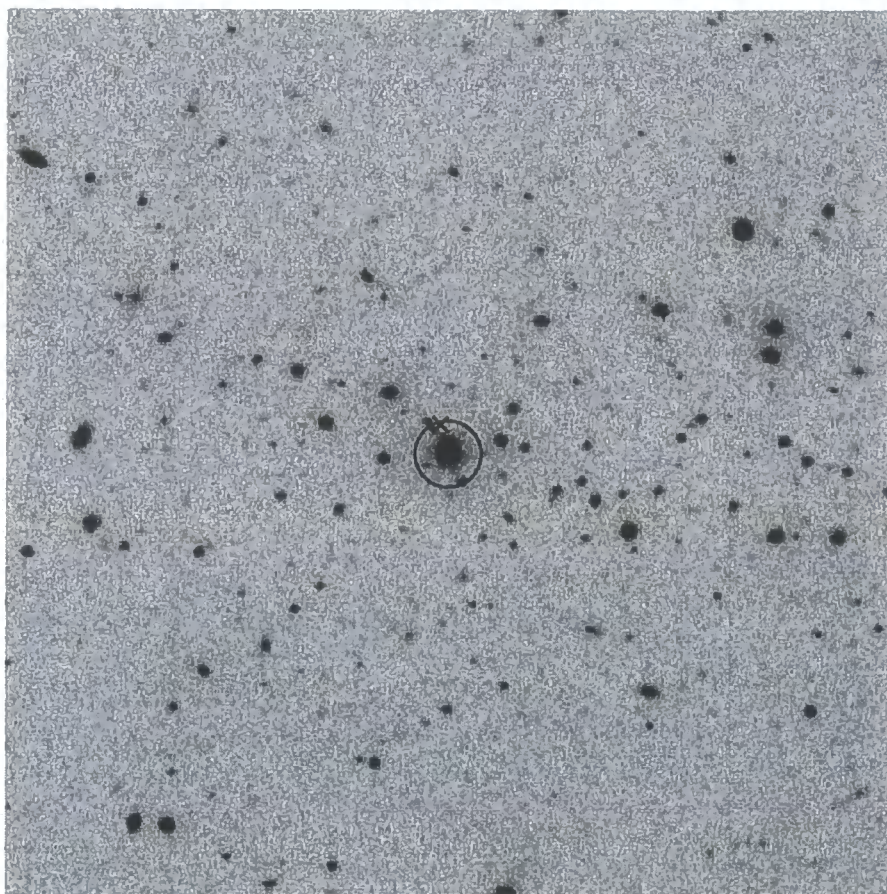


Figure 4.1: 3×3 arcmin I-band image of the central region of the cluster MACSJ0913.7+4056 showing the position of the brightest cluster galaxy (solid circle) and the centre of the X-ray emission (cross)

& Burbidge 1991), the same as that of the host cluster. Consequently, this object is, without any doubt, the BCG. However, without this redshift information, the identification of this galaxy as the BCG would not have been straight forward as the colour-magnitude diagram of R-I colour against I band total magnitude (shown in figure 4.2) shows. Figure 4.2 shows all objects within the UH2.2m image selected as being a galaxy regardless of position.

In figure 4.2 the BCG is marked by the solid circle and the solid line shows the bi-weight fit to the cluster red-sequence (as described in section 3.1.2). It can be seen that, as expected and as its name suggest, the BCG is considerably brighter than the other cluster galaxies, nearly 2 magnitudes brighter than the next nearest cluster red-sequence galaxy. However, it is also 0.4 magnitudes bluer than the fit to the red-sequence as defined by the 'normal' cluster galaxies. The identification process is further confused by the presence of galaxies such as the three marked by broken circles in figure 4.2. Examination of the images of these galaxies shows that they are located away from the centre of the main over-density of galaxies and have morphologies which suggest that they are spiral galaxies. These galaxies are most likely foreground to the cluster and yet are a magnitude fainter and 0.2 magnitudes redder than the BCG. However, in this cluster, the BCG is very close to the X-ray position which confirms its identification but as has been stated, this is not always the case for clusters with lower X-ray luminosities where the position is based upon the detection of fewer photons. A Chandra image of this cluster confirms that this is a cluster but that the central galaxy is host to a heavily obscured AGN (Iwasawa et al 2001.)

It is clear from this example that any selection method based solely on the magnitude, colour or proximity to the X-ray position cannot be relied upon to correctly identify the BCG. Instead a combination of these methods was used to perform the identification. The colour-magnitude diagram was used to determine the red sequence for a cluster and then all galaxies at, or brighter than, the 'tip' of the red sequence are considered regardless of colour. These galaxies are then examined by eye to throw out objects that are either obviously foreground (by their size and morphology) and those that are away from the centre of the projected galaxy over-density. In 90% of cases, this technique leaves a single bright galaxy

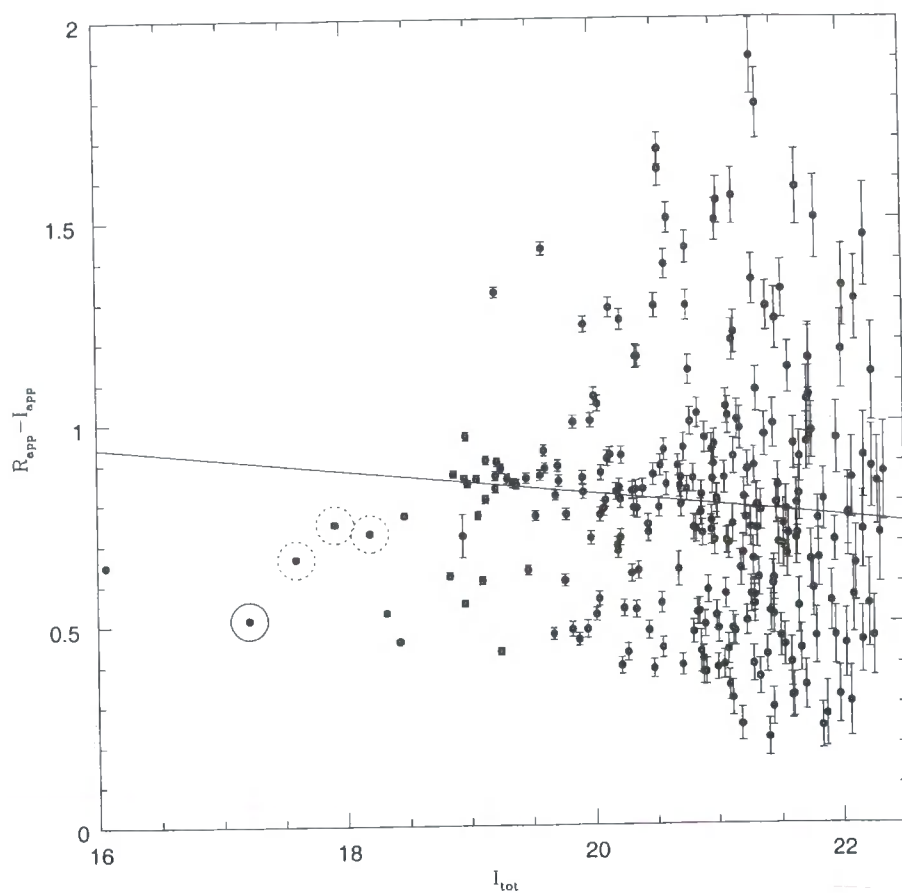


Figure 4.2: Colour-Magnitude diagram of MACSJ0913.7+4056 showing R-I aperture colour against I-band total magnitude. The solid line shows the bi-weight fit to the cluster red-sequence, the dashed circles show three bright foreground galaxies and the solid circle marks the brightest cluster galaxy.

that is the unambiguously BCG. In the remaining cases, the selection is between several galaxies of similar magnitude and colour in the core of the cluster, potentially undergoing a merger. In these cases, the galaxy with the lowest total magnitude is chosen as the BCG.

4.4 Brightest Colour Galaxy Magnitude

4.4.1 5 arc-second aperture photometry

Initially, the aperture magnitudes of the BCG sample were measured using a fixed 5 arc-second aperture. Clearly, in any study that spans a range of redshifts, using a fixed spatial scale aperture is not the correct thing to do as the colour of a galaxy can change; going from redder in the core to bluer in the outskirts. However, the aim of this was to provide a reference for using the brightest cluster galaxy as a standard candle to enable crude photometric redshifts to be measured for other massive clusters at this redshift. The 5 arc-second aperture magnitude Hubble diagram for the MACS BCG sample is shown in figure 4.3. As the aim of these aperture magnitudes is to provide a basis for photometric redshifts, k corrections have deliberately been omitted from the magnitudes presented in this figure as, obviously, a correct k correction could not be computed for a galaxy for which the redshift is being estimated.

It can be seen from this figure that there is a trade-off to be made when selecting which band to use for photometric redshift. There is less scatter in the I band - redshift relationship which makes it more suitable to use as a redshift indicator, but this is moderated by the fact there is much less range in the I-band magnitude across this redshift interval when compared with, for example, the V band. It is for this reason that the R-band was chosen as a compromise (along with instrument features in the I-band) choice to use for the photometric redshift studies described in section 5.6.1. Other than for use as a redshift indicator, no further analysis of the BCG population was performed using the fixed aperture magnitude or colours.

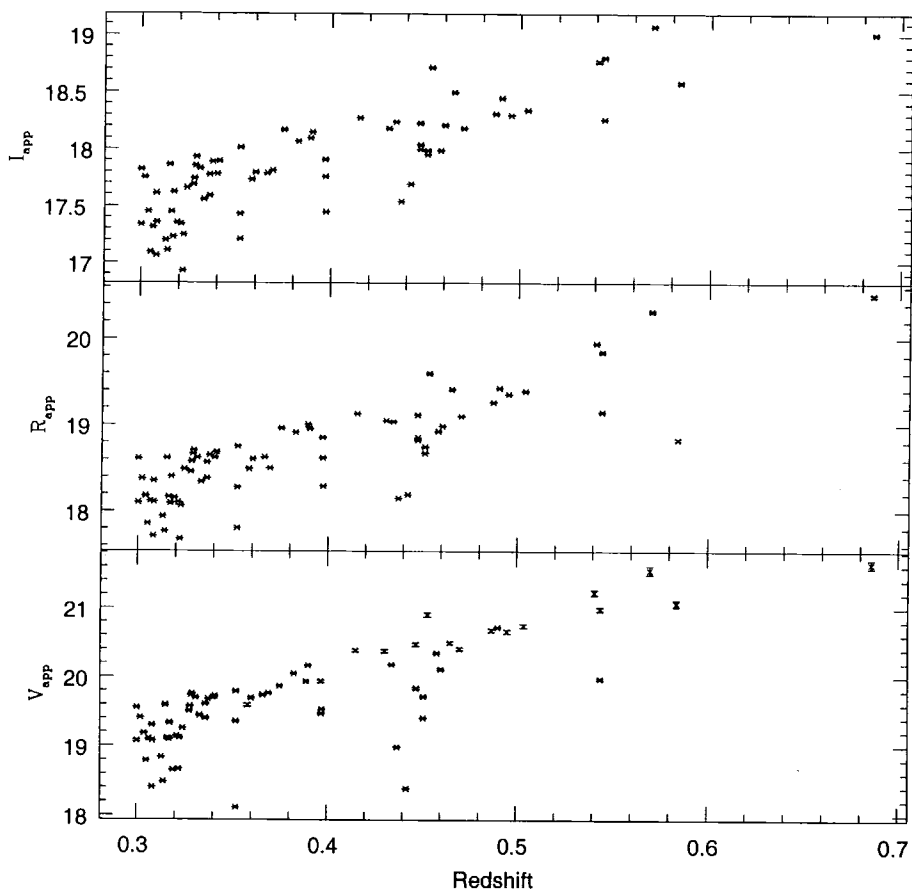


Figure 4.3: Variation of the 5 arc-second aperture apparent magnitude of the brightest cluster galaxy in each of the 105 photometric and non-contaminated MACS cluster in each of the I (top), R (middle) and V (bottom) bands.

4.4.2 Thirty-Two Kpc photometry

In order to avoid the aperture effects of surface density profiles (BCG galaxies are well fit by a deVaucouleurs profile (Nelson et al. 2002)) and possible effects of colour gradients across the galaxy, a fixed metric aperture was used. Additionally, it has been a classic observation of the brightest cluster galaxy population that they vary little in luminosity within a fixed metric aperture which has led them to be used as standard candles. In contrast with most normal elliptical galaxy populations, 50% of BCG galaxies are observed to have extended halos of starlight (Brough 2003). Studies where the surface brightness profile of K-band selected samples of BCG galaxies have shown that in the galaxies that have such halos, the galaxy's light profile can be fitted using a normal $r^{1/4}$ profile out to a radius of 16 Kpc before the halo light begins to dominate. For this reason, an aperture of (projected) 32Kpc diameter was chosen to be used for the study of the MACS BCG population to ensure maximum sampling of the galaxy without contamination from the halo light.

The presence of this halo light also prevents the use of so called total magnitudes for these objects. Figure 4.4 shows the Hubble diagram of I, R and V band total magnitudes as measured by the SExtractor `MAG_AUTO` method.

The `MAG_AUTO` method in particular (although several other methods of measuring the total magnitude also suffer from this) does not appear to handle the presence of the BCG halo and so can get the magnitude of the BCG incorrect. This is particularly visible in the distribution of the magnitude with redshift for the V band magnitudes shown in figure 4.4 which can be seen to be split into two separate populations. This appears to correlate with the BCG having a distinct halo, although this correlation is not robust enough to use as a simple indicator of the presence of such a halo as it is also dependent upon the seeing conditions. Due to this population splitting, which is entirely an artifact of the way in which SExtractor attempts to measure the total magnitude, it can clearly be seen that the measurements of the total magnitude for this population of galaxies is not robust, to the extent that, using the total magnitude, negative V-R colours can apparently be obtained. For this reason, it is the aperture magnitude that is used to study the

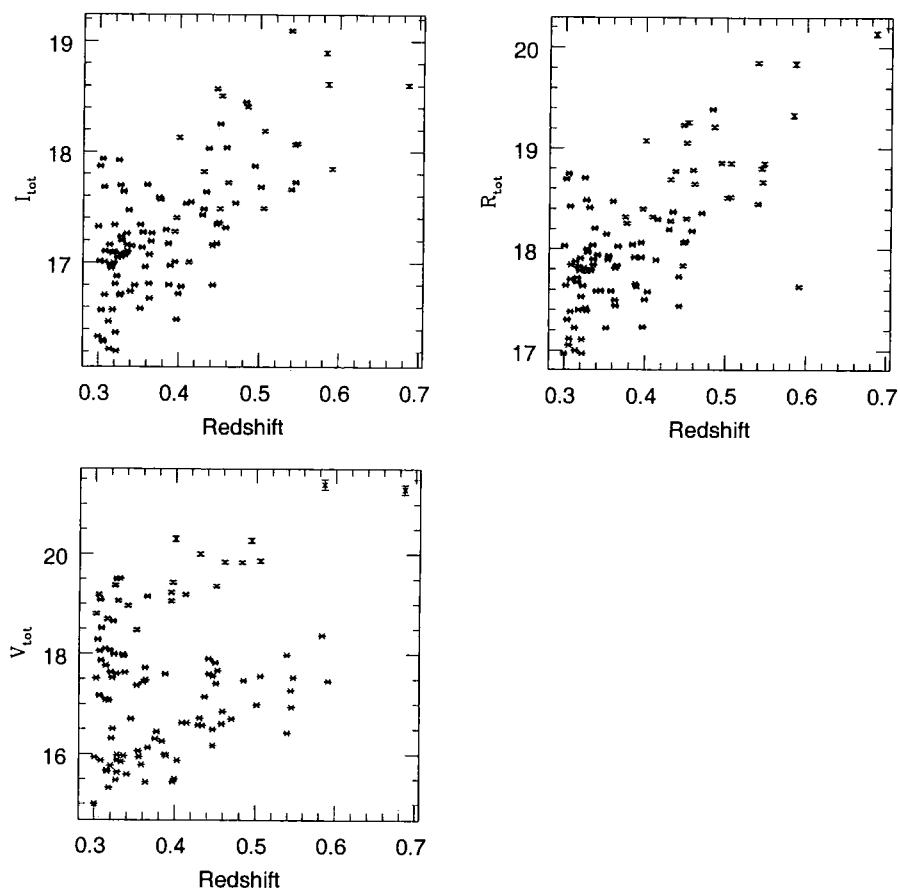


Figure 4.4: Variation of the apparent total magnitude of the brightest cluster galaxy in each of the 105 photometric and non-contaminated MACS cluster in each of the I (top), R (middle) and V (bottom) bands.

photometric properties of these objects.

The I-band total magnitude along with the R-I, V-I and V-R aperture colours are shown in table 4.1. As has been stated, the MACS survey is not yet public and so the cluster X-ray luminosity and redshift and the position of the BCG are not listed in this table, this information will be made available following the publication of the MACS catalogue. Included in table 4.1 are all of the MACS clusters (105 in total) that were taken in photometric conditions and where the BCG has an uncontaminated detection. eg. in the observation of MACSJ2245.0+2637, the BCG is beneath the blooming from a nearby bright star and so is excluded from table 4.1 and the analysis.

Table 4.1: The I band total magnitude; R-I, V-I and R-V aperture colours for the 105 photometric MACS clusters

Cluster	I_{total}	$R_{app}-I_{app}$	$V_{app}-I_{app}$	$V_{app}-R_{app}$
MACSJ0010.8+2909	17.08	0.77	1.66	0.89
MACSJ0014.3-3022	17.00	0.73	1.67	0.93
MACSJ0018.5+1626	18.07	1.17	2.46	1.28
MACSJ0025.4-1222	18.61	1.24	2.59	1.35
MACSJ0027.8+2616	17.70	0.79	1.92	1.12
MACSJ0032.1+1808	17.57	0.81	1.92	1.11
MACSJ0035.4-2015	17.13	0.82	2.00	1.18
MACSJ0110.1+3211	17.14	0.79	1.82	1.02
MACSJ0111.5+0855	18.40	0.95	2.12	1.17
MACSJ0140.0-0555	18.25	0.85	2.22	1.36
MACSJ0150.3-1005	16.67	0.83	1.76	0.93
MACSJ0159.0-3412	17.00	0.90	2.19	1.29
MACSJ0242.5-2132	16.22	0.68	1.41	0.72
MACSJ0257.1-2325	17.49	1.05	2.40	1.35
MACSJ0257.6-2209	16.20	0.82	1.86	1.04
MACSJ0308.9+2645	17.34	0.84	1.91	1.07
MACSJ0326.8-0043	17.34	0.81	1.80	0.98
MACSJ0329.6-0211	17.36	0.72	1.45	0.73

...continued from previous page

Cluster	I_{total}	$R_{app}-I_{app}$	$V_{app}-I_{app}$	$V_{app}-R_{app}$
MACSJ0404.6+1109	16.96	0.75	1.84	1.09
MACSJ0416.1-2403	17.28	0.81	2.01	1.20
MACSJ0417.5-1154	16.80	0.61	1.45	0.83
MACSJ0429.6-0253	16.72	0.85	1.72	0.86
MACSJ0449.3-2848	17.69	0.78	1.80	1.02
MACSJ0451.9+0006	17.42	0.86	2.19	1.32
MACSJ0454.1-0300	19.09	0.97	2.04	1.06
MACSJ0455.2+0657	17.17	0.89	2.25	1.36
MACSJ0520.7-1328	17.10	0.79	1.80	1.01
MACSJ0521.4-2754	17.16	0.76	1.79	1.02
MACSJ0547.0-3904	16.99	0.80	1.31	0.50
MACSJ0553.4-3342	17.48	0.93	2.33	1.40
MACSJ0611.8-3036	17.33	0.59	1.66	1.07
MACSJ0647.7+7015	17.84	1.26	2.48	1.22
MACSJ0712.3+5931	16.71	0.73	1.96	1.22
MACSJ0717.5+3745	17.72	1.12	2.37	1.25
MACSJ0744.8+3927	18.60	1.49	2.64	1.15
MACSJ0911.2+1746	18.18	0.99	2.37	1.37
MACSJ0913.7+4056	17.15	0.50	0.70	0.20
MACSJ0916.1-0023	17.09	0.76	1.82	1.06
MACSJ0940.9+0744	17.26	0.80	1.87	1.06
MACSJ0947.2+7623	16.79	0.86	1.79	0.93
MACSJ0949.8+1708	17.29	0.84	1.98	1.13
MACSJ1006.9+3200	16.78	0.84	2.09	1.24
MACSJ1044.9-1400	17.19	0.69	1.95	1.26
MACSJ1105.7-1014	17.54	0.85	2.11	1.26
MACSJ1108.8+0906	17.53	0.92	2.23	1.30
MACSJ1115.2+5320	17.31	0.94	2.36	1.42
MACSJ1115.8+0129	17.27	0.71	1.59	0.88

...continued from previous page

Cluster	I_{total}	$R_{app}-I_{app}$	$V_{app}-I_{app}$	$V_{app}-R_{app}$
MACSJ1131.8-1955	16.30	0.76	1.69	0.93
MACSJ1133.2+5008	16.97	0.91	1.84	0.93
MACSJ1141.6-1905	17.93	0.88	1.83	0.95
MACSJ1142.4+5831	16.37	0.74	1.72	0.98
MACSJ1149.5+2223	18.06	1.04	2.20	1.15
MACSJ1206.2-0847	17.63	0.80	1.94	1.14
MACSJ1218.4+4012	16.57	0.72	1.72	1.00
MACSJ1226.8+2153	18.03	0.86	2.15	1.29
MACSJ1236.9+6311	17.01	0.62	1.65	1.02
MACSJ1258.0+4702	17.64	0.79	1.88	1.09
MACSJ1305.9+2630	16.29	0.80	1.77	0.97
MACSJ1311.0-0310	17.87	0.98	2.27	1.29
MACSJ1319.9+7003	16.70	0.77	1.82	1.05
MACSJ1322.8+3138	17.10	0.75	1.71	0.95
MACSJ1331.5-1736	17.20	0.77	1.81	1.03
MACSJ1347.5-1144	17.48	0.76	1.73	0.97
MACSJ1354.6+7715	17.40	0.94	2.02	1.08
MACSJ1359.1-1929	18.56	0.80	1.97	1.16
MACSJ1359.8+6231	17.23	0.82	1.83	1.00
MACSJ1411.3+5212	18.03	0.77	1.90	1.12
MACSJ1423.8+2404	17.66	0.88	1.71	0.82
MACSJ1427.6-2521	16.57	0.87	1.86	0.99
MACSJ1452.9+5802	16.95	0.78	1.83	1.04
MACSJ1526.7+1647	17.47	0.76	1.77	1.00
MACSJ1532.8+3021	16.81	0.70	1.20	0.50
MACSJ1542.0-2915	18.13	0.95	2.14	1.19
MACSJ1551.9-0207	16.33	0.76	1.72	0.96
MACSJ1621.3+3810	17.72	0.91	1.99	1.08
MACSJ1644.9+0139	17.15	0.79	1.82	1.03

...continued from previous page

Cluster	I_{total}	$R_{app}-I_{app}$	$V_{app}-I_{app}$	$V_{app}-R_{app}$
MACSJ1652.3+5534	16.98	0.74	1.72	0.97
MACSJ1720.2+3536	17.17	0.83	1.92	1.08
MACSJ1731.6+2252	16.80	0.87	2.07	1.20
MACSJ1738.1+6006	17.05	0.81	1.88	1.06
MACSJ1752.0+4440	17.26	0.83	1.94	1.11
MACSJ1806.8+2931	17.32	0.76	1.70	0.93
MACSJ1824.3+4309	18.44	0.95	2.36	1.40
MACSJ1931.8-2634	16.58	0.61	0.93	0.32
MACSJ2003.4-2322	16.97	0.74	1.71	0.96
MACSJ2049.9-3217	16.87	0.74	1.78	1.04
MACSJ2050.7+0123	17.07	0.78	1.88	1.10
MACSJ2051.1+0215	16.80	0.75	1.79	1.03
MACSJ2113.9+1330	16.71	0.65	1.37	0.71
MACSJ2129.4-0741	18.89	1.24	2.46	1.21
MACSJ2134.6-2706	17.07	0.74	1.83	1.08
MACSJ2135.2-0102	17.92	0.77	1.80	1.02
MACSJ2140.2-2339	16.47	0.74	1.63	0.89
MACSJ2149.3+0951	17.58	0.79	1.71	0.91
MACSJ2201.9-2730	17.68	0.74	1.41	0.66
MACSJ2211.7-0349	16.49	0.84	2.08	1.23
MACSJ2214.9-1359	17.68	1.06	2.36	1.30
MACSJ2219.1-1844	17.82	0.87	2.16	1.29
MACSJ2228.5+2036	17.53	0.86	2.13	1.27
MACSJ2229.7-2755	17.04	0.81	1.60	0.79
MACSJ2241.8+1732	17.09	0.77	1.69	0.92
MACSJ2243.3-0935	18.50	0.88	2.19	1.31
MACSJ2245.4+2808	16.74	0.84	1.91	1.07
MACSJ2311.5+0338	17.87	0.84	1.83	0.99
MACSJ2334.2+0736	17.00	0.88	2.11	1.22

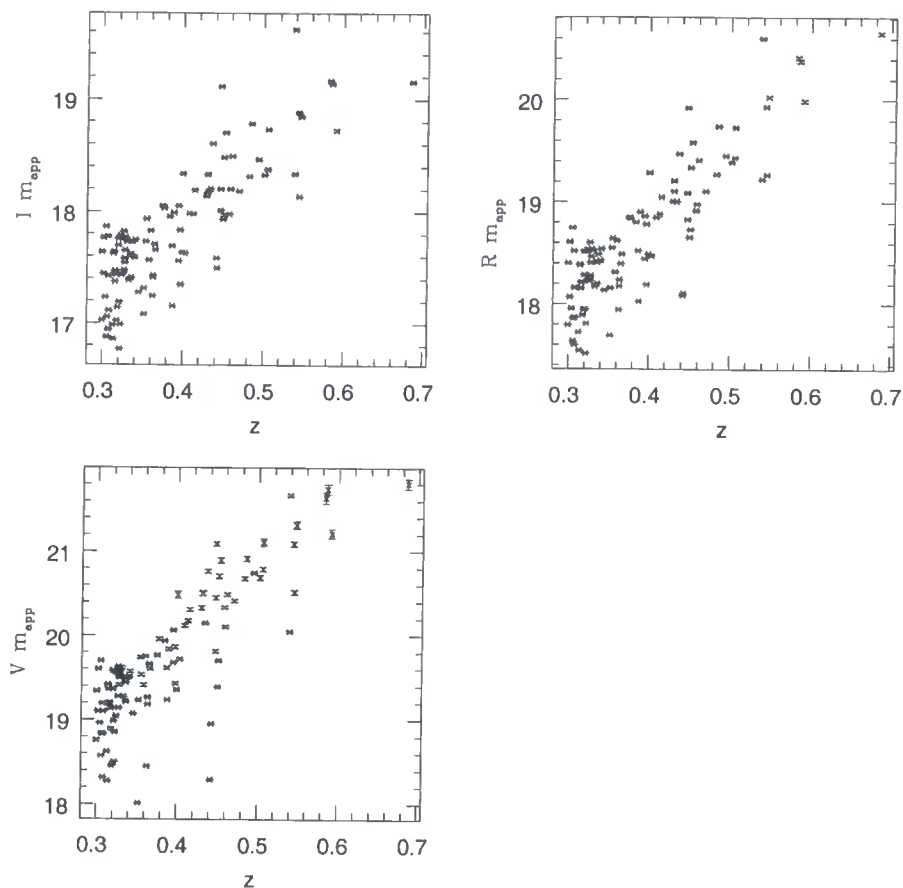


Figure 4.5: Variation in the projected 32Kpc aperture apparent magnitude of the brightest cluster galaxy in each of the 105 photometric and non-contaminated MACS cluster in each of the I (top left), R (top right) and V (bottom left). These aperture magnitudes are used to study the colours of these galaxies in section 4.5.

The I, R & V band projected 32 Kpc aperture magnitude Hubble diagrams are shown in figure 4.5. Comparison with figure 4.4 shows the much reduced scatter in the aperture magnitudes compared with the total magnitude measurements, confirming that the aperture magnitude is more robust measurement for this population of galaxies. When compared to a simple geometrical dimming fit, there is found to be a RMS scatter of 0.34 magnitudes in the I band, 0.38 magnitudes in the R band and 0.52 magnitudes in the V band. This is entirely consistent with bluer bands being increasingly insensitive to the stellar mass of the galaxy and the 0.24 magnitude scatter found for K-band observations (Collins and Mann 1998).

In order to properly study the variation in magnitude of the MACS BCG sample,

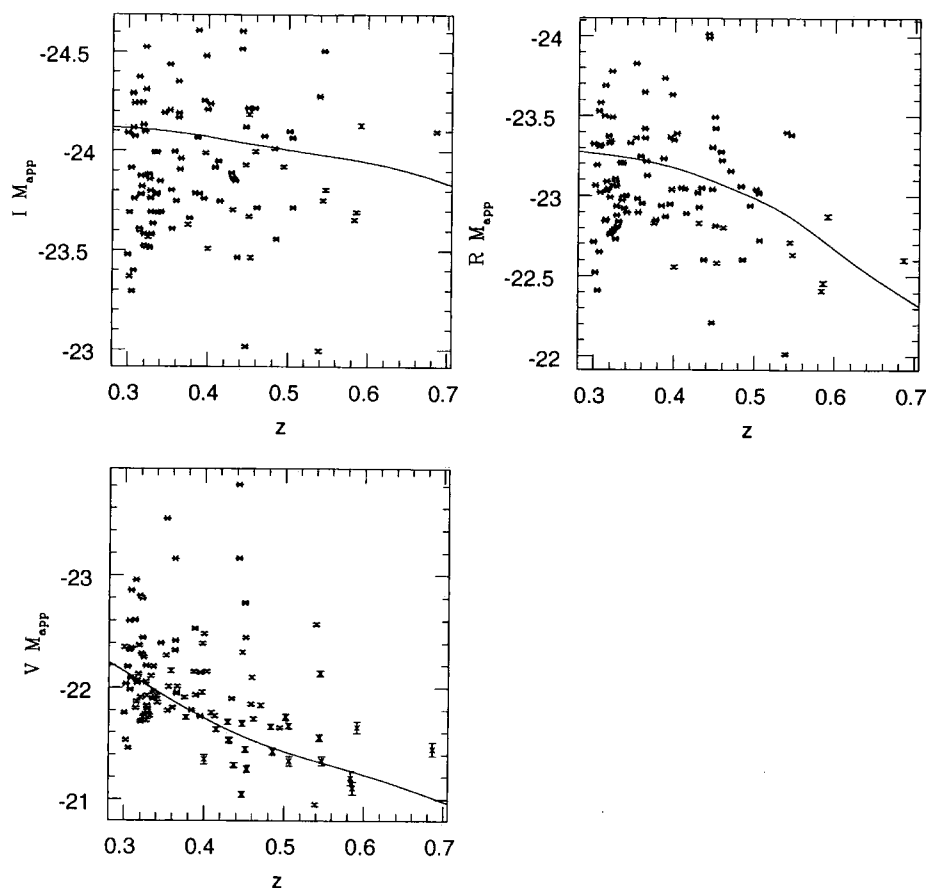


Figure 4.6: Variation in the absolute magnitude of the brightest cluster galaxy in each of the 105 photometric and non-contaminated MACS cluster in each of the I (top left), R (top right) and V (bottom left) bands. Due to the previously discussed uncertainty in the model predictions for the V band, k corrections have not been applied to these data, the (estimated for the V band) k correction being traced by the solid line in each panel.

the apparent 32Kpc magnitudes were converted into absolute magnitudes and the absolute magnitude-redshift relationship is presented in figure 4.6.

This figure shows that there is a difference in the variation of absolute magnitude of these objects with redshift from the I to V bands. The I band shows very mild brightening with redshift, fitting a linear relationship to the data gives a slope of -0.135 ± 0.81 magnitudes per unit redshift, in opposition of the value of 0.69 magnitudes per unit redshift expected from the k-correction alone. In contrast, the R and V bands show opposite trends (1.08 ± 0.97 magnitudes per unit redshift for the R band and 2.21 ± 0.97 magnitudes per unit redshift for the V band,) consistent



with the variation expected from the k-correction.

The interpretation of this result is not simple as there are two competing effects on the observed magnitude. In addition to the colour correction which pushes the observed V-band magnitude further into the rest-frame Ultra-Violet of the object, accounting for a large amount of the observed V band magnitude-redshift variation, there also is the selection effect of the flux-limited nature of the MACS survey. This flux limit results in higher X-ray luminosity clusters being preferentially selected at higher redshifts which, assuming that the relationship between BCG magnitude and cluster mass holds at this redshift, will bias the absolute magnitude-redshift relationship toward brighter BCGs at higher redshift as is seen in the I-band result.

In order to investigate this selection effect, the variation in the absolute magnitude of the BCG sample is shown plotted against the X-ray luminosity of the host cluster in figure 4.7. It can clearly be seen from the I-band magnitudes plotted in figure 4.7 that there is a correlation between the luminosity of the brightest cluster galaxy and the X-ray luminosity of its host cluster as found by other authors in the K-band (Brough et al 2000) and confirms that the relationship between the BCG and its host cluster still holds at these luminosities and redshifts. Again, as was done for the absolute magnitude, fitting a linear trend to this relationships reveals a slope of -0.0158 ± 0.008 magnitudes per 10^{44} erg/s, demonstrating that there is a relationship between the brightest cluster galaxy and the cluster in which it resides, although this effect is seen here with only 2σ significance. This relationship is discussed in the light of the colour of the BCG in section 4.5.

In figure 4.7, there can be seen two BCG galaxies which appear to be less luminous than would be expected from the trend set by the other MACS BCGs. This two galaxies reside in the clusters MACSJ0454.1-0300 and MACSJ1359.1-1929, two clusters where there is not a single, bright, galaxy dominating the core of the cluster, rather a collection of galaxies of similar magnitudes. This effect of how dominating the central galaxy is is addressed section 4.4.3.

In their study of the relationship between the K-band absolute magnitude and the X-ray luminosity of its host cluster, Brough et al. conclude that BCGs in high redshift, high luminosity clusters have not experienced any mass growth since $z=1$. They define high redshift to be $z \geq 0.1$ and high luminosity to be 2.3×10^{44} erg s $^{-1}$,

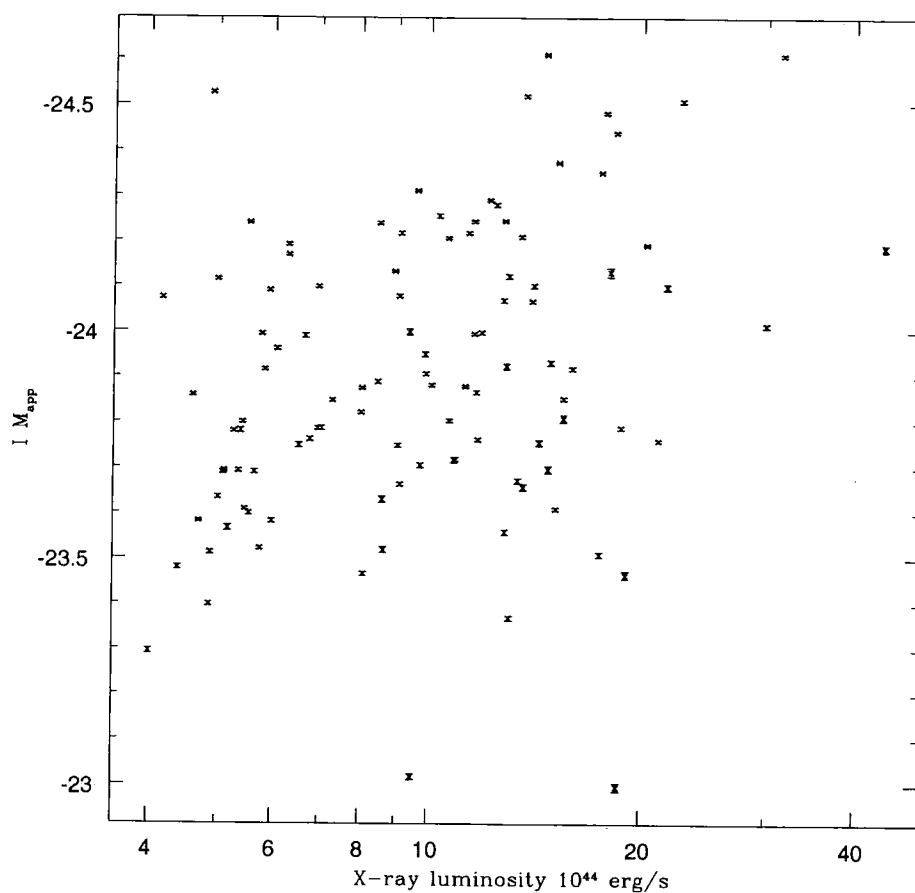


Figure 4.7: Variation in the absolute magnitude of the brightest cluster galaxy with X-ray luminosity in the I band. The R and V bands are not shown as these magnitudes are dominated by their k-correction.

placing the MACS clusters entirely within this high-luminosity, high-redshift bin. However, hierarchical models of cluster formation imply that clusters are continually accreting mass through mergers which leads to the increase in the X-ray luminosity of the cluster through the mass / luminosity relationship. In order to preserve the absolute magnitude - redshift relationship seen in figure 4.6 and the absolute magnitude - X-ray relationship seen in figure 4.7 it is clear that if the hypothesis that the clusters are accreting mass is correct then the BCG population must also be accreting mass to maintain these relationships, at odds with the Brough et al. result who find that the K band magnitudes of BCG galaxies are consistent with a passively evolving population, implying no change in the BCG over time.

4.4.3 Central Dominance

Clearly not all BCGs dominate the centre of their clusters as much as others. Figure 4.1 shows that the central galaxy of MACS0913.7+4056 is very much bigger and brighter than the other nearby galaxies whereas MACSJ2243.3-0935 (shown in figure 4.8) has no such extremely dominant BCG and, instead, the core of the cluster is made up of two galaxies of similar size.

Hierarchical models of cluster formation (such as Cole et al. 2000) suggest that the largest and brightest objects in the universe form at late times from the assembly & merger of smaller objects. As the most luminous (in terms of purely stellar luminosity) objects in the universe, the BCG population as we see it locally must also have formed at a relatively recent epoch. With such a presumably rapidly evolving population, as clusters are observed at higher and higher redshifts, it should be possible to constrain theoretical models of structure formation through the assembly of the BCG population.

As their name suggests, the principle feature of BCG galaxies is that they dominate the core of a cluster by being bigger and brighter than any of the other cluster galaxies. In order to quantify this degree of dominance of the BCG over the rest of the cluster galaxy population, the formalism of Kim et al. (2002) was followed in that the degree of dominance of the BCG is defined by:

$$\Delta m = \frac{(m_2 + m_3)}{2} - m_1$$

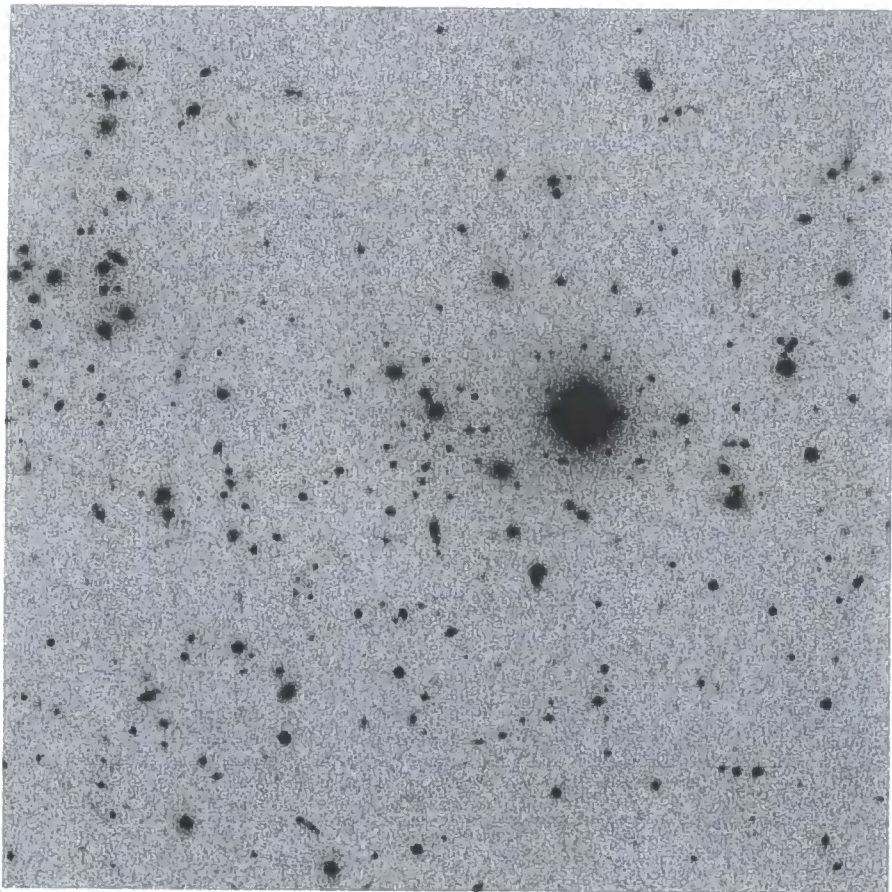


Figure 4.8: 3×3 arcmin I-band image of the central region of the cluster MACSJ2243.3-0935 showing that this cluster is not dominated by a single large galaxy.

where Δm is the degree of dominance and m_1 , m_2 & m_3 are the magnitudes (in this case the 32Kpc aperture magnitudes) of the first (i.e. the BCG), second and third brightest cluster galaxies. The magnitudes of the second and third brightest cluster galaxies are taken from those galaxies colour-selected from the elliptical colour-sequence that lie within 1Mpc (projected) of the BCG. This selection effect may result in some mis-identification of the correct m_2 and m_3 galaxies if they are undergoing star-formation as has been seen in the BCG population itself. These galaxies will be excluded by the colour-selection which will bias the degree of dominance toward higher values. However, unlike the BCG which can be identified by their position, correctly selecting other bright-star-forming cluster galaxies without contamination from foreground galaxies is virtually impossible without spectroscopic redshifts. The effect of this possible missing population is modified somewhat by the degree of dominance being measured against the mean of the (apparently) second and third brightest galaxies, which also has the advantage of more accurately reporting the degree of dominance of clusters where there are two galaxies that are significantly brighter than the rest of the population rather than a single BCG.

Figure 4.9 shows the degree of dominance of 111 MACS clusters. This is a larger number of BCGs than are presented in table 4.1 as the degree of dominance only requires relative photometry and consequently there are 6 clusters that do not have correctly calibrated absolute photometry that can be used in this comparison. The degree of dominance is calculated separately in the I, R and V bands although the identifications of m_1 , m_2 & m_3 are performed only in the I-band.

It can be seen in figure 4.9 that there is no strong trend in the central dominance of the MACS clusters with redshift. There is a faint trend visible in each of the three bands, although this is at low statistical significance (less than 1σ .) From this lack of strong trend and the fact that roughly half of the clusters are seen with large degrees of central dominance in the I-band (Kim et al define large degrees of dominance to be $\Delta m \geq 0.65$) it is clear that the redshift of the MACS survey is not sufficiently deep to reach back to the epoch of BCG formation. However, although it is clear that in many cases the BCG is highly evolved due to their very high degrees of dominance, there is a significant range in the degrees of dominance across the whole MACS redshift range. This suggests that the BCGs in these clusters have

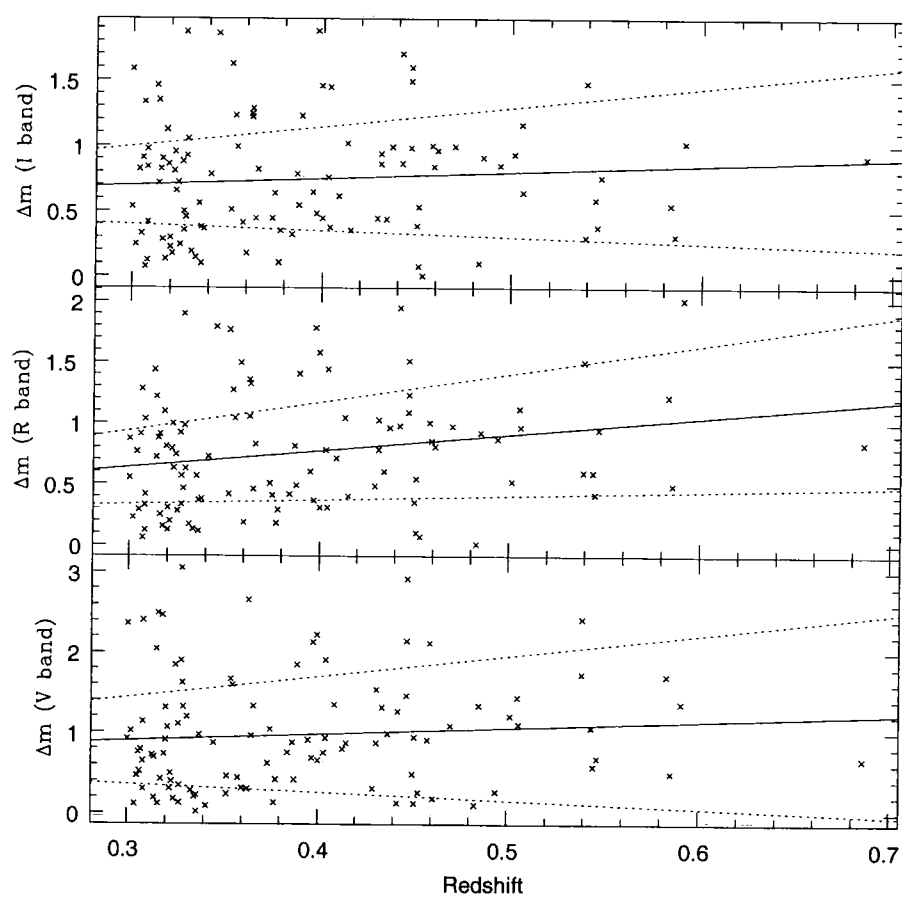


Figure 4.9: The degree of dominance of the brightest cluster galaxy against redshift in the I (top), R (middle) and V (lower) bands

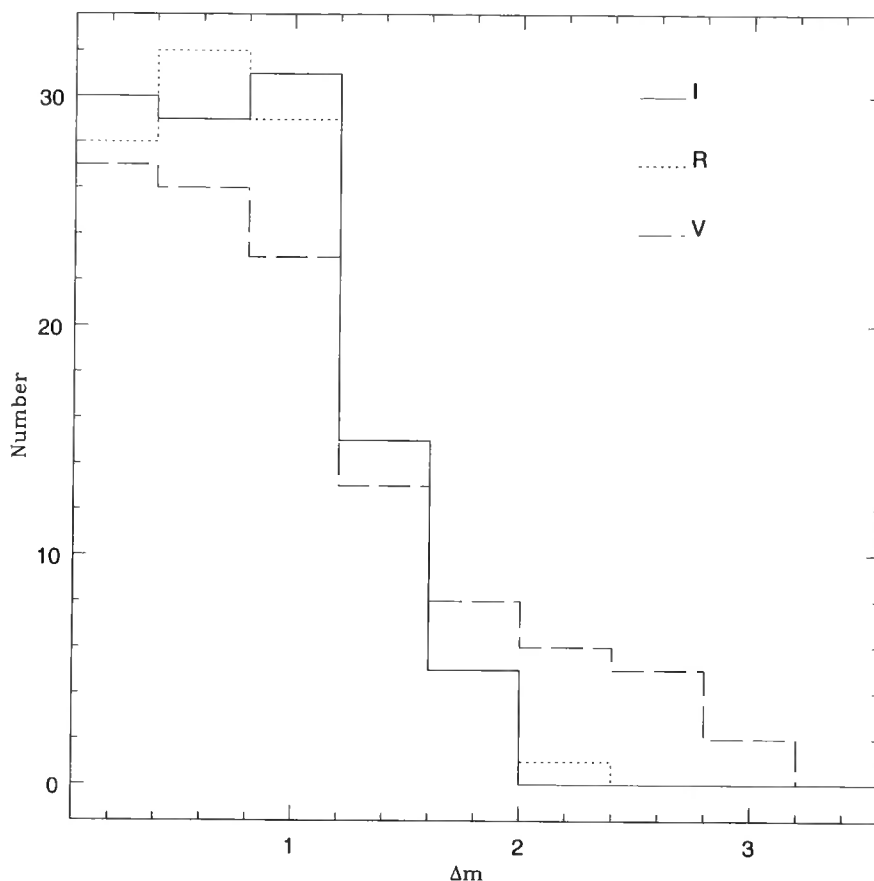


Figure 4.10: Histogram showing the distribution of degree of dominance in the I, R and V bands for the I-band selected sample of 111 MACS clusters.

undergone significant evolution at earlier times but also that a significant proportion of the population continue to form at these redshifts.

It can also be seen in figure 4.9 that there is a much greater range in the degree of dominance in the V-band when compared to the R and I bands. The distribution of the degree of dominance for the three bands are shown in figure 4.10. Kim et al do not report in which band their degrees of dominance were measured.

It appears that the I and R band have a similar distribution of degrees of dominance whereas the V band show considerably more variation. There are no clusters that have $\Delta m > 2$ in the I band, only one in the R band where there are 13 clusters that have this degree of dominance in the V band. It should be stressed that these degrees of dominance are calculated from the same I-band selected sample of BCGs and therefore this cannot be a simple selection effect. As the magnitude of

a galaxy becomes more sensitive to activity when bluer bands are considered, the change in the degree of dominance must be due to increased activity in the central galaxy. This reinforces the role that the BCG is presumed to play in the formation of clusters as this result shows that if there is any activity (eg. star-formation) taking place in the core of a cluster, it is preferentially going to be taking place in the BCG. This has important implications for simulations of galaxy clusters as current theories rely on feedback from some energy source (eg. star-formation or radio sources) heating the intra-cluster medium to reduce the amount of gas cooling. The extended range in the degree of dominance in the V-band over the R and I bands shows that there is a greater amount of activity on the BCG (as observed in the V band) than would be expected if the amount of activity was simply scaled with the mass of the galaxy (as observed by the I-band degree of dominance.) This result shows that not only is there clearly activity in the centres of massive galaxy clusters but that this activity is preferentially concentrated at the BCG, in the very centre of the potential well.

Having seen that there is a variation in the degree of dominance, the relationship between the degree of dominance of a BCG and its absolute magnitude was probed and is shown in figure 4.11. As might be expected, it can be seen that there is a relationship between the degree of dominance and the BCGs absolute magnitude in both the I and R bands. Fitting linear relationships to these trends reveals slopes of 0.676 ± 0.27 degrees of dominance per magnitude in the I band and 0.505 ± 0.25 degrees of dominance per magnitude in the R band. This trend of brighter objects being the most centrally dominant is consistent with there being conservation of mass in the centre of the clusters. If the brightest cluster galaxy has grown to be an extremely large and bright galaxy, there will be less material available for the other galaxies to grow and so it is seen that the bright galaxies are also the most dominant. Figure 4.11 also shows that there is no well defined trend in the relationship between the degree of dominance and the absolute magnitude of the BCGs in the V band. In particular, it can be seen that there is a considerable number of bright galaxies that are not especially centrally dominant in the V band, or alternatively, there is a sub-population of BCG galaxies that contain something (either star-formation or an AGN) that provides a source of blue light above and

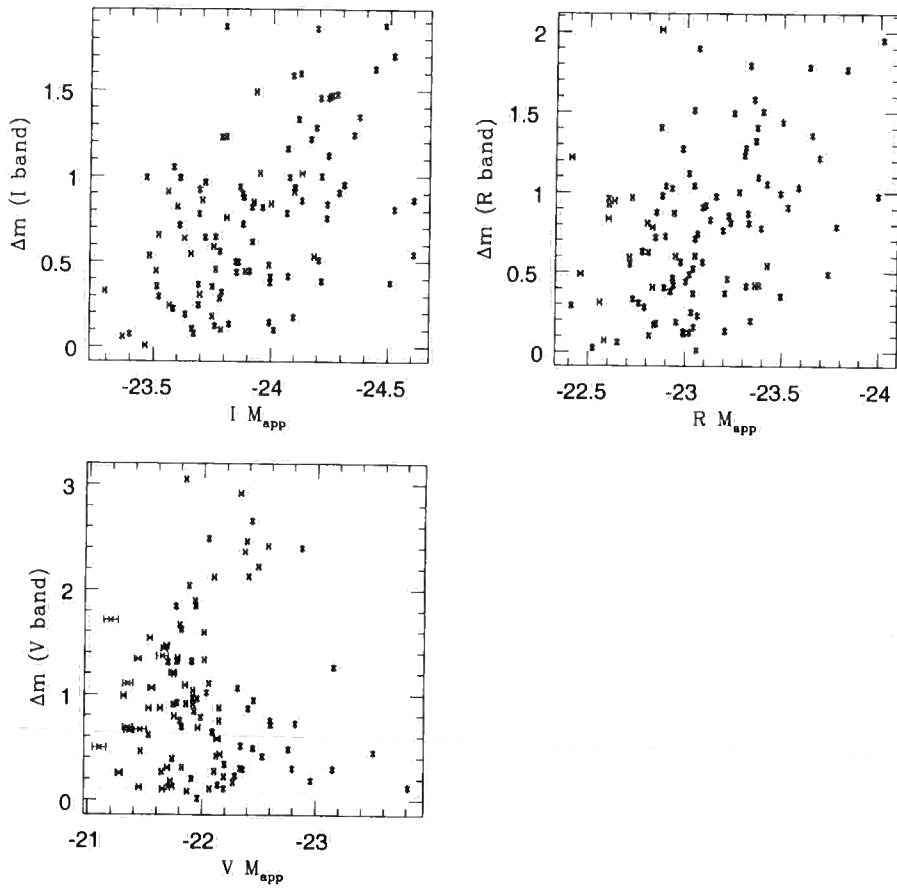


Figure 4.11: The degree of dominance of the brightest cluster galaxy against its absolute magnitude I (top left), R (top right) and V (lower) bands

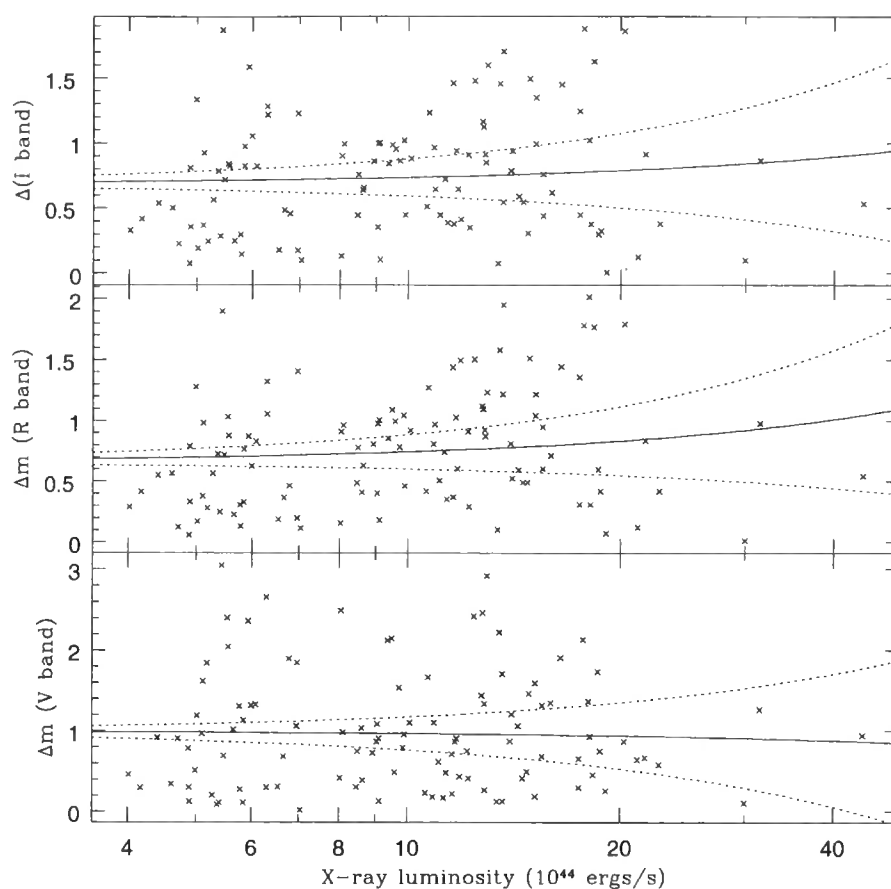


Figure 4.12: The degree of dominance of the brightest cluster galaxy against the host cluster X-ray luminosity in the I (top), R (middle) and V (lower) bands

beyond that which would be expected from the mass of the BCG alone. There is a strong caveat to these V-band results. The identifications of the first, second and third brightest cluster galaxies have been made in the I band, consequently, the galaxy that is (for example) the third brightest in the I-band may not necessarily be the third brightest in the V band. It is for this reason that (with the exception of the remainder of this section) it is the I band degree of dominance that is used for comparison with other BCG properties. The objects with excess blue-light emission are discussed in light of their colour in section 4.5

As with all other X-ray flux-limited surveys, the variation with luminosity must be considered to constrain the selection effects. The variation in degree of dominance with X-ray luminosity is shown in figure 4.12. As can be seen, there is no variation in the degree of dominance with X-ray luminosity, demonstrating that

this degree of dominance result is not merely an effect of the mass of the clusters.

It has been shown in this study of the magnitudes of the MACS BCGs that there is no significant variation in the degree of dominance as measured in the I-band with either redshift or X-ray luminosity. This implies that the variation in the amount of activity in the BCG population as observed via the increased range of degree of dominance in the V-band happens in all clusters at all redshifts and in clusters of all sizes. As noted, this work was built upon the formalism used by Kim et al (2002) for a sample of 211 lower redshift, lower mass clusters selected from the Sloan Digital Sky Survey Early Data Release (Stoughton et al. 2001) When the full Sloan Catalog is released it will be possible to combine both the Sloan results with those presented here to constrain the evolution of the BCG population across a large mass and redshift range. The preliminary results presented in Kim et al. show that 57% of SDSS cluster are highly centrally dominated which is similar to the the figure of 52% found in this work.

4.5 Brightest Cluster Galaxy Colour

Obviously, the magnitude of a galaxy tells only half the story. For each of the 105 BCGs galaxies observed in photometric conditions, the projected 32 Kpc aperture colour was measured from the seeing matched frames. The colour of these galaxies against the redshift of the host cluster is shown in figure 4.13. In this figure, the galaxy colours have been corrected for galactic extinction using the Schlegel et al. (1998) maps calculated using the NASA Extragalactic Database (NED) calculator.[†] The solid lines are the no-evolution predicted colour for an elliptical galaxy from King & Ellis (1985). Although this model is relatively old, it has been shown by other authors that there is little observable difference between different models of the magnitude of BCG galaxies at these redshifts (Brough et al. 2000). In order to compensate for unknown colour-corrections between the models and the data, the predicted colours have been fitted to the median galaxy colour at redshift 0.3.

It can be seen from figure 4.13 that, in general, the brightest cluster galaxies form a trend along the model prediction, showing that they are, for the most part,

[†]available at <http://nedwww.ipac.caltech.edu/forms/calculator.html>

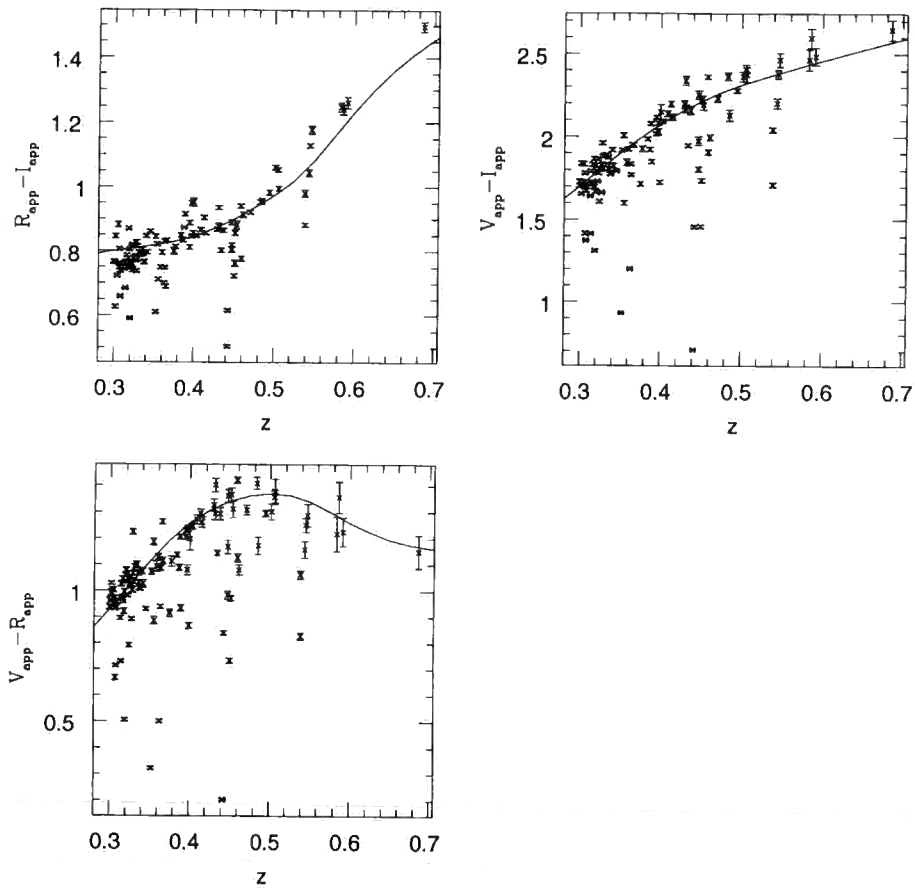


Figure 4.13: The projected 32 Kpc aperture colour for the sample of 105 MACS BCGs plotted against redshift for each of the R-I (upper left), V-I (upper right) and V-R (lower) colours. The solid lines on each panel are the King and Ellis no evolution predicted colours for elliptical galaxies at this redshift fitted to the observed data as $z=0.3$

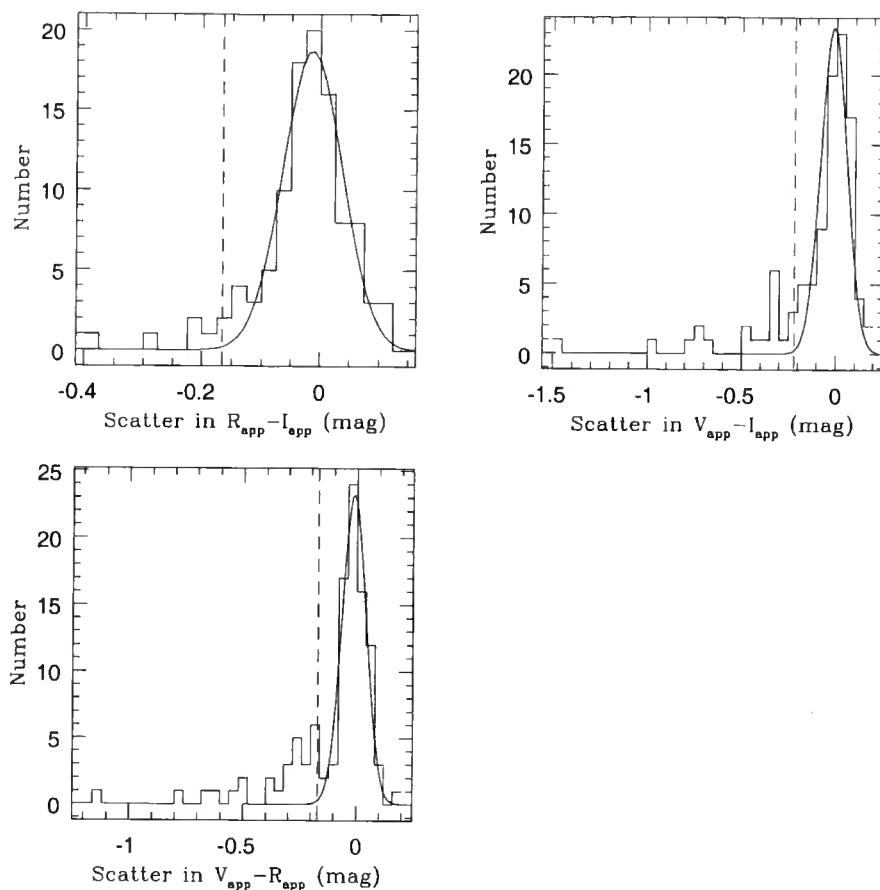


Figure 4.14: Histograms showing the scatter in colour ($\text{Colour}_{\text{model}} - \text{Colour}_{\text{observed}}$) in each of the R-I (upper left), V-I (upper right) and V-R (lower) colours. The solid line shows the best fit Gaussian curve and the dotted line shows the 3σ deviation from the centre of the Gaussian fit.

normal elliptical galaxies dominated by an old stellar population. However, there are clearly a number of galaxies that are considerably bluer than this relationship, indicating that they are experiencing some form of activity, either an active nucleus or star-formation. In order to quantify the number of galaxies that are bluer than expected, the distributions of the difference (scatter) in the BCG colour from the model is shown in figure 4.14. The scatter was calculated in the sense of $\text{colour}_{\text{model}} - \text{colour}_{\text{observed}}$ such that a bluer colour corresponds to negative scatter.

Figure 4.14 shows that the bulk of the galaxies are normally distributed around the model with an extended tail bluewards. The solid lines in figure 4.14 show the best fit Gaussian to the distribution for each of the three colours. It can clearly

Table 4.2: The number of BCGs significantly ($> 3\sigma$) brighter than the normal colour distribution for the I, R and V bands.

Colour	Blue Excess	σ
R-I	7 (6%)	0.051
V-I	20(19%)	0.068
V-R	27(26%)	0.052

be seen that in all three colours, there are no BCG galaxies that are scattered redwards by any statistically significant amount. This is to be expected as, with the exception of reddening by dust which is not expected to be a significant effect for this population of galaxies, there are few physical effects that can make a galaxy appear to be redder than it would be expected to be. Consequently, the distribution of galaxies redder than the peak can be used to constrain the scatter in the colour due to the photometric errors in the measured magnitudes and their associated derived colours. Having fitted the distribution of galaxy colour, the number of galaxies with differences in colour of more than 3σ were counted and are shown in table 4.2. Obviously, the number of galaxies counted in this way is dependent on the quality of the photometric data (which is reflected in the value of σ) and future studies, for example the Sloan Survey, will be able to tackle this problem (albeit at lower redshifts) with a much greater accuracy and so table 4.2 includes the σ value of the best fit Gaussian curve used in this study to allow future direct comparison.

It can be seen from the data in table 4.2 that the blue excess increases from 6% in the R-I colour to 26% in the V-R colour. This colour dependence is to be expected as the sensitivity to activity increases with bluer bands. It should be stressed that this excess is a lower limit as there could be some faintly active objects that are washed out in the scatter associated with the systematic photometric errors. Theoretical simulations of galaxy clusters have shown that a central energy source, such as a radio emitting AGN, can eject enough energy into the intra-cluster medium to slow down or even stop any of the gas cooling (Quilis et al 2001) However, this requires the central galaxy to have an activity cycle of 50% whereas this sample only reveals the activity cycle to be roughly half that. Clearly energy injection from the BCG

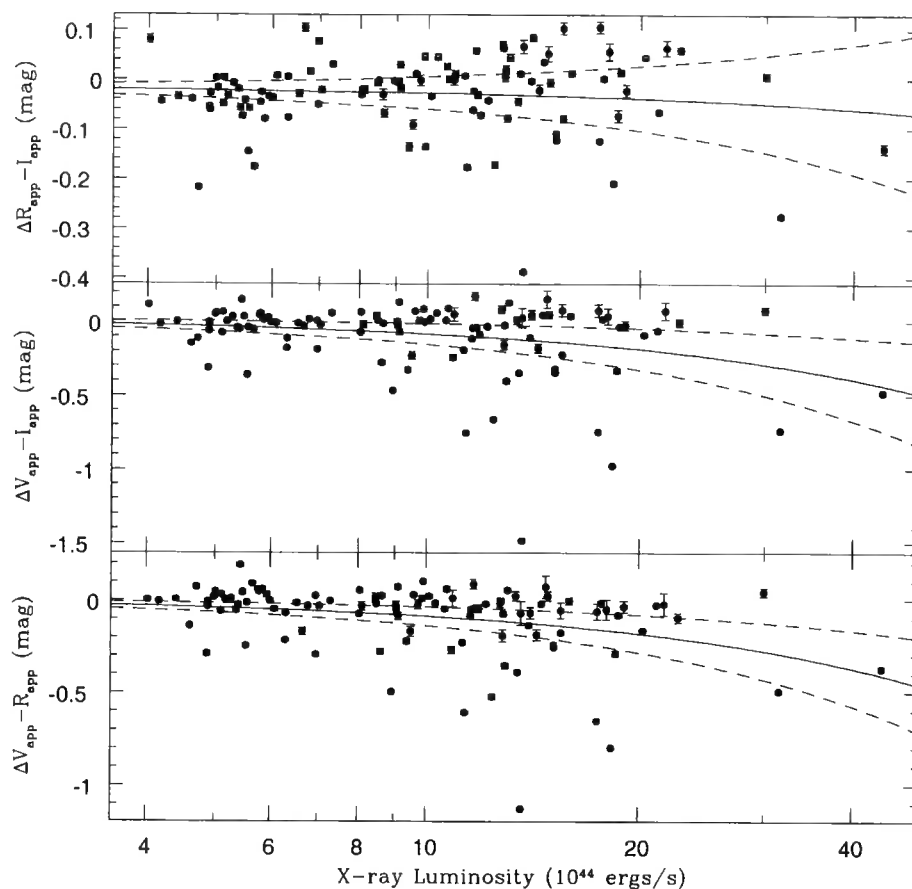


Figure 4.15: The scatter in the colour of the Brightest Cluster Galaxy with the bootstrap best fit line (solid) and 1σ confidence region (dashed line)

is going to have an effect on the intracluster medium but, on the basis of this data set, it cannot on its own prevent all of the gas from cooling. This figure of 26% is also extremely similar to the figure of 27% that Crawford et al. (1999) found for the number of BCG galaxies that contain emission lines in their spectra. Indeed, several of the blue MACS BCG galaxies have been found to have emission lines, for example the brightest galaxy in MACSJ1621.3+3810 (Edge et al 2003).

Having shown that there is a sub-population of BCG galaxies that appear to be considerable bluer than would be expected for an elliptical at that redshift, the relationship between the colour of the BCG was compared against the properties of the BCGs host cluster. The scatter in the colours of the BCG against the X-ray luminosity of its host cluster is shown in figure 4.15

This figure shows that BCGs with very much bluer than expected colours reside

Table 4.3: Statistics for the high ($\geq 10^{45}$ ergs/s) and low ($< 10^{45}$ ergs/s) cluster X-ray luminosity sub-samples. Shown are the sample mean and median, the probability (P) that the samples are drawn from the same parent population based upon the K-S statistic and the bootstrap fit slope of the linear trend fit to the data

Colour	Mean (mags)		Median (mags)		P (%)	Trend
	High	Low	High	Low		
R-I	-0.025±0.09	-0.031±0.06	-0.0013	-0.027	1.1	-0.001±0.003
V-I	-0.152±0.32	-0.041±0.12	-0.031	-0.0084	18	-0.010±0.007
V-R	-0.157±0.24	-0.040±0.12	-0.059	-0.010	0.4	-0.009±0.005

in clusters with extremely high X-ray luminosity, this is particularly apparent in the V-I and V-R colours. The solid lines on figure 4.15 show the boot-strap fitted linear relationship to the data and the dashed lines shows the 1σ confidence limits. There is only a faint trend found in the relationship between R-I colour and the X-ray luminosity of the cluster. This is as expected as this is the colour that is most sensitive to the galaxy mass and no radical trend in mass would be expected. Stronger trends are seen in the V-I and V-R bands, although still only at low statistical significance. In order to more quantitatively demonstrate the effect of the X-ray luminosity on the colour of the BCG, the BCG sample was split into two sub-samples, those in ‘low’ ($< 10^{45}$ ergs/s) X-ray luminosity clusters and those in ‘high’ (10^{45} ergs/s) luminosity clusters. It should be noted that these definitions of high and low are only relative to the MACS sample, Brough et al (2000) set the distinction between high and low to be 1.9×10^{44} , a factor of 5 lower. The cumulative distribution of the scatter in the colour for the X-ray luminosity split sub-samples for each of the three bands is shown in figure 4.16

When Kolmogorov-Smirnov (K-S) statistics are applied to these distributions, it is found that the probability of the two distributions being drawn from the same parent population is 1% for the R-I sample, 18% for the V-I sample and 0.4% for V-R. These statistics along with the others for these luminosity split samples are summarised in table 4.3

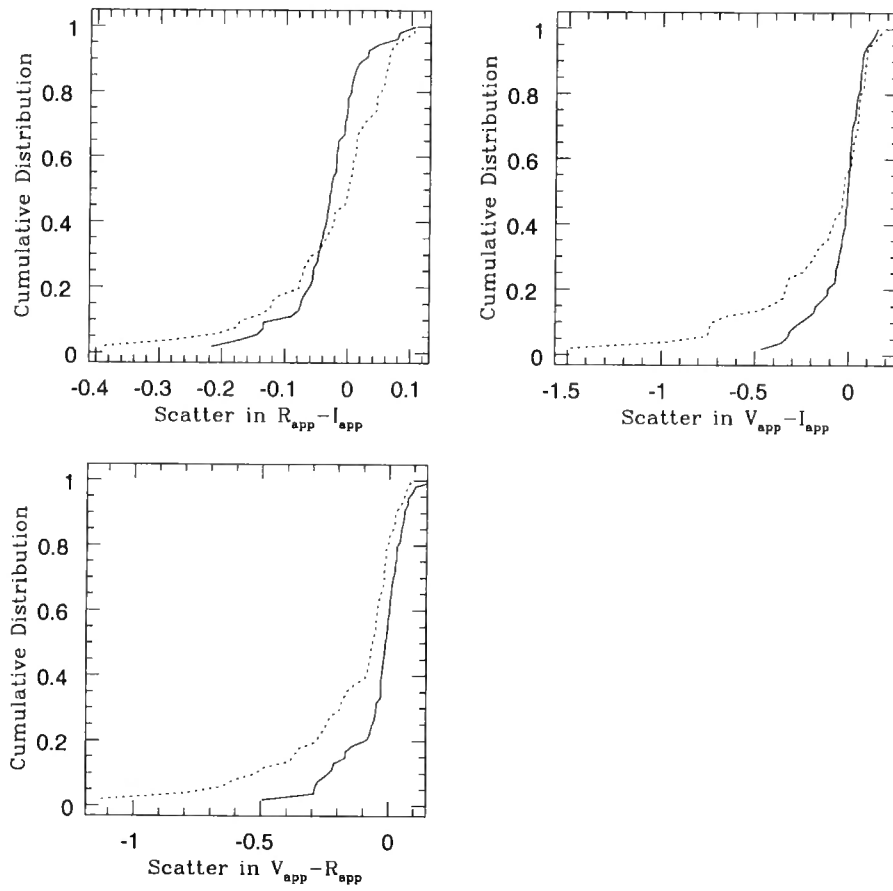


Figure 4.16: Cumulative distribution of scatter in BCG colour for high and low X-ray luminosity sub-samples for each of the R-I (top left), V-I (top right) and V-R (lower left) colours.

The data in table 4.3 shows that in all statistical tests in the V-I and V-R bands, the high X-ray luminosity sample is bluer than the low luminosity one and the K-S statistic shows that these are in fact distinct populations, although none of the individual tests are particularly well constrained. The fact that there is no difference in the mean or median for the two samples in the R-I statistics shows that this difference is not simply due to mass effects, the difference in colour must be due to increased amounts of activity within the BCGs that reside within high luminosity clusters. This lends support to the idea of cooling flows as, in high luminosity clusters, the predicted rate of cooling is at its highest and so it is in these clusters that one would expect to see active BCGs.

In order to see what sort of BCGs are undergoing the observed activity, an identical analysis to that performed for the cluster X-ray luminosity was undertaken for the scatter in the observed colour of a BCG against the degree of dominance (Δm) for that BCG. If cooling flows are the explanation for the blue galaxies, it would be expected that these galaxies would need to be sat at the very centre of the cluster potential and that they would be accreting the cooled gas from the intra-cluster medium. This should result in the bluest BCG galaxies also having the highest high degrees of dominance as they grow at an accelerated rate with respect to the rest of the cluster population. The scatter in the colour of the BCG against the I-band degree of dominance is shown in figure 4.17.

As was expected, it can be seen that the bluest BCG galaxies are also the ones that are the most centrally dominating, suggesting that these galaxies have accreted a large proportion of the cooled intra-cluster medium which is showing itself in the form of star formation. As was done for the X-ray luminosity study, the BCGs were split into two sub-groups with high ($\Delta m > 0.67$) and low ($\Delta m \leq 0.67$) degrees of dominance. The cumulative distribution for these sub-groups in the 3 separate colours is shown in figure 4.18.

Figure 4.18 shows that the distributions for the high and low central dominance cluster are much more similar than was seen in the distribution for the scatter with X-ray luminosity (c.f. figure 4.16.) This is reflected in the K-S statistics where the probabilities of the two populations being drawn from the same parent population rise to 18%, 14% and 18% for the three colours respectively. The statistical results

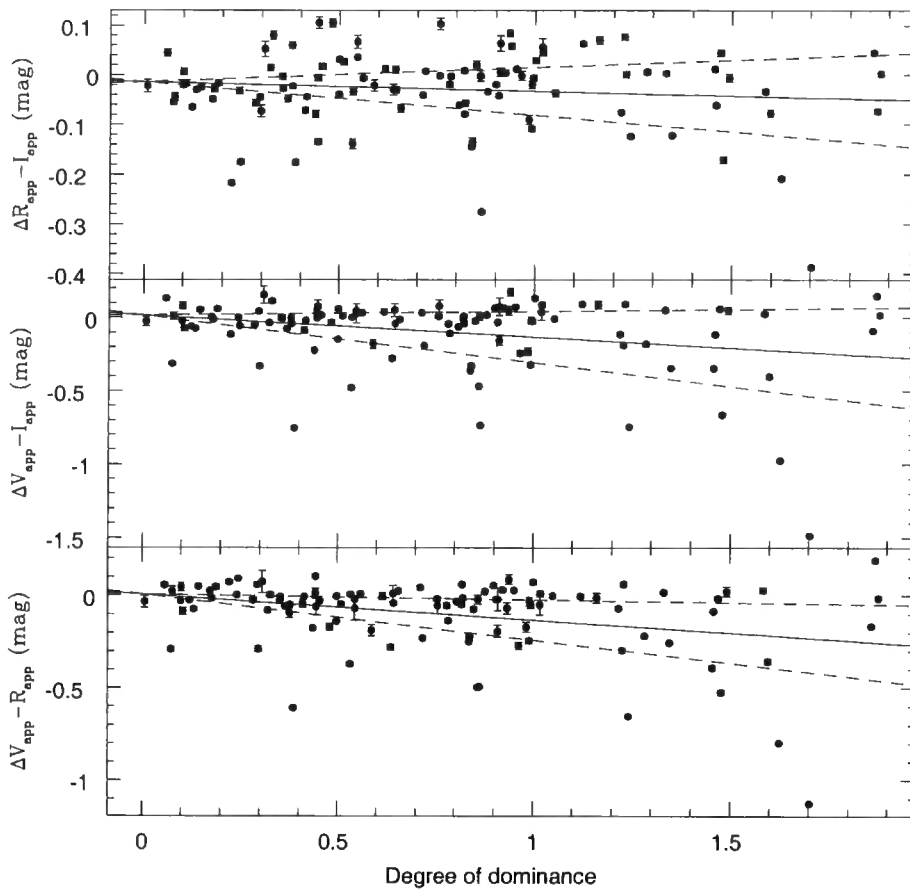


Figure 4.17: The scatter in the colour of the Brightest Cluster Galaxy against the I-band calculated degree of dominance with the bootstrap best fit line (solid) and 1σ confidence region (dashed line)

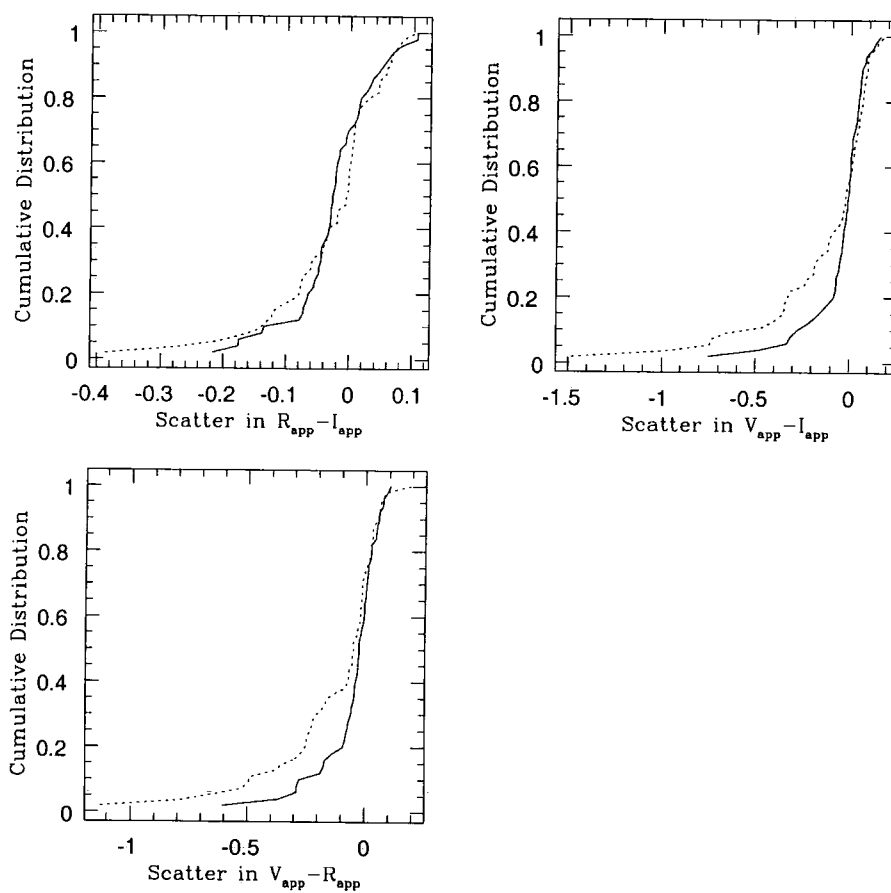


Figure 4.18: Cumulative distribution of scatter in BCG colour for high and low degree of dominance sub-samples for each of the R-I (top left) , V-I (top right) and V-R (lower left) colours.

Table 4.4: Statistics for the high ($\Delta m > 0.67$) and low ($\Delta m \leq 0.67$) cluster X-ray luminosity sub-samples. Shown are the sample mean and median, the probability (P) that the samples are drawn from the same parent population based upon the K-S statistic and the bootstrap fit slope of the linear trend fit to the data

Colour	Mean (mags)		Median (mags)		P (%)	Trend
	High	Low	High	Low		
R-I	-0.030 ± 0.09	-0.002 ± 0.06	-0.0026	-0.025	18	-0.019 ± 0.048
V-I	-0.136 ± 0.30	-0.049 ± 0.16	-0.023	-0.0076	14	-0.150 ± 0.175
V-R	-0.135 ± 0.23	-0.054 ± 0.13	-0.048	-0.025	18	-0.138 ± 0.109

for the high and low central dominance sub-samples are shown in table 4.4.

As with the result for the X-ray luminosity samples, it can be seen that in the V-I and V-R colours, the highly dominating BCG galaxies are bluer than the less dominating ones and the K-S statistic shows that it is most likely that the two samples are not part of the same parent population. As these degrees of dominance are calculated from the I-band magnitudes, this effect cannot result from a simple mass effect, nor can it be due to mergers as, in hierarchical models, mergers happen between objects of similar sizes and so merging BCGs would be expected to have low degrees of dominance (in a post BCG merger, the BCG will have accreted the other galaxies of near its size, leaving only much smaller galaxies and hence a high degree of dominance). This provides more evidence that activity, in the form of either star-formation or an AGN, preferentially happens in BCGs that are considerably brighter than the rest of the galaxy population and that reside in highly X-ray luminous clusters. This compares favorably with the empirical description of the X-ray profile of a typical cooling-flow cluster, the X-ray profile is observed to be sharply peaked toward the centre.

It is interesting to note that the K-S statistic for the scatter in colour against X-ray luminosity shows that the high and low populations are less likely (at 1%, 18% and 0.4% probability) to be drawn from the same parent population than the similar statistics for the scatter in colour against central dominance (at 18%, 14% and 18%

respectively.) From this, it can be concluded that the X-ray luminosity of a cluster has far more effect on the likelihood of an individual BCG being active than it being by far the largest galaxy in the cluster. This would indicate that it is the interaction between the cluster and the galaxy that drives the observed activity in the BCGs rather than it just being a property of the galaxy size or position. This observational result links the activity of the BCG galaxy to the X-ray emitting gas in the intra-cluster medium which then lends support to the idea of feedback between a central power source (either winds from ongoing formation of massive stars or emission from an AGN) and the rate of cooling of the intra-cluster medium gas. However, in order to preserve the colour - X-ray luminosity relationship, whatever is fueling the activity, either providing supplies of gas for star formation or material falling onto the central black hole, must work efficiently otherwise active BCGs would still be seen in lower X-ray luminosity clusters where the feedback had successfully damped the supply of cold gas.

4.6 Brightest Colour Galaxy-Cluster Alignment

There have been several reports over the past two decades of an alignment effects between cluster galaxies and their host clusters and large scale structure, (see Djorgovski 1986 for a review). In 1982, Bingelli used 44 Abell cluster at $z < 0.1$ to study this effect in clusters and found a tendency for Brightest Cluster Galaxies to be aligned with their parent clusters. Kim et al. (2002) performed a similar study for BCG galaxies in the Sloan Digital Sky Survey Early Data Release (Stoughton et al. 2001) and found that, for a sample of 115 clusters at low redshift $0 < z \leq 0.45$ there was a tendency for BCG galaxies to be aligned with the host cluster and that this effect was stronger in those clusters where the BCG was highly dominant.

Although this sample covers a similar number and reaches a comparable redshift to the MACS survey, these clusters are, on average, much poorer than the MACS clusters. This reported alignment effect was studied within the MACS sample to constrain this effect for the most massive clusters at this redshift.

Firstly the position angle of the brightest cluster galaxy was obtained via the THETA output parameter from SExtractor. This THETA parameter is counted

counter-clockwise from NAXIS1 of the input image. See Bertin & Arnouts (1996) for a full description of how the THETA parameter is calculated.

Secondly, the orientation of the host cluster was determined from the cluster galaxy distribution. Cluster galaxies were colour-selected and only those galaxies falling within a projected 1Mpc circular aperture centred on the BCG galaxy were used to calculate the orientation. This leaves a sample of coordinate positions from which the cluster orientation was calculated using a matrix method.

In Cartesian coordinates, 2 dimensional space can be described using a 2×2 matrix which is obtained from the expansion of $(x + y)^2$:

$$\begin{pmatrix} x^2 & xy \\ yx & y^2 \end{pmatrix}$$

From this, a matrix describing the distribution of the galaxies within the cluster can be described by the matrix

$$\begin{pmatrix} \langle x^2 \rangle & \langle xy \rangle \\ \langle yx \rangle & \langle y^2 \rangle \end{pmatrix}$$

where

$$\begin{aligned} \langle x^2 \rangle &= \sum_{i=1}^n \frac{x_i^2}{n} \\ \langle xy \rangle &= \langle yx \rangle = \sum_{i=1}^n \frac{x_i y_i}{n} \\ \langle y^2 \rangle &= \sum_{i=1}^n \frac{y_i^2}{n} \end{aligned}$$

with x_i and y_i being the x (NAXIS1) and y (NAXIS2) coordinates of the i th colour-selected cluster galaxy.

It is true for any matrix that it can be diagonalized in the form

$$\mathbf{R} \begin{pmatrix} \langle x^2 \rangle & \langle xy \rangle \\ \langle yx \rangle & \langle y^2 \rangle \end{pmatrix} \mathbf{R}^T = \begin{pmatrix} \langle x'^2 \rangle & 0 \\ 0 & \langle y'^2 \rangle \end{pmatrix}$$

where \mathbf{R} is the rotational matrix and \mathbf{R}^T is the transpose of that matrix.

Clearly to match SExtractor's determination of the orientation of the BCG, the rotational matrix should be defined in such a way as to measure the orientation of the cluster counted counter-clockwise from the x-axis. Figure 4.19 shows a schematic

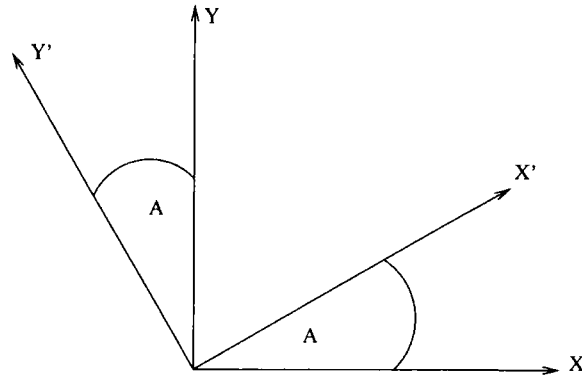


Figure 4.19: Schematic of the transformation of the base vector set (X,Y) to the base vector set (X',Y') under the counter-clockwise rotation A .

of a rotation of counter-clockwise angle A between the orthogonal base vectors X,Y and X',Y' .

From the geometry of this configuration, it is clear that under this rotation the rotational matrix \mathbf{R} is of the form

$$\begin{pmatrix} \cos A & \sin A \\ -\sin A & \cos A \end{pmatrix}$$

Clearly, solving for the values of this rotational matrix will allow the angle, A , between $NAXIS1$ and $NAXIS2$ and the major and minor axes of the cluster galaxy distribution X' and Y' . Comparing the values of $\langle X' \rangle$ and $\langle Y' \rangle$ determines which of these base vectors is the major axis of the cluster and so allow the calculation of the angle between the BCG and it's host cluster.

In order to solve this problem, the Single Value Decomposition (SVD) algorithm from Numerical recipes (Press et al.) was used which, for a given matrix $a(1:m,1:n)$ returns the values of the rotational matrix \mathbf{R} , which can then be solved for the rotation angle A , and the non-zero elements of the diagonal matrix.

Slight care must be taken with the different coordinate systems returned by the SExtractor determination of the angle of the BCG and the angle determined by the SVD method. SExtractor returns an angle which is in the range -90 to $+90$ degrees whereas the SVD algorithm, as it involves calculating the inverse cosine of a number, returns an angle in the range -45 to $+45$ degrees. This range increases to -45 to $+135$ degrees when an extra 90 degrees is added on to those clusters where Y' not X' is the semi-major axis as determined by the values of $\langle X' \rangle$ &

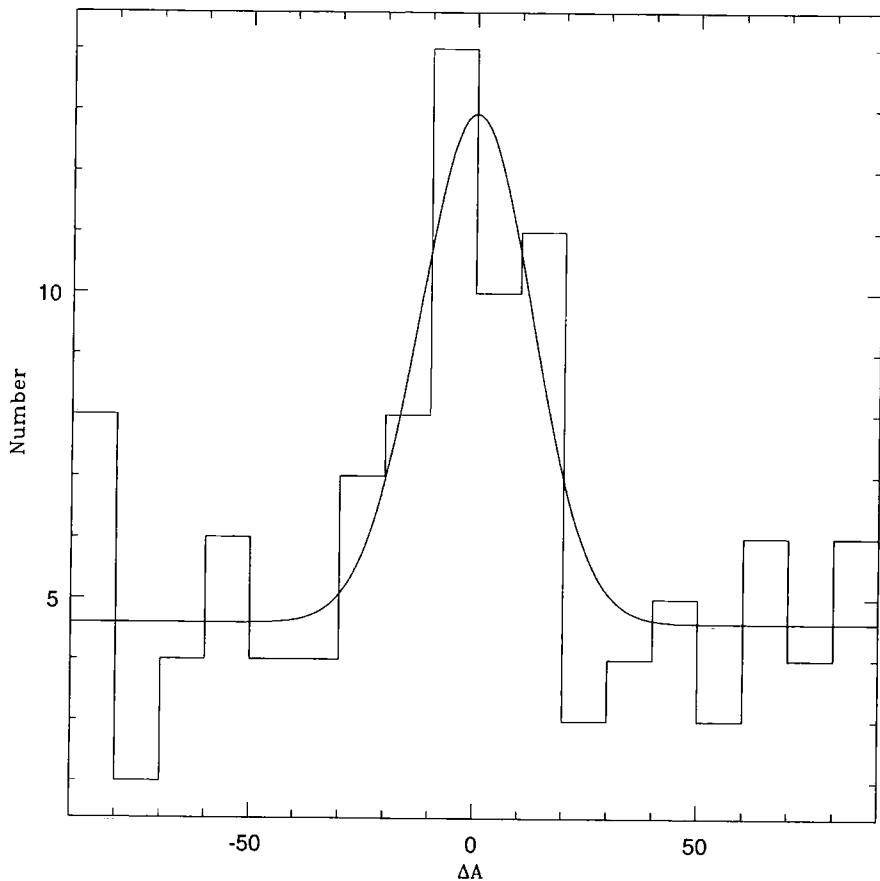


Figure 4.20: Histogram showing the difference in angle between BCGs and their host cluster. The solid line shows the best-fit Gaussian curve.

$\langle Y' \rangle$. However, it is then trivial to convert this into the SExtractor coordinate system. Lastly, when comparing the difference in angle between the BCG and the host cluster, coordinate transformation errors must be avoided as, for example, in the case where the cluster is at a position angle of +80 degree and the BCG is at a position angle of -70 degrees, it is obvious that the angle between the cluster and BCG is 30 degrees, not 150 degrees.

Having taken all of these coordinate transformation issues into account, the distribution of the difference in angle between the BCG and its host cluster is shown in figure 4.20

A clear excess of galaxies can be seen around $\Delta A=0$ (corresponding the BCG and cluster being aligned.) The solid line in figure 4.20 shows the best fit to this data parameterized as a Gaussian curve (plus a constant offset) which when fitted

is found to have a σ of 12.3 ± 5 degrees. There are 24 BCG galaxies within the range $-10 \leq \Delta A \leq 10$ degrees out of a total sample of 105 clusters, which is equivalent to a 5σ over-density. This is in agreement with the Kim et al. result where 19 galaxies out of a sample of 66 were aligned within the same range of angles. The secondary peak for $\Delta A < -80$ is a feature of the co-ordinate system and arises from situations where both the cluster and BCG do not have distinct major axes (i.e. appear to be circular), and should be ignored.

This result is significant in that it shows that not only are BCG galaxies preferentially aligned with their parent cluster, but that this correlation is extremely strong as the alignment is seen over a narrow range of angles. As clusters are seen to accrete matter over time, it is reasonable to assume that, as they go through a cycle of merger and relaxation, the semi-major axis of the cluster is likely to change over time and certainly is unlikely to be same as when the cluster was formed. In order to keep the relationship between the axis of the BCG and that of its host cluster it is clear that the BCG must also accrete matter to change its semi-major axis. In order for the BCG to change its axis in the same direction as that of its host cluster, it must accrete matter along the same vector as that of the parent cluster which strongly suggests that the BCG undergoes significant mergers, preferentially with galaxies from merging groups, which will then naturally lead to the BCG /cluster alignment effect through the conservation of angular momentum. Clearly this fits in well with the paradigm of hierarchical growth of structure through like-for-like mergers rather than a model where the BCG slowly accretes matter over time.

Having shown that the BCG / cluster alignment is seen in the MACS clusters, the sample was split into two samples, one where the BCG is highly dominant ($\Delta m > 0.67$) and one where the BCG is less dominant ($\Delta m \leq 0.67$). The histogram showing the distribution of the high and low central dominance populations is shown in figure 4.21

It can be seen that, unlike the similar study for BCGs in the Sloan Digital Sky Survey, the BCG / Cluster alignment effect for the MACS clusters appears to be just as strong in those clusters that are weakly centrally dominated as in those that are strongly centrally dominated whereas Kim et al. found that the less dominant BCGs were less likely to be aligned with their host galaxy. A K-S test performed

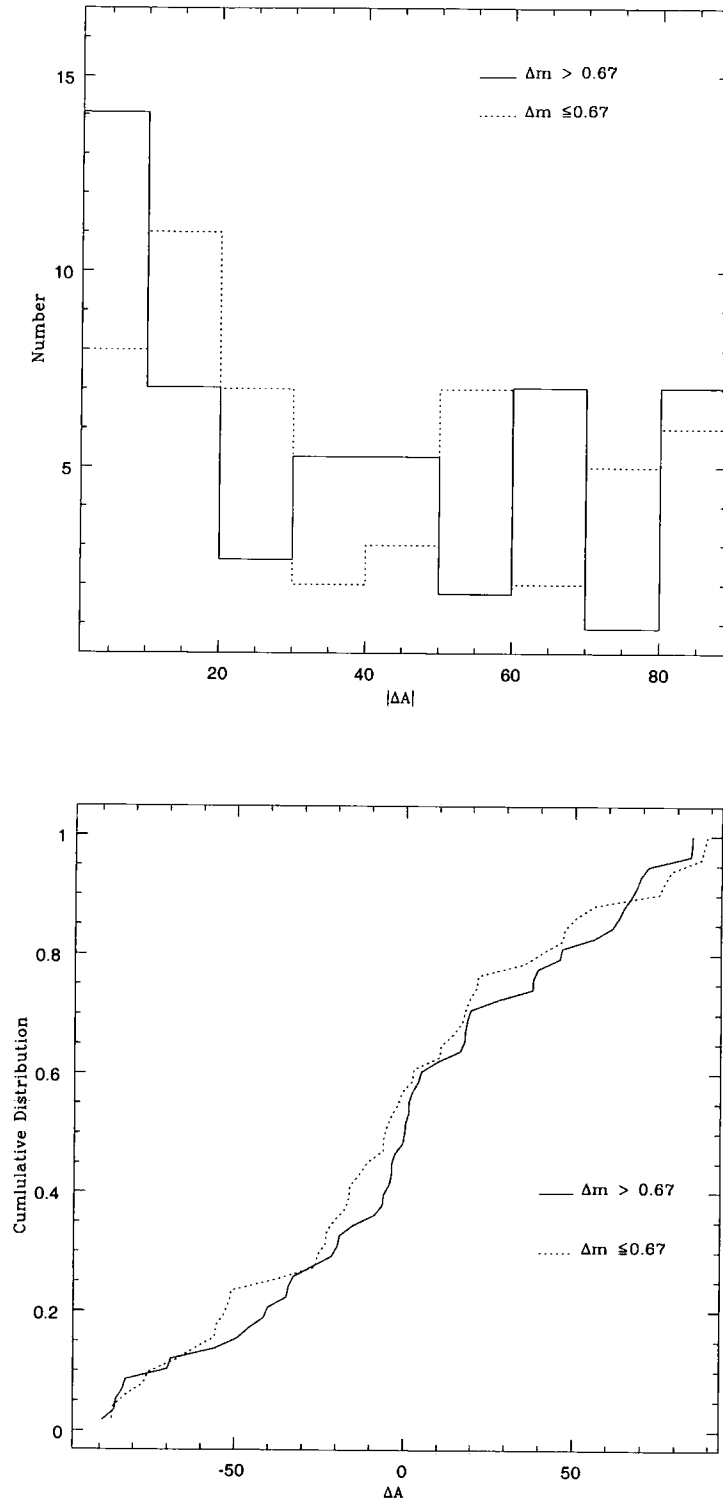


Figure 4.21: Histogram (top) and cumulative distribution (lower) showing the distribution of difference in angle between the BCG and its host cluster split into high ($\Delta m > 0.67$) and low ($\Delta m \leq 0.67$) degree of dominance samples

on these sub-groups suggests that these two populations are drawn from the same parent population at the 84% level. It is clear that this result is inconsistent with the conclusion drawn from the Sloan study that the less dominant BCG galaxies show a weaker alignment with their host cluster than strongly dominant BCGs. The Sloan clusters cover a similar redshift range to the MACS clusters with 57 clusters included in their sample at $0.3 < z < 0.45$. However, due their very different selection functions, the MACS clusters are, on average, significantly more massive than the optically selected Sloan ones. This leads naturally to the conclusion that the strength of the BCG / Cluster alignment is dependant upon the mass of the host cluster.

4.7 Future Aims

This chapter has concerned itself with conclusions drawn from the V,R and I band imaging of the MACS clusters taken with the UH2.2m telescope. As has been discussed, the redder the band in which a galaxy is observed, the more sensitive the observations are to the stellar mass of that galaxy. Although the I-band is suitable for a crude mass selection, to do this mass-selection properly (and to compare with previous studies of BCGs) K-band data would be preferable. An application was made to the United Kingdom Infra-red Telescope to do exactly this and four nights were awarded in October 2002 to this project. However, poor weather prevented suitable data being taken. It is hoped that that these observation can be repeated at a future time.

4.8 Conclusions

In this chapter the properties of the Brightest Cluster Galaxies of 105 clusters from the MACS survey have been studied from the V, R and I band observations of these clusters. The method of selecting the BCG has been described and shown that in many cases, the atypical colour of the BCG can make its selection non-trivial and that a combination method of magnitude, colour and position must be employed to correctly identify the BCG.

The 5 arcsecond aperture magnitude Hubble diagram was presented for use as a basis for photometric redshifts of clusters using the BCG population as a standard candle. The total (MAG_AUTO) magnitude Hubble diagram was also presented and used to show how the total magnitudes are unreliable due to systematic way in which the detection algorithm handles the presence of an extended halo of starlight.

The suitability of using the 32Kpc projected aperture magnitude was discussed and this was used to measure the apparent and absolute magnitudes of the MACS BCGs. The absolute magnitude was found to be correlated with the X-ray luminosity of the BCGs host cluster, confirming the link between BCG and host for clusters at these redshifts and luminosities.

The degree of dominance of the BCG over its next brightest cluster counterparts was calculated and shown to exhibit no trend with either redshift or cluster X-ray luminosity, from which it is concluded that the presence of high dominance BCGs at these redshifts indicate that the population has undergone significant evolution at previous times and that the range in degrees of dominance demonstrates that the BCG population continues to evolve at this epoch. The greater range in the degree of dominance in the V band compared to that of the I band is interpreted as evidence that the BCG population is undergoing more activity than the rest of the cluster elliptical population.

The colours of the BCG population were examined and found to consist of a normal distribution of colours around a no-evolution model with a scatter consistent with previous work and the photometric errors but with a significant tail of blue galaxies that contains up to a quarter of the total number of BCGs. This sub-population of blue BCGs is interpreted as being those BCGs that are undergoing some form of activity and provides half the number of active objects required to damp the effect of cooling flows in numerical simulations of feedback in clusters. The scatter in the colour of the BCG appears to be correlated with the X-ray luminosity and the degree of dominance. The correlation with the cluster X-ray luminosity is observed to be greater than the correlation with degree of dominance from which it is concluded that the interaction with the host cluster has a greater effect on the BCG than its position.

The alignment effect between BCGs and their host cluster was studied and found

that a highly significant number of BCGs were strongly aligned with their host cluster. No difference was found in the alignment of strongly and weakly dominant BCGs in contrast with an earlier result from the Sloan Early Data Release. From this it is concluded that the interaction between the BCG and its host is strongly linked to the mass of the cluster.

Chapter 5

Finding Clusters - MACS in the South

*A man travels the world in search of what he needs
and returns home to find it.*

George Moore (1852-1933)

The suitability of the South Pole as a site for S-Z effect observations is discussed and the need for a sample of MACS-like clusters suitable as targets for such observations identified. Details of CCD observations made using the SUSI2 instrument at the NTT telescope, La Silla, Chile are given along with the specific problems faced in the reduction of this data. Particular attention is given to the scattered light visible in the CCD images and allowing for the gap between the instrument detectors. The cluster identification process is described and its effectiveness demonstrated via the number of galaxies detected within a fixed aperture. Two techniques for estimating the redshifts of clusters are explored; using the 5" aperture magnitude of the BCG and fitting the colour-magnitude sequence.

5.1 Sunyaev-Zel'dovich effect observations at the South Pole

The Sunyaev-Zel'dovich effect (introduced in section 1.3.3) is caused by photons from the Cosmic Microwave background being scattered to higher energies via Compton scattering by energetic electrons, such as those found in the hot intra-cluster medium in the core of rich clusters. The magnitude of this effect is proportional to the path integral of the electron pressure along the line of sight unlike the X-ray luminosity which is proportional to the square of the electron density. In the same way that rich, massive clusters can be observed via their X-ray luminosity due

to the hot, dense gas in their cores, this same high density of energetic electrons make them ideal candidates for S-Z observations. The magnitude of the S-Z effect is not affected by the redshift of the target cluster and so, due to the smaller projected size, high redshift clusters actually provide better targets than low redshift ones.

The South Pole is an excellent site for measuring the S-Z effect as both its high altitude and long periods of dry weather provide near perfect conditions for the sub-mm observations in which the S-Z effect is seen. However, although the South Pole is an excellent site for S-Z work and clusters are suitable candidates for such work, there is a shortage of suitable targets in the Southern Hemisphere. This is a result of the majority of cluster surveys, and certainly the majority of the X-ray selected clusters surveys that probe the most massive (and therefore most useful for this application) clusters being based in the Northern Hemisphere. The notable exception to this is the REFLEX survey (Böhringer et al 2001) which is a southern hemisphere based survey. However, at the time of writing, the REFLEX survey has not been published but scaling from the Brightest Cluster Survey (Ebeling et al. 1998), there is unlikely to be more than 12 clusters within the REFLEX survey suitable for S-Z work, of which only 3 are likely to be at redshift greater than 0.3

Given this lack of suitable targets and the S-Z observations proposed at the South Pole eg. the ACBAR bolometer array on the Viper telescope (Griffin et al. 1998, Romer et al. 2001) there was clearly a need for the identification of X-ray luminous (and hence massive) clusters of galaxies in the Southern Hemisphere.

5.2 MACS in the South

In the Northern Hemisphere, the MACS survey (Ebeling, Edge & Henry 2001) has been successful in identifying massive clusters. In order to meet the need for a sample of MACS-like clusters in the South, an application for observing time was made to the European Southern Observatory (ESO) for period 70A. The application was successful and three nights were awarded on the 3.58 metre New Technology Telescope (NTT) at the La Silla Observatory, an European Southern Observatory facility located in central Chile, to use the Superb Seeing Imager 2 (SUSI2) instrument.

Table 5.1: Summary of the characteristics of the SUSI2 detector array

	SUSI2
Detector	2 x EEV 2048x4096, 15 μ m pixels (Identified as ESO CCD #45 & #46)
Pixel Scale	0.08 (Unbinned) 0.16 (2x2 binned) 0.24 (3x3 binned)
Gain	0.45 (#45) 0.44 (#46)
Field of View	5.5 x 5.5 arcmin
Quantum efficiency	R (74%) V (82%)
Readout time	56 seconds (Unbinned) 16 seconds (2x2 binned) 9 seconds (3x3 binned)

The SUSI2 instrument is mounted at the Nasmyth focus A of the NTT. It employs a mosaic of two 2048 \times 4096, 15 μ m pixel, thinned, anti-reflection coated EEV CCDs. A summary of the detector characteristics is given in Table 5.1. The detectors are arranged such that there is a physical space between the detectors which results in an 8" gap between the usable science areas. The detector has a pixel scale of 0.08" per pixel which, including the gap between the CCDs, results in a field of view of 5.5 \times 5.5 arcmin. The filter wheel of the instrument can hold 6 filters, of which the Bessel V (central wavelength 544.17nm) and R (central wavelength 641.58nm) band filters were used, the transmission curve of these two filters is shown in Figure 5.1

This instrument and telescope combination was chosen as the imaging campaign for MACS North has shown that a large, eight metre class, telescope is not necessary for imaging clusters at $0.3 < z < 0.7$, a two metre class telescope is perfectly adequate for this purpose. SUSI2 was chosen over the other NTT imaging instrument, EMMI, as SUSI2 has better throughput, allowing deeper images to be taken for the same integration time. Additionally, SUSI2 has a much smaller pixel scale (0.08 arc-seconds per pixel), allowing excellent seeing to be utilised should these

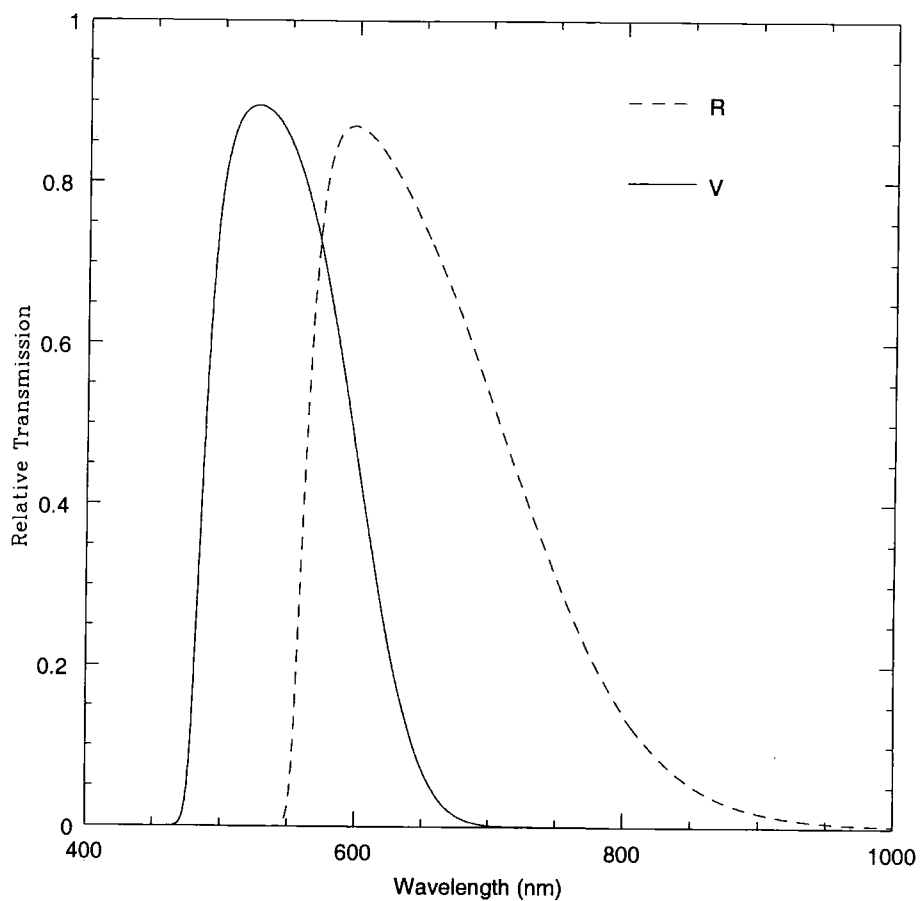


Figure 5.1: The response curves for the broad-band V (solid line) and R (dashed line) filters used by the SUSI2 instrument on the NTT. The data used to create this figure is available from the ESO NTT website http://www.la.eso.org/lasilla/Telescopes/NEWNTT/susi/susi_2002.html

conditions occur.

5.3 Observing strategy

Wherever possible, the target selection for the Southern clusters was performed in exactly the same way as was done for the Northern MACS clusters. The X-ray flux limit and hardness ratio limits were maintained, including the requirement that $|b| > 20$ although, obviously, the declination constraint (previously $\delta > -40$) was relaxed. The selected X-ray sources were then checked against Digital Sky Survey images to confirm that there was no obvious optical counterpart for the X-ray point source eg. a bright star or QSO. In many of these images, a faint galaxy can be seen which often turns out to be the cD galaxy at the core of the target cluster. After this process was complete, a target list of 87 was left, which is consistent with the number expected from the similar study in the North.

The observing strategy for the identification of clusters in the Northern MACS survey was that a 3x180 second exposure in R band taken with the UH2.2m telescope was taken and then visually examined for the presence of a cluster, except for those clusters where the X-ray flux and the lack of any counterpart in the DSS images indicates that any cluster would be extremely distant, in which case a 3x240 sec I band image was used. This strategy had to be slightly modified for the southern clusters as the amount of telescope time available for the project was (and is still) much more limited. Longer exposures were used for the identification of target clusters which then do not need to be repeated for those targets which turned out to be clusters. For all targets, 3 point dithered exposures of 3x240 seconds in the R band were taken during the first two nights, regardless of the expected redshift of the target. The three exposures were made in a three point dither pattern of (0",0"), (10",10") and (-10",-10") arcsec. This dither pattern was chosen to ensure that no object fell within the chip gap on all three of the exposures. The I band was not used for the cluster identification due to the large amount of fringing * that

*Fringing is an effect caused by the thinned CCD acting as an interferometer, causing interference patterns to be seen across the image. For more details of fringing within SUSI2, see http://www.ls.eso.org/lasilla/Telescopes/NEWNTT/susi/susi_2002.html

the SUSI2 instrument suffers in the I band which would have made real time cluster identification extremely difficult.

The detector was used in the 3×3 binned configuration giving an effective pixel scale of $0.24''$ per pixel. The average seeing at the La Silla site is $0.97''$ and the 25 percentile seeing is $0.70''$, truly exceptional seeing conditions would have been required for the 3×3 binned detector to be under-sampled. Running the detector in this configuration has the advantage that the read-out time for the CCD array is only 9 seconds, allowing more targets to be observed within a single night. The R-band images taken in the first two nights were de-biased and roughly flat-fielded and median combined at the telescope and then examined by eye and those clusters that appeared to be optically rich were selected to be re-observed in the V-band. This optical selection technique is not ideal and the resulting clusters will be biased toward low redshift systems as it is these that appear, visually, to be the most massive. However, problems with the flat-fielding at the telescope prevented this selection being performed in a more systematic manner, as was originally planned (these flat-fielding problems are discussed in section 5.4.2.) For targets identified as being massive galaxy clusters, 3×400 sec V-band images were taken to allow colour selection of cluster members and to allow photometric redshifts to be measured; the observations taken are summarised in Table 5.2.

The R-band exposures taken in night 3 were repeat observations of clearly massive clusters where the seeing was poor, typically in excess of $1.4''$. In total 58 clusters were observed, of which 3 are cross-overs from the MACS Northern survey and are used as a control sample. The efficiency of the observing run was reduced due to two target of opportunity overrides for Gamma Ray Burst 021004. In total, two hours were lost to the TOO which would have meant that 3 three more clusters could have been observed in the R-band on the 5th of October and 3 more observed in the V band on the 7th October.

5.4 Data-reduction

Wherever possible, the data reduction of the SUSI2 imaging data was performed in a standard way and the process was kept in as close a manner as possible to the

Table 5.2: Summary of observations taken with the New Technology Telescope

Date	Passband(s)	Targets observed
5th October 2002	R	27
6th October 2002	R	28
7th October 2002	R&V	15

data-reduction performed on the UH2.2m data which is described in section 2.3. However, the SUSI2 instrument is sufficiently different in that it employs two CCD detectors (identified as ESO CCDs #45 and #46) that there were some significant differences in the way in which the data were handled. Although the instrument has two detectors, the data are read out through a single output and are presented in a single fits file. A schematic of the data structure is shown in Figure 5.2.

When the instrument CCDs are used in the 3x3 binned configuration, each image measures 1428x1365 pixels made up of a prescan (16 columns), active (682 columns) and overscan (16 columns) regions for chip #45 with an identical layout for chip #46. The overscan area for chip #45 combined with the prescan for chip #46 together fill the gap between the two detectors which results in the physical geometry of the two detectors being preserved in the science images.

5.4.1 De-biasing

As with the UH2.2m data, the first stage in the data reduction process is to de-bias the images. As might be expected, the two chips that make up the SUSI2 detector array have different bias levels and so must be de-biased separately. The bias levels of the two chips are illustrated in Figure 5.3.

As Figure 5.3 shows, Chip #45 has a higher bias level (306.4 ± 2.1 ADU) than chip #46 (298.3 ± 2.1 ADU) due to the differing efficiencies of the electronics within, and attached to, each of the two detectors. In order to debias the images, the frame was split into the left and right chips using the IRAF IMCOPY command. Each chip was de-biased separately using CCDPROC, sampling the bias along the overscan region on the right hand side of each chip. The left and right chips were then rejoined using the IMJOIN task to regain the geometrical arrangement of the

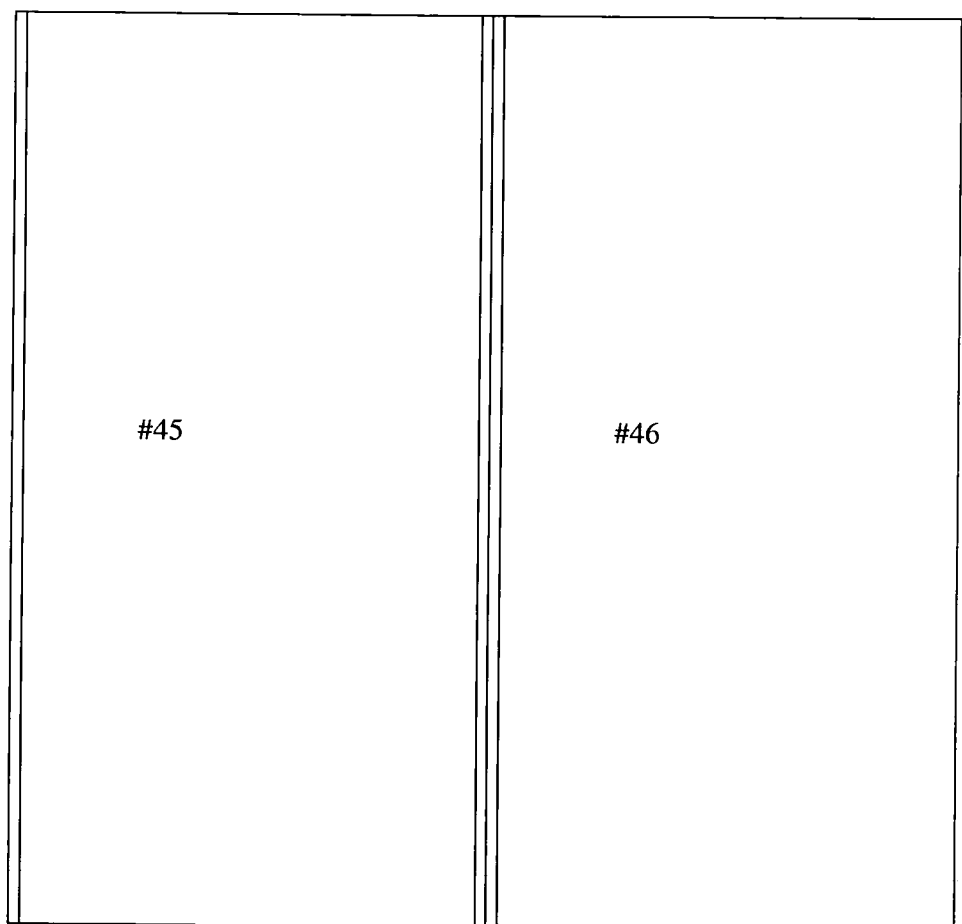


Figure 5.2: Schematic of data of NTT/SUSI2 data structure in 3x3 binned configuration. Chip #45 (left) with 16 prescan, 682 active and 16 overscan columns. Chip #46 (right) has identical geometry. The overscan region of chip #45 added to the prescan region of chip #46 combine to fill out the 8 arcsec gap between the detectors, maintaining the physical geometry of the science areas.

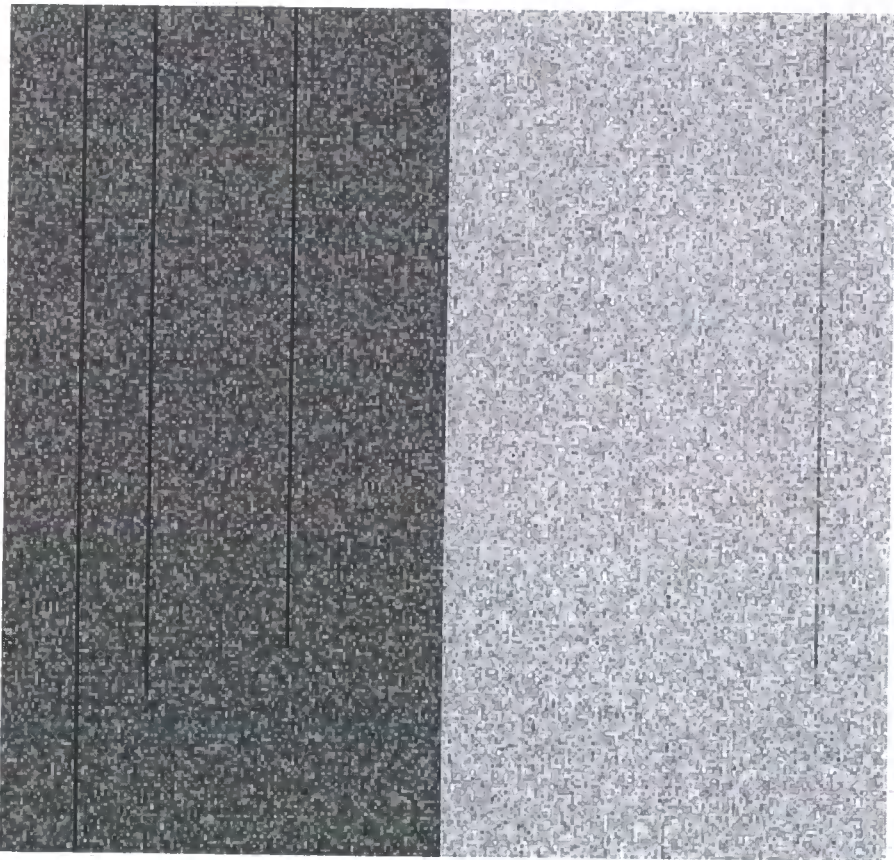


Figure 5.3: ONTT.2002-10-06T09:42:55.074, a bias frame taken in the morning of the 6th October 2002. Chip #45 (left) can be seen to have a higher bias level than chip #46 (right)

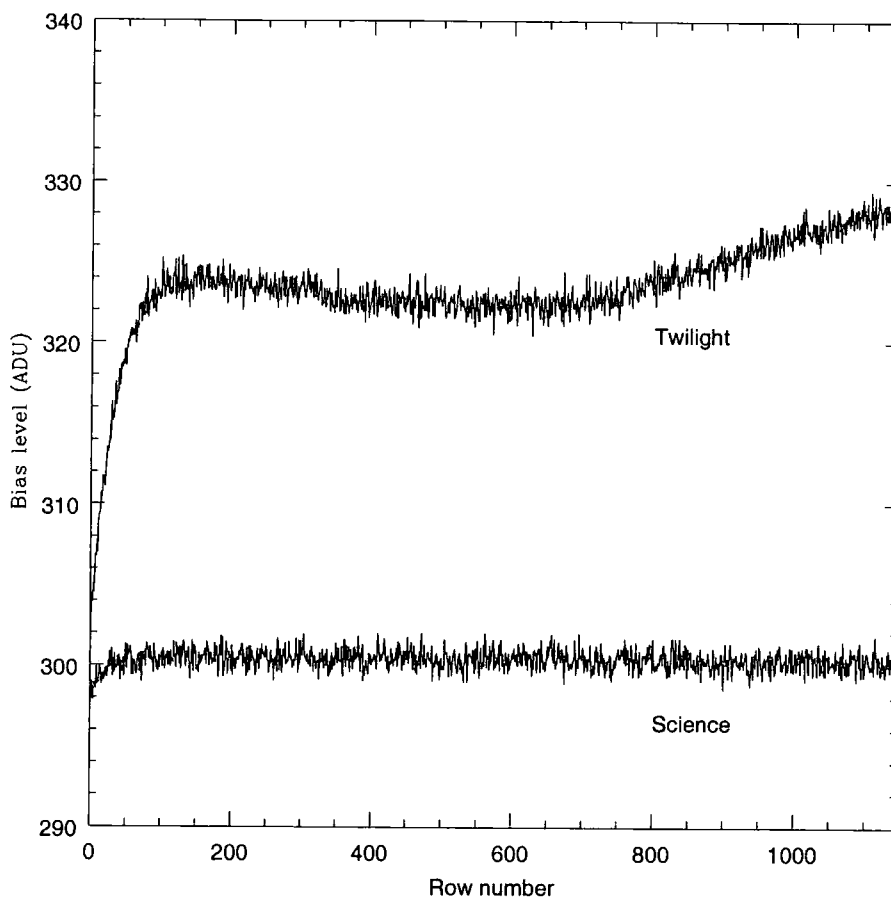


Figure 5.4: Bias structure in ONTT.2002-10-06T23:13:47.815, as measured along the overscan region of CCD #45, a twilight flat field and ONTT.2002-10-07T00:58:03.572, one dither pointing in the observation of J195642.5-431515.

detectors.

5.4.2 Flat-fielding

The next stage in the reduction process is to flat-field the images. A series of flat-fields were taken in twilight to be used in the reduction of the data. During the reduction, while combining the individual flat-field frames together, it was discovered that the flat-field frames have a different bias structure to the science frames, as shown in Figure 5.4.

It can be seen from this figure that the bias structure in the twilight flat is substantially different from that in the science frame in both overall value, the

twilight frame has a much higher level, and in structure; the science frame has a flat bias structure whereas the twilight frame shows considerable structure. The origin of this difference is not known. With such a difference in bias structure, the flat-fields produced by combining the twilight exposures do not produce a flat-field frame suitable for reducing the data, systematic residuals remained in the science frames. It was this that prevented the data from being reduced in real time at the telescope and prevented the selection of high-redshift candidate clusters for second colour imaging. It was clear during the initial data-reduction performed at the telescope that the images were not being correctly flat-fielded and that the derived photometry could not be trusted.

Instead, the science images were flat-fielded using the super-flat technique in which the science frames themselves are used to create the flat-field. The super-flat technique relies on each science field being observed in a series of dithered exposures in which the size of the dither should be at least twice as large as the largest object in the field and that the field is not crowded. If these conditions are met then, in a sufficiently large number of exposures, any given pixel will be off source in the majority of the frames. Consequently, median combining a large number of exposures will produce a suitable flat field. All of the science frames for an individual night were combined using the IMCOMBINE task to produce the super-flat for that night and individual science frames were flat-fielded using the CCDPROC task. The flat-fielding process involves dividing the science frames by the normalised (to unity) flat-field, the normalisation being handled internally by the CCDPROC task. Although it has been shown that the two chips of the SUSI2 detector have different responses, the frames were normalised together (unlike the de-biasing process where they were done separately.) This results in the differing response being factored into the flat-field normalisation and so being divided out of the science frames.

5.4.3 Image combination

The fact that the SUSI2 instrument detector is made up of two chips results in special attention needing to be paid to the way in which the dither pointings are

combined to produce the final science frame. In particular, care must be taken to deal correctly with the gap between the chips. Initially, IMCOPY was used to copy the section of the frame containing the science and overscan of the left chip and the prescan and science area of the right chip, effectively trimming away the prescan region of chip #45 and the overscan region of chip #46. The IMREPLACE task was then used to set the pixel values in the remaining over/pre scan regions (the gap) to '-1'. The images were then aligned using the IMALIGN task and median combined using the IMCOMBINE command with the LTHRESHOLD parameter set to be '0'. Having set the value of the chip gaps to be below this threshold, these pixels are disregarded when the images are combined, resulting in only the other two pointings of the dither pattern being combined over the gap region. As the frames were median combined, any object detected within these regions will have the correct pixel values, but these regions of the science frames will have different noise characteristics to the rest of the image, as these parts of the frame effectively only have two thirds of the exposure time.

With the exception of the flat-fielding, de-biasing and accounting for the gap between the chips, the data were reduced as described in chapter 2. Photometric calibration was performed from a series of Landolt standards observed and object detection was performed using the SExtractor programme using the same seeing measuring parameters and, in the case of the multi-colour imaging, seeing matching.

5.4.4 Scattered light

When the basic data reduction was completed, many of the science frames still showed large scale features, which at first inspection appear to be errors in the flat-fielding. However, these features are seen to change on timescales that are much shorter than would be expected for flat-fielding errors which leads to the conclusion that these fields are subject to scattered light from an unknown source within the SUSI2 instrument.

Figure 5.5 shows the de-biased, flat-fielded, median-combined R-band images of J003704.1-713821 and J033252.2-845256. These images have been cut at the 90% level to enhance the background level. The apparent background level can

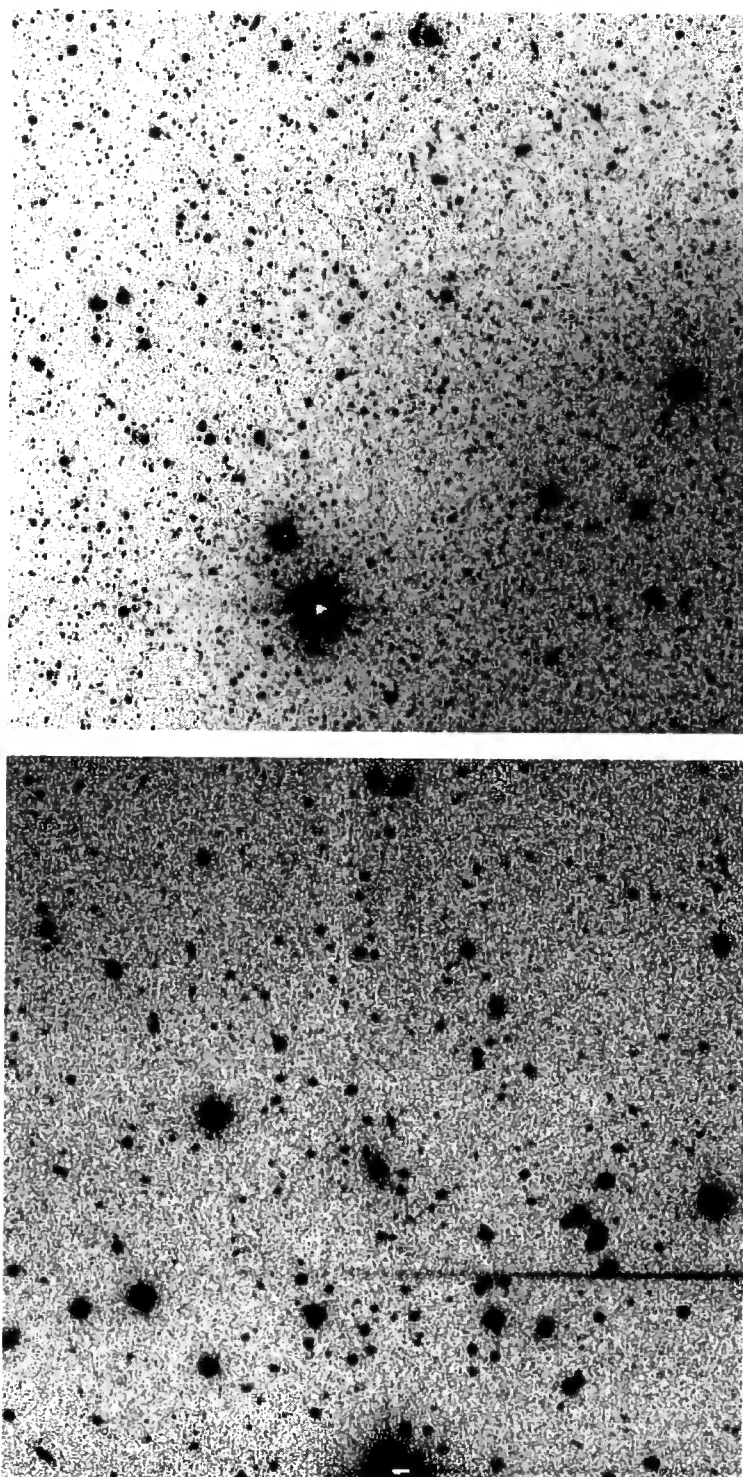


Figure 5.5: 3x240 second R-band images taken consecutively of J003704.1-713821 (top) and J033252.2-845256 (lower) clearly showing the variable sky background.

been seen to vary from being high in the lower right hand corner of J003704.1-713821 to being high in the upper left hand corner of J033252.2-845256. In the case of J003704.1-713821, the background level varies from a mean pixel value of 1289 in the top left hand corner (measured in a 100×100 pixel section) to a mean pixel value of 1365 in the lower right hand corner. This corresponds to a 4σ variation in the background across the diagonal. These images were taken consecutively, each being composed of three 240 second exposures which, including readout time and the time taken to slew between targets, results in there only being only 30 minutes separating the beginning of the observation of J003704.1-713821 and the finish of the observation of J033252.2-845256. This is far too short a timescale for significant changes in the CCD response due to thermal or other such effects, especially as these observations were taken in the middle of the night when temperature variations would be expected to be minimal. Flexure in the instrument is unlikely to be responsible as, other than the variation in background, there is no visible degradation in image quality. For J003704.1-713821, the seeing measured from the image is $0.98''$ whereas the Differential Image Monitor (the La Silla automated seeing monitor) reported the seeing to be $0.9''$ at the same time which would seem to suggest that the telescope was operating correctly and that the variation in apparent sky background was not due to misalignments in the optical path.

Consequently, it was concluded that this contamination is due to scattered light from an unknown source entering the instrument. The SUSI2 website (available at <http://www.la.silla.org/lasilla/Telescopes/NEWNTT/susi/susi.html>) makes reference to there being a scattered light problem earlier in the instruments history and that the problem was solved in August 1998 when the encoder was fitted with velvet to keep out parasite light. This observing run appears to show that either the problem of the scattered light was not solved completely, as is suggested by the SUSI2 website, or that the non-reflective coating has begun to fail over time.

The effect of this scattered light was tested using the photometric standards that were taken to establish the photometric calibration of the imaging. These standards were observed twice, once normally and once with the detector carousel rotated by 90 degrees. This results in the same star being detected in a vastly different part of

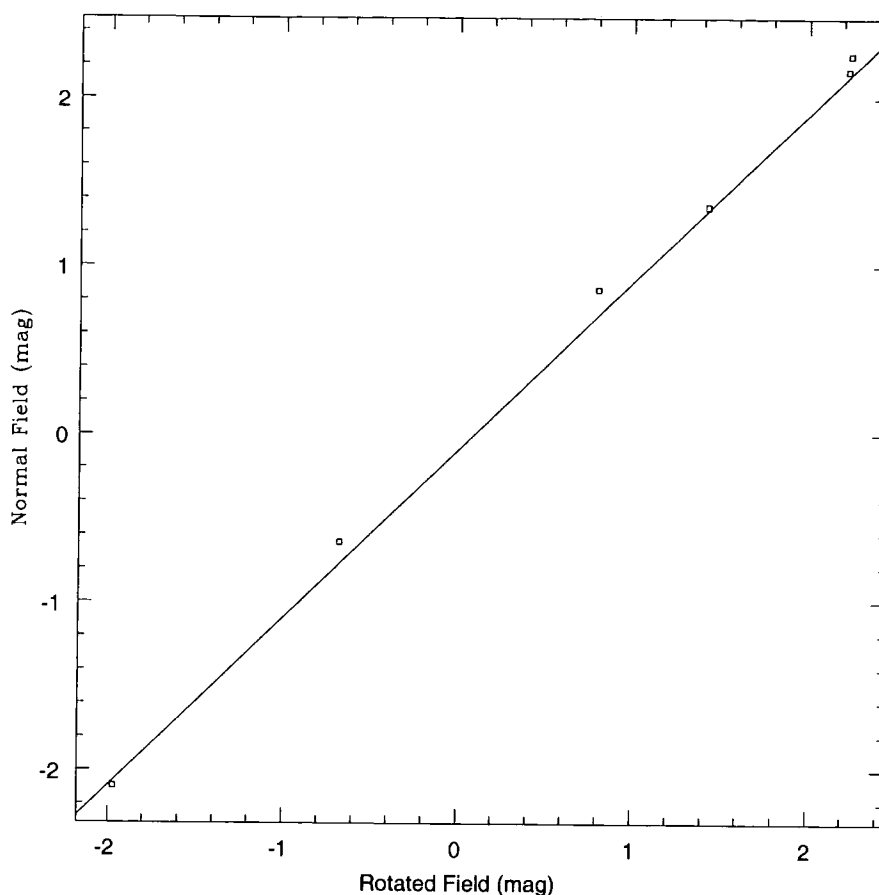


Figure 5.6: The magnitude of the standard stars in Landolt 95 plotted against the same stars detected with the detector carousel rotated by 90 degrees

the chip, originally to ensure that the flat-fielding process was correctly dividing out the different efficiencies of the two chips as described in section 5.4.2. It was hoped that SExtractor would be able to account for the scattered light within its local background fitting. In order to examine this, the observations of rotated standard star fields were examined for evidence of non-random variations in the detected magnitudes.

Figure 5.6 shows the variation in the detected magnitude of the stars in the standard star field Landolt 95. The scatter in the measured magnitude of these standard stars is 0.06 magnitudes which is consistent with these differences being normal random errors on the magnitude measurement. From this it is concluded that the SUSI2 observations are photometric despite the scattered light problem and that the SExtractor local background map successfully accounts for the varying

background levels.

5.5 Cluster Identification

From the work done in the Northern MACS survey, it has been found that a visual examination of the imaging is a suitable way of differentiating between clusters and non-clusters. The X-ray selection technique used ensures that any cluster that is sufficiently massive to be the source of the X-ray emission will be readily visible in the optical imaging. Although this does introduce the possibility of human error, there are several reasons why this has proved to be the best approach. As with any new detection, no redshift information is available and so no assumptions about the expected projected size of any cluster can be made. Similarly, it is hard to differentiate between a small group of galaxies at low redshift from the most massive ellipticals in the core of cluster at high redshift. Additionally, the positional uncertainty in the ROSAT positions results in there being no guarantee that any target cluster will appear in the centre of the image of that field. With these uncertainties, developing automated methods for the pattern recognition required is extremely difficult, whereas the human eye is extremely proficient in this. Figure 5.7 shows an example of this process. These two ROSAT sources have similar X-ray fluxes, $1.93 \times 10^{-12} \text{erg cm}^{-2}$ for RXSJ201127.9-572507 and $1.92 \times 10^{-12} \text{erg cm}^{-2}$ for RXSJ211822.1-54202 (within the detect cell on the 0.1-2.4 keV band.) RXSJ201127.9-572507 can be clearly seen to have a rich cluster near the centre of the image whereas RXSJ211822.1-542026 shows no such excess of galaxies. The identification of the X-ray source RXSJ211822.1-542026 remains unclear, although from this image, it would appear that a background quasar is the most likely explanation. The image of RXSJ211822.1-542026 also shows another example of the scattered light problem prevalent within the imaging, this time appearing as an irregularly shaped object rather than as a variation in the background levels. Due to their irregular shape, such features are assigned a high FLAGS value by SExtractor and so are readily excluded. In order to help the selection process, the results of the star-galaxy separation were overlaid on the image of each cluster candidate to ensure that the selection was not confused by the presence of foreground stars.

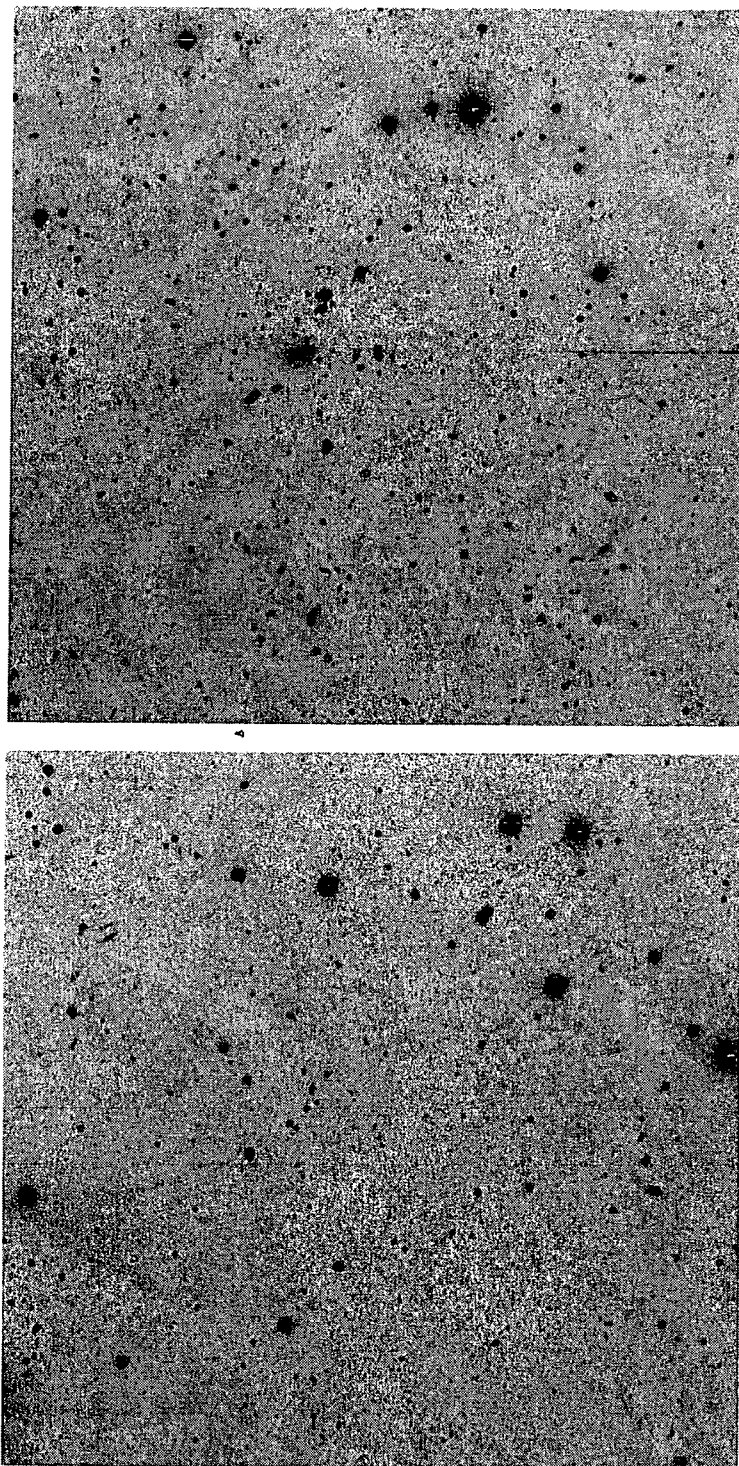


Figure 5.7: 3x240 second R-band images taken with SUSI2 showing RXSJ201127.9-572507 (top) which is clearly a massive galaxy cluster and RXSJ211822.1-542026 (lower) which shows no obvious counterpart for the X-ray emission.

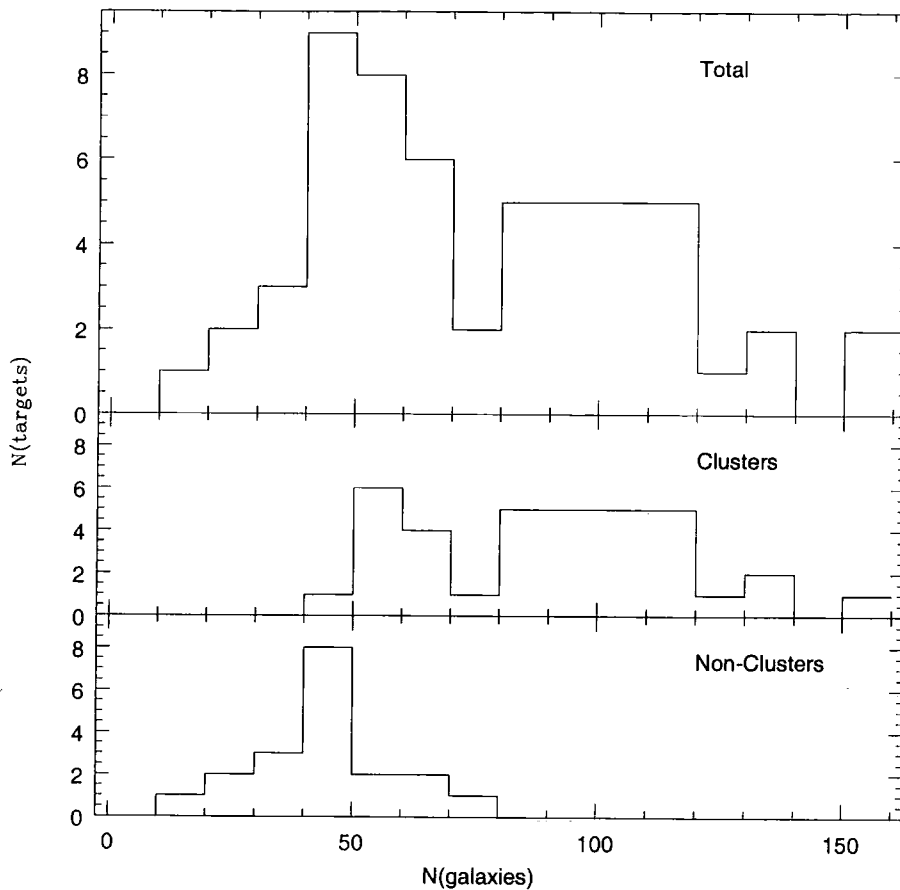


Figure 5.8: Histogram showing (top) the total number of objects selected as being a galaxy within a 2 arcmin aperture in the 3x240sec SUSI2 exposures. This can be broken down into those objects classified as being a cluster (middle) or not (bottom).

This became extremely important as several of the candidate fields lay at relatively low galactic latitude and the correct identification of the cluster galaxies would otherwise have been almost impossible.

In order to test that the selection of cluster candidates was satisfactory, the number of galaxies within 2arcmin of the apparent centre of the cluster was used to confirm that the visual inspection of the images wasn't missing any clusters. For those not classified as being a cluster, all galaxies within 2arcmin of the centre of image were used. The results are shown in figure 5.8 which shows the total number of galaxies detected within the aperture for all frames, those classified as containing clusters, and those not.

It can be seen that, to the depth of this imaging, there are no non-cluster fields

that contain more than 80 galaxies and only 3 non-cluster fields that contain more than 50 galaxies. There are no cluster fields that contain less than 45 galaxies and only 12 cluster fields contain less than 80 galaxies. Of these, 4 are apparently nearby systems and a further 5 appear to be distant.

5.6 Photometric Redshifts

For each of the identified clusters, an attempt was made to estimate the redshift of the cluster using photometric means. For all clusters, a redshift was estimated using the aperture magnitude of the brightest cluster galaxy and for those with two colour imaging, a fit to the colour-magnitude red sequence was made. The results of the cluster identification and the redshift estimation are shown in table 5.3 at the end of this chapter.

5.6.1 Brightest Cluster Galaxy

A classic observation of clusters is that the brightest cluster galaxy (the BCG) is seen to vary little within a fixed metric aperture (e.g. Sandage 1972a,b) and as such are suitable for use as standard candles for estimating redshifts. As was shown in section 4.4.1 for the Northern MACS sample, a 5" diameter aperture, although not a fixed metric, is still a suitable aperture for such a study. For each cluster candidate the 5" aperture magnitude was extracted, extinction corrected and compared against the results gained for the Northern MACS clusters shown in figure 4.3. With, for the most part, only a single image; the identification of the brightest cluster galaxy is slightly more difficult than with multi-colour imaging and associated colour selection. The identification of the brightest cluster galaxy was performed by eye as part of the cluster identification process and in 80% of cases, there is no confusion as to the identity of the BCG. For example in figure 5.7, the cD is unmistakably visible at the centre of the galaxy distribution, close to the X-ray position. However where there were several large galaxies in the centre of a cluster core, the brightest galaxy was chosen even if this object was not the closest to the apparent cluster core. This will bias the estimated redshifts towards

lower values but given the scatter in the apparent magnitude of the objects the effect on the estimated redshift of this selection will be small when compared to the overall error on the estimate.

5.6.2 Colour-Magnitude

For those 15 clusters with two filter colour imaging, a more sophisticated redshift determination technique was used. It has been shown for the Northern MACS clusters that fitting the colour-magnitude sequence and evaluating that fit at an apparent magnitude of $I=19$ can be used as a redshift indicator. For each cluster with R and V band imaging, the cluster sequence was fitted using the same bi-weight fitting routine detailed in section 3.1.2. The colour-magnitude diagrams for the southern clusters are shown in figure 5.9

As was done for the Northern sample, the fit to the cluster sequence was evaluated to give a colour for each cluster. One of the clusters with both R and V band imaging was a control cluster drawn from the Northern MACS survey, MACSJ221457.8-135954. This cluster was used to zero-point the colour-redshift relationship, removing the problem of colour corrections due to the different filter and CCD response between the NTT and UH telescopes. For each cluster, the sequence fit colours were fitted to the King and Ellis predicted colour/redshift relationship (zero-pointed to MACSJ221457.8-135954.) and are shown in figure 5.10

It can be seen from this figure that the predicted V-R colour of an elliptical galaxy is not a monotonically increasing function. This leads to possible uncertainty in the estimated redshift for a given colour. This degeneracy is broken using the magnitude of the brightest cluster galaxy redshift which is used to constrain which region of the colour-redshift space the redshift cluster lies within. The scatter in the fit to the colour-magnitude sequence for the Northern MACS survey shows a scatter about the King & Ellis colours of ± 0.05 magnitudes which corresponds to an error in the redshift measurements of ± 0.03 .

The colour-magnitude based redshift determination was performed without any prior knowledge of the redshift of the cluster, with the obvious exception of the MACS control clusters. A subsequent literature search revealed that two of the

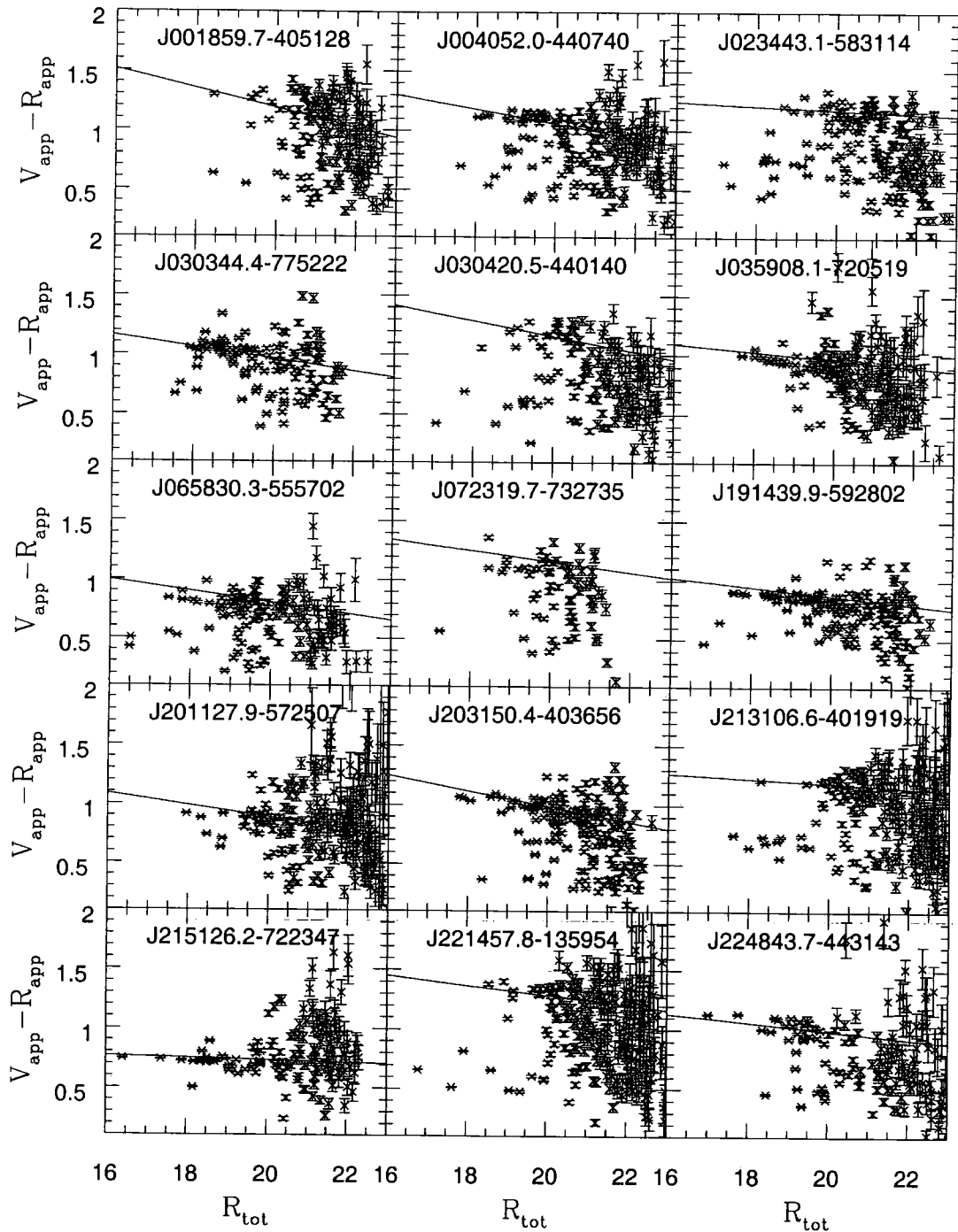


Figure 5.9: Colour-Magnitude diagrams for clusters observed from the NTT. Shown are the aperture colours plotted against total magnitude for all objects classified as being a galaxy.

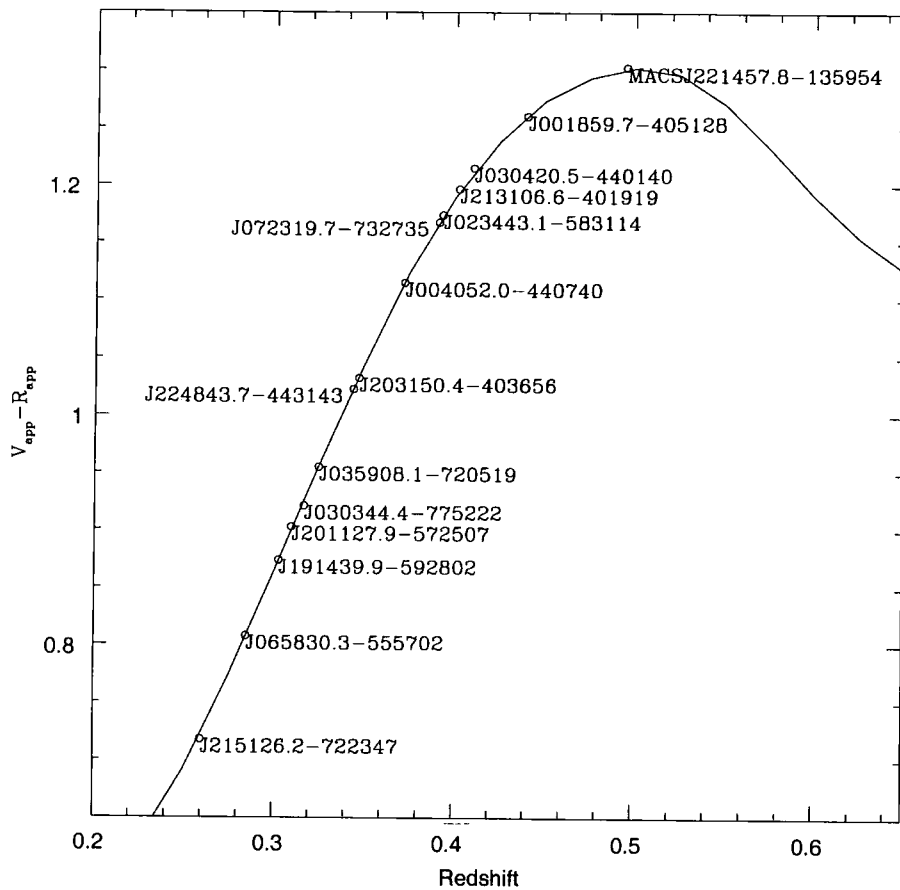


Figure 5.10: The colour of the fit to the cluster colour-magnitude sequence evaluated at 19th magnitude plotted against the estimated redshift for that cluster. Shown also is the King & Ellis colour vs redshift for an elliptical galaxy normalised to MACSJ221457.8-135954.

15 clusters with colour-magnitude based estimated redshift have spectroscopic redshifts. J065830.3-555702 is listed within the NASA Extra-galactic Database (NED) as having a redshift of 0.296 (Tucker et al 1998) based upon 13 redshifts taken at the NTT in December 1993. J224843.7-44314 is the ACO cluster S1063 and is listed in NED as having a redshift of 0.252 (de Grandi et al 1999), which is inconsistent with the colour-magnitude sequence estimated redshift for this cluster of 0.344. For the de Grandi et al redshift to be correct, reference to figure 5.10 shows that the evaluated fit to the colour-magnitude sequence would need to be wrong by 0.35 magnitudes. Given the photometric nature of the observations, this was thought to be highly unlikely. Further investigation shows that the redshift listed in de Grandi et al. is in fact itself an estimated redshift and is attributed to the original cluster paper catalogue by Abell et al. This cluster was known to be part of the REFLEX survey and the estimated redshift was confirmed as the cluster has an unpublished redshift of 0.3465 (Guzzo 2002). The difference in the spectroscopic redshift from the estimated one is 0.011 for J065830.3-555702 and 0.0025 for J224843.7-44314, both well within the error bound of 0.03 suggested by the scatter in the colour-magnitude fit.

5.6.3 Brightest Cluster Galaxy redshift revisited

In order to determine the error on these redshift estimates, the brightest cluster galaxy based estimated redshift was plotted against the colour-magnitude based estimated redshift, shown in figure 5.11.

Included in figure 5.11 are all the clusters with NTT two colour imaging with the addition of the two MACS clusters for which only a single R band was taken. For these two clusters, the BCG based redshift estimate is plotted against the MACS spectroscopic redshift. The mean difference between the BCG and C-M estimate is -0.01 ± 0.04 , which confirms that the brightest cluster galaxies are not as accurate a way of measuring redshifts as they have a large scatter and, as expected, they appear to systematically under-estimate the redshift of a cluster due to either multiple bright galaxies leading to selection errors or foreground galaxy contamination. Figure 5.11 shows particularly clearly the ‘quantisation’ of the BCG

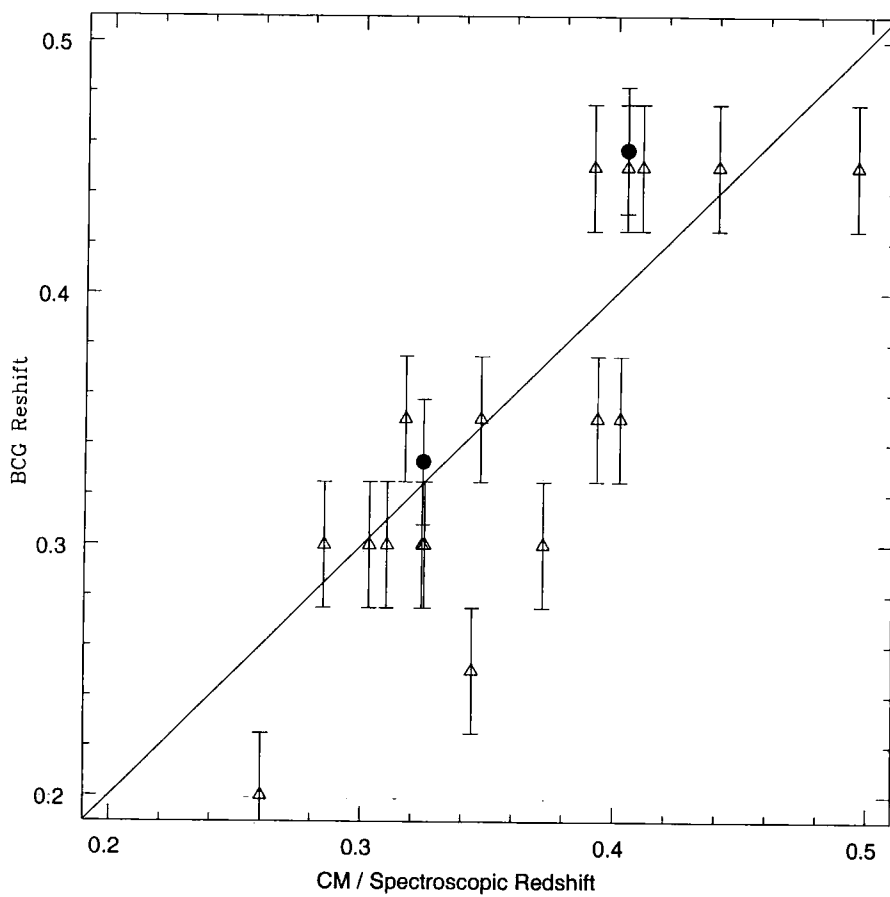


Figure 5.11: The estimated redshift based upon the 5" R-band aperture magnitude of the brightest cluster galaxy plotted against the colour-magnitude fit based estimated redshift (open triangles) or spectroscopic redshift for the two MACS clusters (filled circles.)

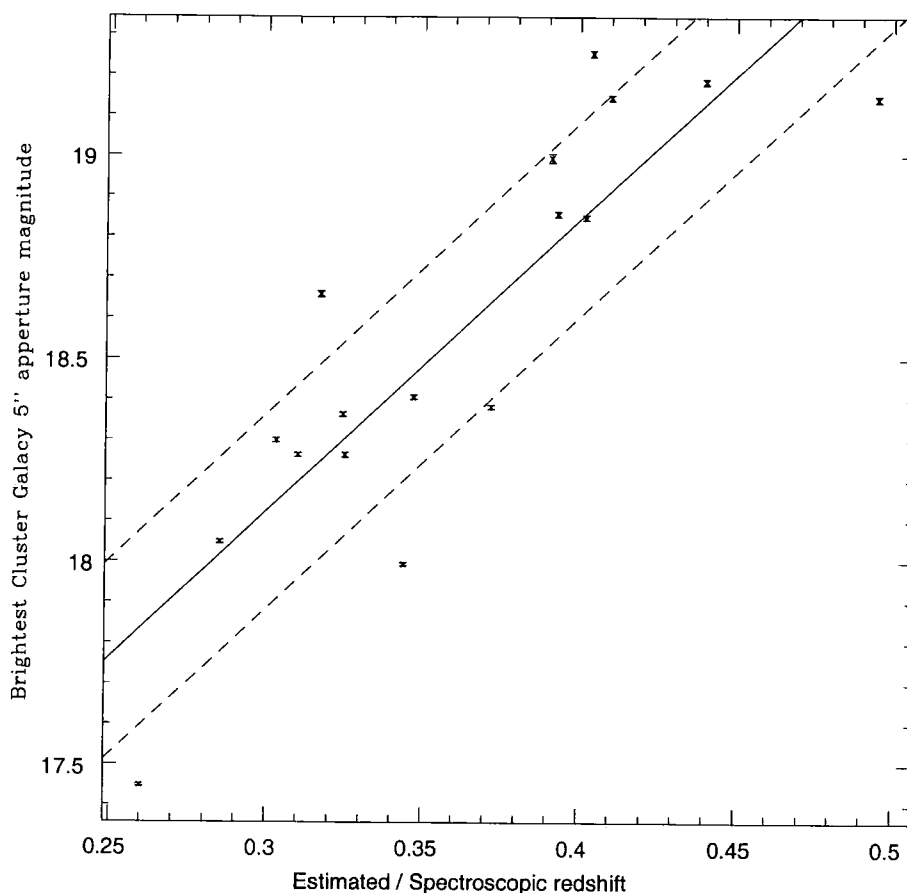


Figure 5.12: The 5 arcsec R-band aperture magnitude of the Brightest Cluster Galaxy redshift against Colour-Magnitude sequence derived redshift

based redshift estimate which came about from these estimates being made with no other redshift information and no indication of the effect of the differing instrument and filters used.

To improve the BCG based redshifts, the magnitude of the brightest cluster galaxy was calibrated against the colour-magnitude based estimate as plotted in figure 5.12 which shows the magnitude of the BCG plotted against CM-based redshift for the 15 clusters with R and V band imaging and the BCG magnitude plotted against the spectroscopic redshift for the two MACS control clusters with only R-band imaging.

Fitting a linear trend to the BCG magnitude / redshift relationship gives a best fit of:

$$z = \frac{M_{BCG} - 16.0}{7.18}$$

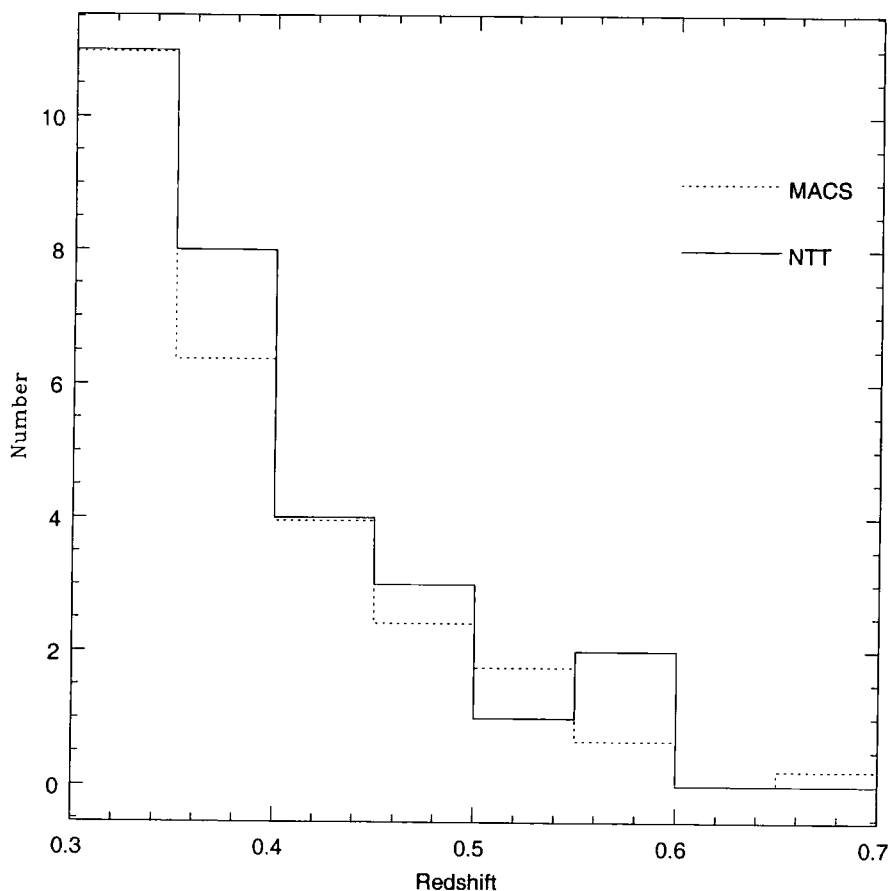


Figure 5.13: The distribution of the estimated (both BCG and C-M based) redshifts of the clusters observed from the NTT. Shown also is the distribution of redshifts of the Northern MACS survey. The distribution of the MACS redshifts has been normalised by the relative geometric area of the two surveys.

with a scatter of 0.24 magnitudes about this relationship which corresponds to an error on the revised BCG based redshift of 0.03. Combining this with the 0.03 scatter found for the Colour-magnitude based redshifts themselves results in a overall error of 0.04. In order to demonstrate that the distribution of estimated redshifts is in agreement with the Northern sample, a comparison of the redshift distribution of the NTT and MACS clusters is shown in figure 5.13 In this figure, the distribution of the MACS clusters has been normalised to the relative area of the two surveys. (the Northern MACS survey extends from declination +80 to -40 and the Southern area covers South of declination -40, giving a factor of 4.556 between the survey areas.) Included in this comparison are all clusters with

revised BCG estimated redshifts > 0.3 or, for those with two filter colour imaging, colour-magnitude based redshift estimate.

It can be seen that the distribution of the redshifts estimated from the colour-magnitude sequence method is in excellent agreement with the distribution of redshifts from the larger survey. Having used the colour-magnitude estimates to correctly calibrate the BCG magnitude-redshift relationship, it is clear that the optical section of rich clusters for V-band imaging has biased the colour-magnitude redshifts towards clusters at low redshift, but there is no apparent overall redshift bias in those clusters originally targeted.

5.7 Summary

In this chapter, the South Pole has been described as an ideal site for observations of the S-Z effect in clusters and detailed the need for a sample of MACS-like (i.e. massive and distant) clusters as a target list for upcoming SZ imaging campaigns at the Viper telescope situated at the South Pole. An observing run to the NTT telescope at La Silla to produce such a target list was undertaken and the specific data-reduction techniques used to reduce this data, in particular the solution to the scattered light and chip-gap problems have been described. The appropriateness of the by-eye cluster identification technique used throughout the MACS project has been demonstrated with an example of how readily this can be done for two fields with similar X-ray luminosity. Two techniques for estimating redshifts for clusters have been described, the first using the aperture magnitude of the brightest cluster galaxy and the second using a bi-weight fit to the colour-magnitude sequence. A simple BCG based magnitude was found to underestimate the redshift with an uncertainty of 0.05 while the Colour-magnitude based magnitudes have been shown to be in very good agreement with previous spectroscopic redshifts with an uncertainty of 0.03. Recalibrating the BCG magnitude-redshift relationship reduces the error on this redshift estimate to 0.04. A full summary of the targets observed at the NTT is shown in table 5.3.

Table 5.3: Summary of targets observed at the NTT showing whether the cluster is classified as being a cluster and the estimated (and spectroscopic where known) redshift.

Target	Passbands	Cluster	Redshift		
			BCG	C-M	Spec
J001453.6-600359	R	N	—	—	
J001859.7-405128	R,V	Y	0.45	0.440	
J002813.6-753732	R	Y	0.357	—	
J003704.1-713821	R	N	—	—	
J004052.0-440740	R,V	Y	0.34	0.372	
J005119.6-705553	R	Y	0.28	—	
J005807.5-460420	R	N	—	—	
J010111.4-420403	R	N	—	—	
J014325.9-450219	R	N	—	—	
J015235.5-285247	R	Y(MACS)	0.46	—	0.404
J021439.0-433319	R	Y	0.56	—	
J021710.7-524432	R	Y	0.31	—	
J023443.1-583114	R,V	Y	0.40	0.393	
J025511.2-612708	R	N	—	—	
J030107.6-470635	R	N	—	—	
J030340.0-563043	R	N	—	—	
J030344.4-775220	R,V	Y	0.37	0.317	
J030420.5-440140	R,V	Y	0.44	0.410	
J032852.3-571552	R	N	—	—	
J033252.2-845256	R	N	0.33	—	
J034448.7-685840	R	N	—	—	
J035908.1-720519	R,V	Y	0.32	0.325	
J040601.5-491601	R	Y	0.25	—	
J041606.1-662851	R	N	0.41	—	
J043647.0-515325	R	N	—	—	
J043913.7-460045	R	Y	0.33	—	

...continued from previous page

Target	Passbands	Cluster	Redshift		
			BCG	C-M	Spec
J050531.2-614456	R	Y	0.33	—	
J052124.2-641851	R	Y	0.07	—	
J054240.9-811557	R	N	—	—	
J054919.1-620509	R	Y	0.36	—	
J060014.8-435351	R	Y	0.26	—	
J065318.4-574515	R	Y	0.33	—	
J065830.3-555702	R,V	Y	0.29	0.285	0.296
J070204.3-544331	R	Y	0.272	—	
J072319.7-732735	R,V	Y	0.42	0.391	
J092544.4-804028	R	Y	0.23	—	
J141158.2-841001	R	N	0.37	—	
J191439.9-592800	R,V	Y	0.32	0.303	
J193610.2-451840	R	Y	0.290	—	
J193811.6-474732	R	N	—	—	
J194422.6-452326	R	Y	0.133	—	
J195642.5-431515	R	Y	0.262	—	
J201127.9-572507	R,V	Y	0.32	0.310	
J203150.4-403656	R,V	Y	0.34	0.347	
J210507.8-493635	R	N	—	—	
J211822.1-542026	R	N	—	—	
J213106.6-401919	R,V	Y	0.40	0.402	
J215126.2-722347	R,V	Y	0.20	0.260	
J220622.6-490921	R	Y	0.56	—	
J221457.8-135954	R,V	Y(MACS)	0.44	0.495	0.501
J222944.5-275538	R	Y(MACS)	0.33	—	0.324
J224843.7-443143	R,V	Y	0.28	0.344	0.346
J225627.0-653320	R	Y	0.47	—	
J230118.9-531705	R	N	0.39	—	

...continued from previous page

Target	Passbands	Cluster	Redshift		
			BCG	C-M	Spec
J233224.3-535840	R	Y	0.39	—	
J233816.5-494353	R	Y	0.20	—	
J234842.8-735746	R	N	—	—	

5.8 Addendum

In October 2003, four of these clusters discovered during this observing run were targeted by Dr Simon Morris and Richard Whitaker (both of the University of Durham) using the LDSS2 instrument on the Magellan II telescope. These clusters were J001859.7-405128, J030420.5-440140, J054919.1-620509 and J070204.3-544331 and were found to be at redshifts of 0.477, 0.461, 0.375 and 0.22 respectively. Combined with the redshifts already obtained and shown in table 5.3, there are 9 of these Southern cluster with spectroscopic redshifts, these redshifts are shown in figure 5.14. With the exception of two clusters for which the estimated redshifts are based upon Brightest Cluster Galaxy aperture magnitudes and as such the ones that are the least reliable, it can be seen that there is an excellent agreement between the estimated and spectroscopic redshifts. The mean difference between the estimated and spectroscopic redshift based upon these 9 clusters is extremely small (-0.0009) with a RMS deviation of 0.033, entirely consistent with the error of 0.04 claimed for the BCG based estimates and the error of 0.03 claimed for the colour-magnitude based estimate.

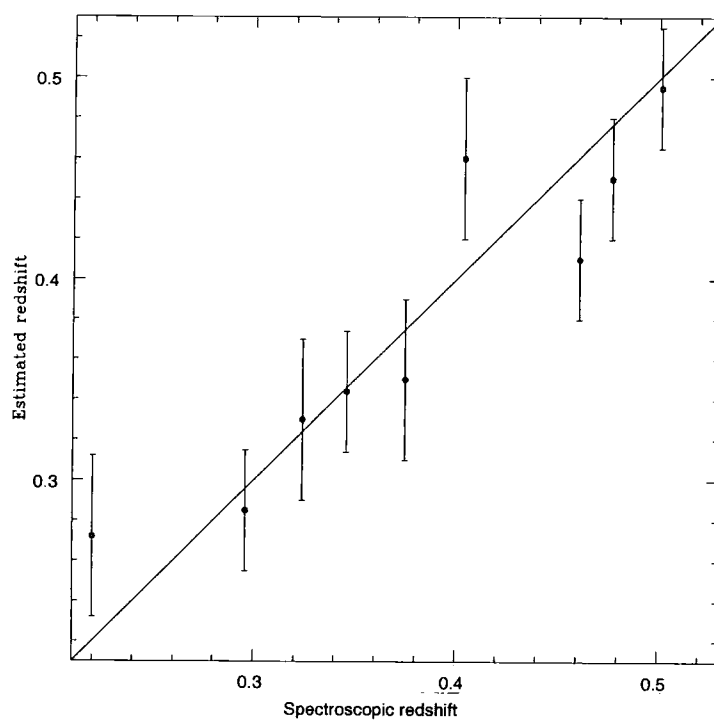


Figure 5.14: Estimated redshift plotted against spectroscopic redshift for the 9 Southern clusters with spectroscopic redshifts. The solid line marks the one to one relationship.

Chapter 6

MACS Spectroscopy and Data Reduction

6.1 Introduction

As has been shown in the preceding chapters, much information can be gathered from studying just images of galaxy clusters. However, observing clusters in this way only looks at a two dimensional projection of the galaxy distribution, all information, except a small amount that can be obtained using photometric redshifts, from along the line of sight is lost. In order to recover this third dimensional information, spectroscopy is used to obtain, primarily, the distance to an object through the measurement of its redshift. Spectroscopy is a vital ingredient in any cluster survey and the MACS survey is no different as spectroscopy is the only reliable way of making the true identification of cluster member galaxies via their concordant redshifts, it can also reveal important clues as to the star-formation history and properties of galaxies through their spectra. In particular through the presence of emission lines, most notably in the case of elliptical galaxies, the dominant population in the cores of massive clusters, the [OII] emission feature, arising from a 'forbidden' electron transition in singly ionised Oxygen, which is a commonly used indicator of on-going star formation.

The members of the MACS team have been performing a comprehensive spectroscopic follow-up program using spectrographs mounted on the UH2.2m, CFH, Gemini North and Keck telescopes, all located at the Mauna Kea observatory in Hawaii. In this chapter, the details of the spectroscopic observations of two clusters MACSJ1720.2+3536 and MACSJ1731.6+2252 made using the GMOS instrument mounted on the Gemini North telescope are given along with the details of the asso-

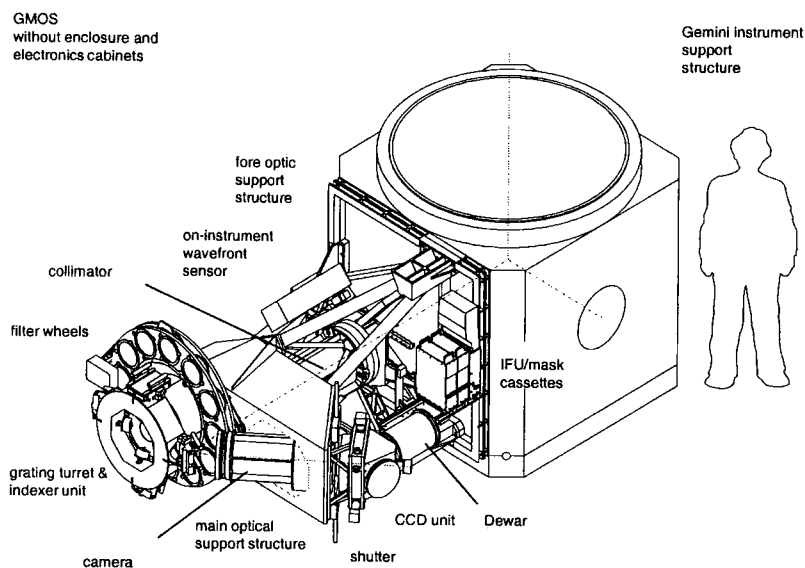


Figure 6.1: Schematic of the layout of the Gemini Multi-object spectrograph without its enclosure and electronics cabinets. Taken from the Durham University Astronomical Instrumentation groups GMOS website (<http://star-www.dur.ac.uk/~jra/gmos.html>)

ciated data-reduction process and the method by which the redshift determinations were made. Redshifts of galaxies in other clusters taken using the LRIS instrument mounted on the Keck-I telescope are used to construct colour-magnitude diagrams of spectroscopically selected cluster galaxies and compared with the results obtained from their purely photometric equivalents.

6.2 The Gemini Multi-Object Spectrograph

The first of the Gemini Multi-Object Spectrographs (GMOS, Hook et al. 2002)* was delivered to the Gemini North telescope in December 2000 and has been available for use by the general scientific community since the 2001B semester, an outline of the instrument is shown in figure 6.1. There is a second, almost identical, GMOS entering operation on the Gemini South telescope, located at Cerro Pachón in the

*The GMOS spectrograph is described in more detail on the Gemini observatory website <http://gemini.ast.cam.ac.uk//sciops/instruments/gmos/gmosIndex.html>

Chilean Andes. However, this instrument and telescope have not been used for any part of the MACS program and so this chapter concentrates solely on the GMOS North instrument. Both instruments were designed and built in a collaboration between the United Kingdom (Astronomy Technology Centre at Edinburgh and the University of Durham) and Canada (Dominion Astrophysical Observatory.)

The GMOS instruments will, when fully commissioned, have multiple operating modes; Imaging, Long-slit spectroscopy, Multi-object spectroscopy, Integral Field Spectroscopy and Polarimetry, of which all but the Polarimetry have been commissioned on the GMOS-North instrument. As the aim of the MACS follow-up program has been to determine redshifts for as large a number of cluster galaxies as possible, the instrument was used in multi-object (MOS) mode. The design of GMOS is based upon the one used extremely successfully at the Canada France Hawaii Telescope with their imaging spectrograph. The operation of the MOS mode relies upon accurately cutting a plate containing many slits which is positioned within the entrance aperture of the instrument. Although having to cut masks in advance would seem to be a disadvantage when compared with near real-time dynamically configurable instruments (for example the 2df spectrograph (Lewis et al. 2002) on the Anglo-Australian Telescope) this design allows an extremely high degree of multiplexing allowing, potentially, hundreds of slits on a single mask. These masks are made using a laser drilling machine which is located at the Gemini observatory headquarters in Hilo, Hawaii

The GMOS instrument is designed to match the best free-atmosphere (i.e. without adaptive optics) seeing conditions experienced at the Mauna Kea Observatory (0.25 arcsec FWHM in 10th percentile conditions Davies et al 1997). The instrument employs a detector array of three EEV CCDs, each consisting of 2048×4068 pixels which are arranged in a row with ~ 0.5 mm gaps between them. A summary of the GMOS detector array characteristics is given in table 6.1. The three EEV CCDs (identified as EEV 9273-16-03, EEV 9273-20-04 & EEV 9273-20-03) have $13.5\mu\text{m}$ pixels which results in a pixel scale of 0.072 arcsec per pixel when the instrument is used in imaging mode. The optical design is such that the instrument can operate from 0.36 to $1.10\mu\text{m}$ although the GMOS North instrument has been optimised for the red end of this optical range.

Table 6.1: Summary of the characteristics of the GMOS North detector array

GMOS North	
Detector	3 EEV 2048 × 4068 chips
Array layout	Chips in a row with ~5mm gaps (Resultant pixel format is 6144 × 4608)
Pixel Size	13.5 μ m square
Pixel Scale	0.072 arcsec/pixel
Field of View	5.5 x 5.5 arcmin

For use in imaging, both for direct astronomical imaging and for MOS pre-imaging (see section 6.3.2), GMOS is fitted with a set of u',g',r',i' and z' filters which are similar to the Sloan Digital Sky Survey filter set, the response of which are shown in the upper panel of figure 6.2 along with the transmission properties of the telescope optics. A full description of the SDSS photometric system is presented in Fukugita et al. 1996. Similarly, for spectroscopy, GMOS is fitted with a set of gratings, the transmission curves of which are shown along with the response curve of the EEV CCD detectors in the lower panel of figure 6.2. A more detailed breakdown of the GMOS filter characteristics is available from the GMOS filters web-page:

(<http://gemini.ast.cam.ac.uk/sciops/instruments/gmos/gmosGratings.html>).

6.3 MACS Spectroscopy

Following the identification of a target field as being one that contains a cluster, it is a naturally following question to ask how big that cluster is. Although mass measurements can be made using optical richnesses and X-ray temperatures, one of the commonly used measure of cluster richness is that of the clusters velocity dispersion, a direct indicator of the size of the clusters gravitational potential. Additionally, despite being an X-ray selected survey, the primary cluster identifications of the MACS clusters have been performed using, in the first instance, single band optical images of the cluster fields. Although this has been shown to be an extremely

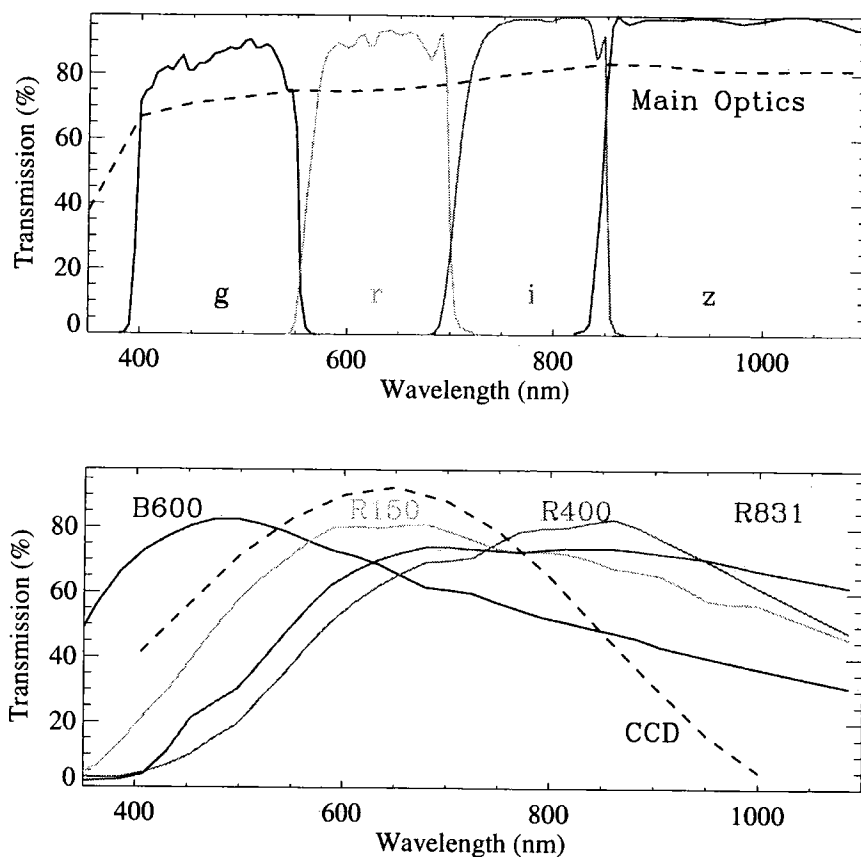


Figure 6.2: The transmission curves of (top) the available optical filters showing also the optical transmission of the telescope main optics and (lower) the transmission curves of the GMOS dispersion gratings showing also the spectral response of the EEV CCD detectors.

efficient way of performing the cluster identification process, it leaves the MACS survey vulnerable to confusion caused by line of sight projection effects that are an inherent source of contamination in any optical survey. Additionally, measuring the redshift of an object is the only currently available way of directly determining the distance to an object and so, as one of the fundamental survey goals was to produce a catalogue of clusters at $z > 0.3$, it is clearly imperative that redshifts be obtained for as many MACS clusters as possible.

As part of the initial MACS cluster identification, low dispersion long-slit spectra were taken using the Wide field Grism spectrograph at the UH 2.2m telescope, of the central galaxy and other potential cluster galaxies that can be simultaneously targeted by appropriately orientating the spectrograph longslit. This was done to establish the redshift of the cluster. However, a small number redshifts are insufficient to determine whether the cluster is sufficiently large to account for the observed X-ray emission. For this, multiple redshifts are required to enable the velocity dispersion of the cluster to be measured, a direct indicator of the mass of a cluster. In order to enable this study, a spectroscopic follow-up campaign has been undertaken using the CFHT Multi-object spectrograph (Le Fevre et al. 1994) and the Low Resolution Imaging Spectrograph (LRIS, Oke et al. 1994) and is being analysed by Elizabeth Barret of the Institute for Astronomy, part of the University of Hawaii. The aim of this campaign has not been to compile a complete sample of cluster galaxy redshifts, in either volume or magnitude range rather, the strategy of this campaign has been to obtain the maximum number of redshifts possible which leads to the selection of targets being dominated by the geometrical effects of placing slits onto the masks.

As part of the initial commissioning of GMOS, a successful application was made to the Gemini time allocation committee for semester 2002A to study four MACS clusters (MACS1720.2+3536 and MACS1731.6+2252, both at redshift 0.39; MACS1149.5+2223 and MACS1423.8+2401 both at redshift 0.54) as part of a project headed by Roger Davies (formally of the University of Durham, now at the University of Oxford) to age-date galaxies from key spectral features (eg. $Mg\beta$ & $H\beta$) using new spectral analysis techniques developed by Worthey 1994 and Vazdekis et al. 2001. Although the specifics of the in-depth analysis of the GMOS

spectra are beyond the scope of this thesis, the details are given here of the reduction of this data, comparable to that performed on the rest of the MACS spectroscopy, i.e. extracting redshifts to measure cluster velocity dispersions.

6.3.1 Object selection

Initial object selection was performed using the UH2.2m multi-colour imaging that has been discussed in great detail in earlier chapters, with the initial target lists being drawn from the object catalogues extracted by SExtractor as part of the data reduction process (c.f. section 2.7.) Initially, star-galaxy separation was performed according to the prescription described in section 2.8 i.e. objects were rejected as being stars if they have $PSTAR > 0.9$ in any of the V, R or I band and then galaxies are selected by progressively selecting objects with $PSTAR < 0.1$ in the I, R and V bands.

Having separated the galaxies from the stars, objects were colour-selected for spectroscopic follow-up. For each of the target clusters, colour-magnitude diagrams containing all the galaxies were generated and then galaxies lying on the cluster red-sequence were selected. Figure 6.3 shows an example of this process for the cluster MACSJ1731.6+2252. This figure shows the $R_{app} - I_{app}$ colour-magnitude diagram for this cluster. The bi-weight fit was made to the red cluster sequence (shown by the solid line in figure 6.3, c.f. section 3.1.2) and then objects were selected if they have a colour within 0.1 magnitudes of this fit (the bounds of this region are shown by the dotted lines in figure 6.3.) This process was repeated for the $V_{app} - I_{app}$ and $V_{app} - R_{app}$ with tolerances of 0.2 and 0.15 magnitudes respectively although the number of objects rejected by using multiple colours is low ($\sim 5\%$.) Having generated the initial target list in this way, the positions of these objects were extracted from the astrometrical solution derived in section 2.9 by fitting the positions of bright stars in these frames to the corresponding positions in the APM catalogue.

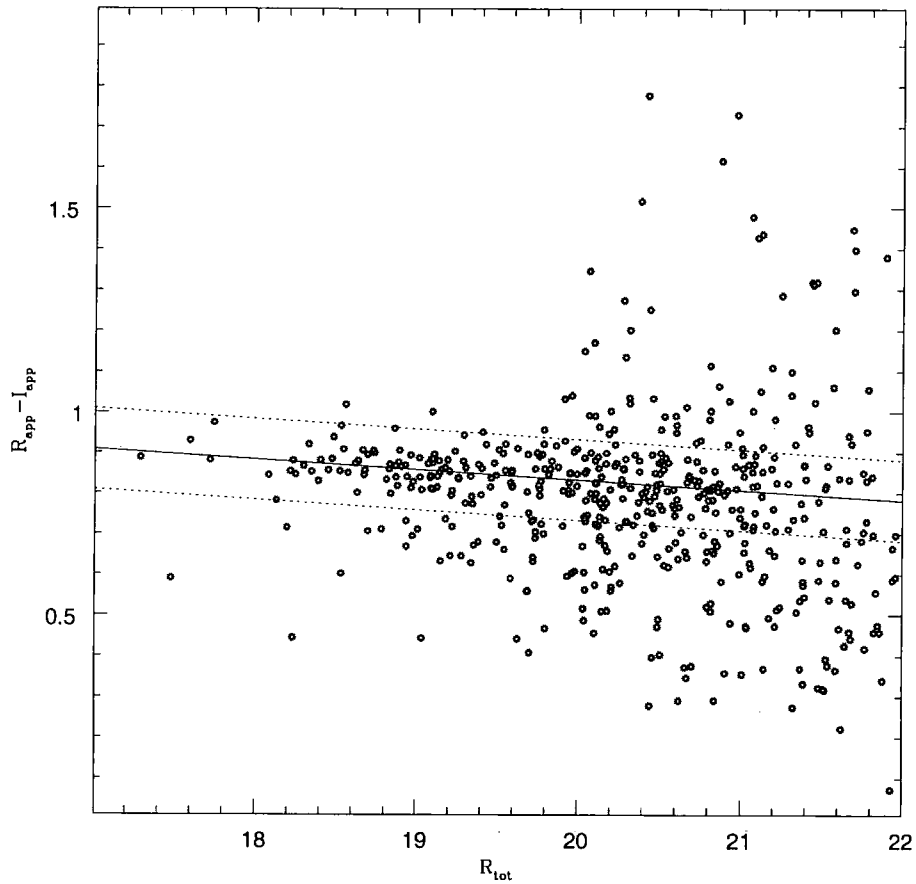


Figure 6.3: $R_{app} - I_{app}$ against I_{tot} colour-magnitude diagram of galaxies in the UH 2.2m imaging of MACSJ1731.6+2252 used to colour select targets for spectroscopic follow-up. The solid line shows the best-fit to the cluster red-sequence and the dotted lines mark the boundaries of the region within which galaxies were selected.

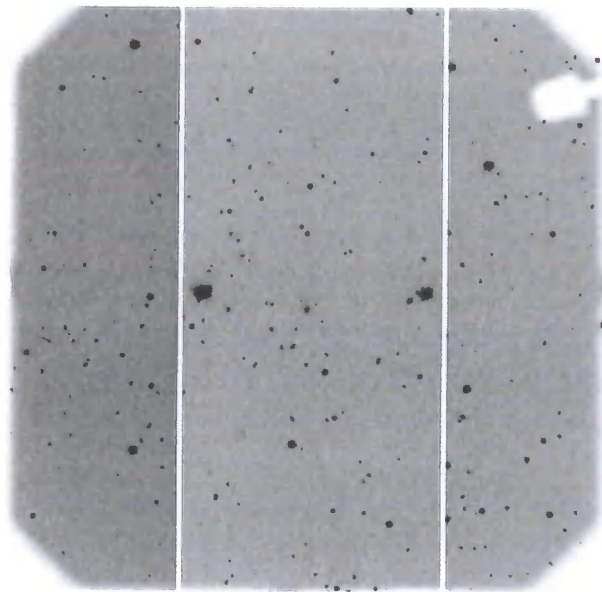


Figure 6.4: The pre-imaging exposure N20020308S0205, one of the pointings in the observation of MACS1720.2+3536. The layout of the three chips is obvious as well as the shadow of the On-instrument Wavefront Sensor.

6.3.2 Pre-imaging and mask design

In order to generate the final object mask, the Gemini observatory operates a system for GMOS similar to that employed at the CFHT in which mask slits are positioned based upon prior imaging of the science field using the instruments direct imaging mode. Figure 6.4 shows an example of such pre-imaging, the Gemini North image number N20020308S0205, one of three 180 second exposures taken using the r band filter as pre-imaging for the observation of the cluster MACS1720.2+3536 on the night of the 8th March 2002. This image shows the three chip layout and the 5.5 arcmin square field of view. It also shows clearly how the two flanking chips are not completely illuminated when the telescope is used in imaging mode and also the shadow of the On-Instrument Wavefront Sensor (OIWFS.) The OIWFS consists of a 2×2 lenslet array on a movable arm that samples the light from a suitably bright guide star. The signal from the OIWFS is fed to the telescope

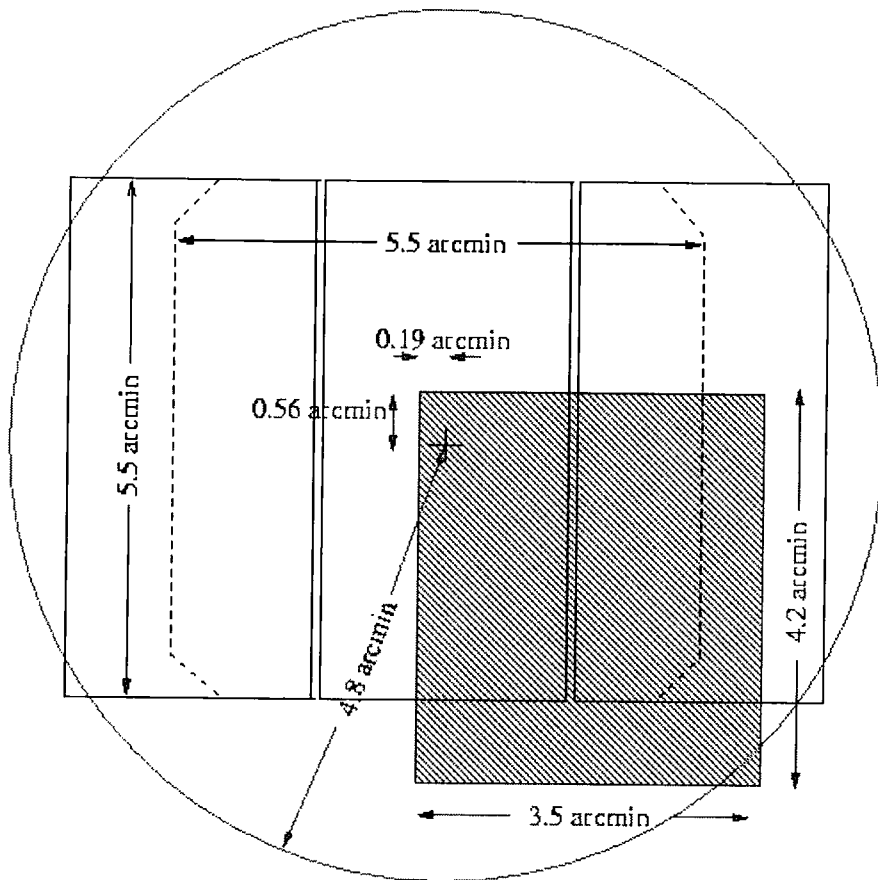


Figure 6.5: Schematic diagram of the patrol area of the OIWFS relative to the GMOS CCD detectors, the dashed lines mark the limits of the imaging field. The OIWFS cannot be used more than 4.8 arcmin from the centre of the imaging field. (diagram taken from <http://www.gemini.edu/sciops/instruments/gmos/gmosOIWFS.html>)

secondary mirror control to allow fast tip-tilt guiding. The OIWFS has a fixed patrol area which is shown in figure 6.5. Clearly, if allowed to, the OIWFS can obscure a large proportion of the science area of the GMOS detector array. In order to minimise this, the UH2.2metre imaging was used to select a guide star and instrument position angle to minimise this occultation. As can be seen from figure 6.4 the effect of OIWFS has been restricted to a limited region in the corner of the instruments field of view.

Following the pre-imaging, the final mask design was performed by Alastair Edge using the design software provided by the Gemini observatory for semester 2002A. The mask design tool uses its own internal astrometrical solution that it

Table 6.2: GMOS observation of MACS clusters taken in the 2002A semester

Cluster	Filter	Date	Exposure time
MACSJ1720.2+3536 mask 1	B600	9th July 2002	6×1800 sec
		17th July 2002	2×1800 sec
MACSJ1720.2+3536 mask 2	B600	17th July 2002	7×1800 sec
MACSJ1731.6+2252 mask 1	B600	12th July 2002	4×1800 sec
		13th July 2002	6×1800 sec
MACSJ1731.6+2252 mask 2	B600	4th August 2002	4×1800 sec

generates from the information in the pre-imaging file header and it's own extraction of sources. It then automatically optimises the allocation of slits to maximise the number of objects observed, with a higher priority being given to brighter objects. However, this approach is not ideal for taking spectra of MACS cluster galaxies as they are usually not the brightest objects in the field and consequently, the majority of targets automatically selected by the software were not colour-selected potential cluster galaxies. This situation was remedied by editing the configuration files generated by the GMOS software and cross-correlating objects in the GMOS catalogue with the UH2.2m colour-selected target list. Objects not in the colour-selected target list were then manually de-prioritised ensuring that only colour-selected galaxies were considered by the slit allocation algorithm.

6.3.3 GMOS observations

In total, six object masks were made, two for each of the lower redshift clusters (MACSJ1720.2+3536 and MACSJ1731.6+2252) and one each for the remaining two higher redshift clusters (MACS1149.5+2223 and MACS1423.8+2401) and were submitted to the 2002A semester queue. Of these masks, only the four masks for the lower redshift clusters were observed, as summarised in table 6.2. The observations shown in this table were accompanied by appropriate calibration data in the form of bias frames, flat fields and arc-lamp observations, taken as part of the Gemini observatory standard operating procedures for queue observing. The remainder of this program was not observed by GMOS and has now been removed from the

observing queues.

6.4 Data-reduction

The reduction of the spectroscopic data was performed using a variant of the data reduction scripts provided by Isobel Hook of the United Kingdom Gemini Support Group, at the GMOS data reduction workshop held at the University of Oxford on the 16th-18th September 2002, which uses the GMOS software provided as part of the Gemini IRAF package.

Data from the Gemini observatory are presented in the form of multi-extension fits (MEF) files. These files have four extensions, numbered zero to 3. Extension zero contains the PHU, the primary header unit which contains all of the information traditionally contained in the header of a fits file such as the date and time that the observation was taken, the exposure time and the airmass of the target. Extensions 1 to 3 contain the data from the three CCDs that make up the GMOS detector array, each with its own smaller header unit containing information specific to that detector. Care must be taken with the way in which these data are handled as the way in which the CCD array is read-out differs from chip-to-chip. Each of the CCDs has 2 amplifiers of which only one, the one that has been demonstrated to have the lowest read-out noise, is actually used. For GMOS North, chips 1 and 2 are read out through the right hand amplifier whereas chip 3 is read out through its left hand amplifier. Consequently, the three chips have a different geometry with regards to the location of the overscan region on that chip, this arrangement is shown in figure 6.6. It is highly unlikely that this configuration will be the same for the Southern GMOS instrument as again, the readout amplifiers actually used will be determined by testing for readout noise in the array.

The data-reduction process for spectroscopy shares many of the same basic steps as for imaging data and so, the first stage in the data reduction process is to debias the imaging. As part of the instrument set-up procedure, bias frames are taken each night as part of the queue observing standard operating procedures and it is these that are used to de-bias the data. The GMOS IRAF package contains a utility GBIAS that takes the individual bias frames and combines them to produce

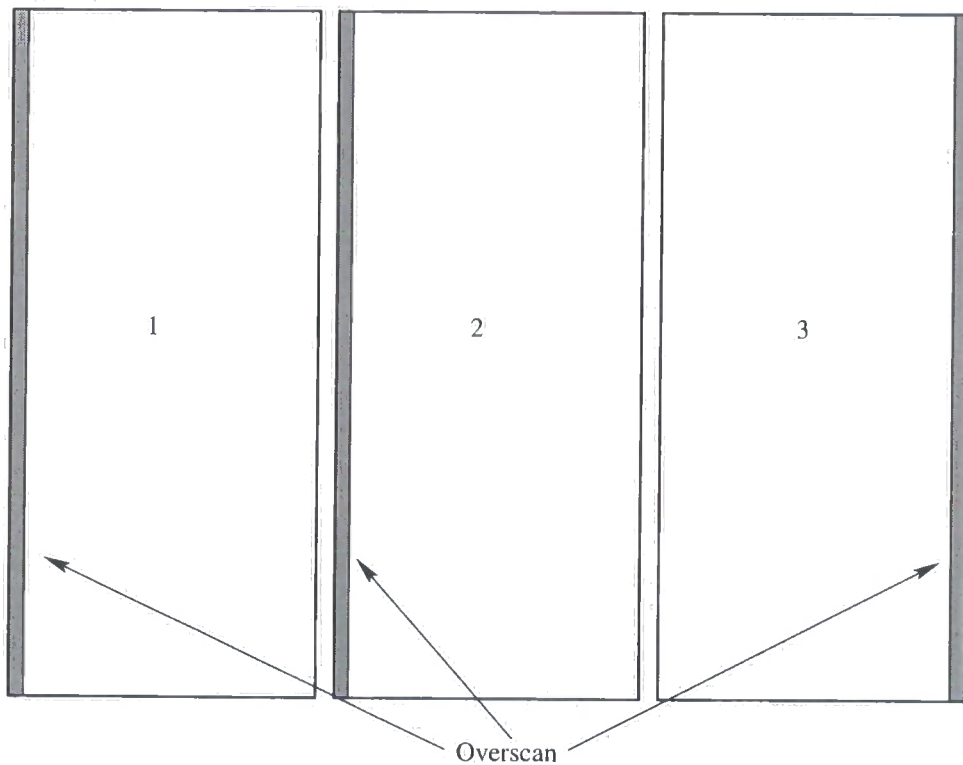


Figure 6.6: Schematic diagram showing the location of the overscan regions in the GMOS-North CCD array. CCD 1 and 2 are readout through the right-hand amplifier and so the overscan is located on the left edge of the image. CCD 3 is read out through the left amplifier and so the overscan region is located on the right.

a suitable averaged bias-frame. In the previous examples of the data-reduction process (c.f. sections 2.3 and 5.4.1), the de-biasing process was performed by fitting the bias level across the overscan region of the chip and then subtracting this from the rest of the frame. However, this approach is not suitable for use with GMOS images as there is significant structure visible in the bias frames, as shown in figure 6.7. It can clearly be seen from this figure that there is structure in each of the three chips and that this structure would not be accounted for by subtracting off a bias level fitted to the overscan region. Consequently, GMOS data must be reduced using full bias frames.

Again, in a similar way to that used for imaging data, the GMOS spectroscopic data must also be flat-fielded. The GMOS IRAF package tool GSFLAT was used to produce a suitable averaged flat-field image by combining several separate flat-field images, removing the bias and normalising the resultant images.

Having produced suitable flat-field and bias frames, the science exposures can now be reduced, using the GSREDUCE task. GSREDUCE first calls GPREPARE, a separate task which formats the raw data, adding information to the fits file headers, to make them ready for the reduction process. The overscan regions are then trimmed off and the bias and flat-field frames are applied to the data. The three chips are then mosaiced using GMOSAIC which combines the three science extensions of the multiple extension fits files into a single image. During this stage a small rotation is applied to the chips to account for the imperfect physical alignment of the CCD detectors, which would otherwise distort the spectra.

Finally, GSREDUCE attempts to cut-out each of the spectra and place each spectrum into its own separate extension of the MEF file. It does this by reading the mask definition file (which contains the location and size of each of the slits on the object mask) and then computes the location and size of each spectrum on the image using the filter and grating information from the fits file header and a configuration file *GMOSgratings.dat*, supplied as part of the GMOS package, that contains the relevant instrument information (eg. the grating resolution.) Unfortunately, whenever the grating is changed within the instrument, the grating cannot be guaranteed to sit in exactly the same place. Although this doesn't have any impact on the quality of the signal being passed to the detector, it does result in the

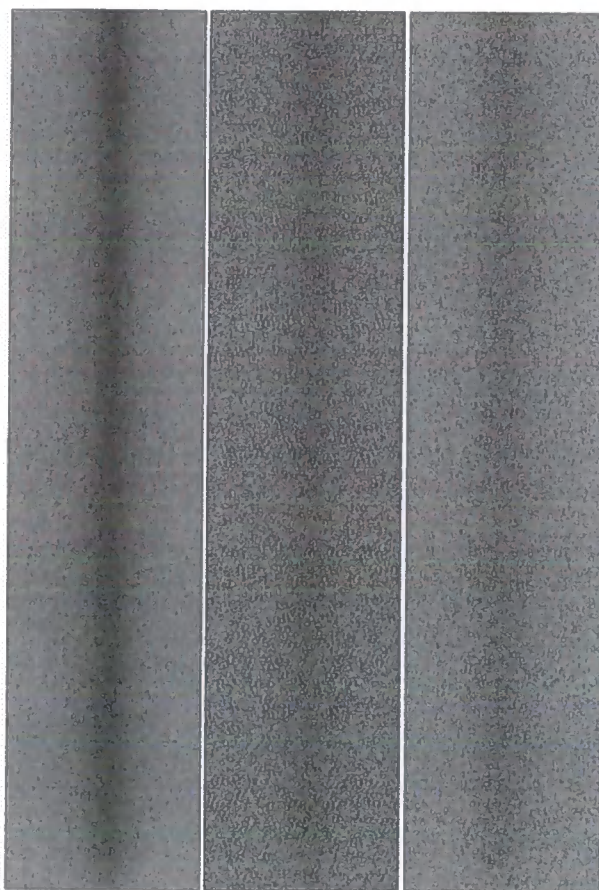


Figure 6.7: A GMOS-North bias frame. Considerable bias structure can be seen running vertically through the centre of each chip.

spectrum apparently moving on the detector array, a translation which GSREDUCE does not automatically compensate for. The immediate consequence of this is that when attempting to clip out the individual spectra, GSREDUCE will, more often than not, incorrectly calculate the position of the spectrum and, in one extreme case during the reduction of the MACS spectroscopy, the position of the spectra were sufficiently translated that GSREDUCE calculated that the gaps between the slits lay directly over the spectra and consequently extracted everything on the images except the spectra. In order to correct for this, the *GMOSgratings.dat* file must be edited by hand to ensure that GSREDUCE correctly extracts the spectra. As these observations were taken during queue rather than classical observing, a separate *GMOSgratings.dat* file is therefore needed for each group of observations.

Having separated the spectra, they are then wavelength calibrated via the observations of the facility CuAr arc lamp. The wavelength calibration is performed several times for each spectrum at intervals across (i.e. perpendicular to the dispersion direction) the individual spectra. This allows a 2D fit to be made to the spectrum and allows the rectification of the spectrum (using the GSTRANSFORM task), removing the curvature introduced by the telescope optics.

At this stage in the data-reduction, the process used for the MACS data diverges from the example scripts provided by the UK Gemini support group. In the example scripts, the individual spectra were extracted, sky-subtracted and then combined. This is an acceptable method for sources bright enough that the individual exposures have a high signal-to-noise ratio. However, for the faintest sources in the MACS exposures, the signal-to-noise was insufficient to allow the accurate extraction of the spectra. Consequently, the spectra were first co-added, sky-subtracted (using GSSKYSUB) and then the spectra extracted using GSEXTRACT.

6.4.1 Redshift determination

Having extracted the spectra in this way, the redshifts of the objects were finally measured using the IRAF task FXCOR. Before this can be done, the spectra must be corrected for both the movement of the Earth in its orbit about the Sun and its rotational velocity, both of which contribute to the line of sight redshift of an object.

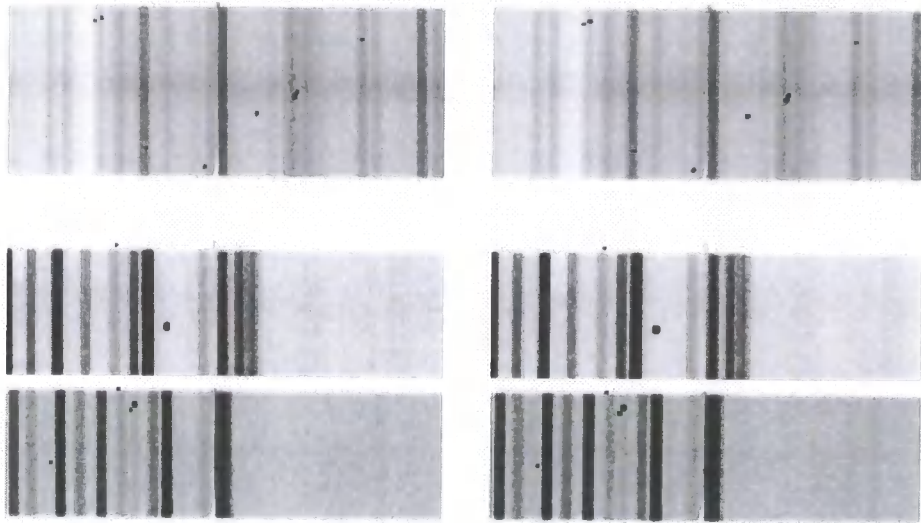


Figure 6.8: Identical regions from the observation of MACSJ1731.6+2252 shown (left) uncorrected spectra showing curvature arising from the telescope optics and (right) the corrected, straightened spectra.

These velocities are corrected for using the `RVCORRECT` task which takes the date and time of the observations from the fits file header and uses the location of the observatory at which the observations were taken (supplied as an input parameter) to calculate a correction to the line of sight velocity which is then written into the fits files headers. This ensures that the measured velocities are in the heliocentric frame of reference, the same frame of reference used for the rest of the MACS spectroscopic follow-up programme.

`FXCOR` determines the redshift of an object by performing a Fourier cross correlation of the object spectra with a number of template spectra and uses the best match to determine the velocity shift of the object relative to the object spectra. The template spectra were provided by Elizabeth Barrett and are the same ones that have been used throughout the MACS spectroscopic campaign. They contain sample spectra for elliptical and spiral galaxies with separate spectra containing strong emission and absorption line features.

The process results in a series of redshift measurements from the matching of the object spectra with each of the template spectra. In order to establish which of these redshift estimates is the most appropriate to use, the Tony and Davis (1979) R value is used as an indicator of the quality of the cross correlation fit, cross-correlations with values of $R_{TD} > 3$ are accepted as being secure redshift determinations. For some galaxies, more than one template-object pair satisfies this criterion, in these cases the redshift of the correlation with the highest R_{TD} value is used. For $\sim 90\%$ of the cases, it is the correlation between the object and the elliptical galaxy template that has the highest R value, as would be expected for galaxies residing in the cores of rich clusters. As a final check, each of the template spectra were de-redshifted to rest wavelength and inspected by eye to check the any visible emission and absorption features to confirm the redshift determination. Figure 6.9 shows 5 typical spectra from the observations of MACSJ1731.6+2252.

The spectra in figure 6.9 are typical of an old stellar population, with the Calcium H and K absorption features and the 4000 angstrom break clearly visible, which is consistent with the picture of elliptical galaxies being composed of an old, passively evolving stellar population. In particular, the lack of any strong [OII] emission feature indicates that these galaxies are not current undergoing any major

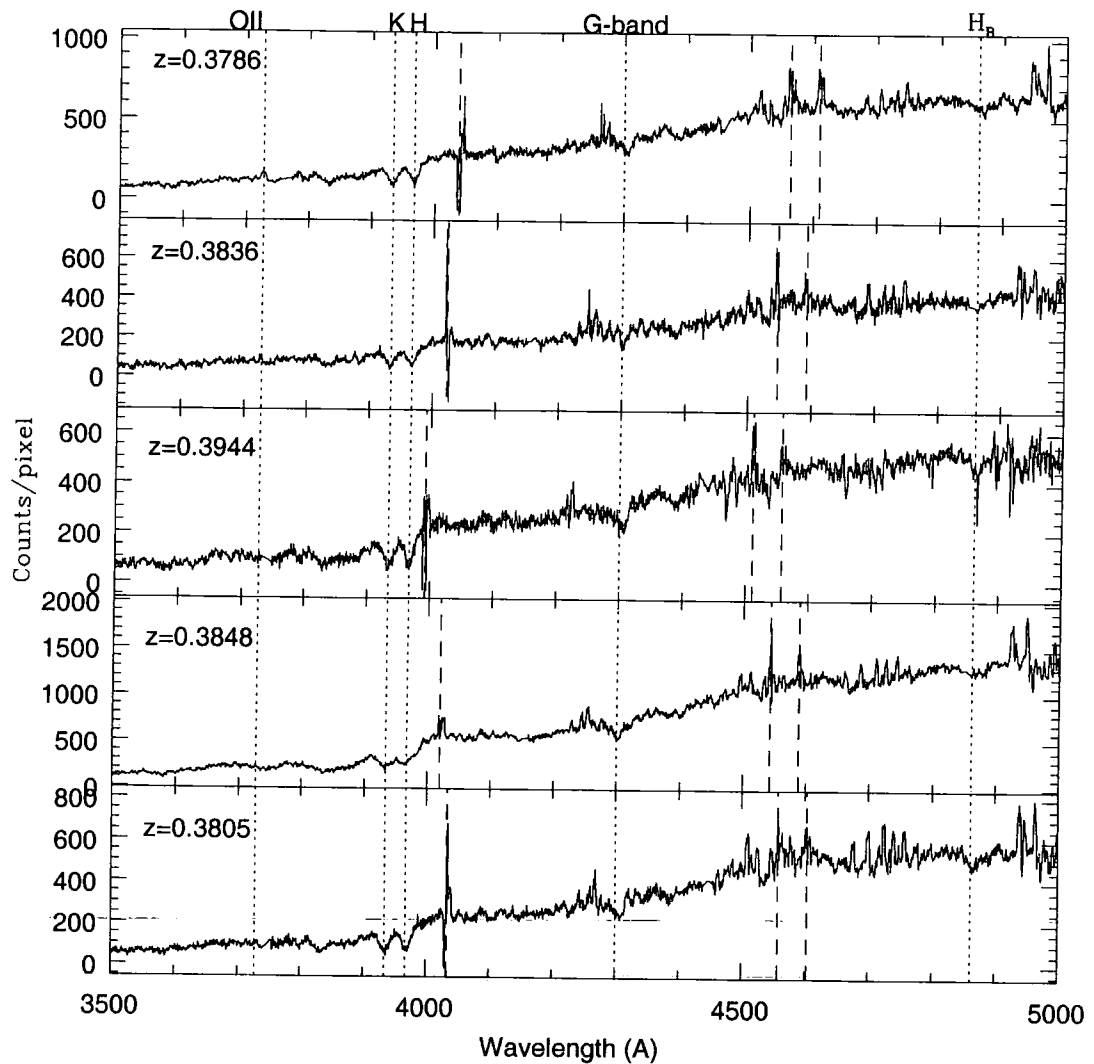


Figure 6.9: Five typical spectra taken from the observations of MACSJ1731.6+2252. The spectra have been de-redshifted to rest wavelength and common spectral features are marked by the dotted lines. The dashed lines mark the position of strong sky lines, these features should be ignored.

star-formation.

6.4.2 Velocity Dispersions

In total, 45 redshifts measurements were secured for each of the target clusters MACSJ1720.2+3536 and MACSJ1731.6+2252 with the remaining slits containing either alignment stars, sources with insufficient signal or objects where the spectrum has been truncated by the edge of the detector array, the distribution of these redshifts is shown in the upper panels of figure 6.10. These plots show how successful the colour-selection of cluster galaxy targets has been, in MACSJ1720.2+3536 only 2 (4% of redshifts obtained for this cluster) galaxies have redshifts more than 0.02 from the rest of the cluster galaxies. In MACSJ1731.6+2252, a similarly small number (3, 6% of the total) of galaxies are found to be background to the cluster. This demonstrates how well the colour-magnitude based photometric selection process works for cluster galaxies as used in earlier chapters. In order to measure the velocity dispersion of these clusters, a 3 sigma clipping method was used, which results in a measured redshift of 0.3866 for MACSJ1720.2+3536 and 0.3876 for MACSJ1731.6+2252 with apparent velocity dispersions of 1157 km/s and 1569 km/s respectively, corresponding to rest-frame dispersions of 834 km/s and 1130 km/s, confirming that these are indeed very large galaxy clusters. For comparison, the local large cluster of galaxies, Coma, has a velocity dispersion of 1082 km/s (Colless and Dunn 1996.)

The close-up redshift histograms of these two clusters (the lower panels of figure 6.10) also reveals details of the structure of these two clusters. MACSJ1720.2+3536 appears to be reasonably well fit by the best-fit Gaussian curve whereas the second cluster, MACSJ1731.6+2252, shows a much more disturbed distribution. The most likely explanation for this is that MACSJ1731.6+2252 is undergoing some form of a merger event and should more redshifts be obtained for this cluster, the separate cluster substructures will be most likely be resolved. This demonstrates the power of spectroscopy to resolve velocity substructure, which is apparent from even this relatively modest number of redshifts, in contrast to photometric methods (for example the symmetry work presented in section 3.3) where substructure is extremely diffi-

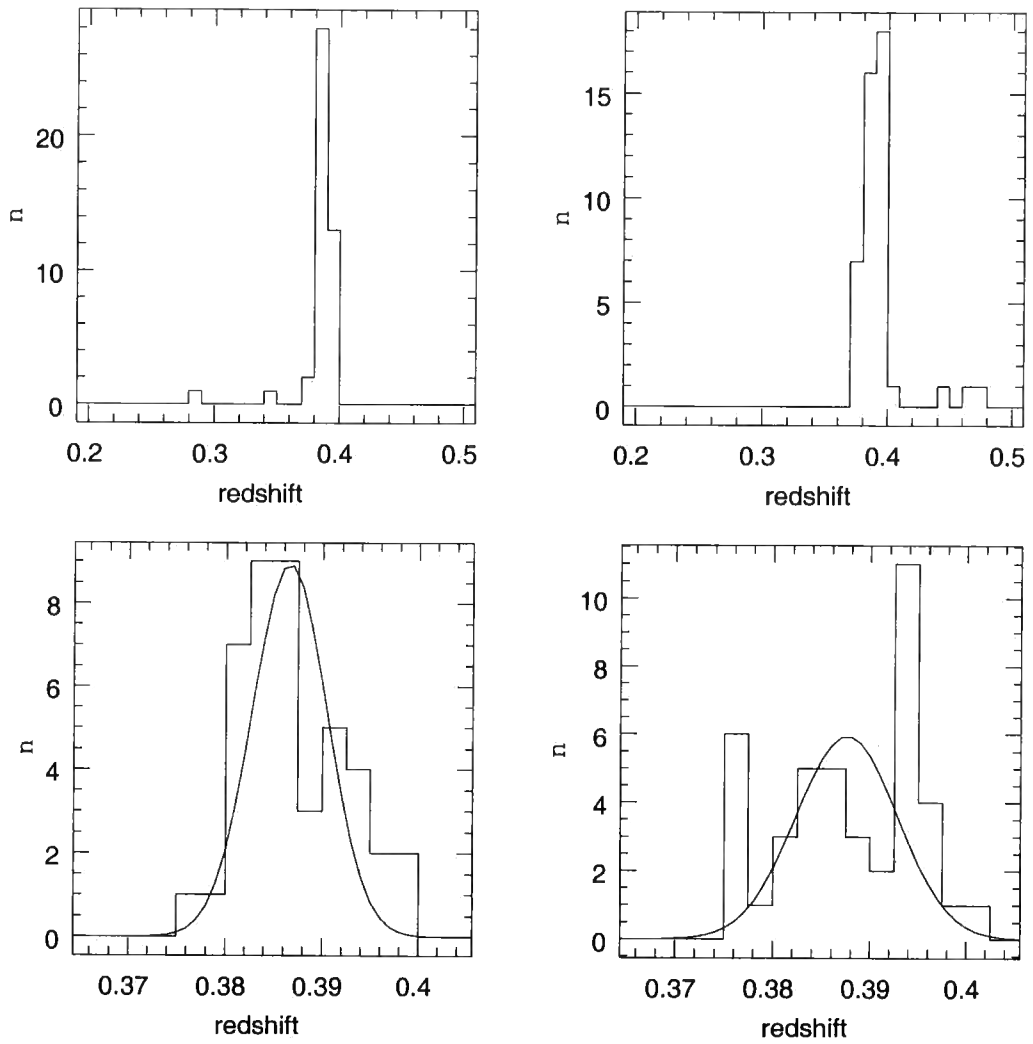


Figure 6.10: Velocity dispersion histograms of MACSJ1720.2+3536 (upper and lower left) and MACSJ1731.6+2252 (upper and lower right) with the best fit Gaussian velocity distributions.

cult to quantify. These redshifts will be added to the spectroscopic study of MACS clusters and their substructures being undertaken by other members of the MACS collaboration.

6.5 Spectroscopically selected cluster members

As has been stated, the observations of MACSJ1720.2+3536 and MACSJ1731.6+2252 are only a small part of a much larger comprehensive spectroscopic follow-up of the clusters revealed by the survey.

Unlike the GMOS observations presented in this chapter, the colour-selection of target galaxies for the majority of clusters was performed by taking a horizontal slice across the colour-magnitude diagram, unlike the GMOS selection where a constant offset from the fit to the cluster red-sequence was used. This means that the redshifts taken using LRIS can be used to constrain the errors on the fits to the colour-magnitude sequence due to the mis-selection of galaxies.

In order to test this, six clusters that have been part of the multi-object spectroscopy campaign were chosen. These clusters are MACSJ0025.4-1222 ($z=0.58$), MACSJ0717.5+3745 ($z=0.54$), MACSJ0329.6-0211 ($z=0.45$), MACSJ2129.4-0741 ($z=0.58$), MACSJ0257.1-2325 ($z=0.50$) and MACSJ0647.7+7015 ($z=0.59$.) It is obvious that this sample is highly biased towards the highest redshift objects in the MACS sample. This selection effect arises from the fact that this sample is drawn from the spectroscopic observations made using the LRIS instrument at the Keck observatory. Due to its huge collecting area and the fact that time on this telescope is at an extreme premium, only the highest redshift objects have been targeted by this instrument/telescope combination as part of the follow-up campaign.

For each cluster, the galaxies with measured redshifts were cross-correlated against the original SExtractor catalogues to recover the photometric properties of these objects. The velocity dispersion of these objects were then examined and a 3 sigma clipping was applied to the redshift catalogues to retain only those galaxies that certainly reside within the MACS cluster. Colour-magnitude diagrams containing only these spectroscopically selected cluster member galaxies were then produced and are shown in figure 6.11.

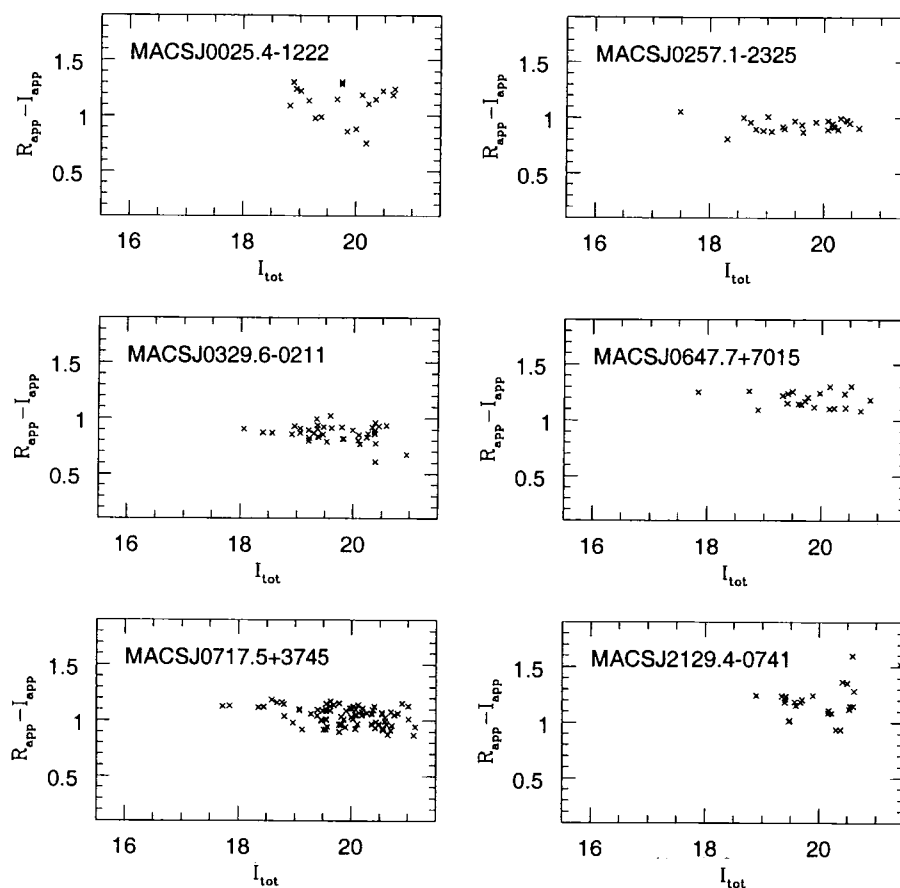


Figure 6.11: $R_{app} - I_{app}$ against I_{tot} colour-magnitude diagrams for spectroscopically confirmed cluster member galaxies of six clusters observed with the LRIS instrument. The scale of the colour-magnitude diagrams is identical to that used for the similar colour-magnitude diagrams presented in Appendix A

Table 6.3: The slope of the fit to the cluster red sequence for photometrically and spectroscopically selected cluster galaxies.

Cluster	Photometric	Spectroscopic
MACSJ0025.4-1222	-0.038 ± 0.031	-0.007 ± 0.099
MACSJ0257.1-2325	-0.038 ± 0.016	-0.007 ± 0.082
MACSJ0329.6-0211	-0.016 ± 0.021	-0.006 ± 0.047
MACSJ0647.7+7015	-0.022 ± 0.124	-0.037 ± 0.050
MACSJ0717.5+3745	-0.027 ± 0.014	-0.053 ± 0.027
MACSJ2129.4-0741	-0.038 ± 0.078	-0.101 ± 0.091

Only the R-I colour of these objects is shown in figure 6.11 as it is in this colour that these objects were originally selected. It is not appropriate to make this comparison in the other two available colours (i.e. V-R and V-I) as the results obtained from the spectroscopic sample will be subject to Malquist bias. This bias arises from objects being selected on the basis of their R-I colour, which will result in the V-R and V-I samples containing objects that would not've been selected if the selection had been made in these colours. At the same time, objects will be missing that would've been selected in these colours. Consequently, it is only appropriate to compare objects in the colours in which their selection was made.

For each of these reconstructed CM-diagrams, the bi-weight fitting routine (c.f. section 3.1.2) was applied, using all of the spectroscopically selected galaxies i.e. unlike the purely photometric fitting, no additional colour selection was performed on these data-set. The fits to the red-sequence of both the photometrically and spectroscopically selected samples are shown in table 6.3.

It can be seen that within the (admittedly large) error intervals, the fits to the cluster red-sequence agree within the two methods. These large errors are to be expected as these clusters are the highest redshift objects in the MACS sample and so are near the limit of the photometry and object selection completeness.

Finally, it can be seen that the error-bars for the spectroscopically selected sample are comparable in size to those generated from the purely photometrically selected sample. As, effectively, the only difference between these two samples is the

way in which the objects have been selected this would imply that this difference in object selection makes no difference to the overall result of fitting the red-sequence. Consequently, the errors on the fits to the colour-magnitude sequence must be derived from photometric errors, caused by the limited depth of the imaging, and the related problem of the modest dynamic range available to fit the cluster red-sequence. These problems could only be overcome by taking significantly deeper imaging using a larger telescope.

6.6 Conclusions

In this chapter, the spectroscopic observations of two clusters (MACSJ1720.2+3536 and MACSJ1731.6+2252) have been shown along with the details of the data-reduction process utilising the tasks within the Gemini IRAF package. Heliocentric redshifts were obtained for 45 cluster members in each of these clusters which reveal the redshifts of the two clusters to be 0.3866 for MACSJ1720.2+3536 and 0.3876 for MACSJ1731.6+2252 with corresponding rest-frame velocity dispersions of 834 km/s and 1130 km/s, demonstrating that these are indeed massive clusters of galaxies.

Colour-magnitude diagrams containing only spectroscopically confirmed cluster members of six clusters observed with LRIS on Keck-I were used to constrain the errors on the fit to the cluster red-sequence made using their purely photometric equivalents. Both the fits to, and the errors on, the bi-weight fits to the cluster red-sequence were comparable between the photometric and spectroscopic colour-magnitude diagrams which strongly suggests that the dominant source of error in fitting the cluster red-sequence is the photometric errors rather than cluster member selection.

Chapter 7

Active Galactic Nuclei in Clusters of Galaxies

7.1 Introduction

For the majority of surveys, a lot of time and effort is invested into making sure that the final object catalogues are complete to the determined survey sensitivity limits. While due diligence and careful survey design can ensure that all of the objects that should be seen are, it can be harder to assess the impact of other classes of objects that satisfy the survey characteristics i.e. possible sources of contamination. In the case of the MACS survey, assessing the levels of any contamination involves searching for possible sources of X-ray contamination that could look like the X-ray emission from a galaxy cluster. For surveys that are based around X-ray data obtained from the ROSAT satellite, the modest point-spread function of the telescope means that point sources can easily become confused with the X-ray emission from clusters. Indeed, the MACS survey has specifically targeted sources from ROSAT All-Sky survey point source catalogue as the X-ray emission from distant clusters is unresolved by the telescope which means that point sources are most definitely present in the parent X-ray catalogue.

Thanks to the dual X-ray and optical selection technique used in the MACS survey, only X-ray sources coincident with over-densities in the apparent galaxy distribution will be selected as being clusters and so the contamination due to individual, isolated, point sources such as galactic supernovae remnants or black holes will be minimal. Consequently, the most probable sources of contamination are extra-galactic X-ray point sources that lie in the line of sight to the clusters. These objects will have the contaminating effect of enhancing the X-ray emission

above and beyond that emitted by the cluster alone. The most likely sources for any such emission are active galactic nuclei (AGN) and quasars.

AGN were first discovered in 1943 when Carl Seyfert identified six spiral galaxies that had unusual, broad, emission lines in their spectra. When images at optical wavelengths of these objects were studied in detail, they all appeared to have extremely bright nuclei and hence were named as active galactic nuclei (AGN) galaxies. Today, objects of this type are named Seyfert galaxies after their discoverer and fall into two broad classifications, type 1 Seyfert galaxies which have “broad” spectral emission lines and type 2 Seyfert galaxies which possess “narrow” spectral lines. Although this original classification holds true, many authors consider the Seyfert classification to be a semi-continuous scale, with subgrades between 1 and 2, and may classify galaxies as being Seyfert class 1.8 (eg. Barcons et al. 2003.) A second important class of AGN are the BL Lacertae objects, named after the prototypical object that defined this classification. BL Lacertae are identified by their lack of emission features which makes the study of these objects difficult as their featureless spectra makes gaining redshifts for these objects extremely challenging.

Optically selected AGN are relatively rare in cluster environments. Studying low ($z \sim 0.04$) redshift clusters, Dressler et. al (1985) found that only 1% of cluster galaxies contains an AGN, as determined by the presence of AGN indicators in their optical spectra. Follow-up work to this project determined that there was no change in this AGN fraction in clusters out to redshift $z \sim 0.5$ (Dressler et al. 1999.) In X-rays, Lazzati et al. (1998) used a wavelet detection algorithm (such as that of Freeman et al. 2000) to disentangle small-scale point source emission from the diffuse cluster emission in ROSAT PSPC observations of the Abell clusters A194 ($z=0.018$) and A1367 ($z=0.022$). In these clusters, 26 and 28 sources respectively were found where only 9 would be expected in a blank field. Similarly, Henry & Briel (1991) found twice as many sources in a ROSAT PSPC observations of A2256 ($z=0.06$) than would be expected for a similar blank field. These results have been confirmed with the modern generation of X-ray telescopes; Sun and Murray (2002) re-observed A1367 with Chandra and resolved 58 point sources, 8 of which are spectroscopically confirmed cluster members.

Having established that AGN do exist in clusters, where do these objects lie

within the dynamic structure of the clusters? Are they all located in the outlying regions of clusters, or are they centrally concentrated? Johnson et al. (2003) used archival Chandra data (first published in Jeltema et al. 2001) to study the $z=0.83$ cluster MS1054-0321 and detected 47 X-ray sources in the $8.3 \times 8.3'$ field of view. They find that the excess of X-ray sources lies at radial distances of between 1 and 2 Mpc, from which they conclude that these emitting objects are actually galaxies falling into the cluster and so AGN activity is related to the environment of its host galaxy. In the context of the MACS survey, if this result holds for the majority of rich clusters, the X-ray flux calculated for even the highest redshift clusters will be unaffected by these AGN as the point-spread function of the PSPC instrument is good enough to separate sources at these large projected separations.

In this chapter, an attempt is made to examine the distribution of AGN in rich clusters by performing a cross-correlation of the Veron-Cetty Veron AGN catalogue with the Abell and ACO cluster catalogues and builds upon the method used by Petrosian & Turatto (1986) and the work of Edge (1991.) This distribution is studied both to gain an understanding of the possible X-ray contamination in the MACS X-ray flux measurements and to attempt to understand the effect of the environment on the activity cycle of an active galaxy.

7.2 The Nature of AGN

The current way of explaining the diversity of AGN is that the wide variety of observed phenomena can be generated through a single central engine, the so-called unified model of AGN emission. First proposed originally for Seyfert galaxies by Antonucci & Miller (1985) and then generalised to encompass almost all AGN activity (see, for example, Antonucci 1993 and Urry and Padovani 1995 and references therein.) A schematic diagram of the unified AGN model is shown in figure 7.1. The unified model consists of a central super-massive black hole, which emits a highly collimated jet of relativistic particles, surrounded by an accretion disk and a large, dusty, torus. The different apparent properties of AGN arise from observing this central engine at different viewing angles. Observers looking directly down the jet will see only the featureless synchrotron emission, leading to the classification

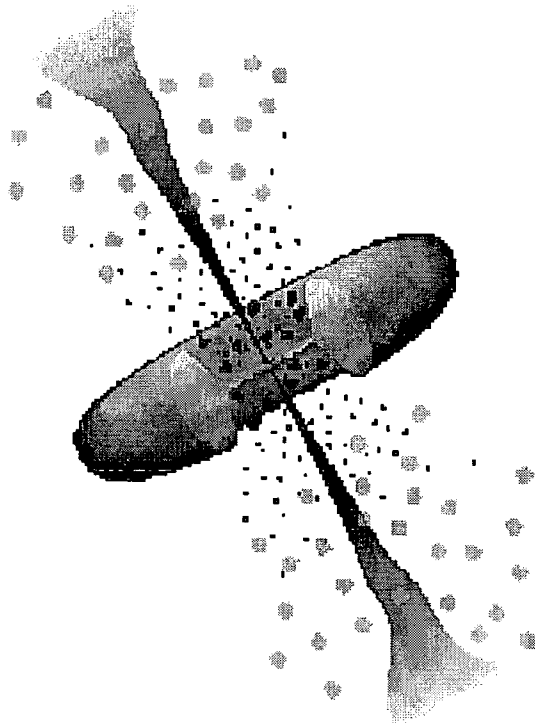


Figure 7.1: Schematic diagram of the unified model of AGN emission. A central black hole emits relativistic jets and is surrounded by clouds of high velocity gas. These clouds and the central engine are shrouded by a large, dusty torus. Taken from Urry and Padovani 1995

of BL Lac objects. As the viewing angle moves away from the jet, the line of sight will probe down into the high velocity gas close to the black hole, resulting in broad emission lines and the resultant classification of Seyfert 1 galaxies. As the viewing angle increases, the torus will occult increasingly more of the central engine, and so the width of the observed emission lines will decrease (Seyfert 2 objects) until, when viewed from side on, only the effect of the jets will be seen in the form of radio lobes produced at the points where the relativistic material that makes up the jet comes into contact with the interstellar medium.

If this model of AGN activity is correct, then clearly all that is required for a galaxy to be a possible host of an AGN is for it to contain a super-massive black hole in its centre. It is now thought that the majority, if not all, galaxies contain such an object and that the formation and evolution of a central black hole may be tied to the evolution of the host galaxy (Magorrian et al 1998) such that the size of a galaxy's bulge is linked to the size of the black hole that it hosts. Clearly if this Magorrian relationship holds then elliptical galaxies, which can be thought of as being essentially huge bulges with no disk, would be expected to be host to extremely massive black holes suitable for powering an AGN. Massive clusters of galaxies provide large concentrations of elliptical galaxies and so contain a large concentration of potential AGN hosts, but as other authors have found, only a small fraction of cluster galaxies actually contain AGN. The studies mentioned above show that there does appear to be an excess of AGN in clusters when compared to the field, but these studies have been limited to a small number of clusters. Does this excess still hold when a much larger number of clusters is examined?

The ninth edition Veron-Cetty Veron (2000) catalogue is used as the source of AGN for this study. This catalogue is a compilation of quasars and active galactic nuclei selected from literature detections and no attempt is made by the catalogue authors to verify the identification or positions of any of the objects in the catalogue. The objects in the Veron-Cetty Veron catalogues are drawn from a wide range of sources and contain objects selected at optical, infra-red, X-ray and Radio wavelengths. As such, the Veron-Cetty Veron catalogue cannot be taken to be complete at any level at any wavelength or redshift. It does, however, remain as one of the largest catalogues of active galaxies and its all sky coverage is the reason

for its selection as the data catalogue for this study.

The Abell (1958) and Abell, Corwin & Olowin (1989) catalogues are used as the input catalogue of galaxy cluster. Although the original catalogue is over 40 years old, it remains the standard catalogue of rich clusters in the local universe. For simplicity both the original 1958 and the supplemental 1989 cluster catalogues will be collectively referred to as being the Abell clusters.

7.3 Establishing an Excess

Before studying the distribution of AGN specifically around clusters, the angular distribution of Veron AGN on the sky with respect to the centres of the Abell clusters was studied to establish whether there is indeed an excess of active objects in the vicinity of clusters. For each Abell cluster, the angular separation of every Veron AGN with a catalogue redshift of less than 0.5 was selected, omitting any AGN listed without a redshift. This redshift limit was chosen to reflect the redshift distribution of the Abell clusters and to avoid biasing the distribution toward clusters by including lensed, high redshift, quasars. The cumulative frequency of the number of AGN within a given angular separation is shown in figure 7.2. Clearly, as found in the X-ray results, there exists an enhanced population of active galaxies associated with clusters. In a random distribution the number of AGN seen will be proportional to the area considered and therefore proportional to the square of the projected separation from the cluster, the 'random' distribution has been produced by fitting a parabola to the AGN distribution, using only those objects at separations greater than 90 arcmin. At more than a degree and a half from the cores of these clusters, this would be expected to be sampling the field galaxy population for even the most nearby, richest clusters. In order to avoid geometrical bias arising from clusters themselves clustering together, AGN are freely allowed to associated with multiple clusters. It can clearly be seen from figure 7.2 that there is an excess of objects at small separations, a K-S test of goodness of fit shows agreement with a random distribution (shown by the solid line in figure 7.2) of only 1%, strongly indicating that the distribution is non-random.

Having established that there are more AGN in the direction of clusters than

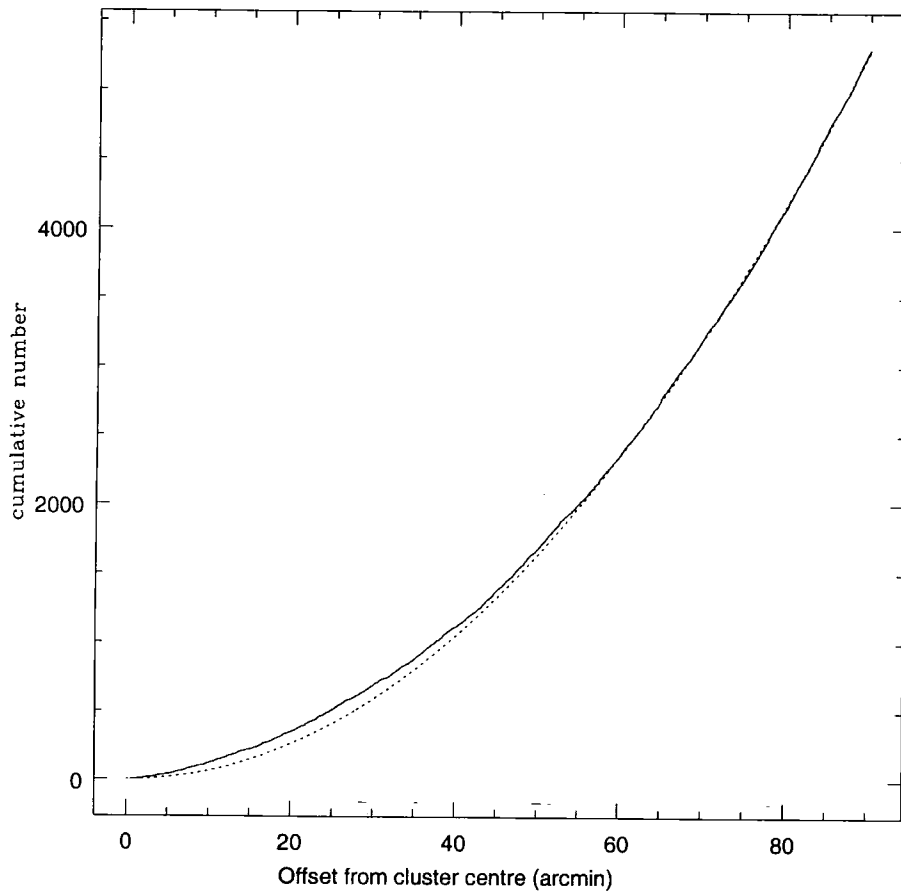


Figure 7.2: The cumulative distribution of AGN with catalogue redshifts of less than 0.5 with respect to the offset to the centre of the nearest cluster. The dotted line traces the cumulative number that would be expected from a random distribution.

would be expected from a random field, a catalogue of AGN in clusters was compiled. An AGN was selected to lie within a given cluster if the difference in redshift between the AGN and the cluster is less than 0.01 and then two subsamples were generated where the projected offset between the cluster and the AGN is less than 4Mpc and 10Mpc. The projected offset between AGN and cluster centre was calculated using the angular offset between the cluster and the AGN, evaluated at the redshift of the cluster. Due to large scale structure, in several cases, particularly in the projected 10Mpc sample, an AGN was selected to lie within multiple clusters. In these cases, only one of the associations is retained, in all cases the association with the smallest projected offset. This selection process revealed 190 AGN associated with clusters on a 4Mpc scale and 499 on a scale of 10Mpc. This method effectively stacks the Abell clusters, producing a catalogue of objects in a synthetic superposition cluster.

7.4 Surface Density

In order to study the radial distribution of AGN in clusters, radial surface density profiles were calculated and are shown in figure 7.3

The vertical axes of these figures have been labelled in arbitrary units. This is because, due to the incomplete nature of both the Abell and Veron catalogues, it is impossible to correct the computed surface density to quantify the magnitude of the AGN surface density, the closest correct units for these surface densities being 2.455×10^{-4} AGN / Mpc² / Cluster. These surface density profiles have been fitted using a King profile, a three parameter model which describes the 2 dimensional, projected galaxy distribution of a cluster and is of the form:

$$\sigma = \sigma_0 \left(1 + \left(\frac{r}{r_c} \right)^2 \right)^{-\alpha}$$

where σ is the surface density, σ_0 is the core surface density, α is the index of the model (physical values lie in the range 0.5 to 1.5) and R_c is the core radius.

The two surface density profiles were bootstrap fitted using only a King model for the 4Mpc sample but using, for the 10Mpc sample, a King model plus a constant to reflect that this sample would be expected to be beginning to probe the field

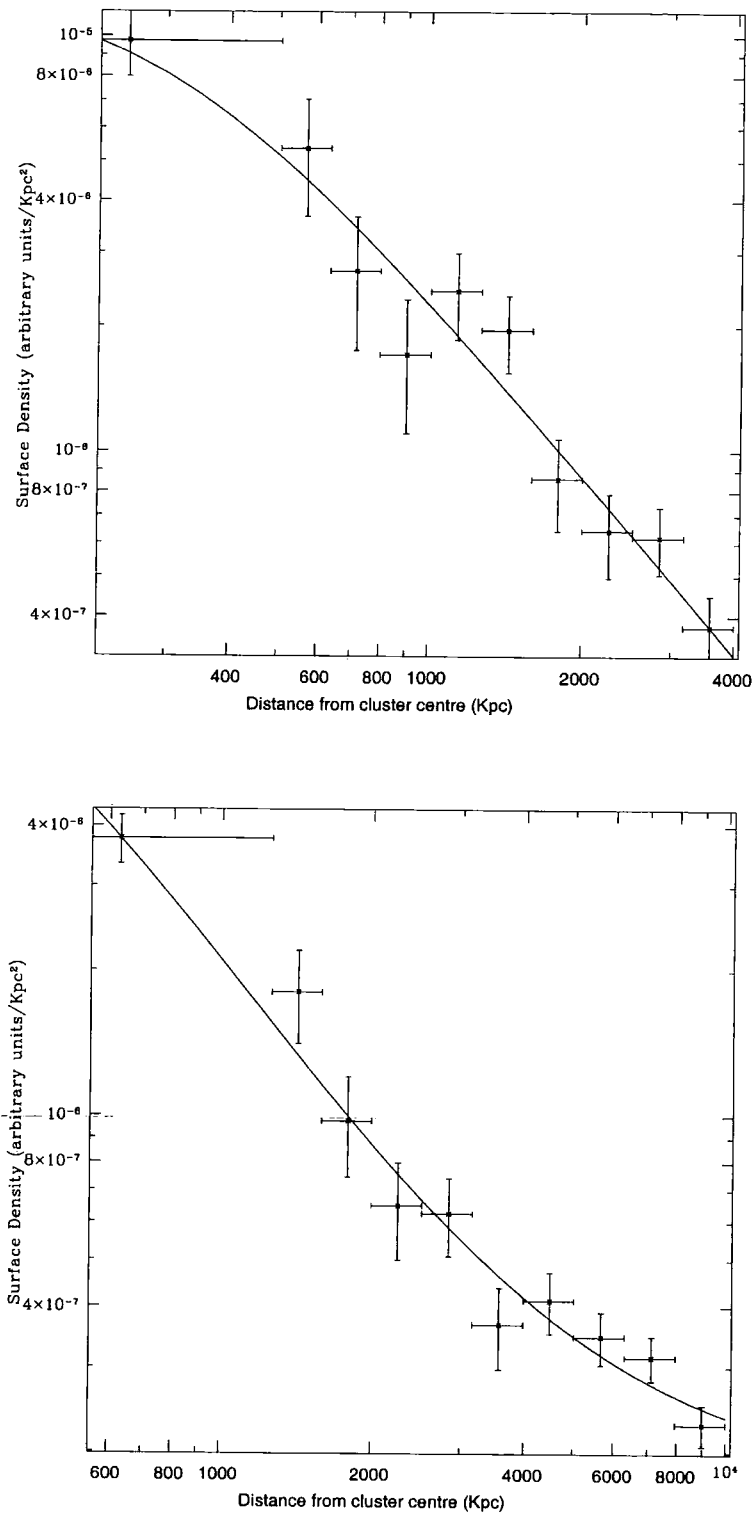


Figure 7.3: Surface density profiles for AGN in Abell clusters within 4Mpc (top) and 10Mpc (bottom) of the cluster centres fitted against King surface density profiles (solid lines.)

galaxy distribution. The two samples appear to be well fit by the King profile, suggesting that AGN are distributed around the centres of clusters in the same way as cluster galaxies. There is certainly no evidence of any excess of objects in the 1-2Mpc region that would suggest that AGN activity is triggered by in-fall into the cluster. The core radii of this King model fits are 329_{-121}^{+136} and 311_{-105}^{+120} Kpc for the 4Mpc and 10Mpc samples respectively which confirms that this sample is probing objects in rich clusters, similar to those that MACS is probing at higher redshift.

Having mapped the surface density profile, it is possible that there may still be substructure in the distribution of AGN that is not seen in the projected galaxy surface density. The centres of the Abell clusters have not necessarily been accurately determined and any errors in the catalogue position of the cluster centre, or that of the AGN, will act to smear-out any signature of in-falling objects.

7.5 Velocity Structure

This obfuscation due to uncertain centring of the cluster and AGN will not, however affect the observed velocity dispersion of AGN around the cluster centres as these observations are independent of the positioning of the cluster centre. Consequently, the velocity structure of the AGN about the cluster centres was traced in an effort to reveal any substructure not seen in the projected galaxy distribution. The velocity dispersions were calculated using the difference in redshift between the AGN and its host cluster and are plotted in figure 7.4.

As with the surface density profile, the velocity dispersion is well described by the distribution that describes the general galaxy distribution, in this case a Gaussian. In particular, the 10Mpc subsample shows an extremely regular distribution with no indication of any substructure that would betray any ignition or quenching of AGN activity due to the changing cluster environment. Bootstrap fitting the distribution reveals velocity dispersions of 862_{-121}^{+135} Km/s and 804_{-114}^{+126} Km⁻¹ for the 4Mpc and 10Mpc samples respectively. These figures are in agreement with the result of 696 Kms⁻¹ found for a sample of Markerian galaxies in Zwicky clusters (Petrosan and Turrato 1986) and the figure of 744 Kms⁻¹ found in a study of normal galaxy velocity dispersions in 69 Abell clusters which further confirms that the velocity

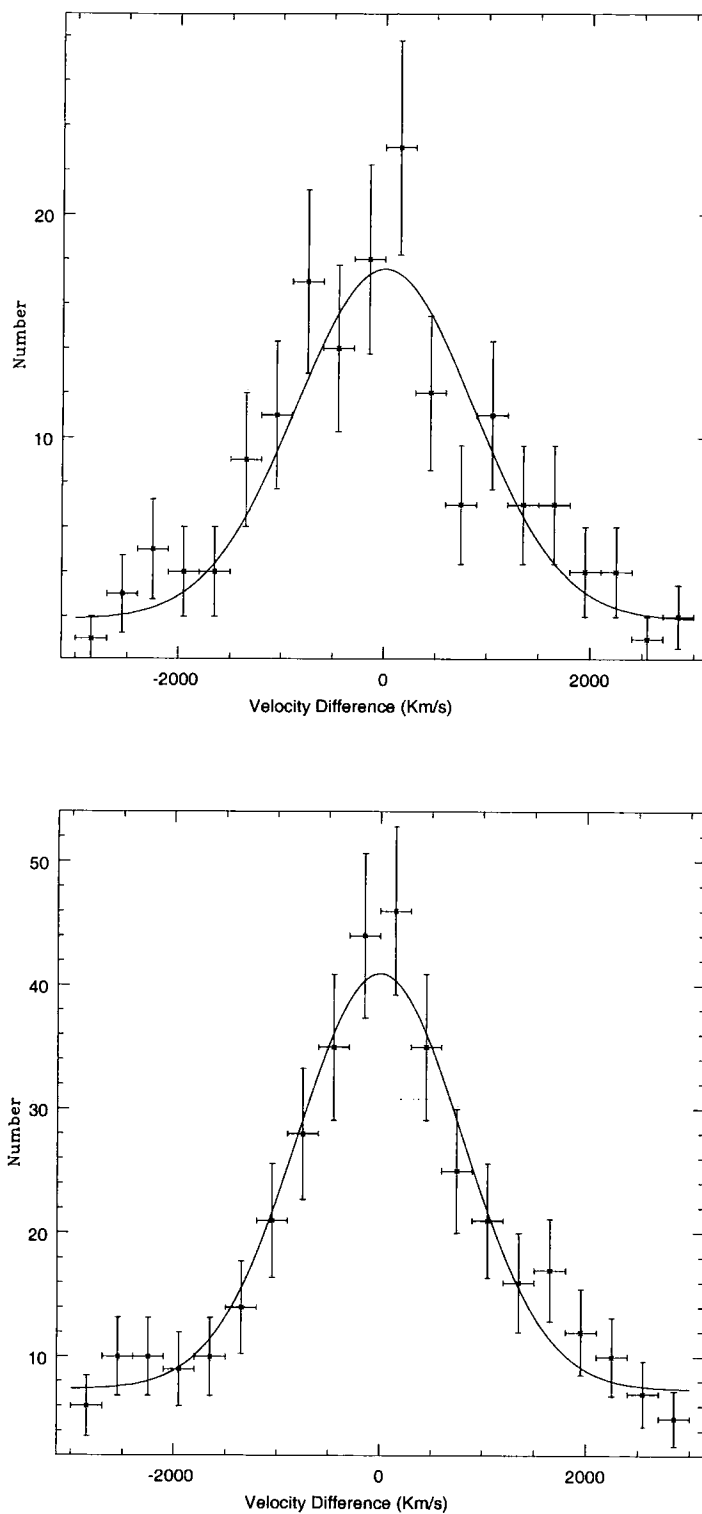


Figure 7.4: Velocity dispersion of AGN with respect to their host cluster for AGN with 4Mpc (top) and 10Mpc (lower) of the apparent cluster centre.

dispersion of AGN is indistinguishable from that of inactive cluster members.

7.6 Conclusions

In this chapter a cross-correlation of the ninth edition Veron-Cetty Veron AGN catalogue with the Abell cluster catalogue was used to study the distribution of AGN within clusters, both as a way of probing the effect of the cluster environment on AGN activity and also to assess the possible effect of unresolved AGN on the X-ray flux measurement of the MACS clusters.

The cross-correlation reveals a sample of 190 and 499 AGN associated with clusters on 4Mpc and 10Mpc scales respectively. These AGN appear to be distributed in the clusters as ordinary member galaxies with core radii of 329_{-121}^{+136} Kpc and 311_{-105}^{+120} Kpc and velocity dispersions of 862_{-121}^{+135} Kms⁻¹ and 804_{-114}^{+126} Kms⁻¹ in contradiction of theories that suggest that AGN activity may be triggered by in-fall of a field galaxy into a cluster. However, there is one caveat to this result that stems from the unknown selection function of the Veron catalogue. The claim of an excess of objects between 1 and 2 Mpc from the cluster core was made using X-ray selected objects whereas the Veron catalogue uses objects detected at all wavelengths. It has long been known that there is an excess of radio emitting objects in the cores of clusters (Roberson and Roach 1990) which could, in effect, balance out any X-ray excess in the outlying regions of the clusters. This effect would only be possible to understand with more careful separation of the AGN by the wavelength in which they were detected.

So what is the implication of this result for the MACS survey? It is clear that the AGN are distributed through their host clusters and so the effect of any AGN cannot be eliminated geometrically. This leaves AGN as being a possible source of contamination in the survey. Fortunately, early analysis of Chandra data appears to show that the effect of X-ray point sources is small compared to the noise inherent in pushing close to the ROSAT detection limit (Ebeling 2002b).

Chapter 8

Miscellaneous Objects

8.1 Introduction

One of the joys of observational astronomy is the feeling of discovery every time a new image is examined. Continual improvements in telescopes and their instrumentation with the associated increased sensitivities, resolution and fields of view makes fresh observations of even well known fields exciting, as previously obscured details reveal themselves. Consequently, more often than not, interesting objects are seen in the field, for example a beautiful grand design spiral, that has little or nothing to do with the target of the observation.

In this chapter, a miscellany of, primarily gravitationally lensed, objects that have been observed along with the MACS clusters is presented. A full study of these objects has proven to be beyond the scope of this thesis, but these objects are recorded here to enable future study.

8.2 Gravitational Arcs

Gravitation lensing is a result of the perturbation of the path of a light ray as it passes through a gravitational field. This perturbation effect is visible on many scales and it was the gravitational lensing of background stars by the sun (as observed by Eddington during the 1919 total eclipse) that was one of the first independent tests of Einsteins theory of General Relativity.

Figure 8.1 shows a schematic diagram of gravitational lensing. The light from the source object (the middle star) is bent by the gravitational field of the lensing mass (the black circle.) The deflected light is detected by the observer and the perturbation to the light path causes the object to appear to be in a different position. Multiple light paths are possible from the source, past the lens, to the observer and

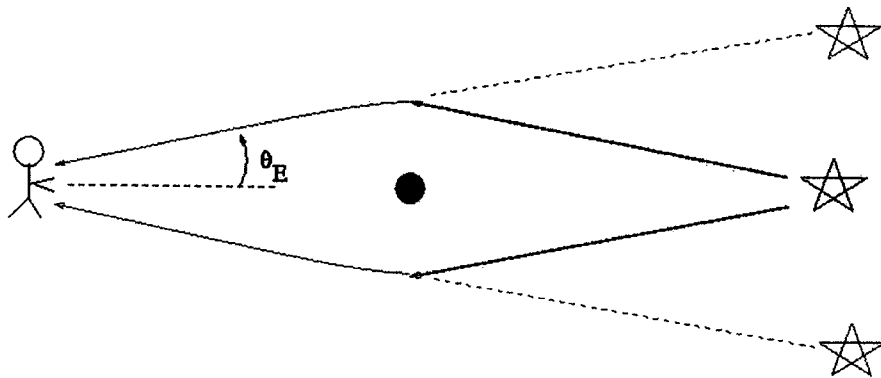


Figure 8.1: This simple model shows how the deflection of light by a massive object can produce multiple images of a single background object.

this can cause apparent multiple images of a single object (demonstrated by the outer two stars in figure 8.1.) Multiply lensed objects are an extremely powerful tool in the study of galaxy clusters as the positions of the multiple images will, clearly, be dependent upon both the true position of the original object and the geometry of the lens causing the disturbance. This allows gravitational lenses to be used to study not only the total mass of an object but also the distribution of that mass within clusters.

All that is required for gravitational lensing to occur is that there is suitable alignment between the lensing cluster, assuming that the cluster is of a sufficient mass, and the background galaxy. This results in the background object being drawn randomly from the background galaxy population, to a limit determined by the strength of the lens magnification and the depth of the imaging. This means that no prior assumptions can be made about the intrinsic expected colour of a lensed galaxy. Coupled with this unknown colour is the effect of the lens itself which acts to distort the shape of the lensed galaxy by an amount determined by the strength and shape of the lens and the path of the light ray through the lensing mass. Consequently, gravitational lensed objects can appear to have semi-arbitrary shape, position and colour, which makes developing automated methods for finding gravitationally lensed objects extremely challenging. In a similar way to other authors (eg. Gladders et al 2003), composite colour images of the MACS clusters were examined visually to search for possible gravitationally lensed objects.

As with any manual process, a visual search such as this is highly subjective and it is entirely possible that objects have been missed. Consequently, the list of possible lensed objects presented here should not be taken as a statistically complete sample. Objects are selected on the basis of their shape (lensed galaxies would be expected to be tangentially distorted) and by having a colour significantly different (either bluer or redder) than the cluster galaxies.

The majority of photometry packages, and certainly the SExtractor programme used for the MACS photometry, are optimised for measuring the properties of normal, regular, galaxies and as such they use circular and elliptical apertures for their photometry and parameter measurements. As has been stated, the shapes of lensed galaxies can be highly irregular and as such are not suitable for automated detection in this way. However, in order to estimate the colours of these arcs, the 5 arcsec aperture magnitude, extracted as part of the standard MACS photometry pipeline, has been used to measure the apparent magnitude and colour of the lensed objects. It should be noted that although an object may appear in the snapshot images shown in the figures, the MACS photometric pipeline detects objects in the I band and so photometry may not be available for faint, blue objects not detected in this, the reddest of the observed bands.

Presented here are the MACS clusters which have candidate lensing objects within them. Each lensed object is identified by a label corresponding to the lettering on the snapshot image of the core of each cluster.

8.2.1 MACSJ0014.3-3022

This cluster contains a single object which appears to be a gravitationally lensed object, betrayed by the object's extremely red colour suggesting an object behind the cluster and therefore almost certainly lensed by the cluster because of its apparent position close to the cluster core.

ID	Mag _{app} (I-band)	R-I	V-I	V-R
A	20.92±0.04	1.37±0.10	2.13±0.19	0.81±0.21

8.2.2 MACSJ0027.8+2616

This cluster has 4 objects which appear to be lensed and by their colours, these objects appear to be multiple images of the same background galaxy. This object appears to be extremely faint in the I-band, the cause of the large errors on the R-I and V-I colours, which would suggest that the background galaxy is an intrinsically blue and hence probably a late type galaxy.

ID	Mag _{app} (I-band)	R-I	V-I	V-R
A	21.92±0.16	0.06±0.17	0.57±0.18	0.51±0.10
B	21.99±0.17	0.24±0.18	0.70±0.19	0.46±0.12
C	21.53±0.11	0.50±0.12	1.24±0.15	0.74±0.12
D	22.53±0.27	-0.12±0.28	0.33±0.29	0.45±0.14

8.2.3 MACSJ0110.1+3211

This cluster contains a single, moderately red object which is classified as being a lensed object due to its red colour and it's approximately tangential alignment relative to the apparent cluster core. Close to the South of the cD galaxy there is another object which appears to be of a similar colour to the lens candidate which is a possible counter-image to this object. However, this object is at low signal to noise and is contaminated by the halo of the cD galaxy and so is not marked.

ID	Mag _{app} (I-band)	R-I	V-I	V-R
A	21.15±0.03	1.01±0.06	1.59±0.16	0.58±0.17

8.2.4 MACSJ0140.0-0555

This relatively bright arc lies close to the apparent core of this cluster and can be seen to be tangentially distorted. The morphology of this arc appears to show a red tangential arc with brighter blue core. Whether this apparent core is intensive to the background object, or due to a chance alignment with a foreground object is unclear.

ID	Mag _{app} (I-band)	R-I	V-I	V-R
A	20.16±0.02	1.07±0.03	1.55±0.06	0.48±0.06

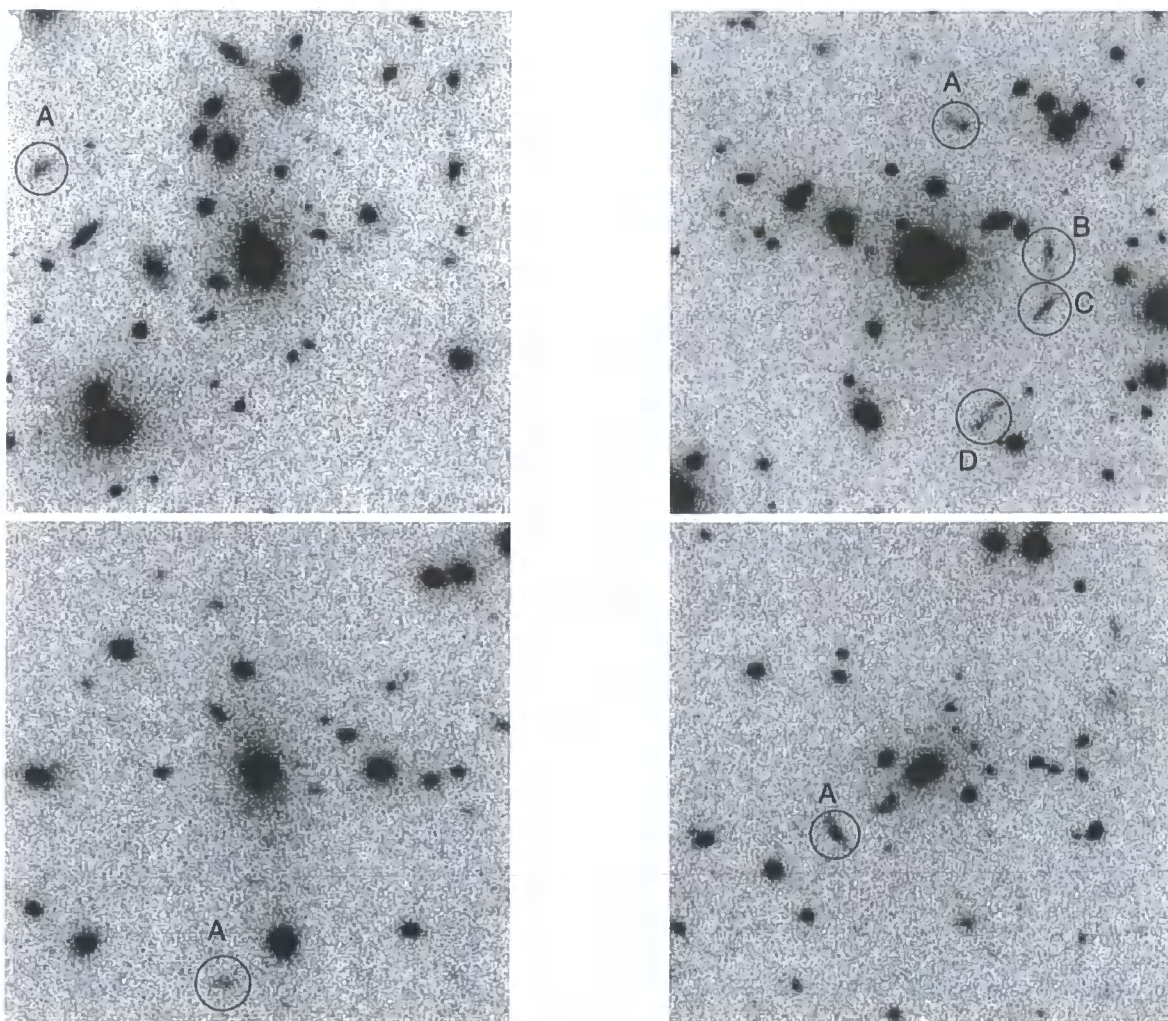


Figure 8.2: 1 arcmin² images showing gravitational arc candidates in MACSJ0014.3-3022 (I band, top left), MACSJ0027.8+2616 (R band, top right), MACSJ0110.1+3211 (R band, lower left) and MACSJ0110.1+3211 (I band, lower right)

8.2.5 MACSJ0152.5-2852

This low-surface brightness arc is aligned tangentially with respect to the core of the cluster. A possible counter-image lies blended with the three cluster galaxies to the South-West of the arc.

ID	Mag _{app} (I-band)	R-I	V-I	V-R
A	22.18±0.14	0.57±0.204005	0.99±0.21	0.42±0.22

8.2.6 MACSJ0242.5-2132

There are 4 arc candidates (A-D) which appear to be multiple images of the same object, although arcs B and C are too faint to be detected in the I-band and object D is extremely close to the detection limit. Object E is much redder (in R-I) than the other arcs and, coupled with it being further away from the cluster core, appears to be an image of a different background galaxy.

ID	Mag _{app} (I-band)	R-I	V-I	V-R
A	21.45±0.03	0.21±0.04	0.85±0.12	0.63±0.11
D	21.32±0.03	0.55±0.04	1.69±0.22	1.14±0.22
E	19.94±0.01	1.09±0.01	1.69±0.06	0.60±0.06

8.2.7 MACSJ0257.6-2209

Two, relatively short arcs are to be found in the South-Western side of the core of this cluster. Within the limits of the photometry and the alignment of the two arcs, it is possible that these are two images of the same object.

ID	Mag _{app} (I-band)	R-I	V-I	V-R
A	21.31±0.03	0.78±0.05	1.84±0.26	1.06±0.26
B	21.48±0.03	0.47±0.05	1.17±0.16	0.70±0.17

8.2.8 MACSJ0326.8-0043

This long, thin, slightly curved object very close to the core of the cluster is almost certainly a lensed background object.

ID	Mag _{app} (I-band)	R-I	V-I	V-R
A	20.66±0.02	1.16±0.06	1.95±0.15	0.79±0.16

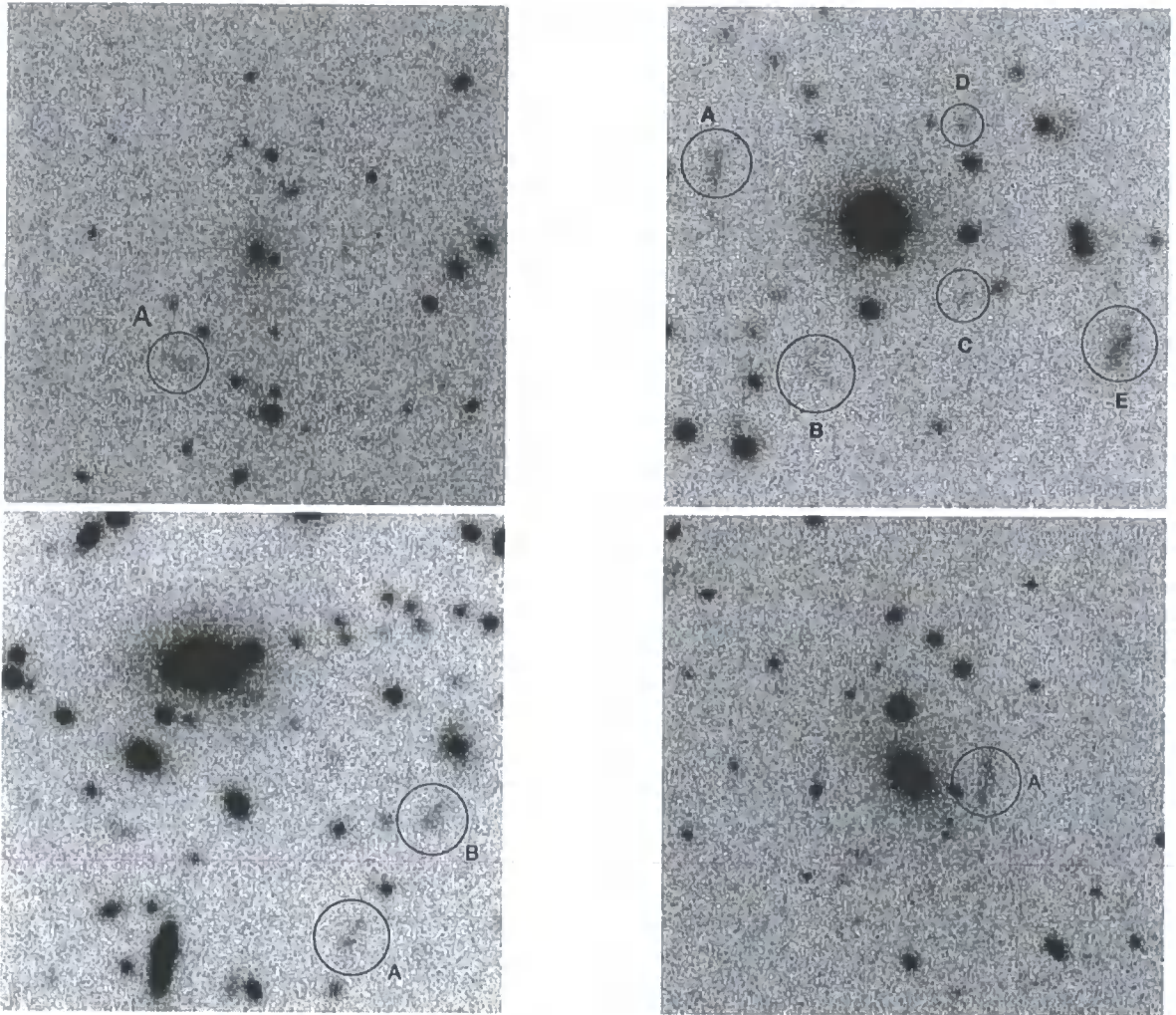


Figure 8.3: 1 arcmin² images showing gravitationally lensed galaxies in MACSJ0152.5-2852 (I band, top left), MACSJ0242.5-2132 (R band, top right), MACSJ0257.6-2209 (R band, lower left) and MACSJ0326.8-0043I (I band, lower right)

8.2.9 MACSJ0404.6+1109

The core of this cluster appears to be surrounded by a ring of 5 extremely red objects, all of similar colours and distances from the brightest cluster galaxy which would suggest that these are all counter-images of the same background object. This object is extremely faint in the V-band exposure, hence the poor photometry in the V-I and V-R colours. Additionally, counter-image E appears to be blended with two cluster member galaxies.

ID	Mag _{app} (I-band)	R-I	V-I	V-R
A	22.20±0.05	1.47±0.17	2.46±0.83	0.98±0.84
B	21.39±0.03	1.36±0.08	1.88±0.23	0.51±0.24
C	21.70±0.04	1.29±0.10	2.53±0.56	1.24±0.57
D	21.40±0.03	1.02±0.06	1.65±0.19	0.63±0.20

8.2.10 MACSJ0416.1-2403

This cluster has an arc candidate to the East of the cluster core, identified by its tangential shape and its blue colour (relative to the apparent cluster member galaxies.) There are a number of low surface brightness objects to the North and North-West of the cluster core which could be counter-images of this same galaxy but their identification is ambiguous due to their faintness.

ID	Mag _{app} (I-band)	R-I	V-I	V-R
A	21.29±0.08	0.63±0.06	1.15±0.04	0.52±0.06

8.2.11 MACSJ0449.3-2848

A single arc is to be found to the North-West of the cD galaxy of this cluster. This arc is further from the apparent centre of the cluster (41 arcsec) than previous examples and has an extremely red appearance.

ID	Mag _{app} (I-band)	R-I	V-I	V-R
A	20.15±0.05	1.25±0.04	1.90±0.09	0.65±0.09

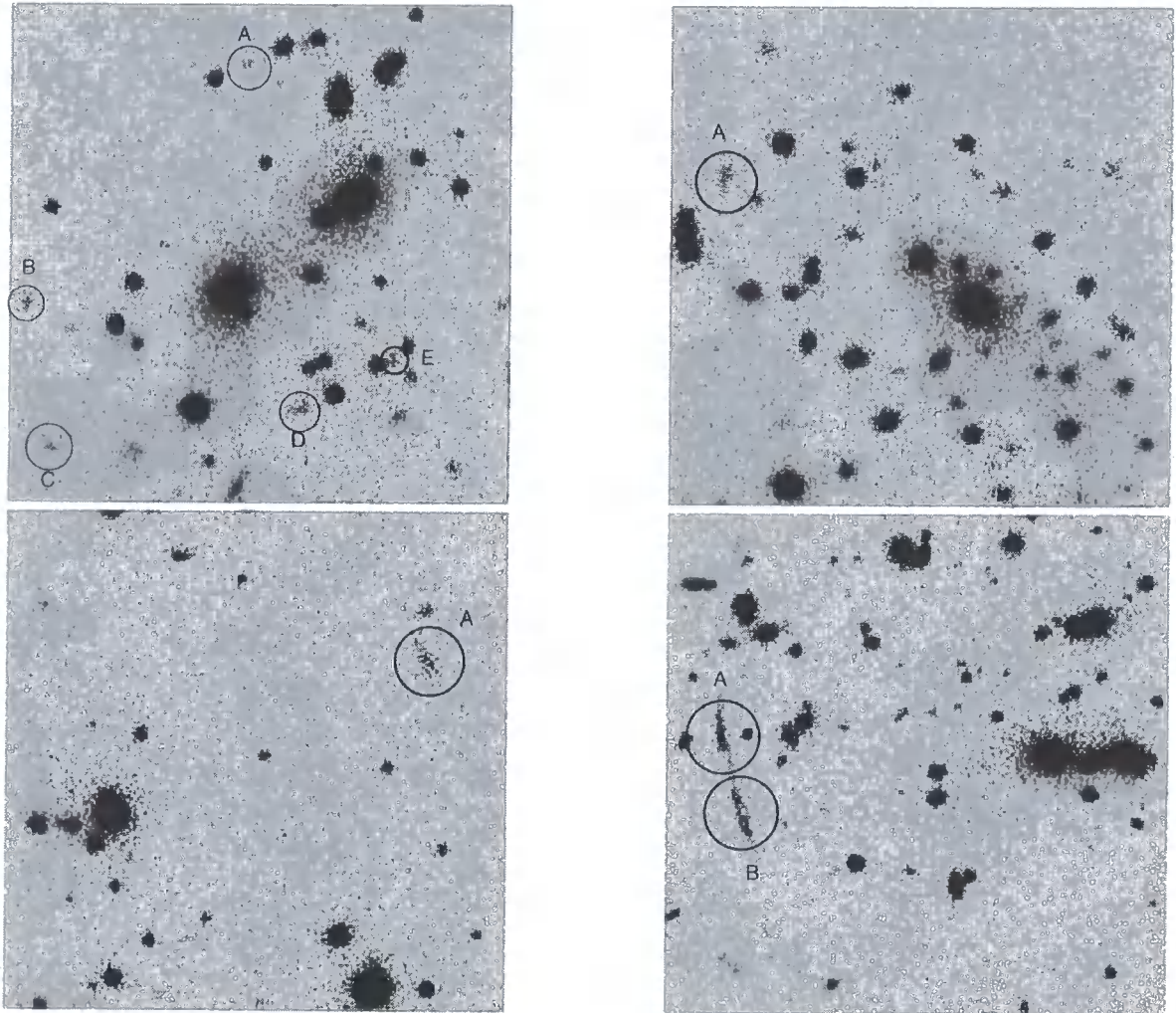


Figure 8.4: 1 arcmin² images showing gravitationally lensed galaxies in MACSJ0404.6+1109 (I-band, top left), MACSJ0416.1-2403 (R-band, top right), MACSJ0449.3-2848 (I-band, lower left) and MACSJ0451.9+0006 (R-band, lower right)

8.2.12 MACSJ0451.9+0006

This cluster is the well known cluster MS0451.6-0305. There is a very bright, double arc to the East of the cluster core, apparently made up of the image of two separate background galaxies.

ID	Mag _{app} (I-band)	R-I	V-I	V-R
A	21.34±0.07	0.21±0.04	0.48±0.08	0.27±0.07
B	20.51±0.06	0.59±0.04	0.76±0.08	0.17±0.07

8.2.13 MACSJ0520.7-1328

Another cluster with a single, red arc identified by its colour and tangentially distorted shape.

ID	Mag _{app} (I-band)	R-I	V-I	V-R
A	20.20±0.03	1.09±0.03	2.17±0.13	1.08±0.13

8.2.14 MACSJ0947.2+7623

There is one possible arc to the South-East of the BCG galaxy with a number of low surface brightness detections close by which could be counter-images of the same object. The photometry of this object appears to be contaminated by light from the halos of both the bright star and the BCG. The object to the West of the arc appears, by its colour, to be a cluster member galaxy.

ID	Mag _{app} (I-band)	R-I	V-I	V-R
A	21.34±0.09	1.19±0.10	1.18±0.07	-0.01±0.11

8.2.15 MACSJ0949.8+1708

There is a single, red arc to the North-East of the cluster core with no apparent counter-images.

ID	Mag _{app} (I-band)	R-I	V-I	V-R
A	20.83±0.07	1.09±0.07	1.86±0.08	0.77±0.10

8.2.16 MACSJ1115.2+5320

This cluster has a ring of apparently lensed objects, potentially all of the same background galaxy. The objects marked A and B in figure 8.5 appear to be 'normal' cluster gravitational arcs. Objects C and D appear as extremely disturbed objects and are obviously being effected by the gravitational fields of the nearby galaxies, which also contaminate the photometry for these objects. Object E is a very extended arc tracing the disturbance to the cluster gravitational potential by the bright galaxy to the South of the cluster core. This object, although obvious in the R-band image shown in figure 8.5, is not detected in the I-band image.

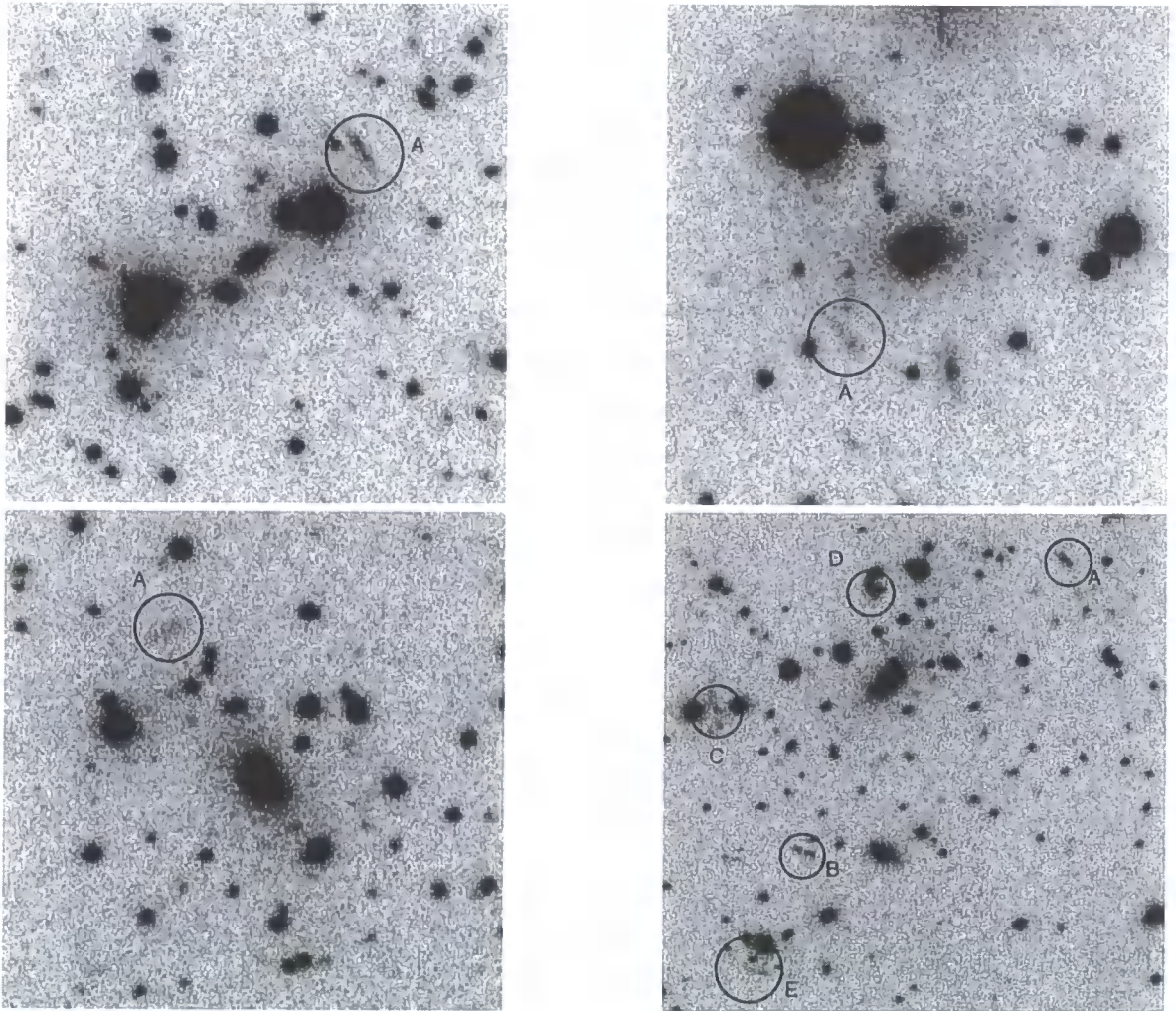


Figure 8.5: 1 arcmin² images showing gravitationally lensed galaxies in MACSJ0520.7-1328 (I-band, top left), MACSJ0947.2+7623 (R-band, top right), and MACSJ0949.8+1708 (R-band lower left.) The lower right hand panel shows a 1.5×1.5 arcmin R-band image showing the core of MACSJ1115.2+5320

ID	Mag _{app} (I-band)	R-I	V-I	V-R
A	21.27 ± 0.07	0.27 ± 0.06	0.57 ± 0.06	0.29 ± 0.05
B	22.54 ± 0.13	0.19 ± 0.10	0.38 ± 0.09	0.19 ± 0.08

8.2.17 MACSJ1133.2+5008

To the East of the cluster core is an unmistakable classic arc, bluer than the cluster members and tangentially curved although the photometry for this object appears to be flawed by the halo of the brightest cluster galaxy. Object B appears, by colour to be a counter-image of this object.

ID	Mag _{app} (I-band)	R-I	V-I	V-R
A	20.57±0.04	0.56±0.07	0.64±0.07	0.08±0.08
B	22.58±0.15	0.24±0.10	0.76±0.13	0.51±0.13

8.2.18 MACSJ1142.4+5831

The core of this cluster is quite complex with the two massive galaxies shown in figure 8.7 located a little away from the brightest cluster galaxies. Disturbed galaxy distributions and the, presumably, disturbed gravitational potentials that they trace makes spotting gravitational arcs more difficult. The bright, blue object (marked A) is located tangentially to the two massive galaxies and so is classified as being an arc candidate. The smaller, fainter, object (B) is of a similar colour to A and is marked as being a possible counter-image to this galaxy, although it is too faint to be detected in the I-band.

ID	Mag _{app} (I-band)	R-I	V-I	V-R
A	20.49±0.06	0.22±0.09	0.28±0.10	0.05±0.06

8.2.19 MACSJ1206.2-0847

This cluster contains one of the most spectacular arcs discovered in the MACS survey. There are three images of what appear to be the same galaxy, a giant arc to the West of the cluster core, a counter-image to the North-West and another to the South-East. Unfortunately, the South-East counter-image appears to be blended with a cluster galaxy, distorting its apparent colour.

As well as the V,R and I band imaging taken for the rest of the MACS clusters, this cluster was also imaged in the J and K bands by Dr A. Edge using UFTI on the United Kingdom Infra-Red telescope during a period of good seeing on the 5th April 2001.

In order to measure a 'correct' aperture magnitude for the giant arc, seeing matched frames were produced by applying a Gaussian smoothing to the J and K band frames to match the V,R and I band seeing matched frames produced as part of the MACS standard photometry pipeline. Photometry of the giant arc was then performed by manually defining an aperture fitted to the arc profile. The area

defined by this mask was then masked out of the science frame and a background image produced by median smoothing over the absent arc. This background image was then subtracted from the science image and the aperture applied to the resulting sky-subtracted images to obtain V,R,I,J and K band photometry.

ID	V	R	I	J	K	R-I	V-I	V-R	R-J	R-K	J-K
A	19.27	20.27	20.99	17.82	15.95	1.00	1.72	0.72	2.45	4.32	1.87
B	20.41	21.34	21.93	18.88	17.14	0.93	1.52	0.59	2.46	4.20	1.74
C	19.66	20.35	21.11	18.43	16.58	0.69	1.44	0.75	1.92	3.77	1.85

Multiple band photometry allows the classification of the background lensed galaxy. Standard template spectral energy distributions of 5 galaxy types were redshifted to match that of the giant arc, the redshift has been measured to be 1.036 (Ebeling et al 2003.) The filter response curves of each of the V, R, I, J and K bands were then convolved with these spectral energy distributions and normalised to the R-band to produce predicted colours for each of the 5 galaxy types at the redshift of the arc, all relative to the R-band. These model $m_\lambda - m_R$ colours were then compared against the equivalent observed colours and are shown in figure 8.6. The colour distribution of this arc is consistent with the background galaxy being a normal spiral of class Sbc.

8.2.20 MACSJ1226.8+2153

MACSJ1226.8+2153 is another cluster containing an unmistakable arc. Bluer than the other cluster member galaxies and tangentially curved, there is little doubt as to the identification of this object as a gravitationally lensed galaxy. The object marked B is a possible counter-image for this galaxy due to its similar (in V-R) colour, although it is bluer than the giant arc in R-I and V-I.

ID	Mag _{app} (I-band)	R-I	V-I	V-R
A	20.69±0.04	0.30±0.03	0.67±0.05	0.37±0.05
B	21.68±0.10	0.06±0.06	0.36±0.09	0.30±0.08

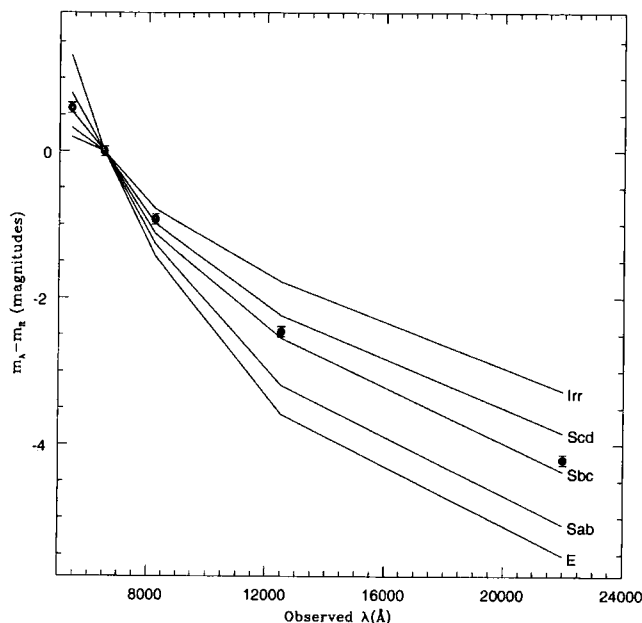


Figure 8.6: R-band relative colours of the giant arc in MACSJ1206.2-0847 shown against the predicted colours of 5 template galaxies redshifted to that of the lensed galaxy.

8.2.21 MACSJ1305.9+2630

This object has been selected because of its tangentially elongated shape. There is a very faint, low surface brightness object to the East of the BCG which supports this being a lensing cluster, although this object is not detected in the I band frame and so there is no photometry available for this object.

ID	Mag _{app} (I-band)	R-I	V-I	V-R
A	19.84±0.04	0.71±0.03	1.12±0.05	0.40±0.05

8.2.22 MACSJ1319.9+7003

This object in MACSJ1319.9+7003 is extremely red, suggesting that it is behind the cluster and therefore lensed. There is a second object (in the centre near the bottom of the image shown in figure 8.8) which, at first inspection appears to be an arc candidate. However this object has not been selected as its colour suggests that it is foreground to the cluster and its morphology appears to curve away from the brightest cluster galaxy, rather than curving tangentially around it as would be expected for a lensed object.

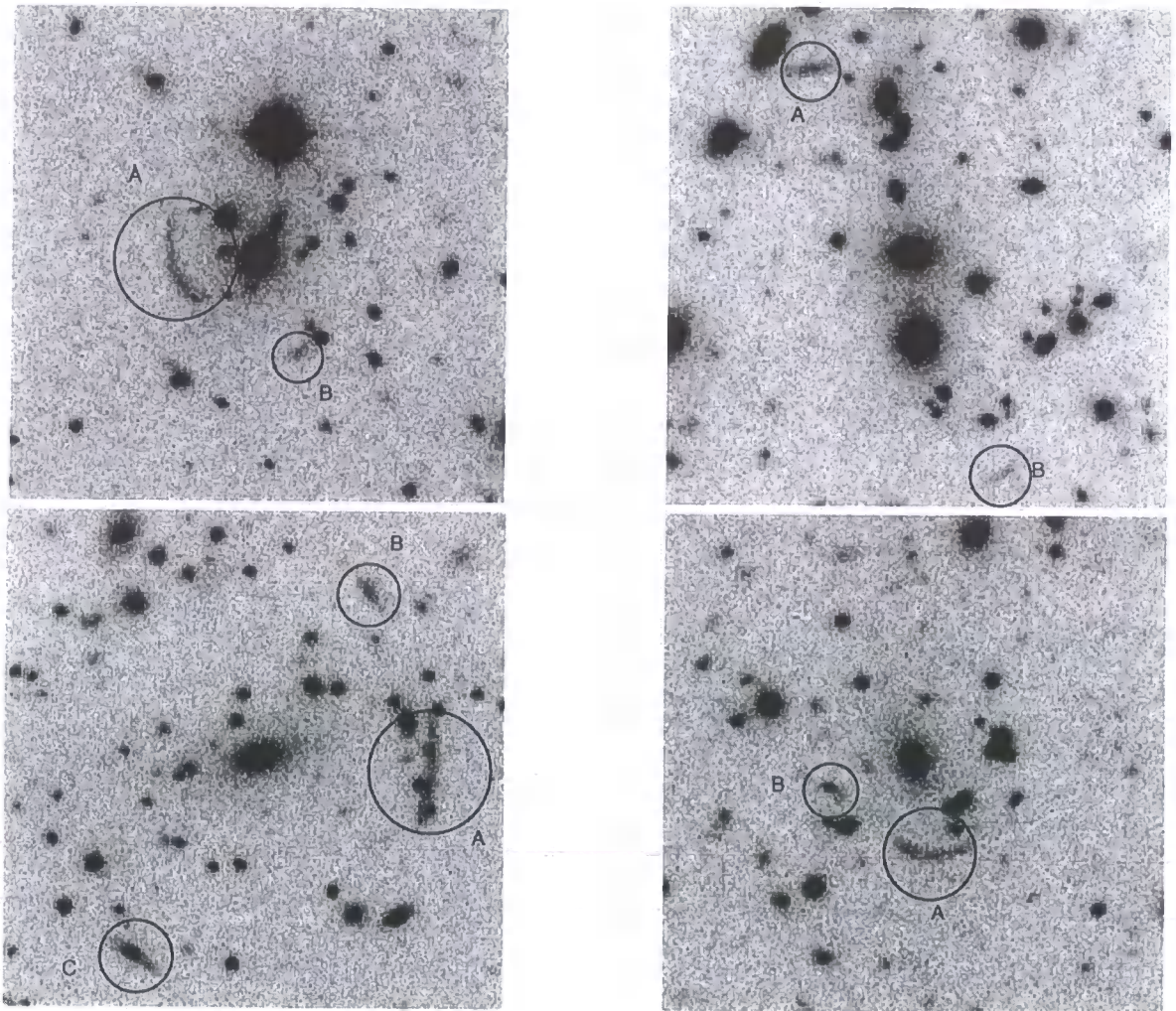


Figure 8.7: 1×1 arcmin images showing gravitational arcs in MACSJ1133.2+5008 (R-band top left), MACSJ1142.4+5831 (R-band top right), MACSJ1206.2-0847 (I-band, lower left) and MACSJ1226.8+2153 (R-band, lower right.)

ID	Mag_{app} (I-band)	R-I	V-I	V-R
A	20.19 ± 0.06	1.48 ± 0.04	2.42 ± 0.15	0.94 ± 0.15

8.2.23 MACSJ1347.5-1144

Another tangential arc, curving around the apparent core of the cluster. Although clear in the R-band image shown in figure 8.8, this object is too faint in the I-band image for it to be detected. These arcs are not new discoveries and details of the lensing features in this cluster can be found in Sahu et al. (1998) and Ravindranath et al. (2002).

8.2.24 MACSJ1354.6+7715

Another cluster with a clear tangential arc close to the cluster core.

ID	Mag_{app} (I-band)	R-I	V-I	V-R
A	21.64 ± 0.17	0.72 ± 0.10	0.83 ± 0.13	0.11 ± 0.14

8.2.25 MACSJ1526.7+1647

Unfortunately blended with several cluster galaxies, there is an extended giant arc visible to the East of the core of the cluster

8.2.26 MACSJ1738.1+6006

As in the previous cluster, unfortunately blended with both a cluster member galaxy and the halo of the brightest cluster galaxy, there is a short arc to the South-East of the BCG.

ID	Mag_{app} (I-band)	R-I	V-I	V-R
A	22.26 ± 0.10	0.80 ± 0.15	1.15 ± 0.13	0.35 ± 0.16

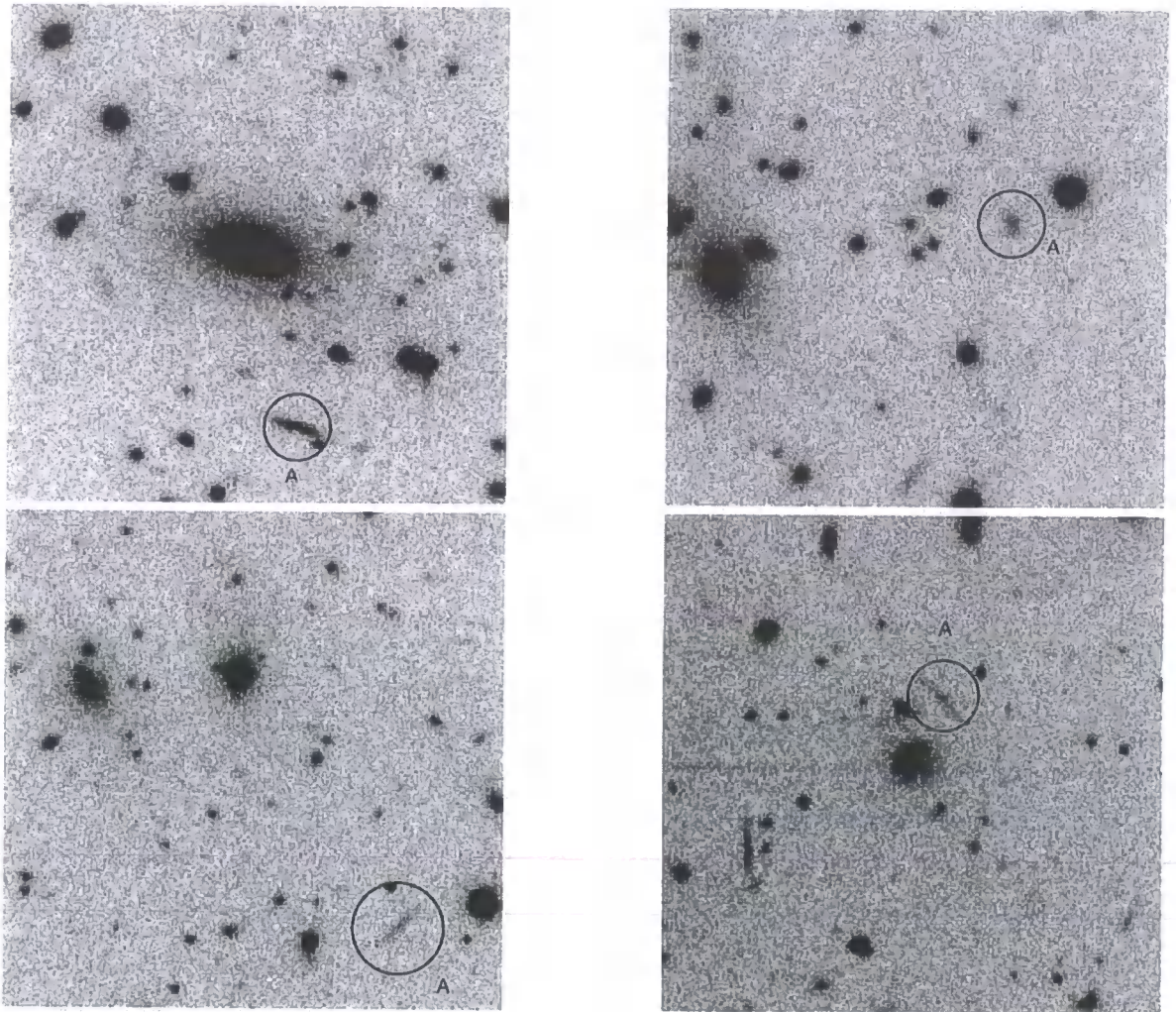


Figure 8.8: 1×1 arcmin images showing the cores and lensed objects in MACSJ1305.9+2630 (R-band, top left), MACSJ1319.9+7003 (I-band, top right), MACSJ1347.5-1144 (R-band, lower left) and MACSJ1354.6+7715 (R-band, lower right)

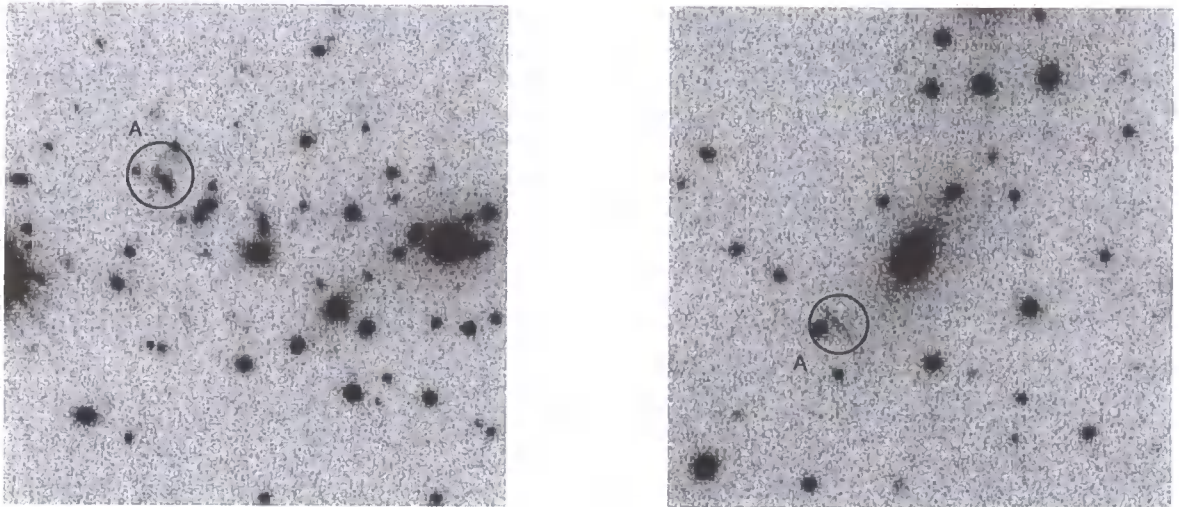


Figure 8.9: 1×1 arcmin images showing the cores and lensed objects in MACSJ1526.7+1647 (R-band, left) and MACSJ1738.1+6006 (I-band, right)

8.3 A Ram pressure stripped galaxy?

The left panel of figure 8.10 shows a galaxy observed in the field of MACSJ0451.9+0006 using WFPC2 on-board the Hubble Space Telescope. While this galaxy is clearly foreground to the cluster, it does show an extremely disturbed morphology, with pieces of the galaxy appearing as though they are falling away from the main disc of material. This morphology is reminiscent of N-body simulations of ram-pressure stripped galaxies, used as an explanation of the apparent evolution spiral galaxies into elliptical galaxies as they fall into, particularly rich, cluster. The right-hand panel of figure 8.10 shows a simulation, taken from Quillis et al. 2000, of a galaxy being stripped of its cold gas by the relative wind of the intra-cluster medium as the, once normal spiral, galaxy falls into a rich cluster.

8.4 Conclusions

This chapter has aimed to catalogue noteworthy objects, mainly gravitational arcs, detected as part of the MACS multi-colour imaging campaign. In total, 26 clusters show signs of strong lensing, 23% of the total number, which is a similar proportion to that of 8 lensing clusters found in a survey of 38 EMSS clusters by Luppino et al. (1999). These objects have been identified by visual examination of the cluster

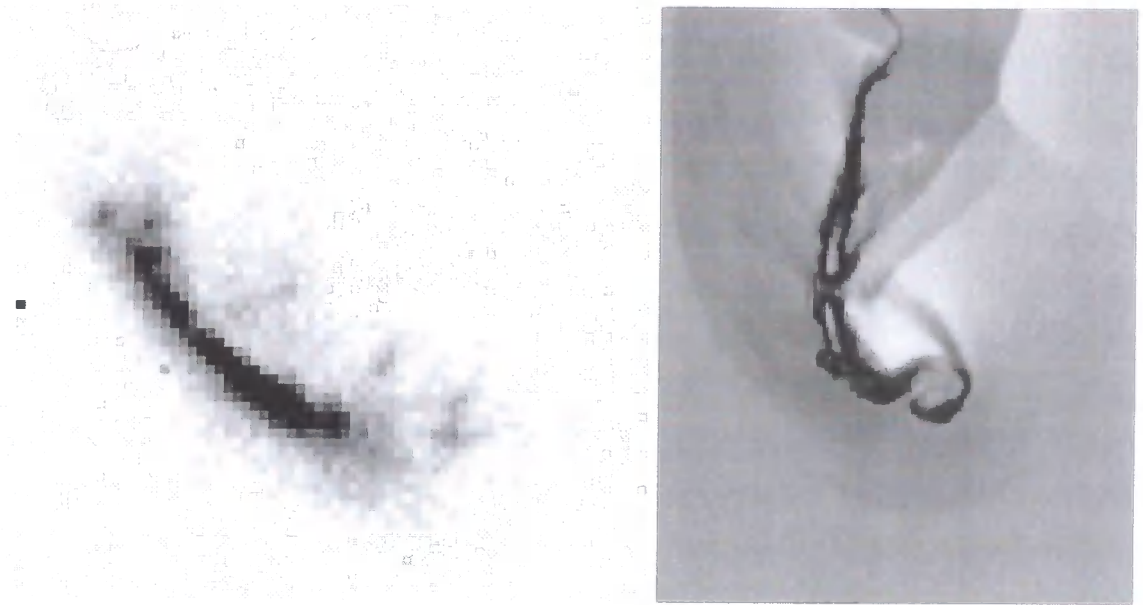


Figure 8.10: Left: 7×7 arcsec WFPC2 image of a possible ram-pressure stripped galaxy in the field of MACSJ0451.9+0006. Right: N-body simulation of a spiral galaxy being stripped of its gas by the intra-cluster medium (taken from Quillis et al. 2000)

images and so it is entirely possible that there are additional objects that have been missed by this method as gravitational arcs are predominantly identified by their morphologies and so the efficiency of detecting this objects is dependent upon the seeing conditions.

Also shown is an example of what appears to be a ram-pressure stripped galaxy, detecting in the field of MACSJ0451.9+0006.

Chapter 9

Conclusions

This thesis has concerned itself with the multi-band imaging taken as part of the follow-up campaign to the Massive Cluster Survey, an X-ray selected sample of massive galaxy clusters at redshifts greater than 0.3. As such, the data presented in this thesis represents the largest currently available sample of clusters in this redshift and X-ray luminosity range.

In chapter one, the aims of this thesis were laid out, being concerned with the analysis of the multi-band imaging taken as part of the follow-up campaign of the Massive Cluster Survey. In particular, the following goals were identified:

- Provide accurate photometry for galaxies in the field of the candidate clusters and establish accurate astrometry for these objects to allow spectroscopic follow-up to confirm their identification as massive clusters through their velocity dispersions.
- Develop reliable methods for selecting cluster member galaxies and use those selected galaxies to independently measure the richness of the MACS cluster candidates to confirm the presence of a cluster sufficiently massive to account for the X-ray emission
- Establish a method of measuring photometric redshifts appropriate to rich clusters at these redshifts to allow the identification and immediate follow-up of the most interesting, highest redshift clusters in future surveys.
- Assess the possibility of contamination of the observed X-ray flux from objects such as AGN, or processes such as mergers, that may act to boost the X-ray emission
- Identify individual objects of scientific interest that warrant more in-depth study.

In chapter 2 the data reduction process applied to the V, R and I band imaging was described and the method by which the MACS photometry was performed. The effect of the seeing on the derived aperture magnitudes was discussed in detail, with particular attention paid to the success of techniques for star-galaxy separation as a function of the accuracy of determining the seeing conditions. The automated technique for measuring the seeing was outlined along with the process by which the variable seeing conditions were accounted for through the production of seeing matched frames.

In chapter 3, the properties of the galaxian population residing in the MACS clusters was examined. Colour-magnitude diagrams of the 111 MACS clusters imaged to date were produced using the V, R and I band seeing matched aperture magnitudes and the I band total magnitude, these diagrams are presented in appendix A. The cluster red-sequence was then fitted using a robust bi-weight routine, the slope of this fit being used to constrain the star-formation epoch of the MACS cluster galaxies to being at high ($z > 1.7$) redshift, in agreement with previous work on the subject. The slope of the fit to the red-sequence of all clusters at $z < 0.4$ was tested against the X-ray luminosity of the host cluster as an indicator of whether the slope of the cluster sequence was affected by cluster richness. No trend was found with luminosity, confirming that the cluster red-sequence appears to be as universal in clusters at these redshifts as it is in nearby clusters.

The fit to the red-sequence was then established as a basis for a photometric redshift by producing a characteristic colour for each cluster by evaluating the fit to the red-sequence at 19th magnitude in the I band. This colour appears to trace the expected colour for an elliptical galaxy at the appropriate redshift with errors of only 0.042 mag in R-I, 0.063 in V-I and 0.057 in V-R, making this an acceptable basis for measuring photometric redshifts.

The richness of the MACS clusters was then examined using first a traditional number counting method, which was found to be unreliable and then an aperture Virial radius. The calculated Virial radii showed sufficient resolving power to identify one MACS cluster that does not appear to be sufficiently rich to account for its X-ray luminosity.

Finally in chapter 3, the symmetry properties of the MACS clusters were ex-

amined as a tracer of merger activity. No trend was found in the cluster symmetry with either redshift or X-ray luminosity, demonstrating that the MACS survey is not biased towards, or against, merging systems.

In chapter 4, the properties of the Brightest Cluster Galaxy (BCG) population were investigated. The effectiveness of several magnitude measurement on this population was investigated with, in particular, the total magnitudes of these objects being found to be unreliable. The degree to which the BCG dominates the rest of the cluster population was examined and found to show no trend with either redshift or X-ray luminosity. The presence of highly dominant BCG galaxies at all redshifts is taken as an indication that this population has already undergone significant evolution before the epoch examined here and the large range of degrees of dominance indicates that this evolution is continuing at the observed epoch.

The colours of the BCG population were examined and found to show a similar distribution and scatter to that found for the evaluated colour of the cluster red-sequence but with a sizable tail of object bluer than would be expected containing up to a quarter of all BCGs. This blue tail was interpreted as being due to activity, in the form of either AGN or star-formation, and is half the figure of 50% required by numerical simulations (as suggested by Quillis et al. 2001) to dampen cooling flows.

A strong co-alignment of the BCG and its host cluster was found and is interpreted as evidence that BCG galaxies grow by preferentially accreting galaxies from in-falling groups.

In Chapter 5, the photometric redshift techniques developed in the preceding chapters were applied to a sample of clusters observed as part of an extension to the MACS survey below declination -27 degrees to provide targets for SZ observations based at the South Pole. The redshift distribution of clusters, based upon the estimated redshifts, found during these observations was found to be in agreement with the distribution of the main MACS survey.

Chapter 6 showed an example of the multi-object spectroscopy of two clusters observed with the 8m Gemini telescope on Hawaii. The apparent velocity dispersions of these two clusters (MACS1720.2+3536 and MACSJ1731.6+2252) were found to be 834 Km/s and 1130 Km/s, respectively confirming that these really are

massive clusters. Colour-magnitude diagrams of spectroscopically confirmed cluster member galaxies were then produced using multi-object spectroscopy taken using the Keck telescope. These diagrams were used to demonstrate that the primary source of error on the fits to the cluster red-sequences is due to the errors inherent in the photometry, caused by the modest depth of the imaging data, rather than the object selection technique.

The possibility of contamination due to AGN was discussed in chapter 7. A cross-correlation of the Veron-Cetty Veron AGN catalogue with the Abell cluster catalogue was used to track the projected spatial density and velocity dispersion of AGN associated with cluster on 4Mpc and 10Mpc scales. AGN were found to be distributed apparently at random within the clusters making AGN contamination in unresolved X-ray surveys a distinct possibility.

Finally, in chapter 8, a miscellany of objects, primarily gravitationally lensed objects, was presented for future study. In total, gravitationally lensed objects are seen in 26 clusters, 23% of the number observed, a figure which should be taken as only a lower limit to the incidence of lensing in clusters at these redshifts.

Future Work

So, what does the future hold for the MACS survey? This thesis has shown that the technique used by the MACS team for selecting clusters is extremely efficient one, with only a single questionable detection. Following this success, this technique is to be extended to both cover a larger area (the beginnings of this extension being shown in chapter 5) and in depth; the ROSAT all-sky survey does not have uniform depth and so there are areas in which the flux limit can be pushed lower.

As for what can be done with the MACS clusters themselves, that is limited only by the imagination of those that choose to study these clusters in more depth, it is hoped that studies of clusters that at the current time concentrate on well known clusters at lower redshifts will be able to use the MACS clusters to extend their studies to higher redshifts.

The V, R and I band imaging presented here is not the only part of the follow-up programme being undertaken by the other members of the MACS collaboration.

A sub-sample of clusters is being imaged using the SuprimCam instrument on the Japanese 8 metre Subaru telescope to allow weak-lensing analysis to be performed to determine the distribution of mass within these clusters. Hubble Space Telescope ACS data is also being obtained for the MACS clusters at $z > 0.5$ to allow the accurate identification of high redshift gravitationally lensed objects. Sunyaev-Zel'dovich effect observations of MACS clusters have also been made and the first results published in LaRoque et al. (2003). Returning to the X-ray, where the MACS survey originated, Chandra data is being obtained to more accurately measure the X-ray luminosity of these clusters, identify contaminating point-sources and to allow the study of the gas dynamics in the cores of these clusters.

The author of this thesis wishes the future generations of astronomers good fortune, fair weather and that his efforts in this work will prove to be of some help in this, the oldest of the sciences.

Chapter A

MACS

Colour-Magnitude

diagrams

In chapter 3, the method by which colour-magnitude diagrams were produced for the 111 currently observed MACS cluster was described, these colour-magnitude diagrams are presented in full in thesis appendix.

The clusters are listed in Right-Ascension order and for each cluster three colour-magnitude diagrams are shown; R-I, V-I and V-R aperture colours against I band total magnitude. The colour-magnitude diagrams contain all objects classified as being a galaxy within the field of the UH 2.2m observations (approximately 7.3×7.2 arcminutes.) The solid line on each diagram shows the bi-weight fit to the cluster red-sequence. All clusters are presented in this appendix, regardless of whether the cluster observations were deemed to be photometric.

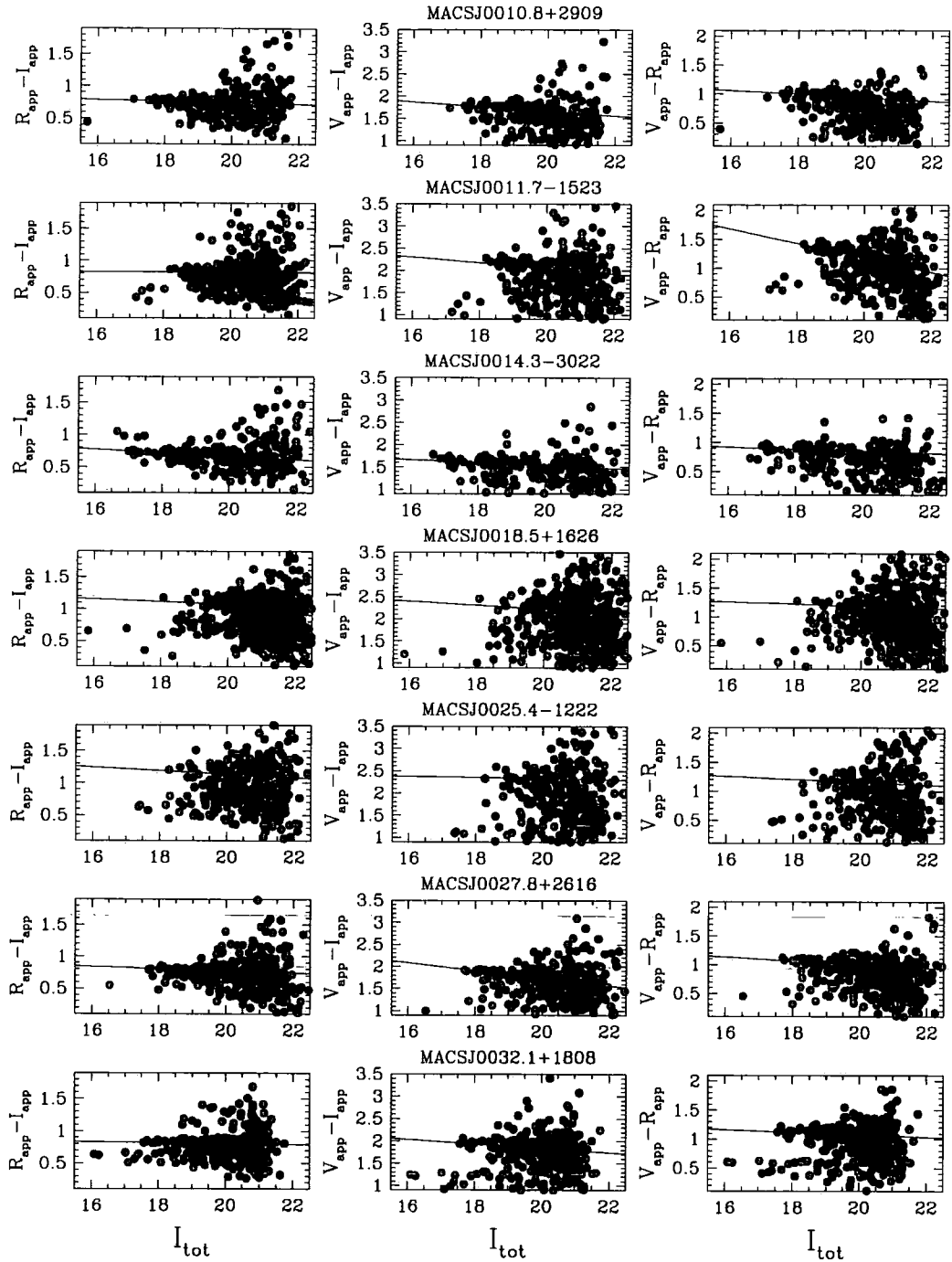
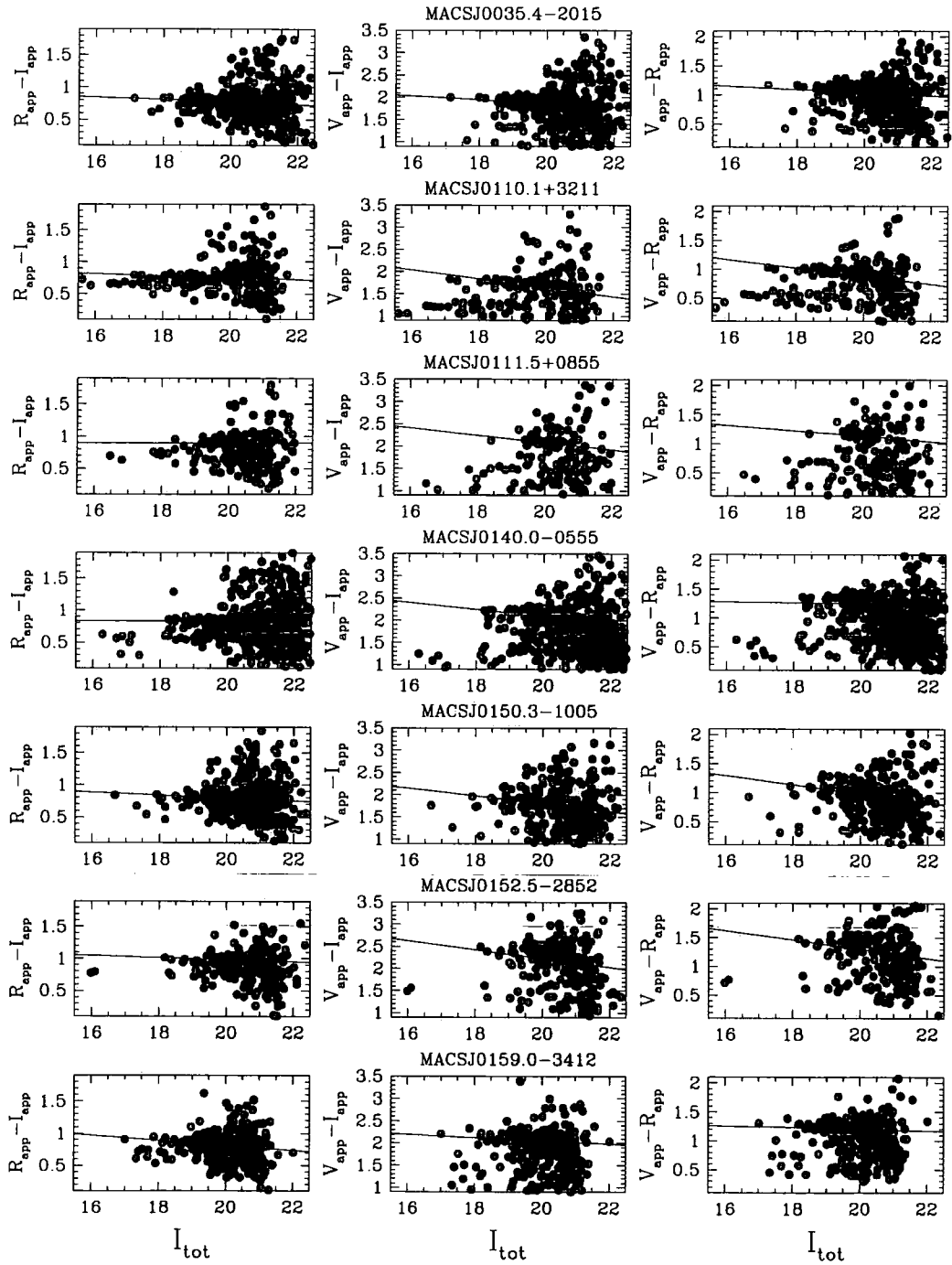
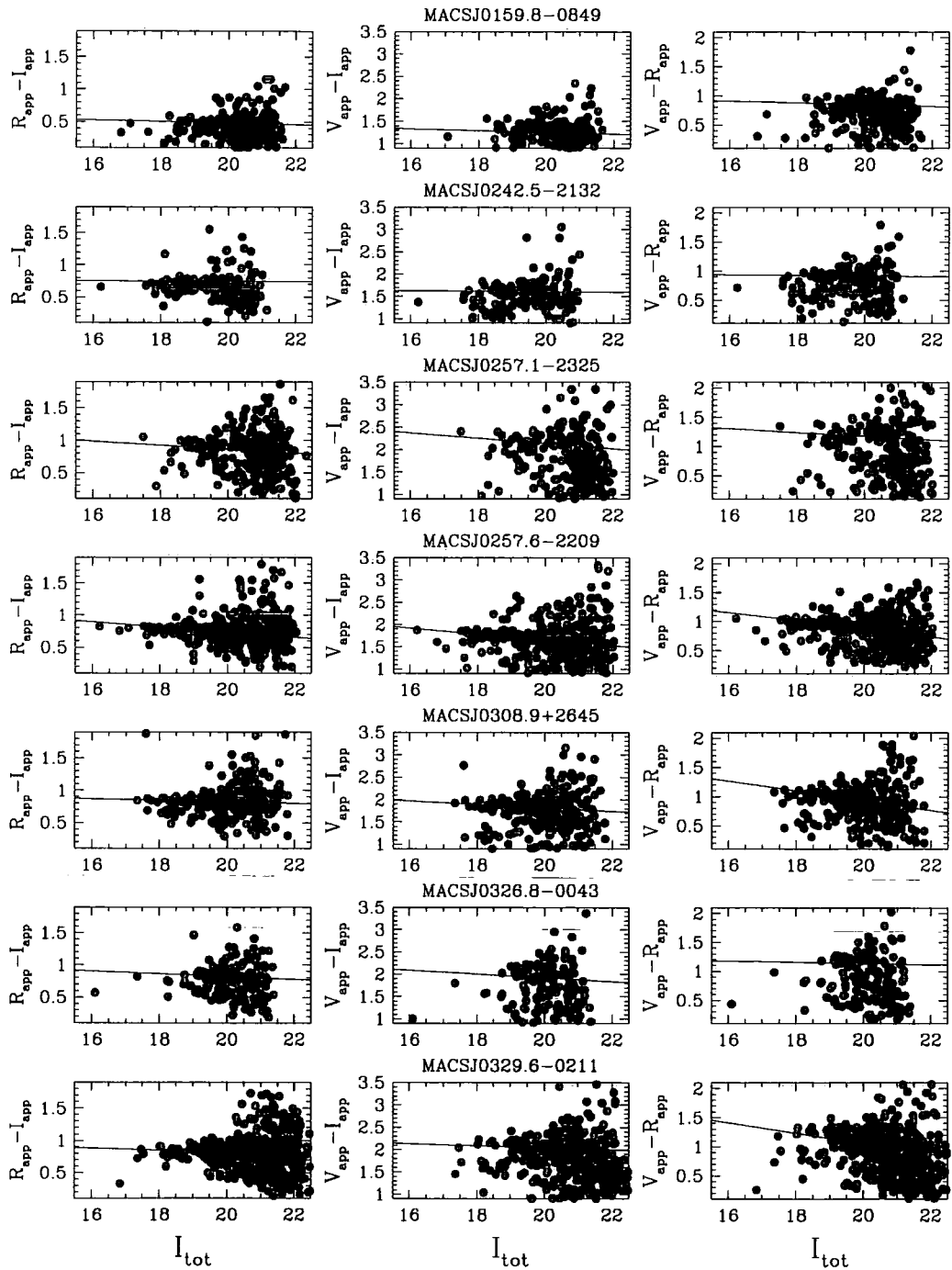
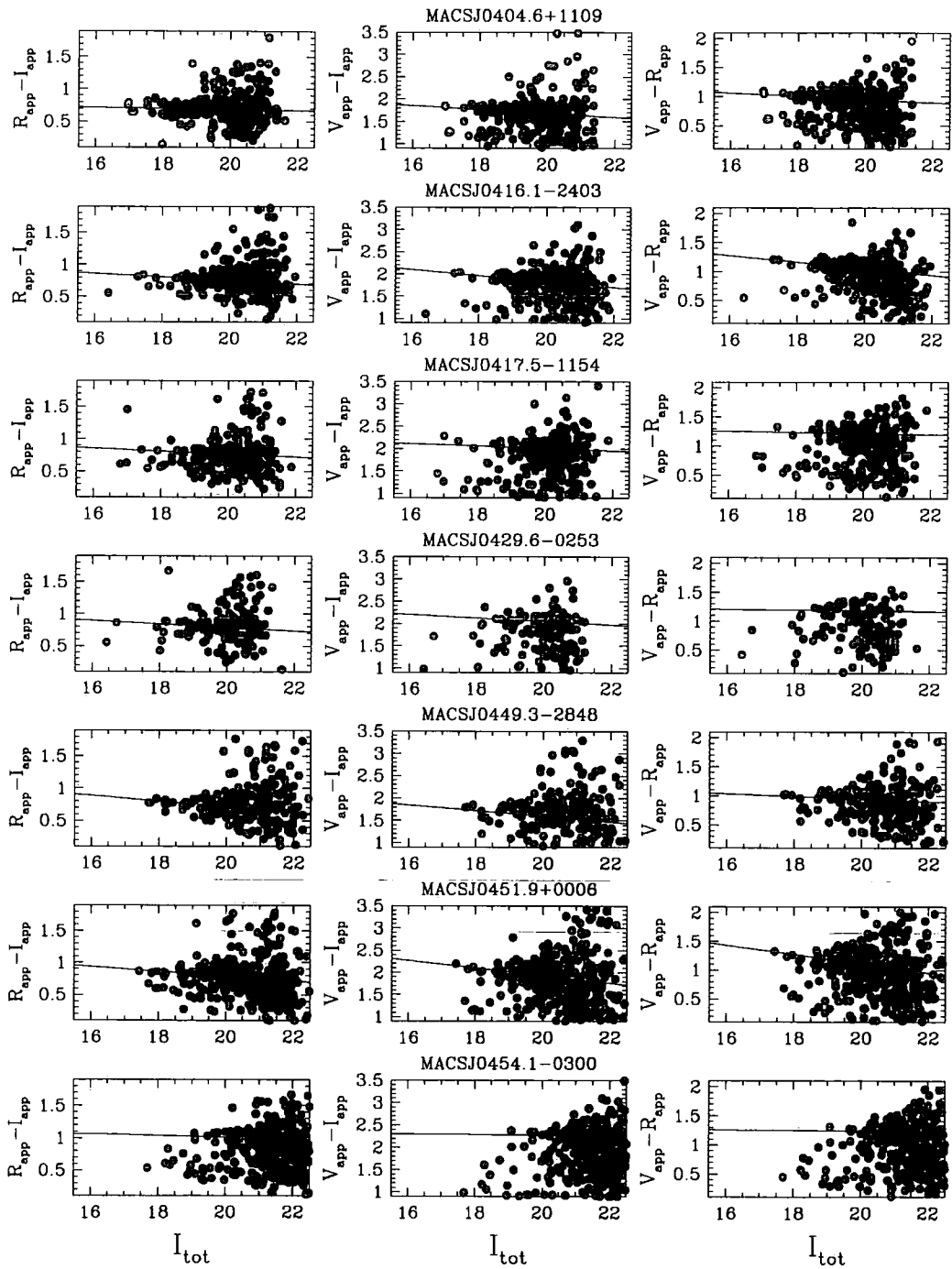
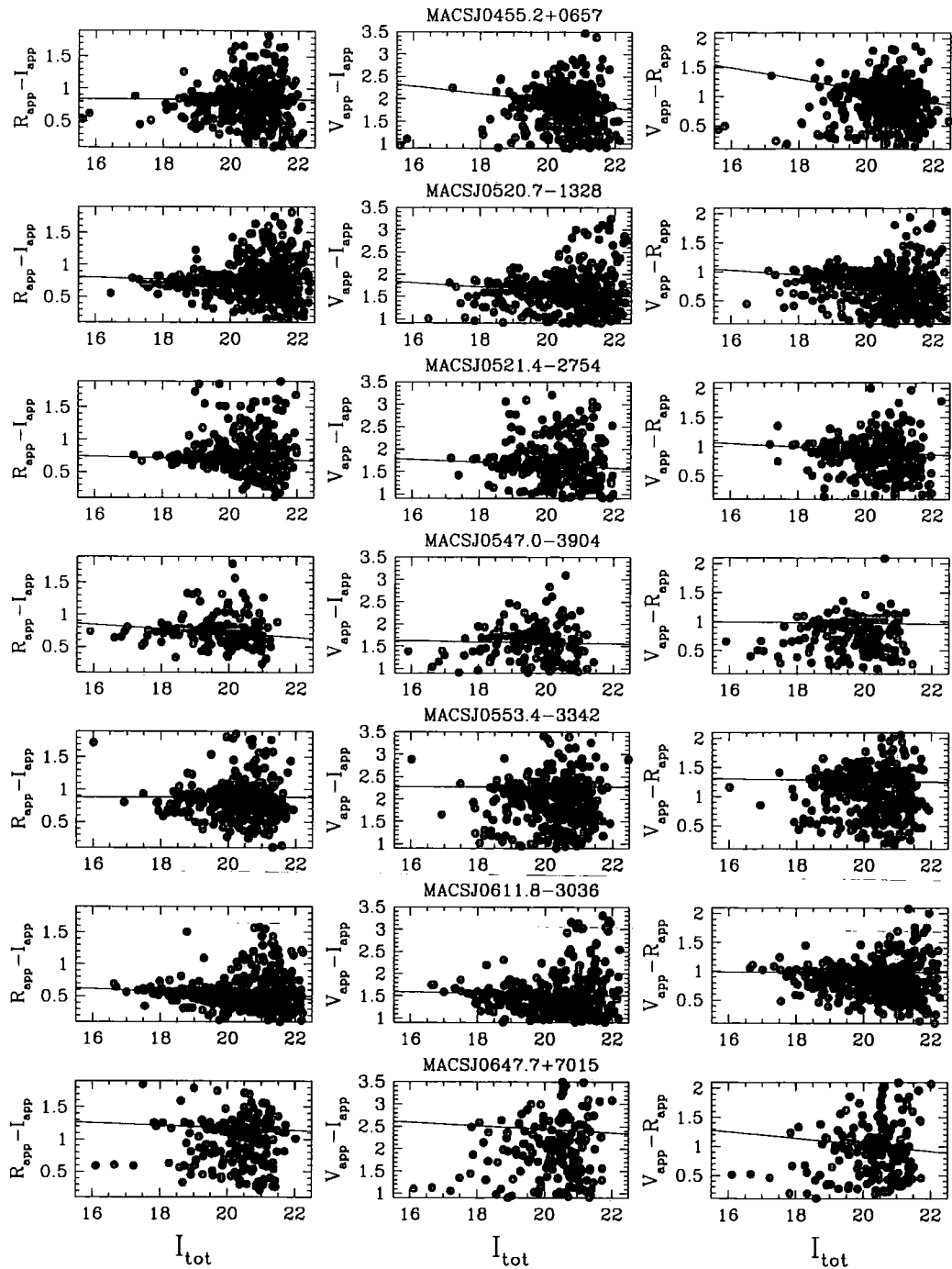


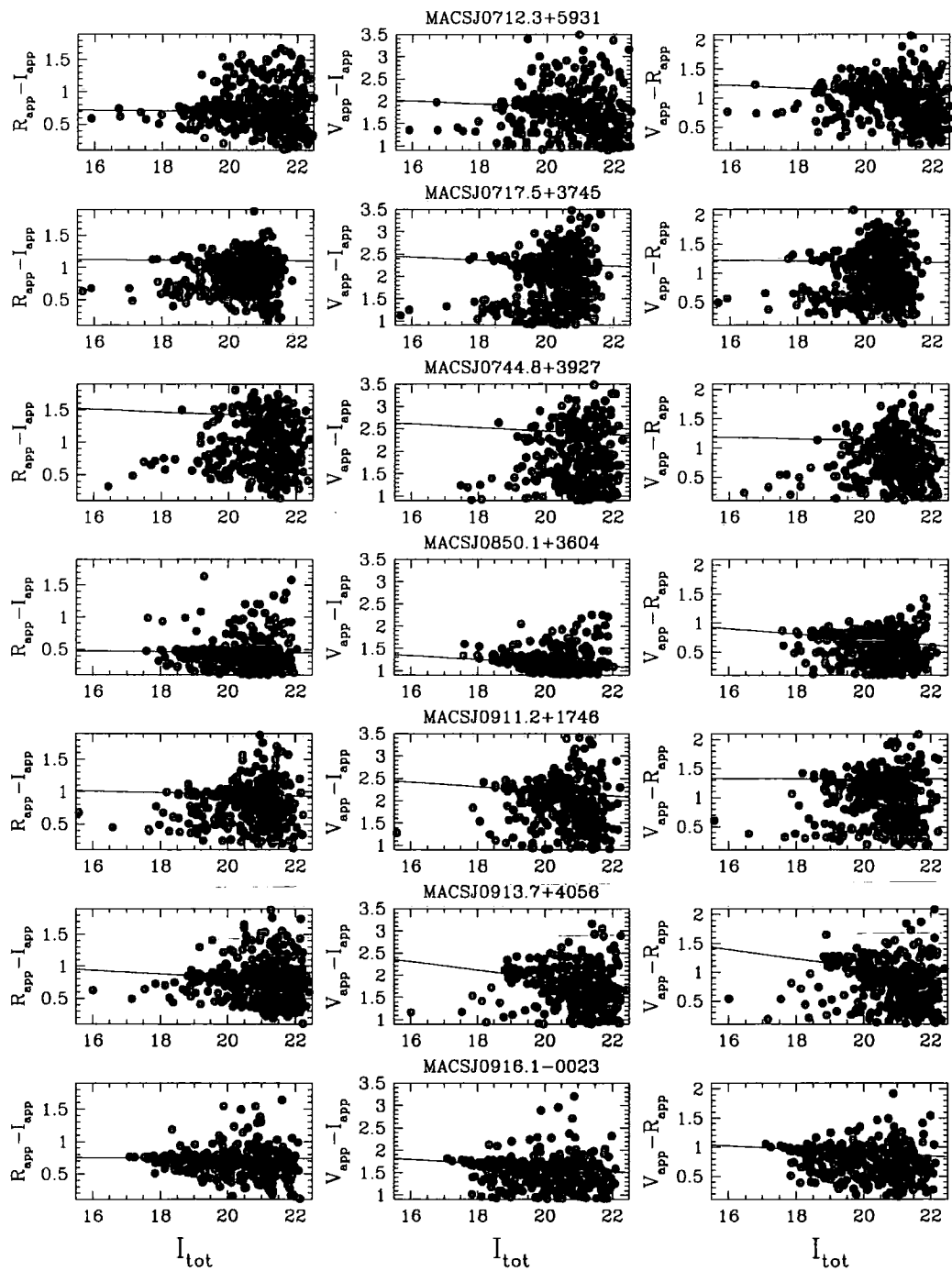
Figure A.1: Colour-magnitude diagrams of clusters in the MACS survey

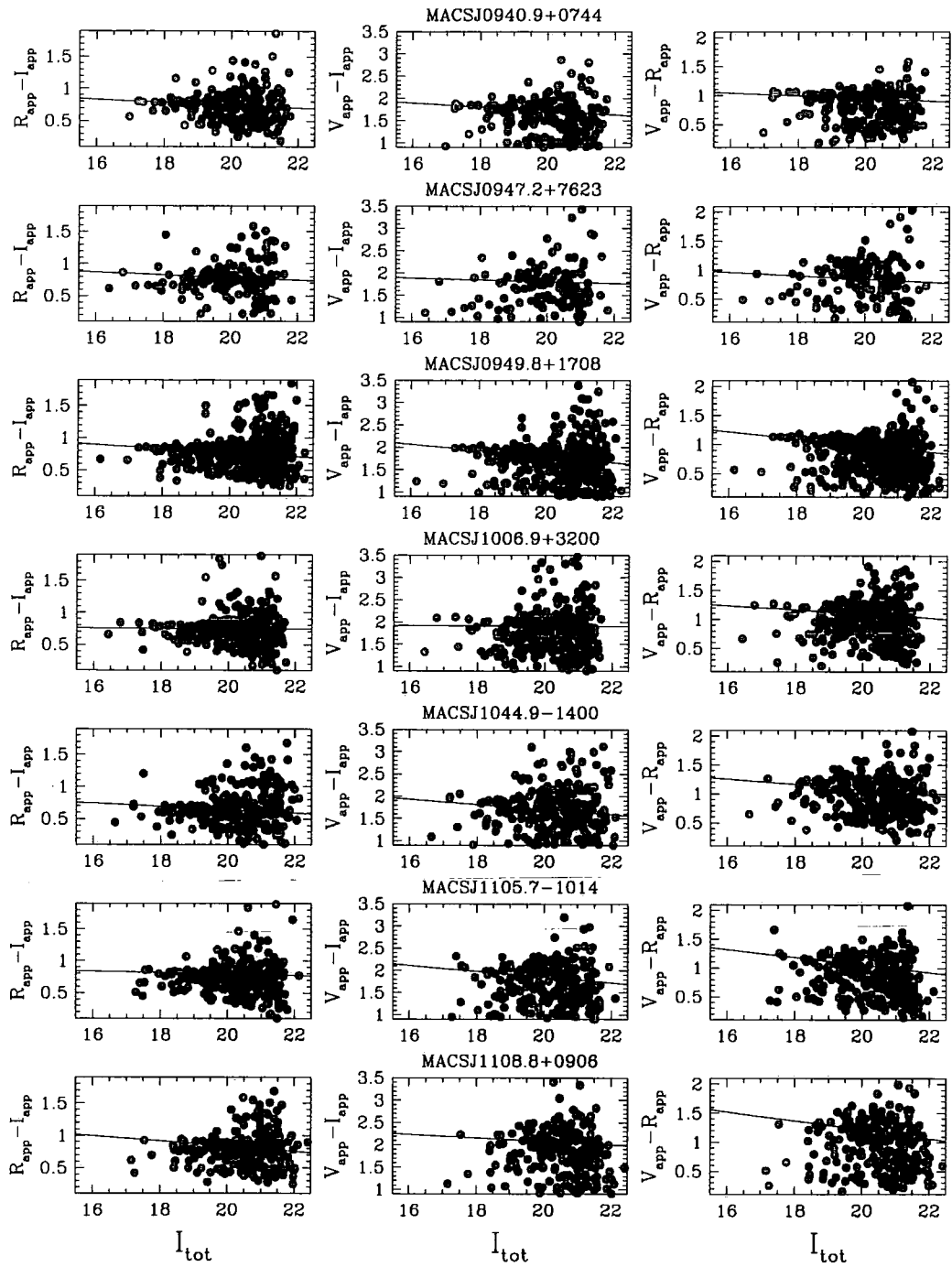


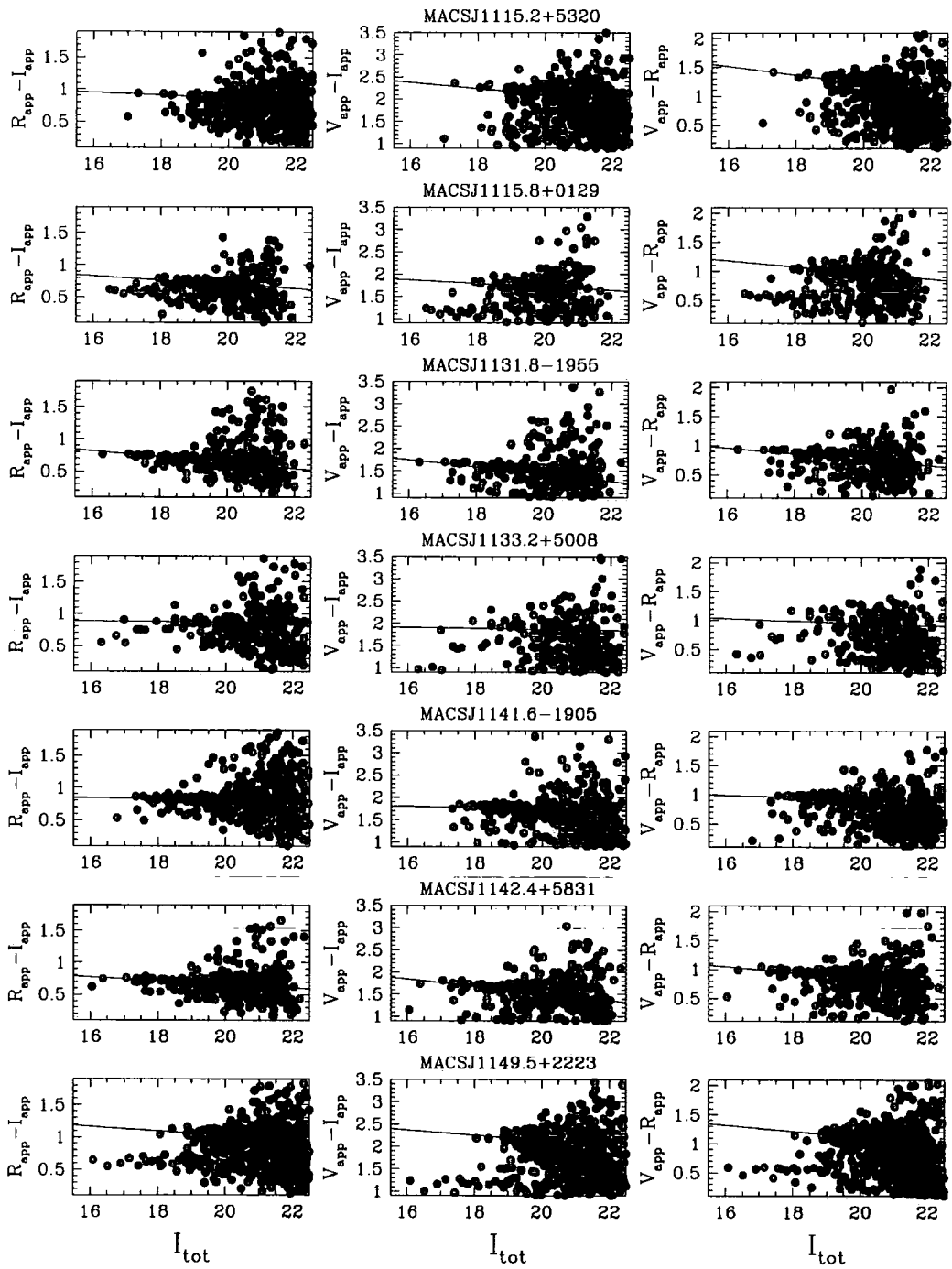


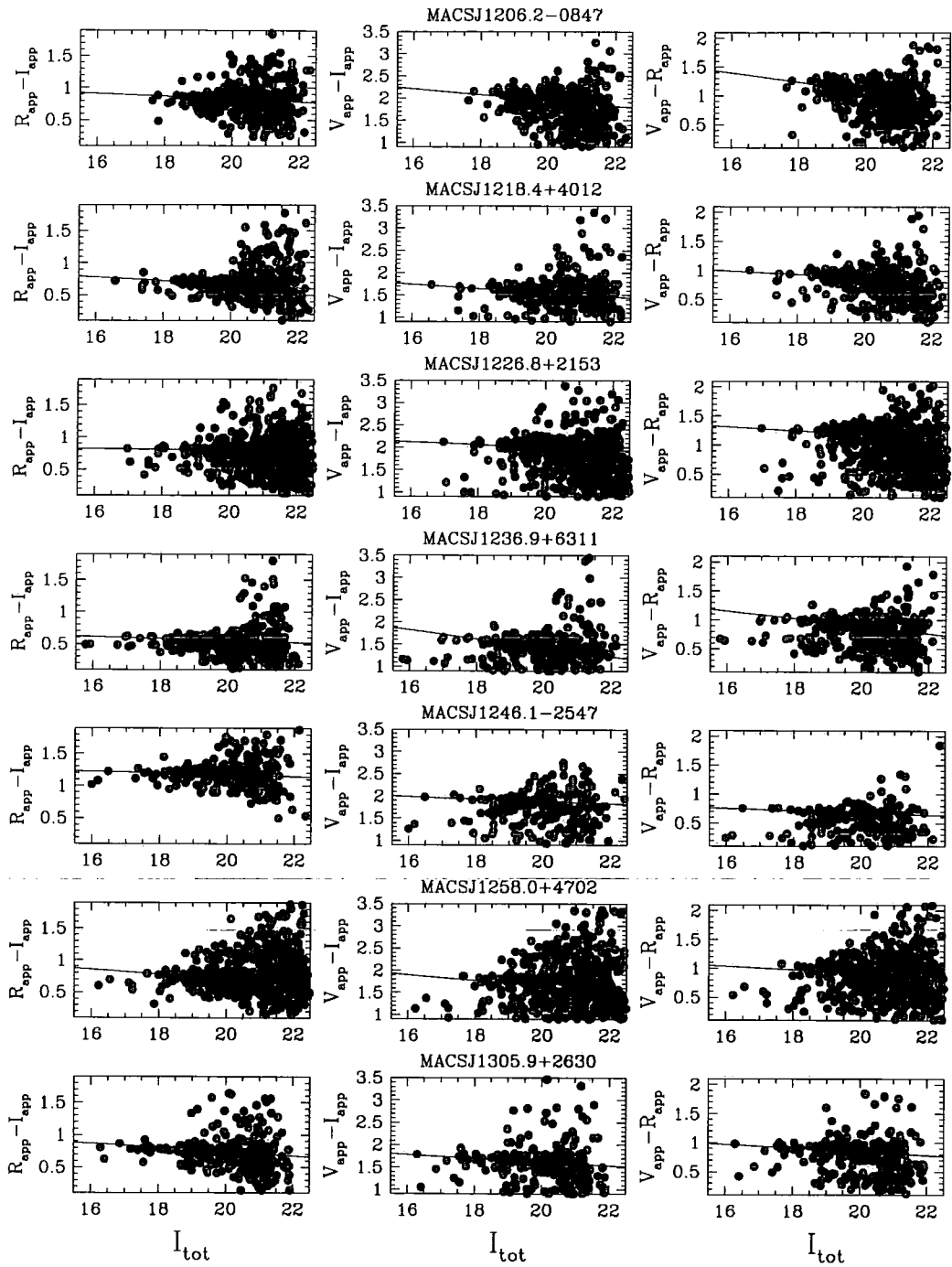


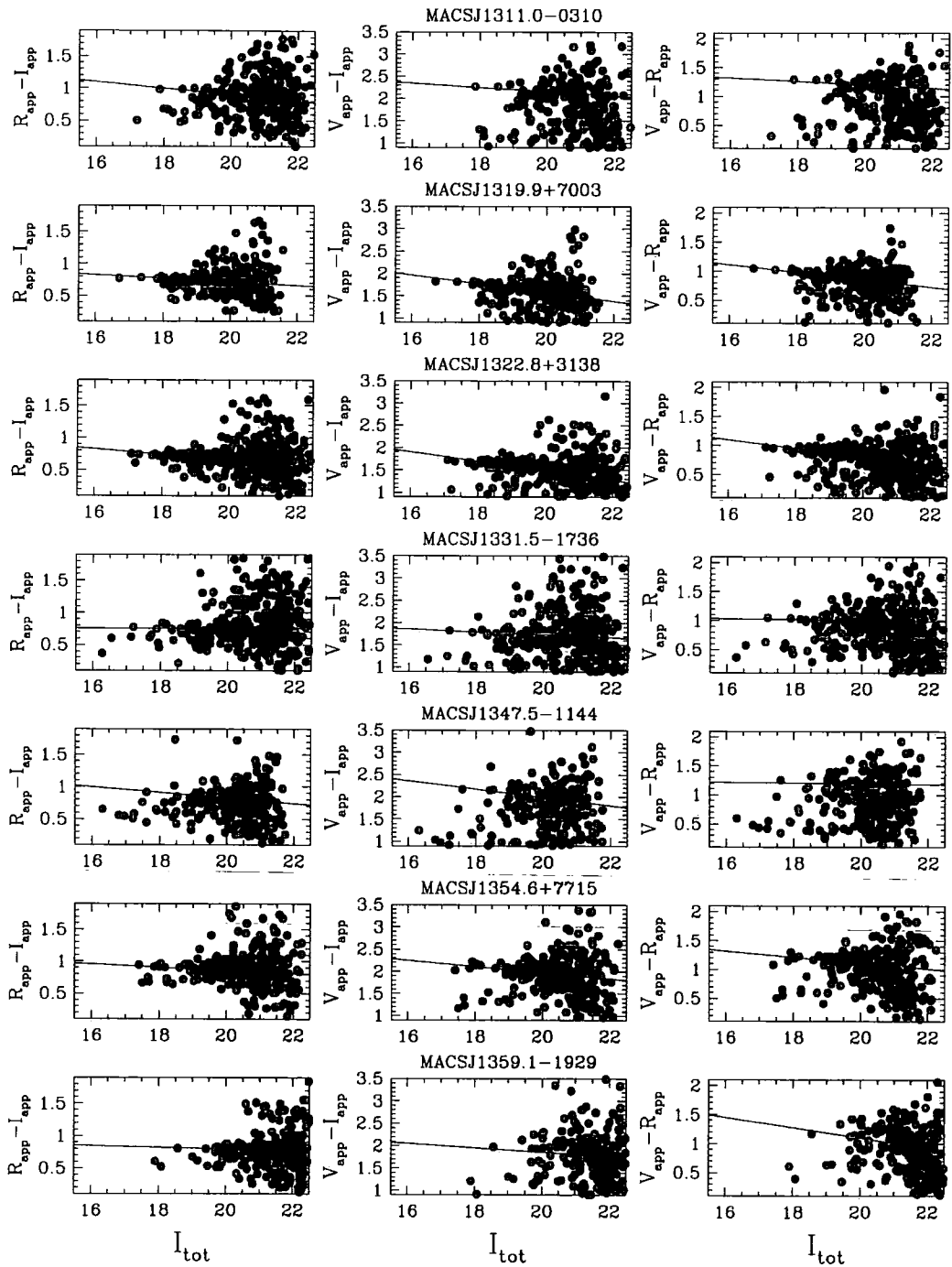


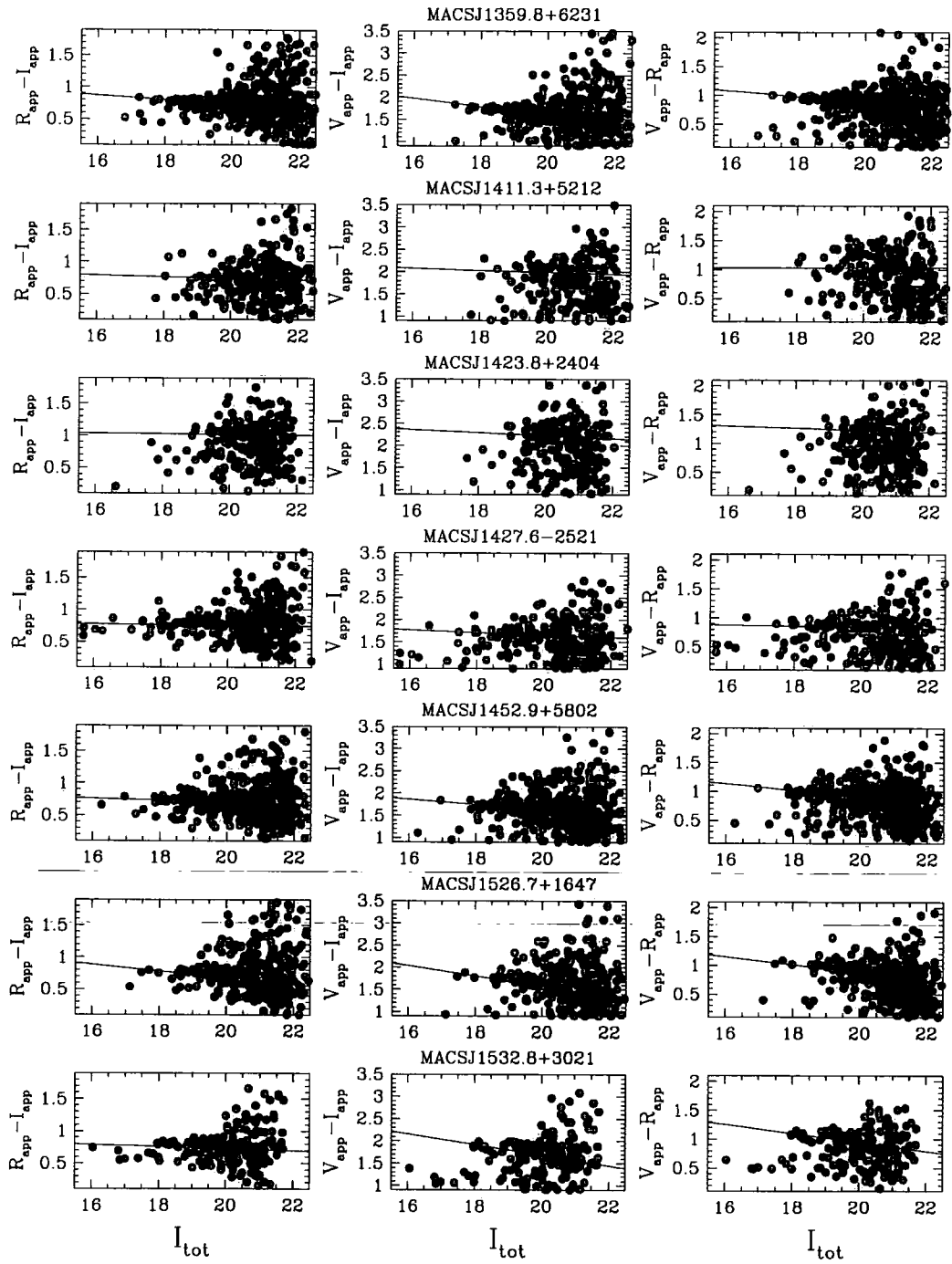


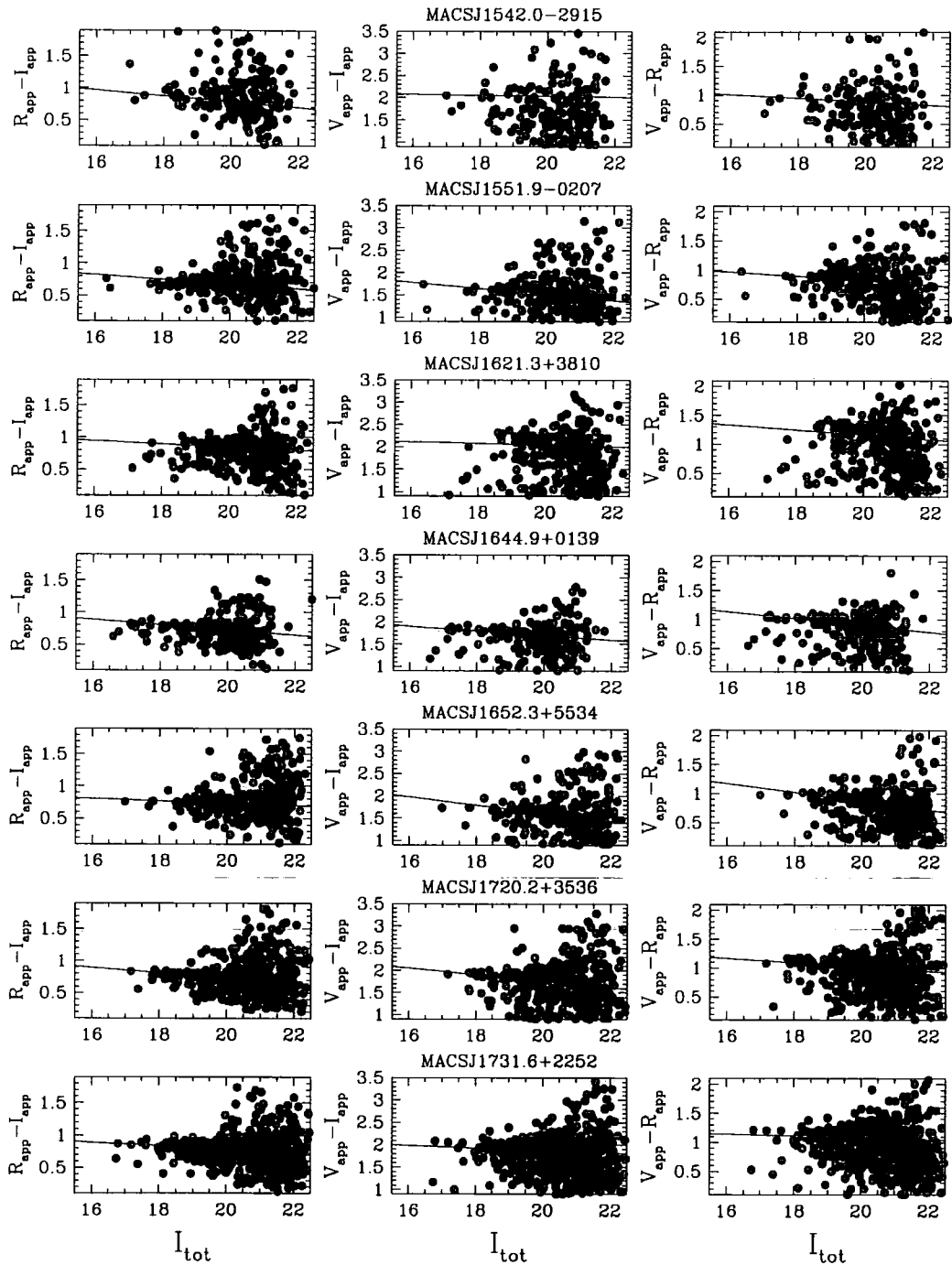


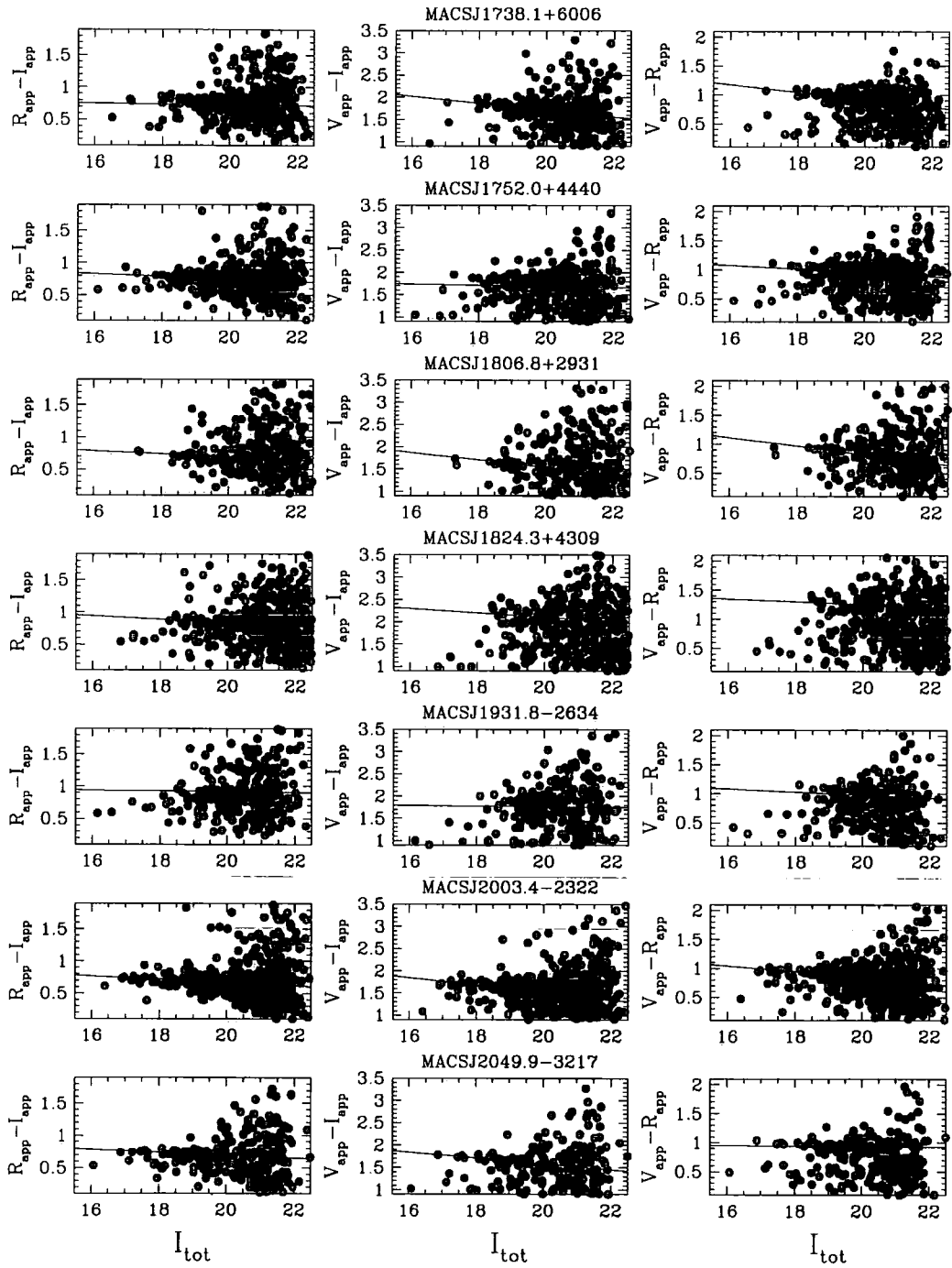


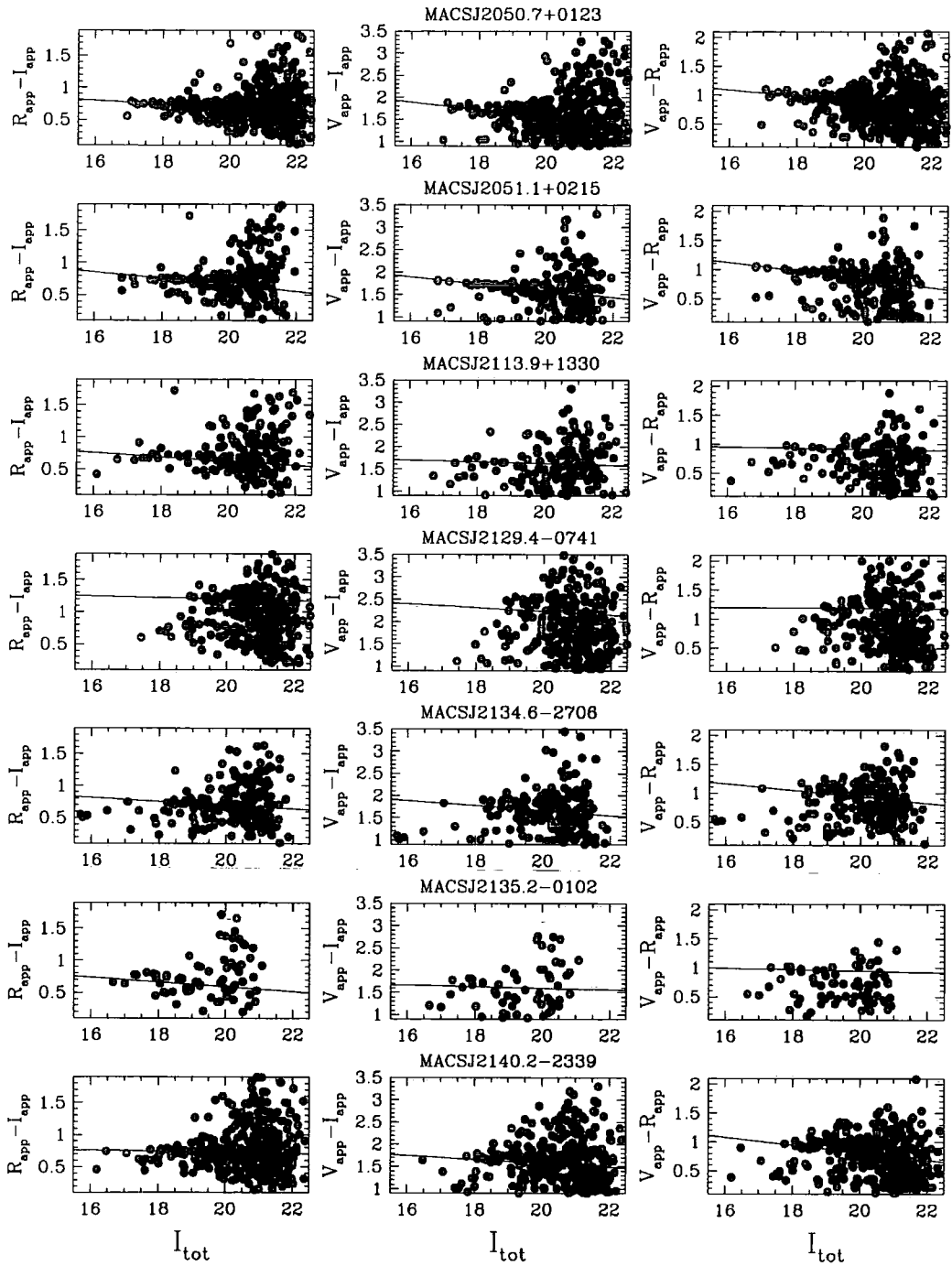


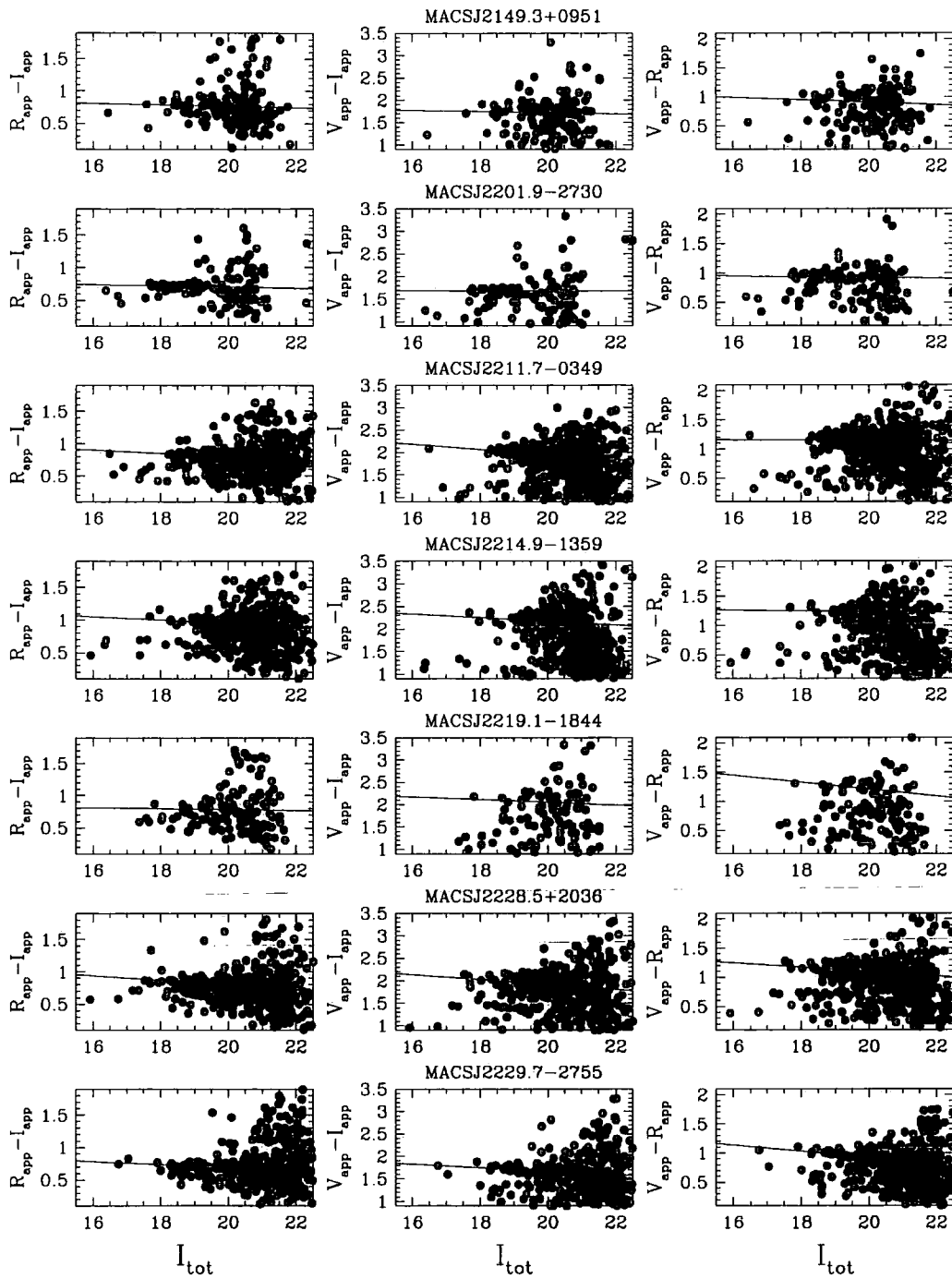


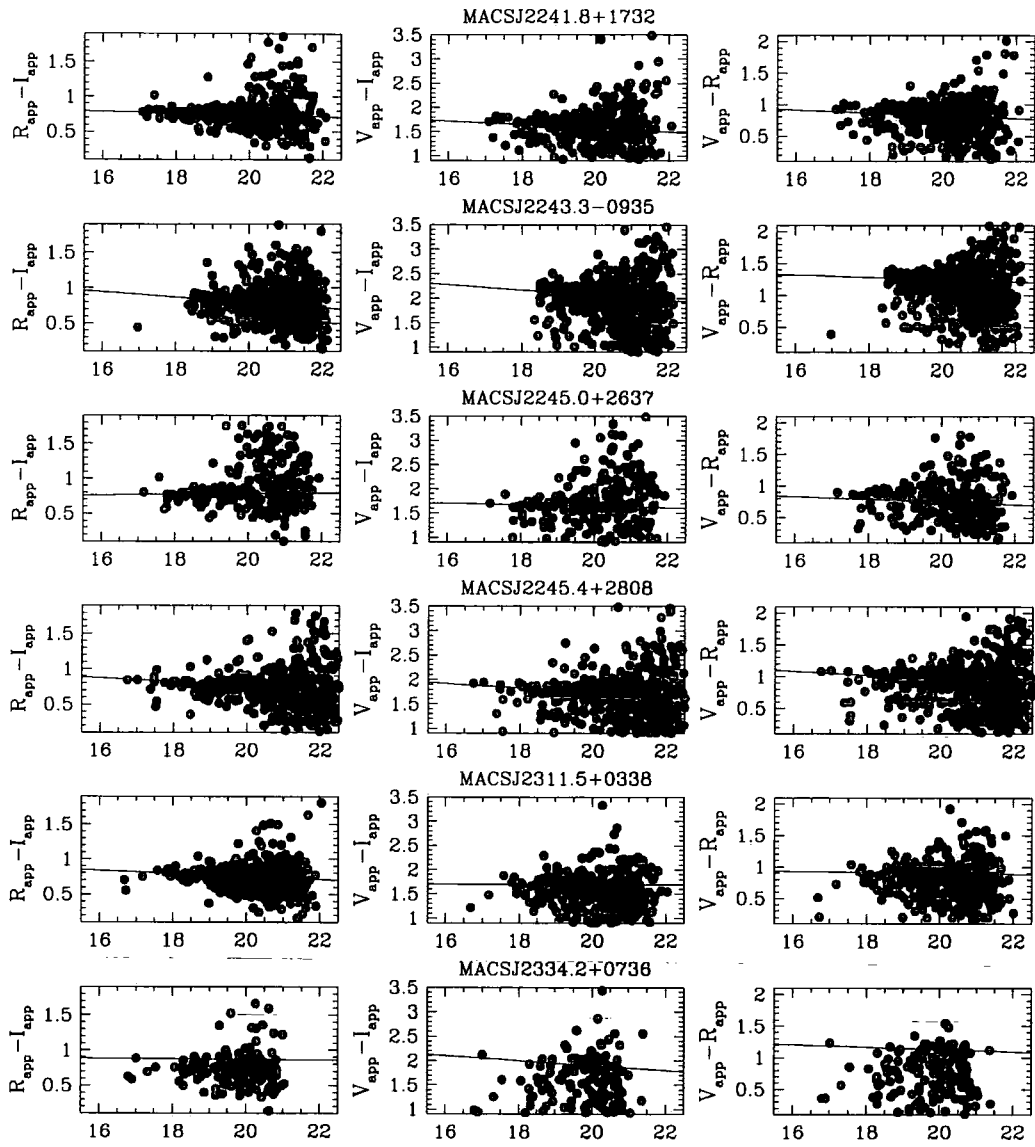












Bibliography

The following abbreviations are used in this bibliography:

A&A: Astronomy and Astrophysics

A&AS: Astronomy and Astrophysics Supplement

AAS: American Astronomical Society

AJ: The Astronomical Journal

ApJ: The Astrophysical Journal

ApJS: The Astrophysical Journal Supplement

ARA&A: Annual Reviews of Astronomy and Astrophysics

CUP: Cambridge University Press

ESO Sci. Rep.: ESO Scientific Report

HEAD: AAS High Energy Astrophysics Division Meeting

IAUS: International Astronomical Union. Symposium

MNRAS: Monthly Notices of the Royal Astronomical Society

Obs: The Observatory

PASJ: Publications of the Astronomical Society of Japan

PASP: Publication of the Astronomical Society of the Pacific

RA: Ricerche Astronomiche Specola Vaticana

RvMP: Reviews of Modern Physics

Sci : Science

SPIE: The International Society for Optical Engineering

- Abell, George O. 1958 *ApJS*, 3, 211
- Abell, George O.; Corwin, Harold G., Jr.; Olowin, Ronald P. 1989 *ApJS*, 70, 1
- Abraham, Roberto G.; Valdes, Francisco; Yee, H. K. C.; van den Bergh, Sidney
1994 *ApJ*, 432, 75
- Allen, S. W. 1995 *MNRAS*, 276, 947
- Allen, S. W.; Fabian, A. C.; Johnstone, R. M.; Arnaud, K. A.; Nulsen, P. E. J.
2001 *MNRAS*, 322, 589
- Allen, S. W.; Taylor, G. B.; Nulsen, P. E. J.; Johnstone, R. M.; David, L. P.; Ettori,
S.; Fabian, A. C.; Forman, W.; Jones, C.; McNamara, B. 2001 *MNRAS*, 324, 842
- Antonucci, R. R. J.; Miller, J. S. 1985 *ApJ*, 297, 621
- Antonucci, Robert 1993 *ARA&A*, 31, 473
- Aragón-Salamanca, A; Baugh, C. M.; Kauffmann, G 1998 *MNRAS*, 297 427
- Bahcall, N. A. 1975 *ApJ*, 198, 249
- Bahcall, N. A. 1977 *ARA&A*, 15, 505
- Barcons, X.; Carrera, F. J.; Ceballos, M. T. 2003 *MNRAS*, 339, 757
- Bartlett, J. G. Tracing Cosmic Evolution with Galaxy Clusters. ASP Conference
Proceedings, Edited by Stefano Borgani, Marino Mezzetti, and Riccardo Val-
darnini. 2002, 268, 101
- Beers, Timothy C.; Flynn, Kevin; Gebhardt, Karl 1990 *AJ*, 100, 32
- Benson, A. J.; Cole, S.; Frenk, C. S.; Baugh, C. M.; Lacey, C. G. 2000 *MNRAS*,
311, 793
- Bertin, E.; Arnouts, S. 1996 *A&AS*, 117, 393
- Binggeli, B. 1982 *A&A*, 107, 338
- Birkinshaw, Mark 2000 *IAUS*, 201, 30

- Böhringer, H.; Schuecker, P.; Guzzo, L.; Collins, C. A.; Voges, W.; Schindler, S.; Neumann, D. M.; Cruddace, R. G.; De Grandi, S.; Chincarini, G.; Edge, A. C.; MacGillivray, H. T.; Shaver, P. 2001 *A&A*, 369, 826
- Bower, Richard G.; Lucey, J. R.; Ellis, Richard S. 1992 *MNRAS*, 254, 589
- Brough, S.; Collins, C. A.; Burke, D. J.; Mann, R. G.; Lynam, P. D. 2002 *MNRAS*, 329, 53
- Brough, S. *Brightest Cluster Galaxies* University of Durham Astronomy Seminar 2003.
- Cardiel, N.; Gorgas, J.; Aragón-Salamanca, A. 1998 *MNRAS*, 298, 977
- Colless, Matthew; Dunn, Andrew M. 1996 *ApJ* 458, 435
- Collins, C. A., Guzzo, L., Nichol, R. C., Lumsden, S. L. 1995, *MNRAS*, 274, 1071
- Collins, C. A.; Mann, R. G. 1998 *MNRAS*, 297, 128
- Cole, Shaun; Lacey, Cedric G.; Baugh, Carlton M.; Frenk, Carlos S. 2000 *MNRAS*, 319, 168
- Crawford, C. S.; Allen, S. W.; Ebeling, H.; Edge, A. C.; Fabian, A. C. 1999 *MNRAS*, 306, 857
- Dalton, G. B.; Efstathiou, G.; Maddox, S. J.; Sutherland, W. J., 1994 *MNRAS*, 269, 151
- Davies, Roger L.; Allington-Smith, Jeremy R.; Bettess, P.; Chadwick, E.; Content, Robert; Dodsworth, G. N.; Haynes, Roger; Lee, D.; Lewis, Ian J.; Webster, J.; Atad, E.; Beard, Steven M.; Ellis, M.; Hastings, Peter R.; Williams, Phil R.; Bond, Tim; Crampton, David; Davidge, Timothy J.; Fletcher, Murray; Leckie, Brian; Morbey, Christopher L.; Murowinski, Richard G.; Roberts, Scott; Saddlemyer, Leslie K.; Sebesta, Jerry; Stilburn, James R.; Szeto, Kei 1997 *SPIE*, 2871, 1099
- Djorgovski, S. 1986, *Nearly Normal Galaxies*, p227, Ed. Faber, Springer-Verlag, NY.

- Donahue, Megan; Mack, Jennifer; Voit, G. Mark; Sparks, William; Elston, Richard; Maloney, Philip R. 2000 ApJ, 545, 670
- Donahue, Megan; Mack, Jennifer; Scharf, Caleb; Lee, Paul; Postman, Marc; Rosati, Piero; Dickinson, Mark; Voit, G. Mark; Stocke, John T. 2001 ApJ, 552, 93
- Dressler, A.; Thompson, I. B.; Shectman, S. A. 1985 ApJ, 288, 481
- Dressler, Alan; Smail, Ian; Poggianti, Bianca M.; Butcher, Harvey; Couch, Warrick J.; Ellis, Richard S.; Oemler, Augustus, Jr. 1999 ApJS, 122, 51
- Ebeling, H.; Edge, A. C.; Böhringer, H.; Allen, S. W.; Crawford, C. S.; Fabian, A. C.; Voges, W.; Huchra, J. P. 1998 MNRAS, 301, 881
- Ebeling, H.; Jones, L. R.; Perlman, E.; Scharf, C.; Horner, D.; Wegner, G.; Malkan, M.; Fairley, B. W.; Mullis, C. R. 2000 ApJ, 534, 133
- Ebeling, H.; Edge, A. C.; Henry, J. P. 2001 ApJ, 553, 668
- Ebeling, Harald; Mullis, Christopher R.; Tully, R. Brent 2002ApJ, 580, 774
- Ebeling, H. Priv Comm. 31st October 2002
- Eddington, A. S. 1919 Obs, 42, 119
- Edge, A. C. 1991 MNRAS, 250, 103
- Edge, A. C.; Stewart, G. C. 1991 MNRAS, 252, 428
- A.C. Edge *Active Galactic Nuclei in Clusters of Galaxies* in "The Nature of compact objects in Clusters" ed. A. Robinson & R.J. Terelevich 1992, CAP, 125
- Edge, A. C.; Ivison, R. J.; Smail, Ian; Blain, A. W.; Kneib, J.-P. 1999 MNRAS, 306, 599
- Edge, A. C. 2001 MNRAS, 328, 762
- Edge, A. C.; Wilman, R. J.; Johnstone, R. M.; Crawford, C. S.; Fabian, A. C.; Allen, S. W. 2002 MNRAS, 337, 49

- Edge, A. C.; Ebeling, H.; Bremer, M.; Röttgering, H.; van Haarlem, M. P.; Rengelink, R.; Courtney, N. J. D. 2003 MNRAS, 339, 913
- Eggen, O. J.; Lynden-Bell, D.; Sandage, A. R. 1962 ApJ, 136, 748
- Ellis, Richard S.; Smail, Ian; Dressler, Alan; Couch, Warrick J.; Oemler, Augustus, Jr.; Butcher, Harvey; Sharples, Ray M. 1997 ApJ, 483, 582
- Fabian, A. C. 1994 ARA & A, 32, 277
- Fabian, A. C.; Sanders, J. S.; Ettori, S.; Taylor, G. B.; Allen, S. W.; Crawford, C. S.; Iwasawa, K.; Johnstone, R. M.; Ogle, P. M. 2000 MNRAS, 318, 65
- Freeman, P. E.; Kashyap, V.; Rosner, R.; Lamb, D. Q. 2002 ApJS, 138, 185
- Fukugita, M.; Ichikawa, T.; Gunn, J. E.; Doi, M.; Shimasaku, K.; Schneider, D. P. 1996 AJ, 111, 1748
- Lazzati, D.; Campana, S.; Rosati, P.; Chincarini, G.; Giacconi, R. 1998 A&A, 331, 41
- Le Fevre, O.; Crampton, D.; Felenbok, P.; Monnet, G. 1994 A&A, 282, 325
- Girardi, M.; Biviano, A.; Giuricin, G.; Mardirossian, F.; Mezzetti, M. 1995 ApJ, 438, 527
- Gladders, Michael D.; Lopez-Cruz, Omar; Yee, H. K. C.; Kodama, Tadayuki 1998 ApJ, 501, 571
- Gladders, Michael D.; Yee, H. K. C. 2000 AJ, 120, 2148
- Gladders, Michael D.; Hoekstra, Henk; Yee, H. K. C.; Hall, Patrick B.; Barrientos, L. Felipe 2003 ApJ, 593, 48
- de Grandi, S.; Böhringer, H.; Guzzo, L.; Molendi, S.; Chincarini, G.; Collins, C.; Cruddace, R.; Neumann, D.; Schindler, S.; Schuecker, P.; Voges, W. 1999 ApJ, 514 148

- Griffin, G.; Peterson, J.; Romer, K.; Alvarez, D.; Cantalupo, C.; Morgan, D.; Newcomb, M.; Vincent, M.; Miller, K.; Novak, G.; Dragovan, M.; Crone, B. 1998 AAS, 192, 5803
- Guzzo, L.; Bohringer, H.; Schuecker, P.; Collins, C. A.; Schindler, S.; Neumann, D. M.; de Grandi, S.; Cruddace, R.; Chincarini, G.; Edge, A. C.; Shaver, P. A.; Voges, W. 1999 *The Messenger*, 95, 27
- Guzzo, L. to Edge, A. Private Comm 2002.
- Henry, J. P.; Briel, U. G. 1991 A&A, 246, 14
- Hewitt, A.; Burbidge, G. 1991 ApJS, 75, 297
- Holwerda "Source Extractor for Dummies." available from <http://www-int.stsci.edu/holwerda/se.html>
- Hook, Isobel; Allington-Smith, Jeremy R.; Beard, Steven M.; Crampton, David; Davies, Roger L.; Dickson, Colin G.; Ebbers, Angelic W.; Fletcher, J. Murray; Jorgensen, Inger; Jean, I.; Juneau, S.; Murowinski, Richard G.; Nolan, Robert; Laidlaw, Ken; Leckie, Brian; Marshall, G. E.; Purkins, Terry; Richardson, Ian M.; Roberts, Scott C.; Simons, Douglas A.; Smith, Malcolm J.; Stilburn, James R.; Szeto, Kei; Tierney, Chris; Wolff, Richard J.; Wooff, Robert 2003 SPIE 4841, 1645
- Hubble, E. P., 1925, *The Observatory*, 48, 139
- Hubble, E. P., 1936, "Realm of the Nebulae", Yale University Press
- Hubble, E. & Humason, M. L., 1931 ApJ, 74, 43
- Infante, L. 1987 A&A, 183, 177
- Irwin, Judith A.; Stil, J. M.; Bridges, T. J. 2001 MNRAS, 328, 359
- Iwasawa, K.; Fabian, A. C.; Etori, S. 2001 MNRAS, 321, 15
- Jaffe, W.; Bremer, M. N. 1997 MNRAS, 284, 1

- Jeltema, Tesla E.; Canizares, Claude R.; Bautz, Mark W.; Malm, Michael R.; Donahue, Megan; Garmire, Gordon P. 2001 ApJ, 562, 124
- Johnstone, R. M.; Fabian, A. C.; Nulsen, P. E. J. 1987 MNRAS, 224, 75
- Johnson, O.; Best, P. N.; Almaini, O. 2003 MNRAS, 343, 924
- Jones, L. R.; Scharf, C.; Ebeling, H.; Perlman, E.; Wegner, G.; Malkan, M.; Horner, D. 1998 ApJ, 495, 100
- Jones, L. R.; Ponman, T. J.; Horton, A.; Babul, A.; Ebeling, H.; Burke, D. J. 2003 MNRAS, 343, 627
- Kauffmann, Guinevere; Charlot, Stephane 1998 MNRAS, 294, 705
- Kim, R. S. J.; Annis, J.; Strauss, M. A.; Lupton, R. H. Tracing Cosmic Evolution with Galaxy Clusters. ASP Conference Proceedings, Edited by Stefano Borgani, Marino Mezzetti, and Riccardo Valdarnini. 2002, 268, 395
- King, Ivan R. 1966 AJ, 71, 64
- King, C. R.; Ellis, R. S. 1985 ApJ, 288, 456
- Kodama, T. PhD thesis, Institute of Astronomy, Univ. Tokyo , (1997)
- Kodama, T.; Arimoto, N. 1997 A&A, 320, 41
- Kodama, Tadayuki; Arimoto, Nobuo; Barger, Amy J.; Arag'on-Salamanca, Alfonso 1998 A&A 334, 99
- Kron, G. E. 1980 RA, 10, 3
- Landolt, Arlo U. 1992 AJ, 104, 340
- Lazzati, D.; Campana, S.; Rosati, P.; Chincarini, G.; Giacconi, R. 1998 A&A, 331, 41
- Lewis, I. J.; Cannon, R. D.; Taylor, K.; Glazebrook, K.; Bailey, J. A.; Baldry, I. K.; Barton, J. R.; Bridges, T. J.; Dalton, G. B.; Farrell, T. J.; Gray, P. M.; Lankshear, A.; McCowage, C.; Parry, I. R.; Sharples, R. M.; Shortridge, K.;

- Smith, G. A.; Stevenson, J.; Straede, J. O.; Waller, L. G.; Whittard, J. D.; Wilcox, J. K.; Willis, K. C. 2002 MNRAS, 333, 279
- LaRoque, Samuel J.; Joy, Marshall; Carlstrom, John E.; Ebeling, Harald; Bonamente, Massimiliano; Dawson, Kyle S.; Edge, Alastair; Holzappel, William L.; Miller, Amber D.; Nagai, Daisuke; Patel, Sandeep K.; Reese, Erik D. 2003 ApJ, 583, 559
- Limber, D. Nelson; Mathews, William G. 1960 ApJ, 132, 286
- Lucey, J. R. 1983 MNRAS, 204, 33
- Lumsden, S. L.; Nichol, R. C.; Collins, C. A.; Guzzo, L. 1992 MNRAS, 258, 1
- Lynden-Bell, D. 1967 MNRAS, 136, 101
- Madau, P; Pozzetti, L; Dickinson, M 1998 ApJ, 498 106
- Maddox, S. J.; Efstathiou, G.; Sutherland, W. J.; Loveday, J. 1990 MNRAS, 243, 692
- McNamara, B. R.; Wise, M.; Nulsen, P. E. J.; David, L. P.; Sarazin, C. L.; Bautz, M.; Markevitch, M.; Vikhlinin, A.; Forman, W. R.; Jones, C.; Harris, D. E. 2000 ApJ, 534, 135
- Magorrian, John; Tremaine, Scott; Richstone, Douglas; Bender, Ralf; Bower, Gary; Dressler, Alan; Faber, S. M.; Gebhardt, Karl; Green, Richard; Grillmair, Carl; Kormendy, John; Lauer, Tod 1998 AJ, 115, 2285
- Makishima, Kazuo; Ezawa, Hajime; Fukuzawa, Yasushi; Honda, Hirohiko; Ikebe, Yasushi; Kamae, Tuneyoshi; Kikuchi, Ken'ich; Matsushita, Kyoko; Nakazawa, Kazuhiro; Ohashi, Takaya; Takahashi, Tadayuki; Tamura, Takayuki; Xu, Haiguang 2001 PASJ, 53, 401
- Markevitch, M.; Ponman, T. J.; Nulsen, P. E. J.; Bautz, M. W.; Burke, D. J.; David, L. P.; Davis, D.; Donnelly, R. H.; Forman, W. R.; Jones, C.; Kaastra, J.; Kellogg, E.; Kim, D.-W.; Kolodziejczak, J.; Mazzotta, P.; Pagliaro, A.; Patel, S.;

- Van Speybroeck, L.; Vikhlinin, A.; Vrtilek, J.; Wise, M.; Zhao, P. 2000 ApJ, 541, 542
- Markevitch, M.; Vikhlinin, A.; Murray, S.; Forman, W.; VanSpeybroeck, L. 2000 HEAD, 32, 1701
- Nelson, Amy E.; Simard, Luc; Zaritsky, Dennis; Dalcanton, Julianne J.; Gonzalez, Anthony H. 2002 ApJ, 567, 144
- Oke, J. B.; Cohen, J. G.; Carr, M.; Cromer, J.; Dingizian, A.; Harris, F. H.; Labrecque, S.; Lucinio, R.; Schaal, W.; Epps, H.; Miller, J. 1995 PASP, 107, 375
- Pearce, F. R.; Thomas, P. A.; Couchman, H. M. P.; Edge, A. C. 2000 MNRAS, 317, 1029
- Peebles, P. J. E. 1970 AJ, 75, 13
- Petrosian, A. R.; Turatto, M. 1986 A&A, 163, 26
- Perlmutter, S.; Aldering, G.; Goldhaber, G.; Knop, R. A.; Nugent, P.; Castro, P. G.; Deustua, S.; Fabbro, S.; Goobar, A.; Groom, D. E.; Hook, I. M.; Kim, A. G.; Kim, M. Y.; Lee, J. C.; Nunes, N. J.; Pain, R.; Pennypacker, C. R.; Quimby, R.; Lidman, C.; Ellis, R. S.; Irwin, M.; McMahon, R. G.; Ruiz-Lapuente, P.; Walton, N.; Schaefer, B.; Boyle, B. J.; Filippenko, A. V.; Matheson, T.; Fruchter, A. S.; Panagia, N.; Newberg, H. J. M.; Couch, W. J.; The Supernova Cosmology Project 1999 ApJ, 517, 565
- Pimblet, Kevin A.; Smail, Ian; Kodama, Tadayuki; Couch, Warrick J.; Edge, Alastair C.; Zabludoff, Ann I.; O'Hely, Eileen 2002 MNRAS, 331, 333
- Press, W.H.; Teukolsky, S.A.; Vetterling, W.T.; Flannery B.P. *Numerical Recipes in FORTRAN (second edition)* Cambridge University Press
- Ravindranath, Swara; Ho, Luis C. 2002 ApJ, 577, 133
- Rood, H. J., Ph.D. Thesis, University of Michigan.
- Quilis, Vicent; Moore, Ben; Bower, Richard 2000 Sci 288 1617

- Quilis, Vicent; Bower, Richard G.; Balogh, Michael L. 2001 MNRAS, 328, 1091
- Randall, S. W.; Sarazin, C. L.; Ricker, P. M. 2002 AAS, 201, 6706
- Romer, A. K.; Cantalupo, C. M.; Gomez, P.; Ade, P. A. R.; Bock, J. J.; Coble, K.; Daub, M. D.; Goldstein, J.; Griffin, G.; Holzzapfel, W. L.; Kuo, C.; Lange, A. E.; Lueker, M.; Newcomb, M.; Peterson, J. B.; Ruhl, J.; Runyan, M.; Torbet, E. 2001 AAS, 199, 142.06
- Romer, A. Kathy; Viana, Pedro T. P.; Liddle, Andrew R.; Mann, Robert G., 2001 ApJ, 547, 594
- Rosati, Piero; della Ceca, Roberto; Norman, Colin; Giacconi, Riccardo 1998 ApJ, 492, 21
- Sahu, Kailash C.; Shaw, Richard A.; Kaiser, Mary Elizabeth; Baum, Stefi A.; Ferguson, Henry C.; Hayes, Jeffrey J. E.; Gull, Theodore R.; Hill, Robert J.; Hutchings, John B.; Kimble, Randy A.; Plait, Philip; Woodgate, Bruce E. 1998 ApJ, 492, 125
- Sandage A.R., 1972a ApJ, 173, 585
- Sandage A.R., 1972b ApJ, 178, 1
- Sarazin, Craig L. 1986 RvMP, 58, 1
- Sarazin, C. L., 1988, "X-ray Emission from Clusters of Galaxies", Cambridge Astrophysics Series, CUP
- Scharf, C. A.; Jones, L. R.; Ebeling, H.; Perlman, E.; Malkan, M.; Wegner, G. 1997 ApJ, 477, 79
- Schlegel, D. J.; Finkbeiner, D P.; Davis, M. 1998 ApJ, 500, 525
- Schlegel, David J.; Finkbeiner, Douglas P.; Davis, Marc 1998 ApJ, 500, 525
- Seyfert, Carl K. 1943 ApJ, 97, 28
- Smail, Ian; Edge, Alastair C.; Ellis, Richard S.; Blandford, Roger D. 1998 MNRAS, 293, 124

- Stanford, S. A.; Eisenhardt, Peter R.; Dickinson, Mark 1998 ApJ, 492, 461
- Spergel, D. N.; Verde, L.; Peiris, H. V.; Komatsu, E.; Nolta, M. R.; Bennett, C. L.; Halpern, M.; Hinshaw, G.; Jarosik, N.; Kogut, A.; Limon, M.; Meyer, S. S.; Page, L.; Tucker, G. S.; Weiland, J. L.; Wollack, E.; Wright, E. L. 2003 ApJS, 148, 175
- Stoughton, Chris; Lupton, Robert H.; Bernardi, Mariangela; Blanton, Michael R.; Burles, Scott; Castander, Francisco J.; Connolly, A. J.; Eisenstein, Daniel J.; Frieman, Joshua A.; Hennessy, G. S.; and 182 coauthors 2002 AJ, 123, 485
- Sun, M.; Murray, S. S. 2002 ApJ, 577, 139
- Terlevich, A. 1998 PhD Thesis, University of Durham
- Tonry, J.; Davis, M. 1979 AJ, 84, 1511
- Tucker, W.; Blanco, P.; Rappoport, S.; David, L.; Fabricant, D.; Falco, E. E.; Forman, W.; Dressler, A.; Ramella, M. 1998 ApJ, 496, 5
- Trümper, J., 1993 Science, 260, 1769
- University of Hawaii Telescopes at Mauna Kea Observatory user manual. 4th Ed, June 1997. Available from: <http://www.ifa.hawaii.edu/88inch/manuals/user.pdf>
- Urry, C. Megan; Padovani, Paolo 1995 PASP, 107, 803
- de Vaucouleurs, G., 1961, AJ, 66, 629
- Vazdekis, Alexandre; Kuntschner, Harald; Davies, Roger L.; Arimoto, Nobuo; Nakamura, Osamu; Peletier, Reynier 2001 ApJ, .551, 127
- M.P. Veron-Cetty, P. Veron 2000, ESO Sci. Rep., 19, 1
- Vikhlinin, A.; Markevitch, M.; Murray, S. S. 2001 ApJ, 549, 4
- Visvanathan, N.; Sandage, A. 1977 ApJ 216, 214
- Voges, W.; Aschenbach, B.; Boller, Th.; Bräuninger, H.; Briel, U.; Burkert, W.; Dennerl, K.; Englhauser, J.; Gruber, R.; Haberl, F.; Hartner, G.; Hasinger, G.;

- Kürster, M.; Pfeffermann, E.; Pietsch, W.; Predehl, P.; Rosso, C.; Schmitt, J. H. M. M.; Trümper, J.; Zimmermann, H. U. 1999 *A&A*, 349, 389
- Wolf, R., 1865, *Astron. Nach.*, 65, 1
- Worthey, Guy 1994 *ApJS*, 95, 107
- York, Donald G.; Adelman, J.; Anderson, John E., Jr.; Anderson, Scott F.; Annis, James; Bahcall, Neta A.; Bakken, J. A.; Barkhouser, Robert; Bastian, Steven; Berman, Eileen; Boroski, William N.; Bracker, Steve; Briegel, Charlie; Briggs, John W.; Brinkmann, J.; Brunner, Robert; Burles, Scott; Carey, Larry; Carr, Michael A.; Castander, Francisco J.; Chen, Bing; Colestock, Patrick L.; Connolly, A. J.; Crocker, J. H.; Csabai, István; Czarapata, Paul C.; Davis, John Eric; Doi, Mamoru; Dombeck, Tom; Eisenstein, Daniel; Ellman, Nancy; Elms, Brian R.; Evans, Michael L.; Fan, Xiaohui; Federwitz, Glenn R.; Fiscelli, Larry; Friedman, Scott; Frieman, Joshua A.; Fukugita, Masataka; Gillespie, Bruce; Gunn, James E.; Gurbani, Vijay K.; de Haas, Ernst; Haldeman, Merle; Harris, Frederick H.; Hayes, J.; Heckman, Timothy M.; Hennessy, G. S.; Hindsley, Robert B.; Holm, Scott; Holmgren, Donald J.; Huang, Chi-hao; Hull, Charles; Husby, Don; Ichikawa, Shin-Ichi; Ichikawa, Takashi; Ivezic, Zeljko; Kent, Stephen; Kim, Rita S. J.; Kinney, E.; Klaene, Mark; Kleinman, A. N.; Kleinman, S.; Knapp, G. R.; Korienek, John; Kron, Richard G.; Kunszt, Peter Z.; Lamb, D. Q.; Lee, B.; Leger, R. French; Limmongkol, Siriluk; Lindenmeyer, Carl; Long, Daniel C.; Loomis, Craig; Loveday, Jon; Lucinio, Rich; Lupton, Robert H.; MacKinnon, Bryan; Mallery, Edward J.; Mantsch, P. M.; Margon, Bruce; McGehee, Peregrine; McKay, Timothy A.; Meiksin, Avery; Merelli, Aronne; Monet, David G.; Munn, Jeffrey A.; Narayanan, Vijay K.; Nash, Thomas; Neilsen, Eric; Neswold, Rich; Newberg, Heidi Jo; Nichol, R. C.; Nicinski, Tom; Nonino, Mario; Okada, Norio; Okamura, Sadanori; Ostriker, Jeremiah P.; Owen, Russell; Pauls, A. George; Peoples, John; Peterson, R. L.; Petravick, Donald; Pier, Jeffrey R.; Pope, Adrian; Pordes, Ruth; Prosapio, Angela; Rechenmacher, Ron; Quinn, Thomas R.; Richards, Gordon T.; Richmond, Michael W.; Rivetta, Claudio H.; Rockosi, Constance M.; Ruthmansdorfer, Kurt; Sandford, Dale; Schlegel, David J.; Schneider, Donald P.; Sekiguchi, Maki; Sergey, Gary; Shimasaku, Kazuhiro; Siegmund, Walter A.; Smee, Stephen;

Smith, J. Allyn; Snedden, S.; Stone, R.; Stoughton, Chris; Strauss, Michael A.; Stubbs, Christopher; SubbaRao, Mark; Szalay, Alexander S.; Szapudi, Istvan; Szokoly, Gyula P.; Thakar, Anirudda R.; Tremonti, Christy; Tucker, Douglas L.; Uomoto, Alan; Vanden Berk, Dan; Vogeley, Michael S.; Waddell, Patrick; Wang, Shu-i.; Watanabe, Masaru; Weinberg, David H.; Yanny, Brian; Yasuda, Naoki
2000 AJ, 120, 1579

